ON STRUCTURE AND SCALING AT FIRST AND SECOND ORDER PHASE TRANSITIONS

by
John Frederick Daniel Marko

Bachelor of Science
University of Alberta
June 1984

SUBMITTED TO THE DEPARTMENT OF
PHYSICS
IN PARTIAL FULFILLMENT OF THE
REQUIREMENTS FOR THE
DEGREE OF
DOCTOR OF PHILOSOPHY IN PHYSICS

at the

MASSACHUSETTS INSTITUTE OF TECHNOLOGY

August 1989

Signature of Author: _____

Department of Physics
August 18, 1989

Certified by: _____

A. Nihat Berker
Professor, Department of Physics
Thesis Supervisor

Accepted by: _____

George F. Koster, Chairman
Departmental Graduate Committee

Science

ON STRUCTURE AND SCALING AT FIRST AND SECOND ORDER PHASE TRANSITIONS

by

John Frederick Daniel Marko

Submitted to the Department of Physics
in August 1989 in partial fulfillment of the
requirements for the Degree of
Doctor of Philosophy in Physics

ABSTRACT

Theoretical investigations of the phase diagrams and the structural properties of various Hamiltonians near their equilibrium phase transitions are presented. First, a lattice model of polar liquid crystals has been developed to study exotic reentrant phenomena in mixtures and bicritical phenomena in pure systems.

Following this, a study of first-order phase transitions in simpler fluids composed of particles interacting only by exclusion interactions is presented. This work treats the full orientational and translational degrees of freedom of the constituent particles using the density-functional approach, which allows calculation of the Landau parameters that couple to combinations of order parameters *ab initio.* A theory for the effect of molecular anisotropy on transitions to phases with either of or both positional and orientational order, and a description the thermodynamics of hard-sphere solids, including their elastic properties have thus been obtained.

At a tricritical point, properties of interest change from the microscopic to the macroscopic. A study of a paradigm for the tricritical point, the two-dimensional Potts model, based on a Monte Carlo renormalization-group approach is presented. The decrease in irrelevance of the next-to-leading thermal eigenvalue at the Potts fixed point is demonstrated as Q, the number of states, is increased toward $Q = 4$.

The advent of the characterization of patterns resulting from nonlinear dynamical systems has revealed that an infinite number of observable scaling exponents can be defined, which are nontrivially related in many cases. A study of the correspondence between simple statistical models and certain multifractal trees indicates that multifractal measures can be classified according to aspects of their geometry that correspond to elementary excitations.

Finally, a new type of scaling analysis is presented that reveals some previously unreported properties of critical phenomena. This idea, which is based on the study of the scaling of moments of an order parameter distribution, will be compared and contrasted to multifractal scaling analysis of singular measures.

Thesis Advisor: A. Nihat Berker
Professor, Department of Physics

Acknowledgements

I am singularly indebted to my advisor Nihat Berker, for his guidance and support, for his excellent teaching, and his inspiring approach to research problems. His many ideas and insights have shaped this thesis, and for them I am grateful.

My parents, my first educators, research supervisors, and grant monitors, receive my greatest thanks for their love and direction.

I have benefited greatly from brilliant teaching of condensed matter physics, and the maintenance of a fantastic research center by Mehran Kardar, John Joannopoulos, Patrick Lee, and Gabriel Kotliar. My interactions with the students and postdocs in the theory group have been an important part of my education: I especially want to thank Charles Kane, Eugen Tarnow, Ken Hui, Jialin Lui, Maya Pazcuski, Ernesto Medina, Terry Hwa, Nick Read, Karin Rabe, Weige Xue, and Slava Serota for many illuminating discussions of scientific and not-so-scientific topics. I also would like to acknowledge many pleasant and rewarding discussions with Joseph Indekeu, Paul Linsay, Stéphane Zaleski, and Bill Curtin.

My home life has been one of Bohemian camaraderie, thanks to my housemates Andrew Cumming, Judy Rankin, John Scott-Thomas, and Janet Leatherwood. I especially thank Andrew for his patient teaching, for sharing his many insights, for our trips to Toronto, and most of all for his steadfast friendship.

I would like to thank Rainer Weiss and Andrew Jeffries of the MIT Gravitation and Cosmology Group for generously allowing me free run of their computational facilities. Computations were also done at the John von Neumann Supercomputer Center under Grant No. NAC-1290.

I was partially supported at MIT by a Postgraduate Scholarship from the Natural Sciences and Engineering Research Council of Canada, and by a Josephine de Kármán Fellowship. The research presented here was also supported by the National Science Foundation under Grants No. DMR-84-18718 and No. DMR-87-19217, and by the Joint Services Electronics Program under Contracts No. DAAL 03-83-K0002 and No. DAAL 03-89-C0001.

Contents

Chapter 1

Introduction

"For us, Ph.D. means 'Phase Diagrams'" - J. O. Indekeu, August 1986

1.1 History of the Study of Phase Transitions

Modern condensed matter theory emphasizes the understanding of emergent properties of physical systems composed of many interacting constituents. These emergent, generally macroscopic properties, such as the average density of a fluid, the net magnetization of a spin system, or the electrical conductivity of a solid are almost always analytic functions of thermodynamical coordinates such as temperature, pressure, or electromagnetic fields. The exceptions to this analytic behavior are of crucial importance: they are the points at which phase transitions occur, and where macroscopic properties of a physical system change dramatically.

The phase transitions that we encounter most frequently are of course the melting and vaporization transitions of water. These are examples where the density and internal energy change discontinuously at the transition, and accordingly these are termed discontinuous, or first-order phase transitions. If we follow the vaporization line for a fluid system, we find that the density difference between the coexisting liquid and gas phases decreases (as pressure and temperature increase, generally) to zero. Beyond this point, the critical point, there is no phase transition to be found between the two fluid phases. The nonanalyticity at the critical point is a different type of phase transition: the first derivatives of the thermodynamical potential are continuous, but higher derivatives display divergences. A phase transition of this type may be termed critical, continuous, or second-order (if the specific heat and susceptibilities diverge).

The nonanalyticities at continuous phase transitions often are of power-law form. In a magnetic system, it is found that as a function of distance from the critical point along the temperature direction $t = (T - T_c)/T_c$, the specific heat diverges as $|t|^{-\alpha}$, the bulk magnetization rises from zero upon entering the ordered phase as $|t|^{\beta}$, and the susceptibility, the response of the order parameter to a field that linearly couples to it, diverges as $|t|^{-\gamma}$. The indices α, β, and γ are known as critical exponents. Experimentally, it is found that the critical exponents are the same for many seemingly

unrelated physical systems (eg. certain liquid-gas, binary alloy, and ferromagnetic transitions share the same critical exponents), suggesting that the understanding of critical phenomena will lead to an understanding of the relationships between diverse physical systems. Systems with the same critical exponents are said to belong to the same universality class.

The theoretical study of critical phenomena began with the identification of the order parameter as the fundamental object of interest. The expectation value of the order parameter is typically zero in the high-symmetry disordered phase, and nonzero in the ordered phase, where the symmetry of the system is broken. Examples of order parameters are the bulk magnetization and the liquid-gas density difference for the ferromagnetic and liquid-gas systems mentioned previously.

Landau[1] recognized that by writing a free energy functional analytic in the order parameter and invariant under the symmetry group of the microscopic Hamiltonian, the minimization of the resulting functional under the assumption of a uniform value of the order parameter led to a theory of spontaneous symmetry breaking. The 'Landau parameters' that appear in front of the various symmetry-invariant order-parameter combinations are presumed to follow from the Hamiltonian, and often enough is known about them from symmetry considerations alone to describe the qualitative phase diagram in terms of thermodynamical coordinates. The critical exponents of Landau theory for all dimensionalities of space, and for all types of order parameters are $\alpha = 0$ (specific heat discontinuity), $\beta = 1/2$, and $\gamma = 1$. Too much universality is thus obtained, in disagreement with experiments and with many available exact results.

The failure of this 'classical' theory, equivalent to the older theories of van der Waals[2] and of Curie and Weiss[3] for critical behavior in liquid-gas and magnetic systems, is due to the fact that it relies on the assumption of a uniform order parameter and thus ignores fluctuations that will generally tend to promote disorder. Fluctuations become more important in systems of lower dimension, where they can

more effectively block coherent effects.

The effects of fluctuations were studied by Ginzburg[4], who showed how below a certain 'upper critical dimension', they modify the critical behavior. For the liquid-gas and magnetic critical points, this dimension is $d_u = 4$. For low enough dimensions, it can be shown that disorder is preferable at all temperatures above zero, suggesting a 'lower critical dimension' below which no finite-temperature critical behavior can be observed. This d_l is usually 2 or 1, depending on if the Hamiltonian is invariant under a continuous or discrete transformation of the order parameter. The goal of the modern theory of critical phenomena is to identify the order parameter, to thereby understand the upper and lower critical dimensions, and then to understand the nature of the phase transitions between these two limits of space dimension.

The key to the modern understanding of critical phenomena was Kadanoff's realization[5] that because the correlation length ξ diverges at the critical point, a rescaling of space $\mathbf{x}' = \mathbf{x}/b$, accompanied by a suitable coarse-graining of the microscopic degrees of freedom, corresponds to a transformation of the underlying free energy functional to a new functional of the same form. Kadanoff showed how this picture could explain relations between the critical exponents, and suggested that the details of the rescaling of the temperature and magnetic interactions near the critical point would lead to determination of the exponents.

Wilson achieved this goal through the invention of the momentum-space renormalization group[6]. This allows a expansion in powers of the deviation from the upper critical dimension $\epsilon = d_u - d$ to be obtained for the critical exponents. This systematic approach to the problem demonstrated that in principle, critical phenomena could be understood using the rescaling approach.

Much has been learned about critical phenomena since the development of the momentum-space RG, both through its extension to different sorts of critical phenomena, and through the use of nonperturbative position-space formulations of the RG. However, problems remain with the use of the RG for low dimensions: for $d = 2$, ϵ

is large, and the expansion appears ill-behaved, while the nonperturbative approaches can lead to erroneous results due to their uncontrolled nature.

Fortunately, new tools continue to appear such as the generalization of the idea of scale invariance to invariance under conformal transformations[7] that has led to a general classification scheme for many two-dimensional critical phenomena. The study of conformal invariance also has led to much new information about criticality in higher dimensions. New exact solutions to statistical models and new techniques, such as mappings to the Coulomb gas[8], have given us other types of exact information about critical phenomena in $d = 2$. The study of critical phenomena, particularly in the presence of disorder, seems to present countless avenues of research.

The study of critical phenomena has led us to develop the renormalization group, and has taught us to apply it to situations where there are scaling symmetries. This general utility of the RG has led to applications of it in areas outside of the realm of equilibrium phase transitions, such as the study of dynamical critical phenomena, many-body quantum mechanics, the transition to chaos in nonlinear dynamical systems with small numbers of degrees of freedom, and the characterization of scale-invariant patterns that appear in strongly driven nonequilibrium systems. The ideas of critical exponents, scaling laws, and universality are thus no longer confined to the annals of statistical mechanics.

1.2 Structure and Scaling Near Phase Transitions

Although critical phenomena can be classified as belonging to one or another of a small number of universality classes, other aspects of the phase transitions that are observed in a given physical system depend in a complicated way on the details of the underlying Hamiltonian. The location of the transitions in terms of thermodynamical coordinates, the nature of the global phase diagram, and the identification of the important order parameter for a particular transition are all problems that are related directly to the interactions and degrees of freedom in the Hamiltonian.

Complex liquid systems such as polymers, micelles, microemulsions, liquid crystals, membranes, colloids, and gels all possess complicated phase diagrams due to the competition and interaction between different orderings. The number of Landau parameters necessary to consider even a small set of order parameters seriously impairs the theoretical understanding of phase transitions in these cases. Thus, it is often advantageous to consider microscopic models for these systems to build intuition and provide guidance for more systematic studies.

In Chapter 2, a model for transitions between the smectic A_1 and A_d and the nematic phases of polar liquid crystals is discussed. The spectacular reentrant phenomena observed experimentally are seen in this model, and in this chapter I describe the development of a theory of phase transitions in mixtures of these materials[9]. I obtain an expanded set of possible phase diagrams, which include many corresponding to experimental results. Also discussed will be the inclusion of second-neighbor intralayer interactions and their effect on the theoretical phase diagram. The additional interactions cause the transition between the two smectics to become first order at low temperatures rather than occuring via continuous transitions to an intermediate nematic phase. The resulting phase diagram is in qualitative agreement with experimental results[10].

A more systematic approach to the development of theories for phase transitions starting with a true fluid Hamiltonian is outlined in Chapter 3. Using results from the functional perturbation theory of liquids, a density-functional expansion of the grand thermodynamical potential can be constructed, where the expansion parameter is the difference between the expectation values of the one-body density operator in the isotropic and ordered phases. Minimizing the functional over the one-body density results in a mean-field theory of phase transitions, and in principle, fluctuations can be taken into account using standard methods of many-body theory.

I have applied this program to the transitions in fluids composed of hard cores of anisotropic shape, and I have found that with the use of liquid state information obtained from a variational study of the Percus-Yevick integral equation, this theory correctly describes the effect of hard-core anisotropy on crystallization transitions, and properly describes transitions to the nematic liquid crystal phase[11, 12]. I also present some exact results for a one-dimensional fluid that elucidate the problems with previous approaches by indicating some basic aspects of liquid structure of anisotropic fluids that have not been widely appreciated[13].

Finally, I present a technique that allows the perturbative density functional expansion to be summed to all orders. To second order, this approach reproduces the theory studied previously, and at higher orders, all two-point sum rules are satisfied exactly. I have applied this theory to the study of hard-core fluids, with results in good agreement with available simulation data. Finally, I present a rather complete calculation of thermodynamics of the hard-sphere solid, and discuss the future developments that seem likely to impact this field.

In Chapter 4 I discuss the use of a combination of the position-space renormalization group and Monte Carlo simulation in a study of the scaling behavior associated with the tricritical and critical phenomena observed in the two-dimensional Q-state Potts model. We find that this technique reveals a slightly irrelevant thermal direction as $Q = 4$ is approached. This presumably corresponds to an additional relevant

direction leading to flows away from the critical Potts fixed point, and the appearance of a first-order transition, for $Q > 4$.

Scale invariant patterns appear in many driven, nonequilibrium dynamical systems, as well as at critical points of equilibrium statistical systems. Scaling analyses of attractors of dynamical systems, growth probabilities of diffusion-limited aggregation clusters, and other nonlinear phenomena indicate that there can be infinite, universal sets of scaling exponents. Chapter 5 first addresses geometrical objects which possess these multifractal scaling properties in the context of the growth of 'trees' which develop asymptotically multifractal cross-sections. The computations of the multifractal spectra for these objects correspond to computations of the free energy of statistical-mechanical systems. This suggests that there may be 'universal' singularities observable in these spectra[14]. I present some preliminary studies indicating that these properties are readily observable using analysis of typical experimental data sets[15]. An application of these ideas linking the zero-temperature behavior of one-dimensional statistical models to the structure of the period-doubling attractor is presented, and the role of disorder and possibilities for the observation of 'finite-temperature' singularities are discussed.

The second half of Chapter 5 reports the result of multiscaling analysis applied to the study of the geometry of critical phenomena. The application of a scaling analysis of the qth moments of the spin distribution of a critical $d = 2$ Ising model shows that the exponents depend nonlinearly on q. This is surprising, since we know that the q-point correlation function scales as b^{qx_h} under a scaling transformation $\mathbf{x}' = \mathbf{x}/b$, where $2x_h = \eta$ is the usual two-point correlation function exponent. Perspectives for this problem are discussed.

Chapter 2

Mixtures and Bicritical Points in the Frustrated Spin-Gas Theory of Reentrant Polar Liquid Crystals

2.1 Introduction

Based on the study of simple statistical models with only one order parameter, we in general anticipate that at lower temperatures, more 'ordered' phases are observed. However, when there is more than one ordering possible in a system, the competition between the different orderings can lead to 'reentrance', the reappearance of a disordered phase at temperatures below (or pressures above) an ordered phase. First observed in 1921 in experiments on ferroelectric phase transitions in Rochelle salt[16] (which is a ferroelectric only between -18 and 24 degrees Celsius at standard pressure), reentrant phase transitions have been seen in liquid crystals[17] and magnetic superconductors[18], as well as in many other experiments on condensed matter.

From a theoretical perspective, the unifying feature of these diverse reentrant phenomena is the existence of more than a single ordering, and that there is 'frustration'[19] of the order parameters. Frustration of the ordering of a system results from the competition between different possible 'goals' of a many-body system where the pursuit of one goal interferes with the successful realization of others. The state that a system chooses (at least if it reaches thermodynamical equilibrium) is that with the lowest Helmholtz potential, $F = E - TS$, where E, S, and T are energy, entropy, and temperature. Disordered states have higher entropies, thus there may be phase transitions to a disordered phase from an ordered phase as temperature is lowered if the energy cost of frustration effects in the ordered states is large. This phenomenon is seen most clearly in the theoretical study of phase transitions in magnetic systems with competing ferromagnetic and antiferromagnetic interactions[20].

Liquid crystal systems have strongly coupled orientational and positional molecular degrees of freedom, and typically display a variety of mesophases between the isotropic fluid phase and the inevitable low-temperature crystal phases. These are typically the nematic fluid(with long-range orientational order, but no translational order), smectic A (in addition to having orientational order, the smectic A phases have weak translational ordering in the form of a one-dimensional density wave; perpen-

dicular to this density wave, the phase is liquid-like), and other, more exotic smectic phases. Since the discovery by Cladis[17] of the reentrant nematic and smectic phases in mixtures of the liquid crystals $HBAB$ and $CBOOA$, experiments on polar liquid crystals have revealed steadily more spectacular phase diagrams, the most involved of which display multiple reentrances where the nematic and smectic A phases are alternately encountered up to three times as temperature is reduced, both in mixtures[21], and in pure materials[22].

In these systems, the rather strong dipole-dipole interactions cancel, and frustration is thus inevitable, under the close-packing conditions of the liquid state. Berker and Walker introduced a model for the pure materials which included the dipole-dipole interactions of molecules with positional and orientational degrees of freedom[23] and discovered that reentrant phenomena appeared quite naturally for values of parameters in the model that were quite physical. The advantage of this microscopic approach is that the parameters are readily understandable, and allow the effects of details of molecular structure to be studied.

The price that is paid for this descriptive power is the discretization of the degrees of freedom of the molecules, and the approximation of studying the statistical mechanics via a prefacing transformation to an Ising spin system. An important feature of this work is the necessity of energetically favorable positions of 'permeation' (the motion of the molecules along the director axis), which is taken to be a consequence of corrugations along the hydrocarbon tails of the molecules.

Further work on this model by Indekeu and Berker revealed the existence of multiple ('quadruple') reentrances[24] in a restricted range of parameter values. This complex phase diagram is in qualitative agreement with that seen in experiments[21, 33], and moreover, the structure of the model molecules that lead to these phase diagrams is similar to that of the experimental materials[25]. Other details of the phase transitions such as relative sizes of specific heat anomalies at different transitions also agree well with experimental results[26].

There are many unanswered questions concerning this model, and in this Chapter, I will focus on two of them. One concerns the fact that the model as developed above applies to pure materials, while experimental results for mixtures are more numerous. Mixture experiments access a larger space of parameters and hence lead to even more diverse diagrams than the pressure-temperature experiments on pure systems. In Section 2.2, mixtures of polar liquid crystals are studied microscopically via the development of the frustrated spin-gas theory. Phase diagrams are calculated in the composition and temperature variables, with nematic, smectic A_d, and smectic A_1 phases joined in a variety of topologies, including multiple reentrances and bubbles. Thus, experimentally observed topologies are reproduced and new topologies are presented. It is found that the doubly and quadruply reentrant phase diagrams, seen experimentally in mixtures of successive homologs such as DB_nONO_2, are obtained for molecules with steric hindrance increasing with tail length. These model mixtures also yield reentrant phase diagrams in the pressure- temperature plane that are similar to those seen experimentally.

One aspect of the spin-gas model as described in Section 2.3, and which is common to all of the previous calculations is that the smectic A_d-smectic A_1-nematic bicritical point is observed at zero temperature, while in experiment, the meeting of the two nematic-smectic transition lines is seen at a finite temperature, below which there can be a direct $A_1 - A_d$ phase transition of first order[10]. In Section 2.3, we consider this question via consideration of the effect of further-neighbor interactions on the phase diagrams. It will be shown that the inclusion of second-neighbor interactions in the microscopic Hamiltonian leads to second-neighbor interactions in the resulting effective spin system. This causes the bicritical point to move to nonzero temperatures, below which a first-order transition between the smectic phases is observed.

2.2 Mixtures in the Frustrated Spin-Gas Theory of Reentrant Polar Liquid Crystals

by J. F. Marko, J. O. Indekeu and A. Nihat Berker

2.2.1 Introduction

If, in a certain physical system, different types of degrees of freedom fluctuate with similar energy scales, the phase transition phenomenon of reentrance is possible: As the system is cooled, one type of degree of freedom may achieve long-range order, but may disorder upon further cooling. The latter is a reentrant phase transition. It is due to the interplay of entropy and energy between the different types of degrees of freedom.

Liquid crystal systems of polar molecules have been observed to exhibit reentrant phase transition phenomena, involving nematic, smectic A_d, and smectic A_1 phases[17, 21]. In recent years, a microscopic theory[23, 24] of these systems has been developed, addressing the coupled positional and orientational degrees of freedom of the molecules. This "frustrated spin-gas theory" has produced [23, 24, 25, 26, 27, 28, 29] reentrant phase diagrams and other observed properties, in quite satisfactory agreement with experiments.

Mixing different liquid crystals greatly increases the range of observed reentrance phenomena, which motivates the current extension of the theory. The particulate character of the spin-gas theory microscopically distinguishes molecules of different structures and interactions, and thus allows extension to mixtures of different species. We obtain a variety of phase diagrams in the composition and temperature variables, exhibiting multiple reentrances and bubbles[30], i.e. regions of one phase totally enclosed by one other phase. Thus, experimentally observed topologies are reproduced and new topologies are presented.

2.2.2 The Frustrated Spin-Gas Theory and Liquid Crystal Mixtures

The molecules that we are concerned with are distinguished by two features: A dipolar head (typically a $-NO_2$ or $-CN$ group) and a hydrocarbon tail. The statistical possibility of frustration, namely the cancellation of the dipolar interactions between a given molecule and many of its neighboring molecules, under certain positional arrangements, is unavoidable under the close-packing conditions of the liquid state. Furthermore, via the corrugated architecture of the tails, the neighboring molecules provide 'substrate fields' to each others' positional fluctuations. These effects are at the heart of the spin-gas theory.

The dipolar interaction between two molecules is

$$V_d(\mathbf{r}_1, \hat{\mathbf{s}}_1, \mathbf{r}_2, \hat{\mathbf{s}}_2) = B\frac{\hat{\mathbf{s}}_1 \cdot \hat{\mathbf{s}}_2 - 3(\hat{\mathbf{s}}_1 \cdot \hat{\mathbf{r}}_{12})(\hat{\mathbf{s}}_2 \cdot \hat{\mathbf{r}}_{12})}{|\mathbf{r}_{12}|^3}, \tag{2.1}$$

where the unit vector $\hat{\mathbf{s}}_i$ and the vector $\hat{\mathbf{r}}_i$ give the orientation and position of the dipole of molecule i, $\mathbf{r}_{12} = \mathbf{r}_1 - \mathbf{r}_2$, and $\hat{\mathbf{r}}_{12} = \mathbf{r}_{12}/|\mathbf{r}_{12}|$. For simplicity, we shall use the same dipole strength B for all components in the mixture (whereas other microscopic features, the tail lengths and the tail-tail interactions, will be differentiated, as seen below). The tail-tail interaction between two molecules of species α and β is rendered by

$$V_t(\mathbf{r}_1, \hat{\mathbf{s}}_1, \mathbf{r}_2, \hat{\mathbf{s}}_2) = J_{\alpha\beta}\hat{\mathbf{s}}_1 \cdot \hat{\mathbf{s}}_2/|\mathbf{r}_{12}|^3, \tag{2.2}$$

where $J_{\alpha\beta} < 0$ reflects dominant tail-tail van der Waals attraction and $J_{\alpha\beta} > 0$ reflects dominant tail-tail steric hindrance. For the interaction between different species, $\alpha \neq \beta$, the arithmetic average is used,

$$J_{\alpha\beta} = \frac{J_{\alpha\alpha} + J_{\beta\beta}}{2}. \tag{2.3}$$

A more complicated tail-tail interaction can also be used. In the present case, the

total interaction is

$$V_{12}(\mathbf{r}_1, \hat{\mathbf{s}}_1, \mathbf{r}_2, \hat{\mathbf{s}}_2) = V_d + V_t = \frac{A_{\alpha\beta}\hat{\mathbf{s}}_1 \cdot \hat{\mathbf{s}}_2 - 3B(\hat{\mathbf{s}}_1 \cdot \hat{\mathbf{r}}_{12})(\hat{\mathbf{s}}_2 \cdot \hat{\mathbf{r}}_{12})}{|\mathbf{r}_{12}|^3}, \qquad (2.4)$$

where $A_{\alpha\beta} = B + J_{\alpha\beta}$.

The calculation proceeds with the consideration of nearest-neighbor triplets of molecules, which is the smallest cluster to include frustration effects and which allows the accounting of correlated molecular triplets as well as correlated molecular dimers. Orientational fluctuations are limited to $\hat{\mathbf{s}}_i = \pm\hat{\mathbf{z}} \equiv s_i\hat{\mathbf{z}}$. Previous calculations[23] show that positional fluctuations transverse to the molecular axes do not, by themselves, yield (or remove) reentrance, and therefore are ignored here. Thus, the molecules positionally fluctuate (permeate) in the z direction at the corners of an equilateral triangle of side a in the xy plane. This length a, interpreted as the average molecular separation, would be reduced by application of pressure, and is thus an inverse measure of the pressure.

In the spin-gas theory, the permeation degrees of freedom are affected by the molecular architecture. First, the tail corrugations create n energetically favorable positions of permeation ("notches") for each of the molecules in the triplet under consideration. The notch-to-notch distance is denoted by Γ. If molecules mutually permeate beyond n notches apart, another molecule will move into the gap thus created and replace a member of the nearest-neighbor triplet. Thus, each member of the nearest-neighbor triplet is limited to the number of notches corresponding to its own structure. Second, the molecules permeate away from the energy minima afforded by the notches, on a length scale δ much smaller than Γ. Internotch and intranotch permeation will be referred to as atomic and librational permeation, respectively. Continuous librations are approximated here by m discrete subnotches. The stability of the calculation in the continuous libration limit has been checked in previous work[28, 29]. Figure 2.1(a) displays these positional fluctuations for n=5 and m=3.

For mixtures, we simply allow the possibility of occupation of the triplet by dif-

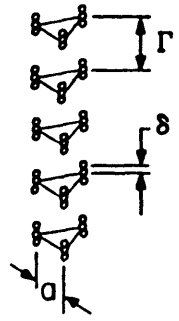

(a)

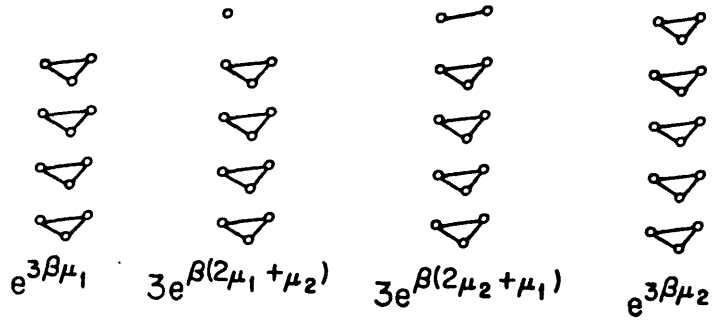

(b)

Figure 2.1: (a) Atomic and librational permeation positions of molecular dipoles in a triplet, for $n = 5$ and $m = 3$. The lengths a, Γ, and δ are indicated.
(b) Atomic permeation positions for a mixture of $n = 4$ and $n = 5$. Given beneath each possible triplet composition is the statistical weight due to chemical potentials and combinatorics.

ferent species, their overall concentration controlled by chemical potentials. Different species have different tail-tail interactions, as mentioned above, and different notch numbers.

The intermolecular interactions are prefaced onto distorted triangular couplings between the orientational variables s_i, by summing over the positional (n_i, m_i) and occupational $(t_i = \alpha, \beta)$ variables. The strongest (K_S), intermediate (K_I), and weakest (K_W) antiferroelectric couplings are projected, in a transformation which for the case of mixtures takes the form

$$\exp(K_S s_1 s_2 + K_I s_2 s_3 + K_W s_3 s_1 + G) = \sum_{\{n_i, m_i, t_i\}} \exp[-\beta(V_{12} + V_{23} + V_{31} - \mu_{t_1} - \mu_{t_2} - \mu_{t_3})], \tag{2.5}$$

where the pairs of molecular labels (12), (23), and (31) span the strongest, intermediate, and weakest antiferroelectric bonds respectively, and where μ_{t_i} is the chemical potential of species t_i. Note that the range of n_i depends on the molecule species given by t_i. For example, Figure 2.1(b) gives the positional configurations sampled in the four distinct occupational configurations for a binary mixture with $n_\alpha = 4$ and $n_\beta = 5$.

The couplings thus obtained are gauged with the ordering condition of the distorted triangular Ising model[31],

$$\sinh(2\bar{K}_1)\sinh(2\bar{K}_2) + \sinh(2\bar{K}_2)\sinh(2\bar{K}_3) + \sinh(2\bar{K}_3)\sinh(2\bar{K}_1) > 1, \tag{2.6}$$

where $\bar{K}_1 \geq \bar{K}_2 \geq |\bar{K}_3|$, as obtained from $\{K_S, K_I, K_W\}$ by changing, if necessary, two signs. Order with local antiferroelectric or ferroelectric orientations reflects the dominance of different permeationally correlated triplets and is associated with the smectic A_d or A_1 phase respectively. Conversely, disorder reflects the dominance of permeationally uncorrelated triplets and is associated with the nematic phase.

The concentrations are computed as

$$x_\alpha = \frac{1}{3}\frac{\partial}{\partial(\beta\mu_\alpha)} \log \sum_{\{s_i\}} \exp(K_S s_1 s_2 + K_I s_2 s_3 + K_W s_3 s_1 + G). \tag{2.7}$$

This completes the spin-gas theory of mixtures. Phase diagrams can now be obtained in the dimensionless variables of temperature $\Gamma^3 kT/B$, concentrations x_α, and inverse pressure a/Γ.

2.2.3 Phase Diagrams for Mixtures

A. Mixing Molecules with Different Tail Lengths but with $A_{\alpha\beta} = A$

We first obtain phase diagrams of mixtures of model molecules that microscopically differ only in notch number, which corresponds to roughly half of the number of carbons in the molecular tail. (The internotch separation Γ is determined by the carbon-carbon bonding and should not change between species.) Different tail lengths affect the possible local permeational states, which in turn contribute to different smectic A phases.

Figures 2.2(a,b) show the permeational states, with the corresponding preferred orientational arrangement, that dominate the two types of smectics: The locally antiferroelectric triplet, contributing to the smectic A_d phase, has lowest energy when formed over a three-notch range (Fig. 2.2(a)), for typical spin-gas model parameters. The locally ferroelectric triplet, contributing to the smectic A_1 phase, has lowest energy when formed over a five-notch range (Fig. 2.2(b)). Thus, if the difference of the mixture species were reflected only in the notch numbers, then the smectic A_1 phase would be more stable for larger ($n \geq 5$) notch numbers and the smectic A_d phase would be more stable for smaller notch numbers. For still smaller notch numbers ($n < 3$), the smectic A_d phase is weakened because atomic permeation does not relieve frustration (Fig. 2.2(c)). Librational permeation relieves frustration (Fig. 2.2(d)), at lower temperatures because large inverse temperatures are needed to emphasize small energy deviations, strengthening the smectic A_d phase. This raises the possibility of multiply reentrant mixture phase diagrams.

Figure 2.3 demonstrates the appearance of the smectic A_d phase as notch number is increased by mixing molecules with $n = 2$, 3, and 4. In a pure system of $n = 2$ molecules, the smectic A_d phase occurs only via librational permeation at low temperatures, as explained above. However, in mixtures of $n = 2$ and 3, a smectic A_d phase stabilized by atomic permeations does occur at higher temperatures. The two smectic A_d regions are separated by a reentrant nematic region. In the right-hand side

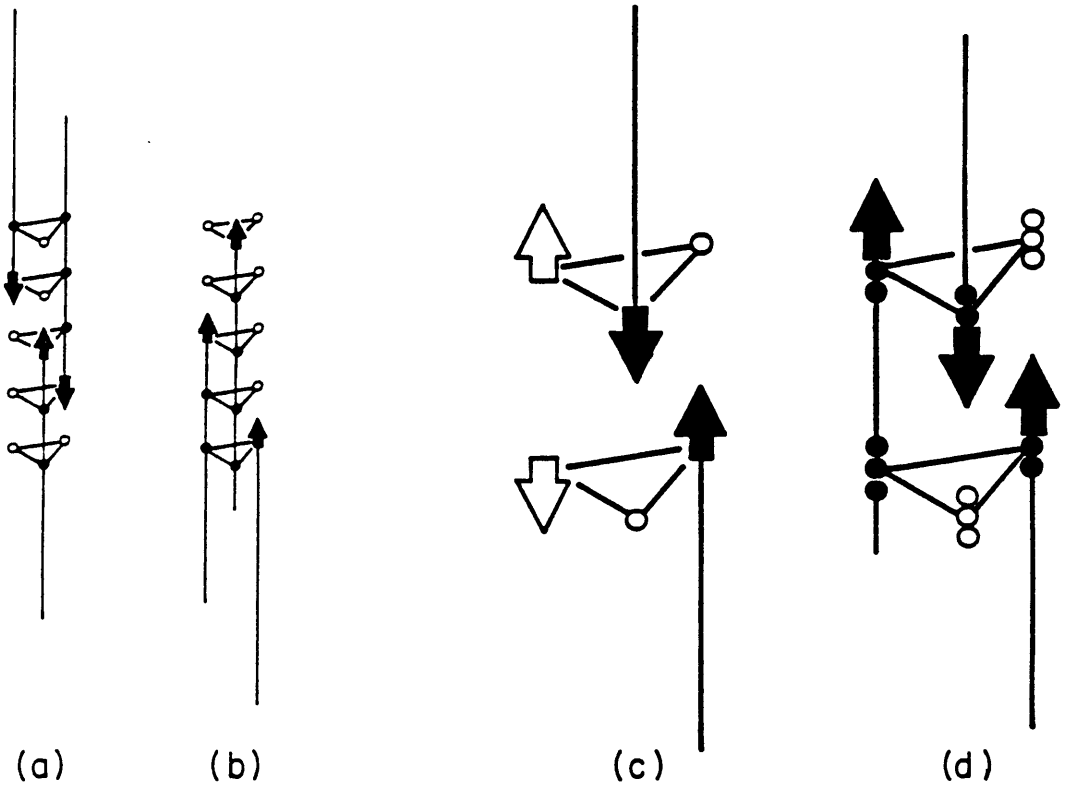

Figure 2.2: (a) Antiferroelectric low-energy triplet, contributing to smectic A_d order. The dipoles occupy a three-notch range.
(b) Ferroelectric low-energy triplet, contributing to smectic A_1 order. The dipoles occupy a five-notch range.
(c) Frustration of the case $n = 2$ and $m = 1$. For any positional configuration of the low-energy antiparallel dipole pair (e.g. dark arrows), the third dipole (open arrow) has the same energy in either positional configuration.
(d) The latter frustration can be relieved by libration. At low temperatures, the $n = 2$, $m = 3$ triplet is antiferroelectrically correlated due to these configurations.

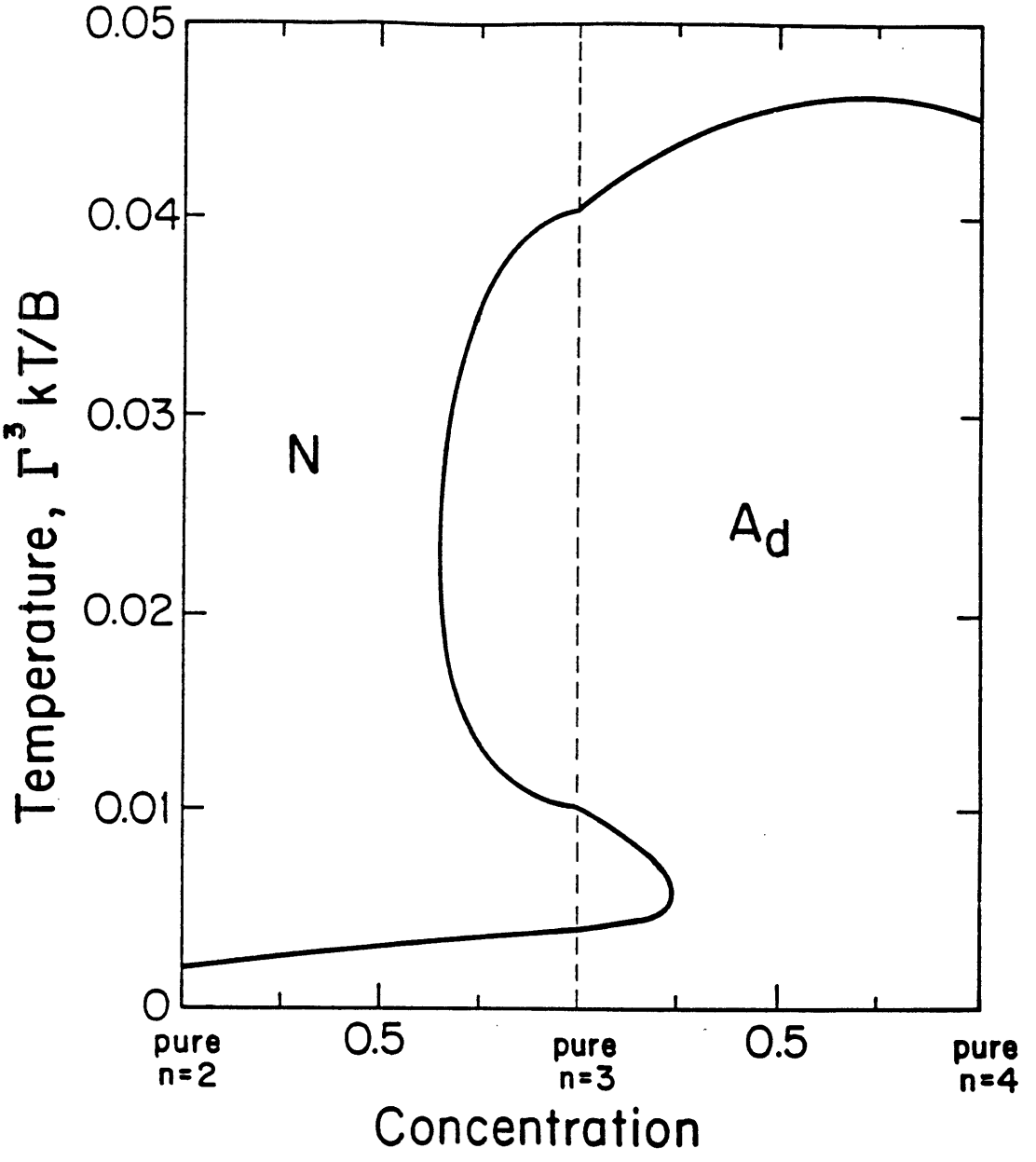

Figure 2.3: Calculated mixture phase diagram in the concentration and temperature variables. The left panel is the diagram for a binary mixture of molecules with 2 and 3 notches. The right panel is the diagram for a binary mixture of molecules with 3 and 4 notches. The concentration of the 3-notch molecule decreases from 1 to 0 from the center to the sides of the diagram. For this figure, $B/A = 1$, $a/\Gamma = 2.2$, $\delta/\Gamma = 0.01$, and $m = 2$ for all species. A doubly reentrant phase diagram is thus obtained, with the smectic A_d unstable toward the frustrated $n = 2$, but stable toward $n = 4$.

of Fig. 2.3, $n = 3$ and 4 molecules are mixed, and we see the merging of the smectic A_d phases stabilized by atomic and librational permeation. This phase diagram is similar to the reentrant phase diagrams[17] of mixtures of $HBAB$ (6-carbon tail) and $CBOOA$ (8-carbon tail).

In mixtures of longer molecules, the smectic A_1 phase appears for cases of $B > A$, which grants low energies to ferroelectric triplets via the attractive tail-tail interaction. Figure 2.4 shows phase diagrams of mixtures of $n = 5$ with $n = 4$ or $n = 6$, for $B/A = 1.48$. Similarity with experiment is seen in Figs. 2.5(b) and (c), which respectively show our calculated a/Γ-temperature phase diagram of the 22% $n = 4$, 78% $n = 5$ model and the experimental pressure-temperature phase diagram[33] of the 22% $6ONPBB$, 78% $9OBCAB$ system. Recalling that a/Γ is an inverse-pressure variable, one notes that compression of the system destabilizes the smectic A_d phase, both in theory and in experiment.

Other phase diagrams result for different choices of molecular constants. Figure 2.5(a) features a reentrant nematic phase that is stable over a wide range of notch numbers, spanning mixtures of $n = 4$ and 5, $n = 5$ and 6, and $n = 6$ and 7. Such isomorphism is observed in some experimental systems of homologous molecules, such as in the mixture[32] of the 8- and 9-carbon-tail members of the '1a' family (Fig. 2.6(b)).

A remarkable aspect of the spin-gas model for single-component systems is that it includes quadruply reentrant topologies[24] ($N - A_d - N - A_d - N - A_1$ as temperature is lowered), similar to those seen in pressure-temperature experiments[22] on single-component materials and also in concentration-temperature experiments[21] on mixtures. Figure 2.6 gives a quadruply reentrant phase diagram, calculated at this juncture, for the mixture of $n = 5$ molecules with $n = 4$ or $n = 6$ molecules. The smectic A_d phase turns out to be unstable to the admixture of the longer homolog, whereas experiment[21] shows such behavior with the shorter homolog. This calculation thus indicates that the difference in tail lengths is not only reflected in the notch

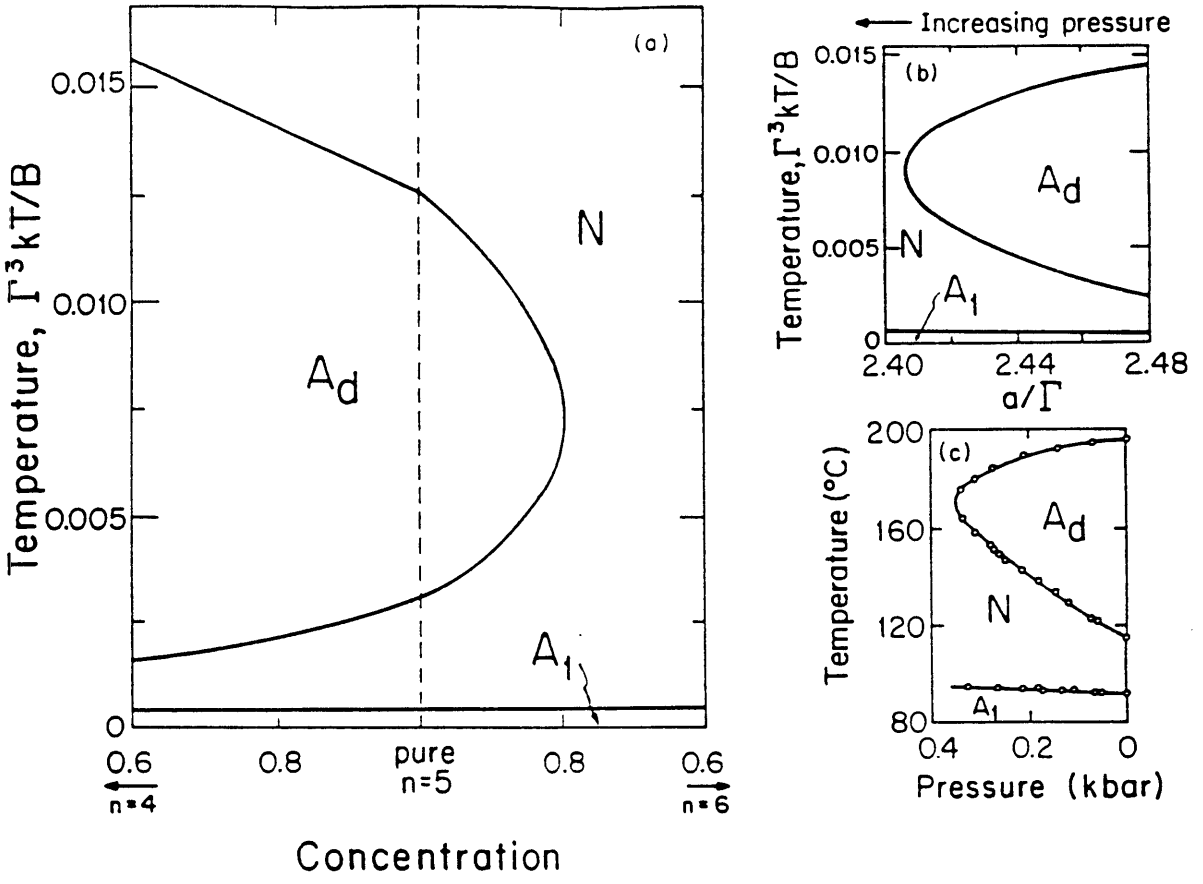

Figure 2.4: (a) Calculated concentration-temperature phase diagram for mixtures of long molecules and $B/A > 1$. Dilution of $n = 5$ molecules by $n = 4$ and $n = 6$ molecules are shown on the left and right panels respectively. The concentration of $n = 5$ decreases from 1.0 to 0.6 from the center to the sides of this composite phase diagram. For this figure, $B/A = 1.48$, $a/\Gamma = 2.48$, $\delta/\Gamma = 0.01$, and $m = 2$ for all species. The smectic A_d is unstable toward the longer homolog.
(b) Calculated a/Γ-temperature phase diagram for 22 % of $n = 4$ and 78 % of $n = 5$ molecules. The smectic A_d is unstable to a decrease in a/Γ, i.e. to a compression of the system.
(c) Experimental pressure-temperature phase diagram for the 22 % $6ONPBB$, 78 % $9OBCAB$ system (Ref. 12). Again the smectic A_d is unstable to the application of pressure.

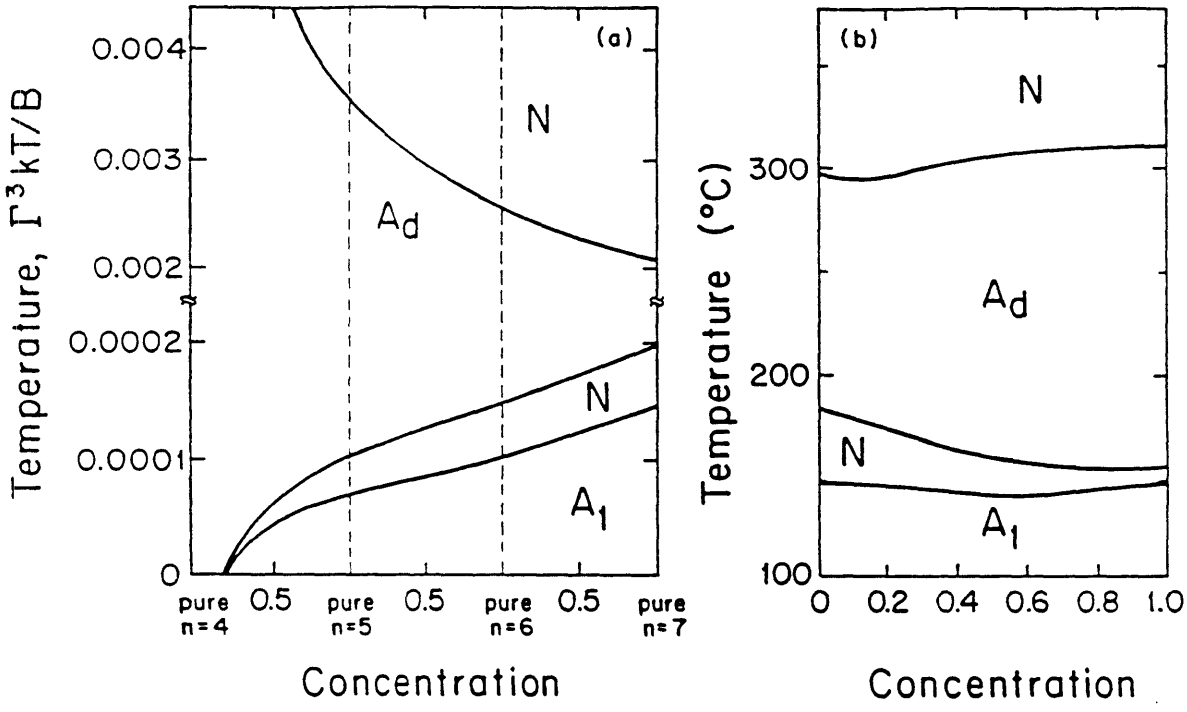

Figure 2.5: (a) Isomorphism across a range of n in the theory. For certain values of the constants (e.g., here, $B/A = 1.46$, $a/\Gamma = 1.725$, $\delta/\Gamma = 0.01$, and $m = 2$ for all species), the reentrant nematic is stable beneath the smectic A_d for mixtures of notch numbers n and $n+1$, from 4 and 5 to 6 and 7.
(b) Experimental phase diagram[32] showing the isomorphism of the mesophases of the 1a compounds for mixtures of tail lengths of 8 and 9.

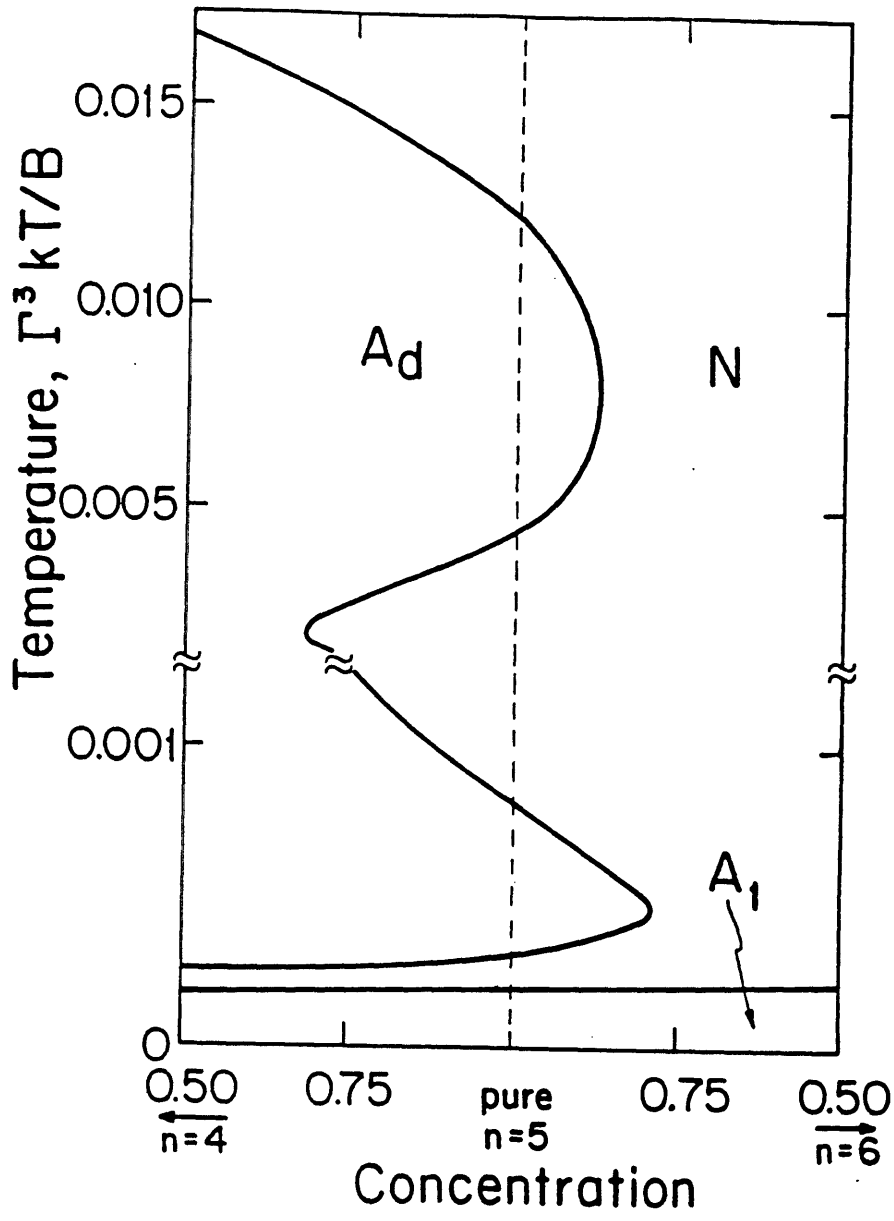

Figure 2.6: Calculated quadruply reentrant phase diagram in the concentration and temperature variables, for mixtures of $n = 5$ with $n = 4$ and with $n = 6$ molecules. Here, $B/A = 1.46$, $a/\Gamma = 2.435$, $\delta/\Gamma = 0.01$, and $m = 2$ for all species.

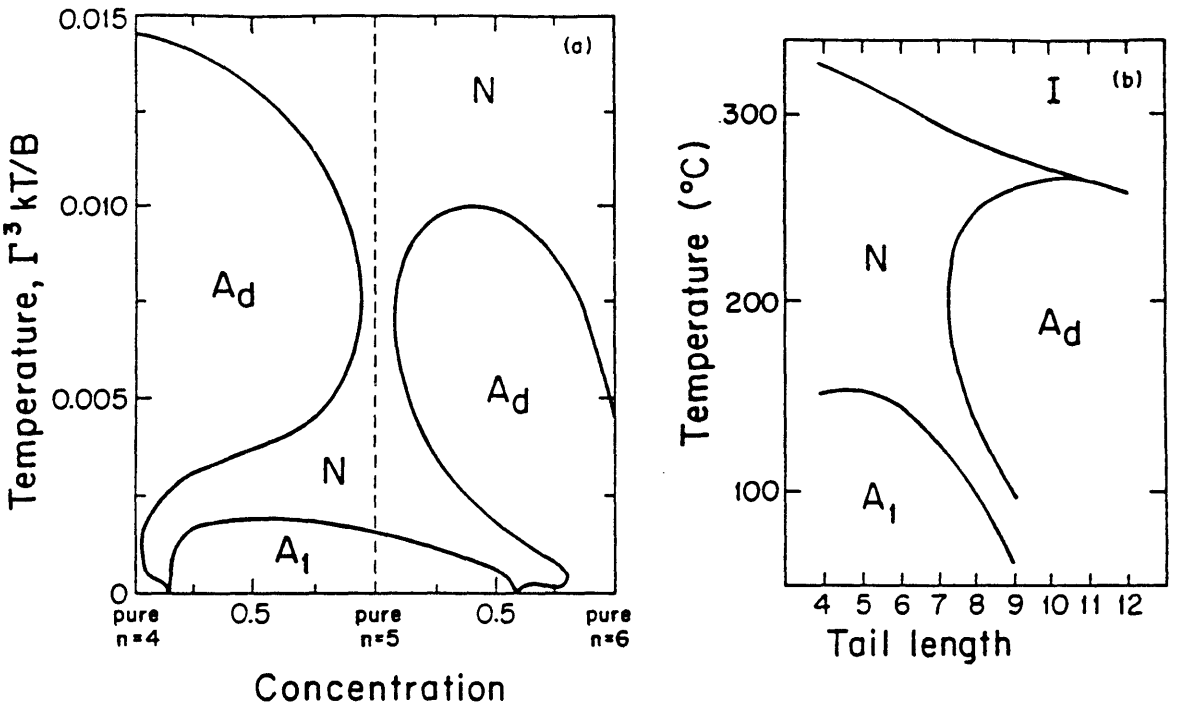

Figure 2.7: (a) Calculated reentrant phase diagram for mixtures of ($n = 5$, $B/A = 1.56$) with ($n = 4$, $B/A = 1.66$) and with ($n = 6$, $B/A = 1.46$) molecules. The other constants are $a/\Gamma = 2.54$, $\delta/\Gamma = 0.01$, and $m = 2$ for all species. The smectic A_d is stable toward pure $n = 4$ and pure $n = 6$, while the nematic and the smectic A_1 are stable toward pure $n = 5$.
(b) Experimental phase diagram[21], similar to the right panel of (a), for mixtures of homologs from the series
$C_nH_{2n+1}O - C_6H_4 - COO - C_6H_4 - CH = CH - C_6H_4 - CN$.

numbers, but also in the tail-tail interactions, which leads us to the calculations in the next subsection.

B. Mixing Molecules with Different Tail Lengths and Different Tail-Tail Interactions

In the spin-gas model, the parameters pertaining to the molecular tails are the notch number n and the tail-tail interaction strength $J_{\alpha\beta}$ which in this section are both allowed to vary between different species.

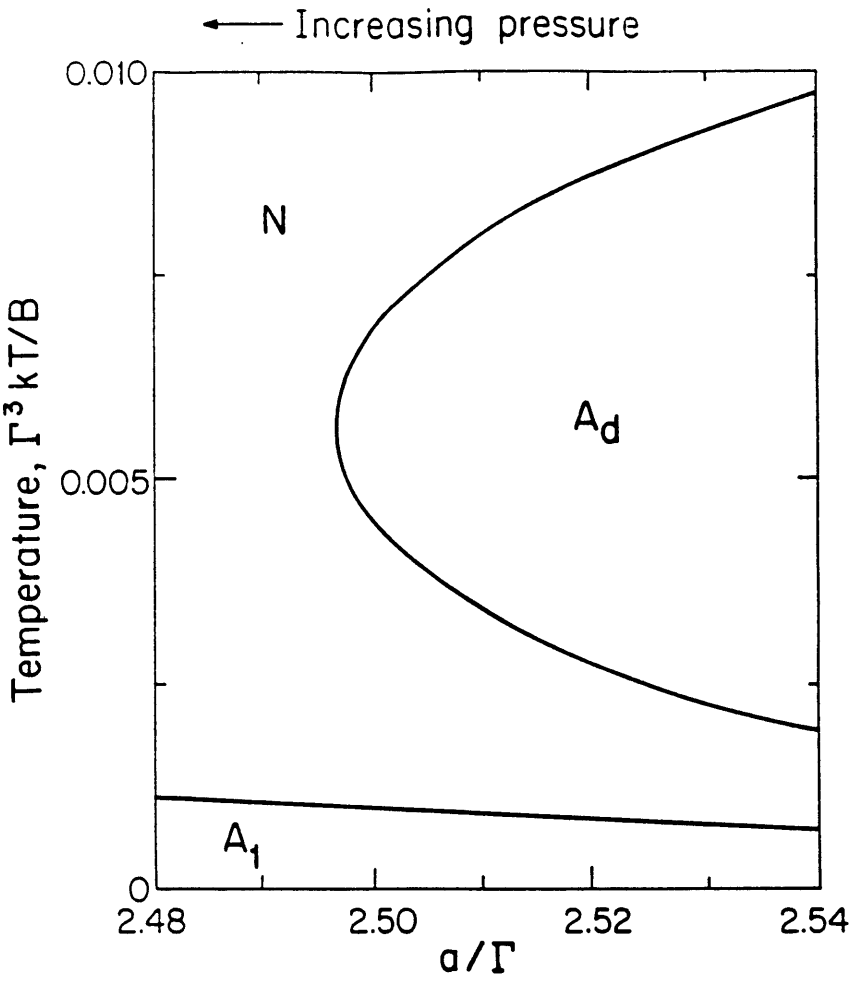

Figure 2.8: Calculated a/Γ-temperature phase diagram for 50 % of each of the ($n = 5$, $B/A = 1.56$) and ($n = 6$, $B/A = 1.46$) molecules of Fig. 2.7(a). The smectic A_d is destabilized by compression.

Figure 2.7(a) is the calculated phase diagram for a family of molecules whose $J_{\alpha\beta}$ becomes slightly less negative with increasing tail length, corresponding to an increased steric hindrance effect with increasing tail length. The smectic A_d at $n = 4$ destabilizes as $n = 5$ is mixed in, so that a reentrant nematic region is seen. At pure $n = 5$, only the nematic and smectic A_1 phases occur. As $n = 6$ is mixed in, the smectic A_d restabilizes, so that another reentrant nematic region is seen. Figure 2.7(b) is an experimental phase diagram[21] across a homologous series, displaying the same topology.

For a 50% $n = 5$, 50% $n = 6$ mixture of the system of Fig. 2.7(a), the calculated phase diagram in a/Γ and temperature is given in Fig. 2.8. The smectic A_d is unstable to the application of pressure, as in the theoretical and experimental phase diagrams in Figs. 2.4(b,c).

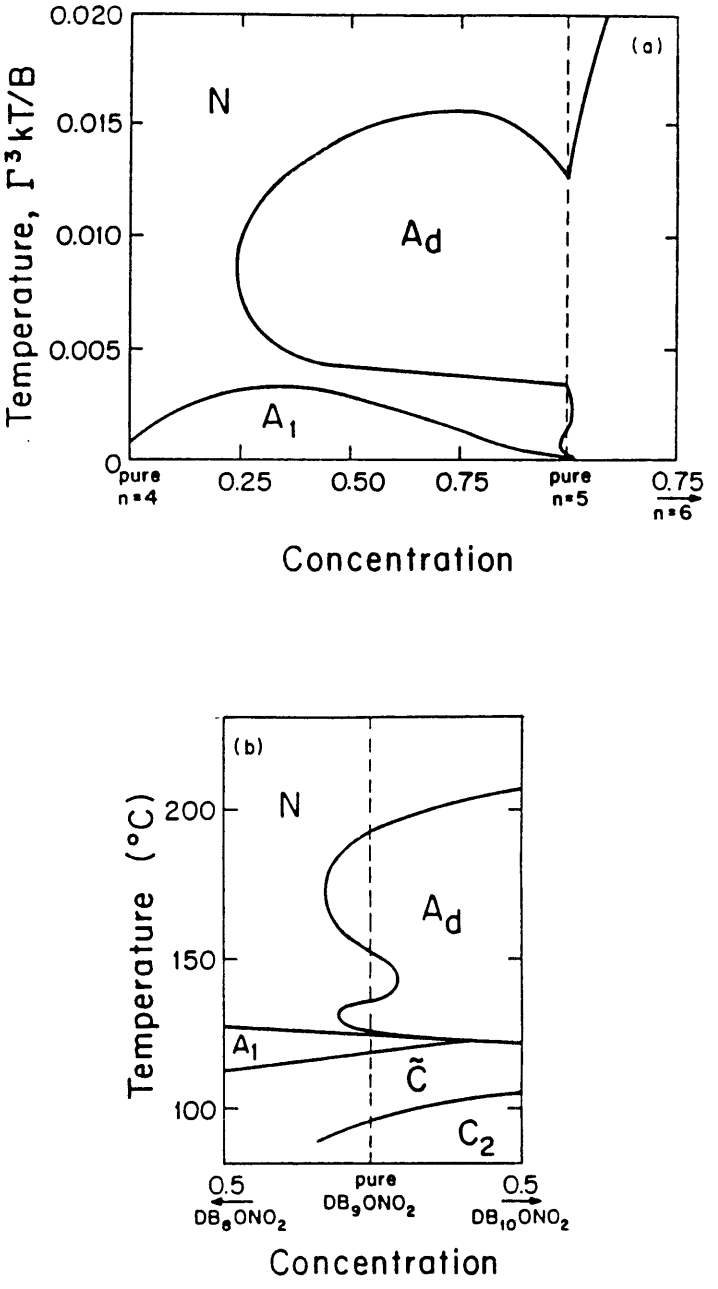

Figure 2.9: (a) Calculated quadruply reentrant phase diagram in the concentration and temperature variables, for ($n = 5$, $B/A = 1.461$) molecules mixed with ($n = 4$, $B/A = 1.900$), left panel, and with ($n = 6$, $B/A = 1.100$), right panel. The other constants are $a/\Gamma = 2.435$, $\delta/\Gamma = 0.007$, and $m = 3$ for all species.
(b) Experimental quadruply reentrant phase diagram, for DB_9ONO_2 mixed with its 8- and 10-carbon homologs[21]. In both theory and experiment, the smectic A_d is unstable toward the shorter homolog.

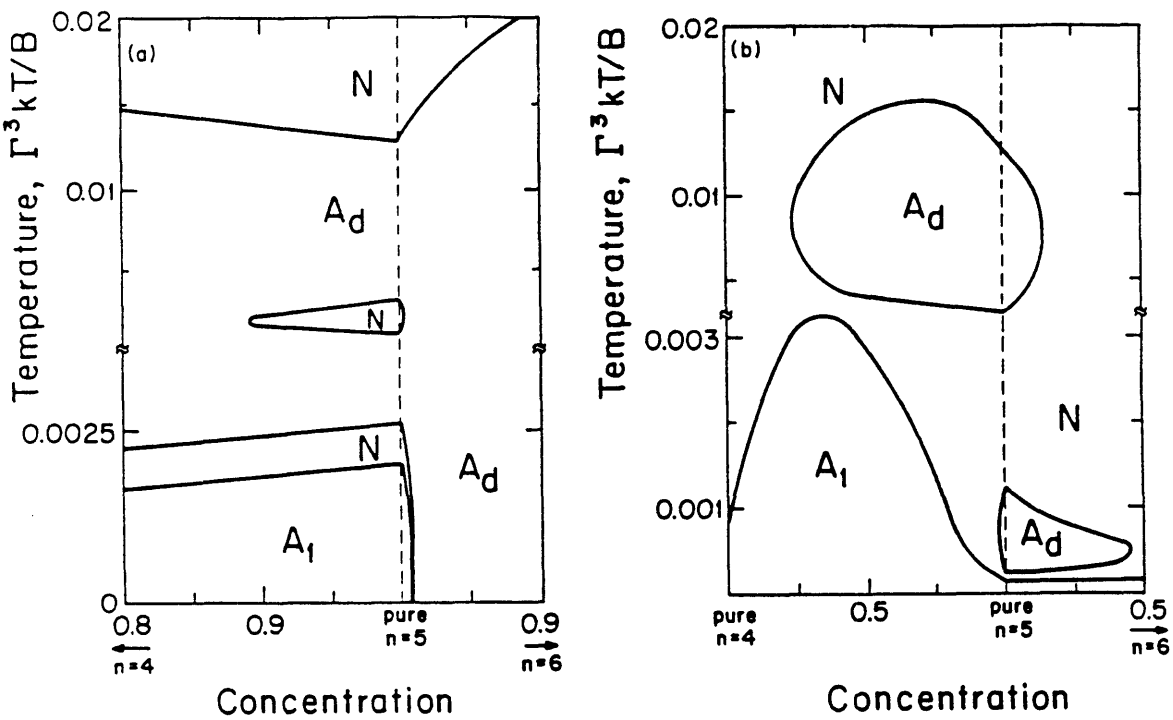

Figure 2.10: 'Bubble phase diagrams' in the concentration and temperature variables. (a) The nematic bubble - a nematic region completely surrounded by the smectic A_d, in mixtures of ($n = 5$, $B/A = 1.461$) with ($n = 4$, $B/A = 1.461$), to the left, and with ($n = 6$, $B/A = 1.100$), to the right. The other constants are $a/\Gamma = 2.435$, $\delta/\Gamma = 0.007$, and $m = 3$ for all species.
(b) The smectic A_d bubbles - smectic A_d regions, stabilized by atomic or librational permeation, completely surrounded by the nematic, in mixtures of ($n = 5$, $B/A = 1.461$) with ($n = 4$, $B/A = 1.900$), to the left, and with ($n = 6$, $B/A = 1.461$), to the right. The other constants are $a/\Gamma = 2.435$, $\delta/\Gamma = 0.007$, and $m = 3$ for all species.

The quadruple reentrance of Fig. 2.6 is indeed reversed, with a larger change in $J_{\alpha\beta}$ across the series, as shown in Fig. 2.9(a). The smectic A_d is here unstable to the introduction of the shorter $n = 4$ into the $n = 5$ system and stable to the introduction of the longer $n = 6$. This is the behavior seen experimentally[21] in mixing the quadruply reentrant DB_9ONO_2 with DB_8ONO_2 or $DB_{10}ONO_2$, as shown in Fig. 2.9(b). However, note that the calculation has a smectic A_d region bulging in the neighborhood of the $n = 5$ axis.

The theory generalized to mixtures contains other types of phase diagrams, two of which are displayed in Fig. 2.10. Thus, enclosed regions ('bubbles') of nematic or smectic A_d are obtained.

This research was supported by the National Science Foundation of the U.S.A. under Contract No. DMR-87-19217 and by the National Fund for Scientific Research of Belgium. JFM was supported by a Postgraduate Scholarship from the Natural Sciences and Engineering Research Council of Canada.

This Section has been published[9] as an article in Physical Review A.

2.3 Finite-Temperature Bicritical Point in the Frustrated Spin-Gas Theory of Reentrant Polar Liquid Crystals

by J. F. Marko, K. Hui, and A. Nihat Berker

2.3.1 Introduction

The spin-gas theory of polar liquid crystals[23, 24, 25, 26, 27, 28, 29] has been a successful tool for understanding how the dipole-dipole and tail-tail interactions of polar rods lead to the spectacular reentrant phenomena that have been observed experimentally[10, 17, 21, 30]. This theory has also been shown to lead to a good description of layer thicknesses[24], dimer concentrations[25], and relative specific heat anomalies[26]. In the previous Section, it was shown how the theory can be extended to describe mixtures, which is a development that allows the direct application of the theory to many experiments. These types of modifications to the basic theory are facilitated by the fact that at its base, the spin gas model is microscopic, starting from a Hamiltonian description employing the orientational and positional degrees of freedom of individual molecules.

A major qualitative failure of the basic model is its inability to describe the low-temperature behavior of the phase diagram. The theory as presented above predicts that the smectic-A_1-nematic and smectic-A_d-nematic transition lines meet at a bicritical point at zero temperature. The question that comes to mind is whether this is merely an artifact of the prefacing of the molecular model onto a two-dimensional triangular Ising model with nearest-neighbor interactions (which always has zero-temperature bicritical behavior), and if this is so, what is the nature of the true low-temperature theoretical phase diagram? A second issue concerns the truncation of the interactions after nearest neighbors in the basic theory. What changes, if any, are made to the phase diagram when further-neighbor interactions are considered?

Here, by looking at the microscopic second-neighbor in-plane interactions, it is shown that an extension of the prefacing transformation used in the basic theory leads to a meeting of the $A_1 - N$ and $N - A_d$ transition lines at finite temperature, below which there is a direct first-order $A_1 - A_d$ transition, as observed experimentally[10, 33].

2.3.2 The Spin-Gas Theory and Its Bicritical Behavior

As in the previous Section, the liquids of interest are composed of molecules with a dipole at one end, and a corrugated hydrocarbon tail at the other. The dipole-dipole interactions are frustrated due to the close-packing conditions of the oriented liquid state (i.e. there is local hexagonal-close-packing of the molecules in planes perpendicular to the director axis in the nematic and smectic phases), and the 'notched' tails provide 'substrate fields' that limit each others' positional motions along the director. In addition to the dipole-dipole interaction, a phenomenological tail-tail interaction is included so that the total intermolecular potential between molecules 1 and 2 is

$$V_{12}(\mathbf{r}_1, \hat{\mathbf{s}}_1, \mathbf{r}_2, \hat{\mathbf{s}}_2) = \frac{A\hat{\mathbf{s}}_1 \cdot \hat{\mathbf{s}}_2 - 3B(\hat{\mathbf{s}}_1 \cdot \hat{\mathbf{r}}_{12})(\hat{\mathbf{s}}_2 \cdot \hat{\mathbf{r}}_{12})}{|\mathbf{r}_{12}|^3}, \tag{2.8}$$

where $\mathbf{r}_i$ and $\hat{\mathbf{s}}_i$ are the position and orientation, respectively, of the dipole moment of molecule i, $\mathbf{r}_{12} = \mathbf{r}_1 - \mathbf{r}_2$, $\hat{\mathbf{r}}_{12} = \mathbf{r}_{12}/|\mathbf{r}_{12}|$, and A and B are constants determining the strength and symmetry of the dipole-dipole and tail-tail parts of the potential. For $A = B$, interaction of point dipoles of moment $\sqrt{B}$ are described, while for $A < B$, there is an additional tail-tail interaction that favors neighboring tails to be together. For $A > B$, the molecule tails favor antialignment, thus the ratio B/A describes the amount and type of tail-tail interaction.

The orientational fluctuations are limited to $\hat{\mathbf{s}}_i = s_i\hat{\mathbf{z}}$, where $s_i = \pm 1$, and positional fluctuations are considered only in the direction parallel to the director $\hat{\mathbf{z}}$. The positions of molecules in the $x - y$ plane are taken to be locally coordinated on a triangular lattice of nearest-neighbor spacing a. This lattice spacing is considered to be the average in-plane molecular spacing, and from stability considerations, is an inverse measure of the thermodynamical pressure. Positional fluctuations in the $x-y$ plane have been considered in previous work[23], and do not qualitatively affect the results.

An important ingredient of the theory is the nature of the out-of-plane positional

flucuations ('permeations') that are allowed by the corrugated molecular tails. These are taken to create n energetically favorable positions for nearest-neighbor permeations. The approach of the spin-gas theory is to focus on the statistical mechanics of a small cluster of molecules in a single smectic layer. Thus, this number of positions corresponds to the molecular length (the molecule length is taken to be thus $l = n\Gamma$, where Γ is a length of order the carbon-carbon spacing in the tail), since permeations beyond the molecular length correspond to configurations where the molecule under consideration has left the layer under study and has been replaced by another molecule. Further fluctuations around these permeations, either discrete or continuous in nature, and are important for the descriptions of exotic multiple reentrances seen in some experiments[21], but for the results of this Section, these additional fluctuations are not important.

The approach of previous spin-gas calculations is to 'preface' the intermolecular interactions onto distorted triangular couplings between the orientational variables by summing over the permeational variables on a nearest-neighbor triplet. The strongest (K_S), intermediate (K_I), and weakest (K_W) antiferroelectric couplings are computed using the prefacing transformation

$$\exp[K_S s_1 s_2 + K_I s_2 s_3 + K_W s_3 s_1] = \sum_{\{n_i\}} \exp[-\beta(V_{12} + V_{23} + V_{31})], \qquad (2.9)$$

where the pairs of molecule labels (12), (23), and (31) span the strongest, intermediate, and weakest antiferroelectric couplings respectively. In past work, the couplings thus obtained have been gauged using the ordering condition of the two-dimensional distorted triangular lattice Ising model[31]

$$\sinh(2\bar{K}_1)\sinh(2\bar{K}_2) + \sinh(2\bar{K}_2)\sinh(2\bar{K}_3) + \sinh(2\bar{K}_3)\sinh(2\bar{K}_1) > 1, \qquad (2.10)$$

where $\bar{K}_1 \geq \bar{K}_2 \geq |\bar{K}_3|$ are obtained from $\{K_S, K_I, K_W\}$ by changing, if necessary, two signs. Order with locally antiferroelectric or ferroelectric correlations re-

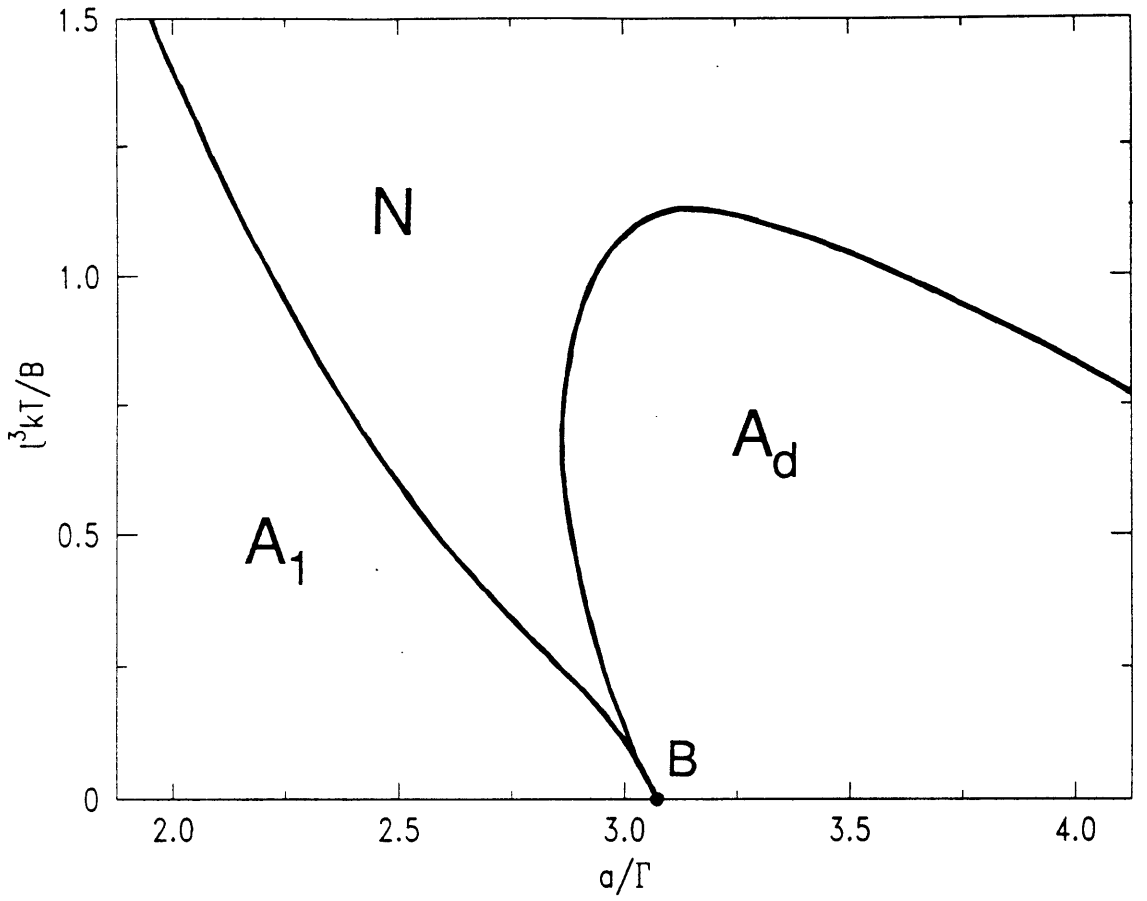

Figure 2.11: The basic smectic A_1 - smectic A_d - nematic (N) phase diagram of the frustrated spin-gas theory, using the triangular lattice criticality condition. Here, $n = 5$, and $B/A = 1.75$. Important features are the reentrant nematic phase, and the zero-temperature bicritical point B where the three phases meet.

flects the dominance of different positionally correlated triplets, which from structural considerations[24] allow the identification of smectic A_d or A_1 ordering, respectively. The paramagnetic phase is identified as the positionally uncorrelated phase, the nematic (N) liquid.

The triangular Ising model has phases which meet at zero-temperature bicritical points, thus it is no surprise that the spin-gas model as described above leads to phase diagrams in terms of temperature l^3kT/B and inverse pressure a/Γ as displayed in Figure 2.11. The interesting features of this phase diagram are first, the reentrant

nematic, which for a range of a/Γ, appears at temperatures below the A_d phase and above the A_1 phase. The second important feature is the zero-temperature bicritical point where the three phases meet, which reflects the behavior of the Houtappel condition (2.10) for large values of the couplings. This last feature is at odds with the results of some experiments on mixtures and pure materials: the smectic $A_1 - A_d$ evolution can occur via a direct first-order transition instead of by continuous transitions to an intermediate reentrant nematic[10].

Figure 2.12(a) illustrates the zero-temperature bicritical behavior in the triangular lattice $d = 2$ Ising model with couplings J_1, J_2, and J_3. Here the phase diagram is considered in terms of the Ising couplings: the relation to the temperature and pressure-like parameters of the microscopic model is given through the nonlinear (but smooth!) transformation (2.9). The graph in (a) is the subspace $J_1 = J_2 = J$, but the property that between any two ordered regions (such as FM and AFM) corresponding to the two smectics there will be a nematic (paramagnetic, denoted PM in the Figure) region, is generic in the space of couplings. The bicritical behavior occurs at infinite coupling, or zero temperature.

In part (b) of Figure 2.12, the phase diagram for the same subspace of a model with an additional interaction is shown. This additional interaction is a second-neighbor interaction that crosses one of the nearest-neighbor bonds of Figure 2.12(a). These crossing interactions are, for illustration, taken to be equal, and are denoted K. In the space $J_1 = J_2 = J$, this model is the well-known $d = 2$ square lattice Ising model with crossing second-neighbor bonds on every elementary plaquette. This model has been extensively studied, and its phase diagram is well understood[34]. The qualitative difference introduced by the second-neighbor bond is displayed in (b): at K equal to the critical coupling of the $d = 2$ square lattice Ising model (which is $J_c = \log(1 + \sqrt{2})/2 = 0.4407...$) and $J = 0$, the critical loci for transitions from the paramagnetic phase to the ordered phases meet at a bicritical point B. Beyond this critical value of K, there is a direct, first-order phase transition between

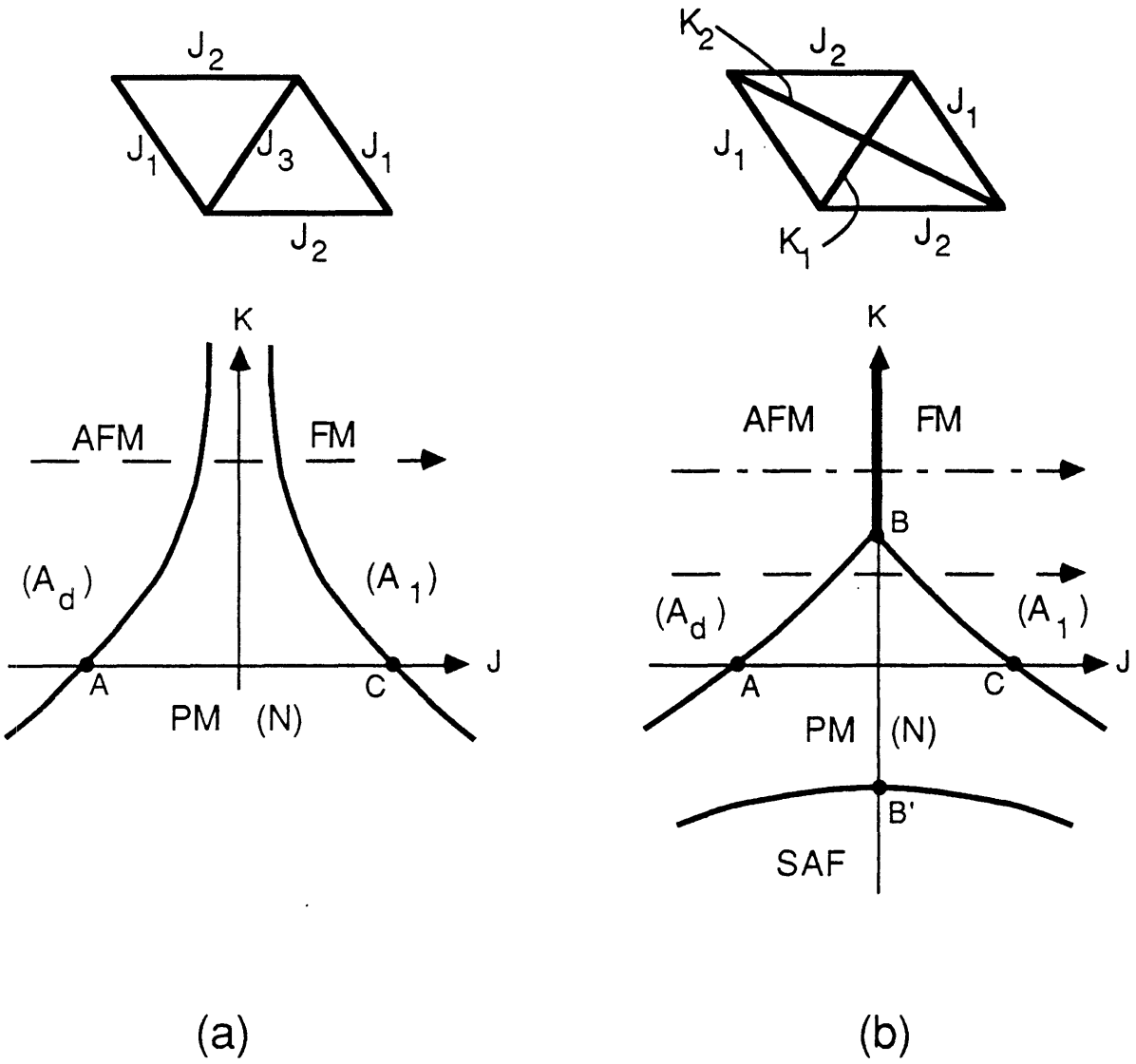

Figure 2.12: Basic mechanism generating zero-temperature and finite-temperature bicritical phenomena in the spin-gas theory.
(a) Triangular lattice theory. Transitions from the A_d to the A_1 phase must always involve an intermediate reentrant nematic (N) phase (dashed line). The phase diagram is the subspace $J = J_1 = J_2$, $K = J_3$.
(b) Triangular lattice theory with one additional second-neighbor interaction. There are $A_d - N - A_1$ transitions (dashed line), but now there is a $A_d - N - A_1$ bicritical point B at finite values of the couplings, and thus there now is a line of direct, first-order $A_d - A_1$ transitions, one of which is traversed by the dashed-dotted line. The phase diagram is the subspace $J = J_1 = J_2$, $K = K_1 = K_2$.

the two ordered phases. Thus there are paths from one ordered phase to another involving an intermediate disordered phase, or for larger crossing couplings (i.e. lower temperature!), there are paths through a direct transition, as indicated by the dashed-dotted line in (b). A last, important feature of this model is that in the $J = 0$ subspace, there are critical points for $K = \pm J_c$ (points B and B' in Figure 2.12(b)), and in fact there is a locus of critical points bordering a 'superantiferromagnetic' or layered antiferromagnetic phase (the region SAF in Figure 2.12(b)).

This suggests a mechanism to generate a finite-temperature bicritical point. If an additional second-neighbor bond strength is computed from the microscopic Hamiltonian, it can then be used as a interaction to cross K_W as obtained from the triangular lattice prefacing transformation (2.9). The bond crossing K_W is the most important second-neighbor interaction, as it will compete with the combined effect of K_I and K_S. At low temperatures, it is possible that the large crossing interactions obtained will cause the transitions between the smectics to become first order, while at higher temperatures, the second-neighbor interaction will be relatively unimportant, and the phase diagram will be determined by the underlying triangular lattice interactions.

The computation of this additional interaction K_L is through the additional prefacing transformation

$$K_L s_1 s_2 + G' = \log \sum_{\{n_1, n_2\}} \exp[-\beta V'_{12}(\{n_i, s_i\})] \tag{2.11}$$

where the potential V'_{12} is V_{12} of (2.8) with a replaced by $\sqrt{3}a$ to give the potential between second neighbors on a triangular lattice. Thus, the interactions of the triangular lattice Ising model with one second neighbor interaction (or equivalently, the fully anisotropic square lattice model with both second-neighbor couplings) are obtained as $\{J_1, J_2, K_1, K_2\} = \{K_S, K_I, K_W, K_L\}$.

This fully anisotropic model has a complicated phase diagram in the four- dimensional coupling constant space, but fortunately, it reduces to exactly soluble models

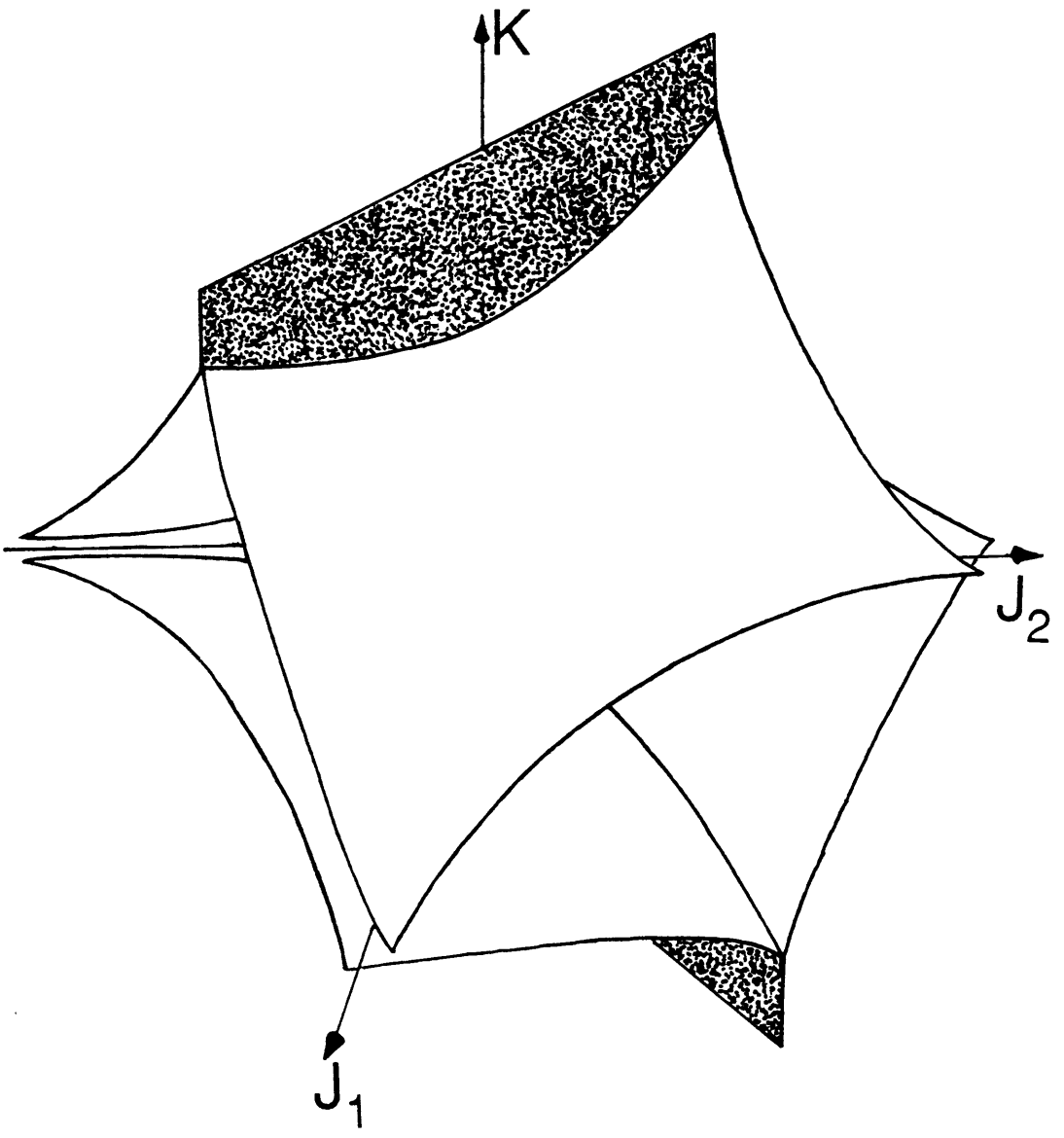

Figure 2.13: Phase boundaries for the square lattice Ising model with equal second neighbor interactions K. Note that the upper sheets are mapped onto the lower by a rotation about the K axis by $\pi/2$ and a reflection through the $J_1 - J_2$ plane. The white surfaces are critical phase transitions, while the shaded surfaces extending from the 'peaks' of the critical manifolds are first-order surfaces.

for the limits $K_1 = 0$ or $K_2 = 0$ (triangular Ising model) and $J_1 = J_2 = 0$ (anisotropic square Ising model). In addition, the general model is invariant under the transformations where one of the J's and both of the K's are changed in sign, and independently under either of the interchanges $J_1 \leftrightarrow J_2$ or $K_1 \leftrightarrow K_2$. This is interesting because it tells us that in the case $K_1 = K_2 \equiv K$, the phase diagram is invariant under the transformation $J_1 \rightarrow J_2, J_2 \rightarrow -J_1, K \rightarrow -K$, which is a rotation through $\pi/2$ in the $J_1 - J_2$ plane and a reflection through the same plane. Thus, not only is B' mapped to B in Figure 2.12(b), but in the more general J_1-J_2-K model, the line bordering the SAF phase is mapped to an equivalent line running through B. The resulting three-dimensional phase diagram, showing the critical and first-order surfaces is shown in Figure 2.13.

In order to gauge the ordering of the thus obtained four-interaction magnetic model, we have proposed an approximate ordering condition that reproduces the exact $d = 2$ critical behavior in the limits observed above, and also is an accurate representation of the results for the uniform model with second-neighbor interactions. The critical ordering condition is

$$\begin{aligned}
&\sinh 2\bar{J}_1 \sinh 2\bar{J}_2 + [\sinh 2\bar{J}_1 + \sinh 2\bar{J}_2] \\
&\quad [\sinh 2(\bar{K}_1 + \bar{K}_2) + \sinh 2\bar{K}_1 \sinh 2\bar{K}_2 | \sinh 2\bar{K}_1 \sinh 2\bar{K}_2 - \cosh \bar{J}_1 \cosh \bar{J}_2|^{-4/7} \\
&\quad A \exp(-|\sinh 2\bar{K}_1 \sinh 2\bar{K}_2 - 1|/\tau)] > 1, \qquad (2.12)
\end{aligned}$$

where $A = 2.558$ and $\tau = 1.889$ are numerical constants determined via a fit of the SAF line to the series approximation[34] and the interactions $\{\bar{J}_i, \bar{K}_j\}$ are obtained from $\{J_i, K_j\}$ by one of the transformations described above. The exponent 4/7 allows the phase diagram in the vicinity of B and B' (i.e. the sharpness of the cusp) in Figure 2.12 to be described by the correct power law, as determined by renormalization group analysis using the exactly known critical exponents at these points (it should be noted that along SAF the critical exponents slowly vary[34]). This condition is

in good quantitative agreement with all exact and numerical information concerning the general model in the regions where the crossing interactions have the same sign. The model with opposite-sign crossing interactions has quite different behavior, and fortunately is irrelevant to this study.

The first-order transitions must be a subspace of the hypersurface $J_1 = -J_2$ for $K_i > 0$, and of $J_1 = J_2$ for $K_j < 0$, from the exact information and from symmetry considerations. An approximate expression completely defining the half-infinite first-order surfaces that is consistent with the SAF boundary of the above expression is

$$\sinh 2K_1 \sinh 2K_2 - \cosh J_1 \cosh J_2 > 0. \tag{2.13}$$

In addition to reducing to the exact result when the J_i vanish, the global behavior inside the subspace of Figure 2.12(b) is in excellent agreement with the available series results[34].

These conditions, along with the fact that the symmetry of the magnetic phase corresponds to the symmetry operations necessary to obtain the interactions $\{\bar{J}_i, \bar{K}_j\}$ allow the phase to be obtained for couplings given by the prefacing transformations (2.9) and (2.11) subject to the condition that the K_i are the same sign. As always in these types of calculations, the aim is to obtain the qualitative phase diagram in terms of the microscopic parameters, not to compute universality-class dependent details such as exponents at the critical phase transitions.

2.3.3 Theoretical Results and Comparison to Experiments

As remarked previously, gauging ordering with the triangular lattice Ising model ordering condition (2.10) leads to a A_d-A_1-N phase diagram with a zero-temperature bicritical point, and a typical reentrant phase diagram is shown in Figure 2.11. In this case, the reentrant phenomena are caused by the crossing of the absolute value of K_S, the most antiferroelectric projected coupling, and K_W, which is the most ferroelectric (least antiferroelectric) coupling, as shown in Table 2.1. Because of the zero-temperature bicritical phenomena in the triangular Ising model, there is a reentrant nematic phase separating the smectics at all finite temperatures. As can be seen from Table 2.1, the projected couplings evolve smoothly, changing from favoring local ferroelectric configurations in the A_1 phase to favoring local antiferroelectric configurations in the A_d phase.

Table 2.1 also contains the second-neighbor coupling as prefaced by (2.11), and it is also smoothly behaved. It is weakly ferroelectric throughout the region of interest of the phase diagram, and rapidly becomes negligible as temperature increases. At low temperatures ($l^3kT/B < 0.3$) K_L becomes comparable to the other interactions in size.

Figure 2.14 displays a phase diagram for the same set of spin-gas model constants as that of Figure 2.11 (namely $B/A = 1.75$, $n = 5$), using the additional prefacing transformation (2.11) and the ordering conditions (2.12) and (2.13). The zero-temperature bicritical point of Figure 2.11 is lifted to finite temperature, and leaves behind in its path a locus of first-order transitions between the two smectic phases. At high temperatures, the phase diagram is qualitatively unaffected. This should be compared to the experimental phase diagram shown in Figure 2.15(a) which shows a similar phase diagram for a binary mixture.

For pure materials, fewer experimental results are available, but one recent study[35] by Raja *et al* of the pressure-temperature phase diagram of the triply reentrant material $DB_{10}ONO_2$, as shown in Figure 2.16, displays the topology of Figure 2.14. This

a/Γ	l^3kT/B	J_1	J_2	K_1	K_2	phase
2.500	0.286	0.385	1.668	1.719	0.481	A1
	0.572	-0.442	0.841	0.921	0.213	A1
	0.858	-0.683	0.601	0.696	0.152	N
2.750	0.286	-0.374	0.909	1.167	0.273	A1
	0.429	-0.670	0.613	0.818	0.174	N
	0.572	-0.804	0.480	0.664	0.128	Ad
	1.144	-0.884	0.354	0.514	0.063	Ad
	1.429	-0.840	0.330	0.483	0.050	N
2.875	0.143	-0.170	1.113	1.895	0.468	A1
	0.429	-0.864	0.419	0.678	0.127	Ad
3.100	0.143	-1.052	0.230	1.275	0.258	Ad
	1.144	-0.880	0.177	0.370	0.023	Ad
	1.429	-0.778	0.158	0.331	0.019	N

Table 2.1: Interactions obtained with the prefacing transformations described in the text. All calculations were for $B/A = 1.75$ and $n = 5$. The second neighbor interaction K_2 is always ferroelectric, and rapidly becomes less important as temperature is raised. At low temperatures however, it becomes comparable to the triangular lattice couplings.

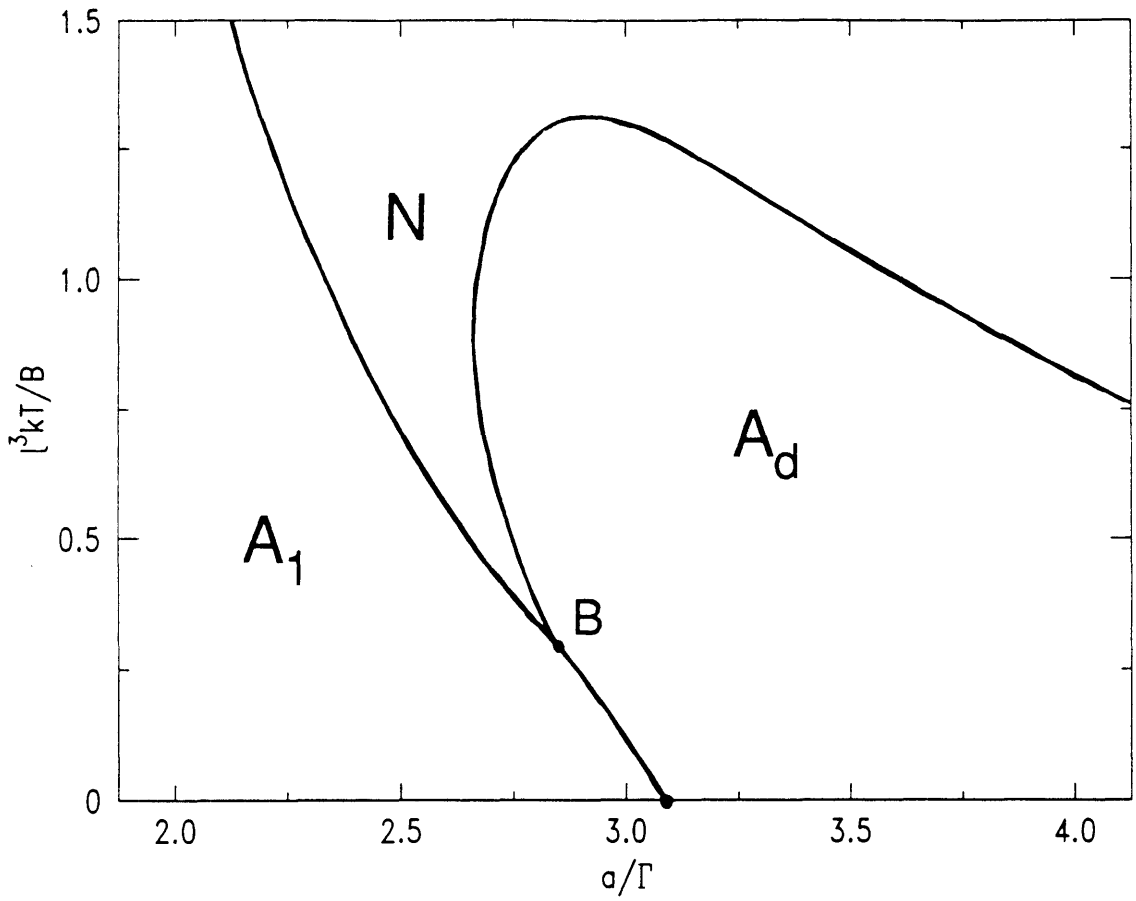

Figure 2.14: Spin-gas theory phase diagram for parameters of Figure 2.11, with second-neighbor interaction included using the additional prefacing transformation and ordering condition described in the text. Now, the bicritical point B is seen at finite temperatures, below which a first-order smectic-A_d-smectic-A_1 transition occurs.

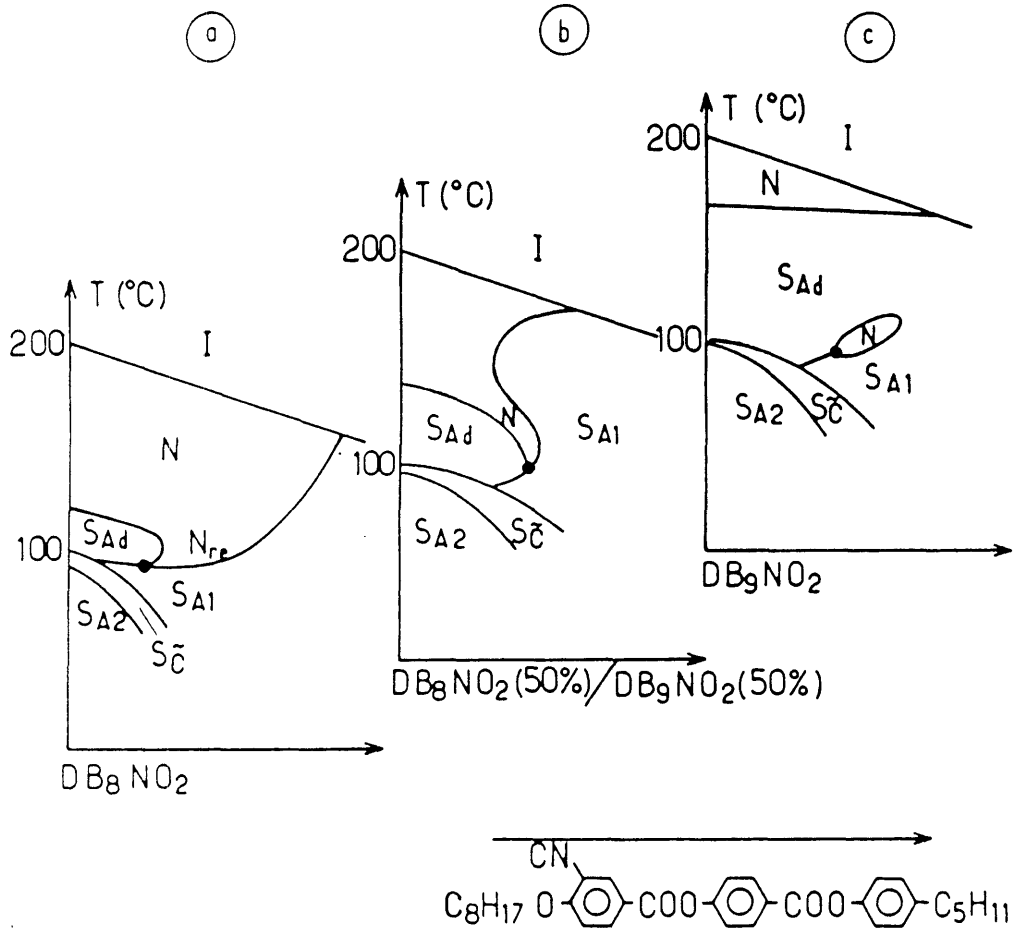

Figure 2.15: Mixture phase diagrams showing A_d-A_1-N bicritical behavior reported by Hardouin[10]. Below the $N-A_1-A_d$ point, the transition between smectics is first order. The sequence (a)-(b)-(c) indicates the result of increasing the concentration of the longer homologue in the DB_8-DB_9 component. In each frame, the x-axis indicates increasing concentration of the third component indicated at the bottom of the figure.

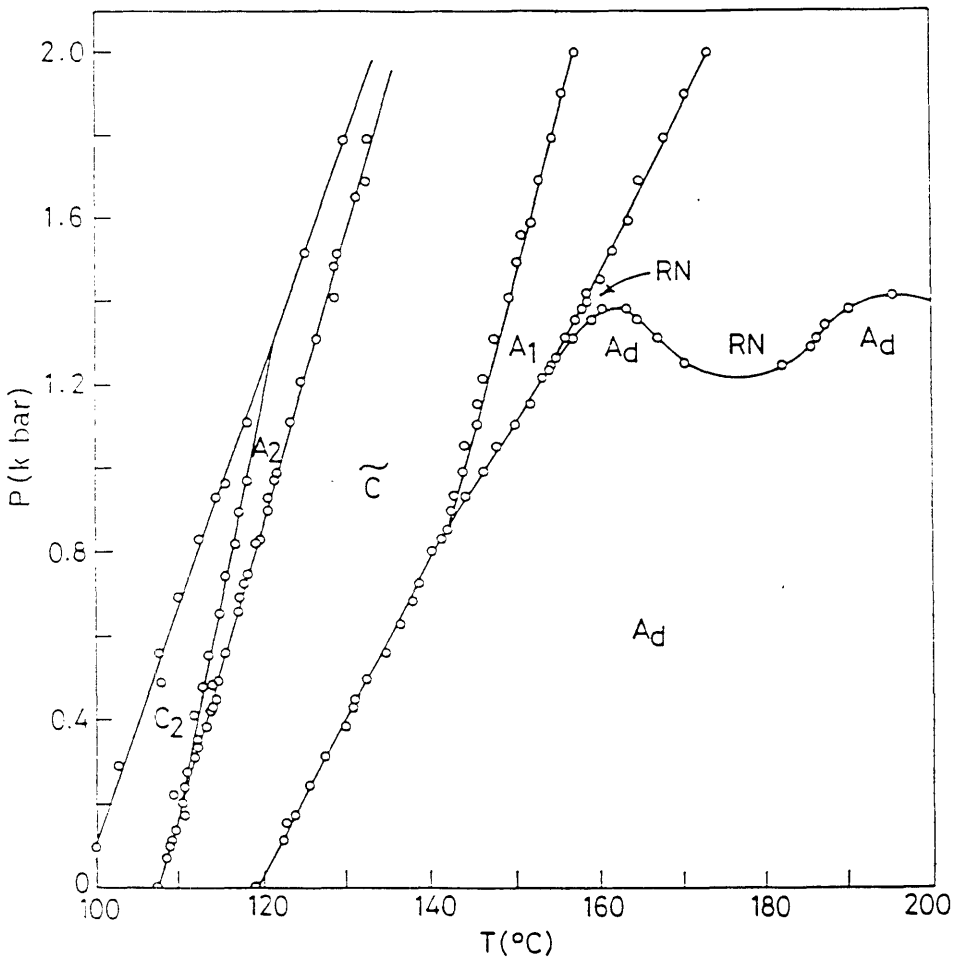

Figure 2.16: Experimental pressure-temperature phase diagram for the pure material $DB_{10}ONO_2$[35]. As pressure is increased, the transition between A_1 and A_d changes from being a direct first-order transition to two continuous transitions involving an intermediate reentrant nematic phase.

is the only pressure-temperature pure material phase diagram with a $N - A_1 - A_d$ point known to us: it seems that usually the two $A - N$ lines do not meet before zero pressure.

It should be noted that recent experiments on mixtures[36] and on the $DB_{10}ONO_2$ pure system[37] indicate that there is a tricritical point along the $A_1 - N$ line, and that the $N - A_1 - A_d$ point is not a bicritical point, but is actually a critical end point terminating the line of $A_d - N$ transitions. This detail, although important from the point of view of critical phenomena, does not affect the global topology of the phase diagram, as the tricritical and critical end points are very close together. Recalling that the prefacing approach as used here connects models in different universality classes, we do not expect the critical phenomena to be preserved.

The results shown in Figure 2.14 are stable over a range of B/A extending from at least 1.5 to 2.0, and as B/A is made larger (corresponding to an increase in effective tail-tail interaction) the smectic A_1 phase becomes more stable. From the comparisons of the spin-gas theory of mixtures to experiments of Section 2.2, it has been concluded that B/A increases with increasing tail length. Thus, the behavior of the bicritical theory is in qualitative agreement with the experimental phase diagrams of Figure 2.15(a) and (b), which indicate that the A_1 phase in fact becomes dominant as a longer homolog is added to the mixture. However, a complete explanation of the intriguing features of this ternary phase diagram, namely the reappearance of the A_1 phase at temperatures above the $A_d - N$ transition and the merging of the smectic phases shown in part (c) of the figure, awaits a study of bicritical phenomena in mixtures.

Helpful conversations with C. Garland and R. Shashidhar are acknowledged. This research was supported by the National Science Foundation under Grant No. DMR-87-19217.

Chapter 3

Density-Functional Theory of Freezing in Molecular Fluids

3.1 Introduction

The modern version of the density-functional method[38] offers an accurate description of freezing via functional expansion of the grand canonical potential in powers of the one-body density about the isotropic fluid phase. This constructive approach should be viewed as the natural route to a free energy functional that can be minimized over one-body distributions $\rho(X)$ to obtain the equilibrium state. The existence of such a functional is of course guaranteed by the density-functional theorem of Mermin[39]. The expansion coefficients are the direct correlation functions (DCFs) of equilibrium liquid theory[40], and in the case of spherically symmetric interactions such as those for the hard-sphere fluid, enough is known about the pair DCF[41] to describe the freezing transition accurately[42, 43, 44].

Little is known about the DCFs of the isotropic fluid phases of nonspherical molecules, and previous attempts to describe phase transitions in dense fluids composed of them have employed guesses about liquid structure[45, 46], using only the thermodynamics of the liquid obtained from simulations as a guide. In addition to not examining the validity of the proposed DCFs, the previous density functional studies of systems of anisotropic particles have not been suitably parametrized to describe the rather narrow distributions that occur in the crystallization of hard-core fluids, or to take into account the possibility that orientational and translational orders can appear simultaneously as well as separately. These shortcomings must be overcome if such theories are to provide useful information.

Section 2 addresses these issues. Density functional theory and background on the hard-ellipsoid model will be presented, and then a new variational approach to obtaining liquid structure information will be described. The results are the first that directly examine the Pynn-Wulf approximation, which is used as the starting point of the optimization. Once this improved DCF is obtained, it is employed in the mean field theory for phase transitions in the fluid. Isotropic to crystal transitions are described, which include the first computations of this type for the oriented solid

phase. As in Monte Carlo simulations of this system, it is found that for small anisotropy, the plastic (orientationally disordered crystal) phase is stable at lower densities than the oriented solid, while at medium anisotropies, the oriented solid becomes the stable ordered phase. Isotropic to nematic transitions are also studied at high anisotropy, and are shown to be strongly affected by optimization of the DCF.

Section 3 examines the static structure of liquids composed of anisotropic particles in a different light than the numerical optimization described above. Exact direct and conventional pair correlations for a one-dimensional fluid of anisotropic hard cores with orientational as well as translational degrees of freedom are obtained. These results indicate that the direct correlation function depends not on interparticle separation (as assumed by the Pynn-Wulf approximation) but on hard-core overlap. This behavior can also be understood from examination of the density expansion for the direct correlation function, which allows the extension of the phenomena to dimensions $d > 1$. For strongly anisotropic particles, this leads to the general conclusion that nonparallel configurations of particles have much less negative direct correlations in the core overlap region than do the interparticle distance-dependent approximations. This is consistent with the trend seen in the numerical work introduced above, and the overlap-volume dependence is consistent to a remarkable degree with the behavior of numerical solutions of nonlinear integral equations for the correlation functions[47]. In addition, this identification of the effect of molecular topology on direct correlations allows the complicated problem of liquid structure in molecular fluids to be more readily understood.

Section 4 examines the possibility of improving the density functional. The results above were obtained from a functional Taylor expansion in powers of the difference between the one-body density expectation value $\rho(X)$ and the uniform liquid state of density ρ_0. As a result, the form of the density functional obtained is mathematically rigorous only for small deviations away from the disordered state. In this Section, an alternate, nonperturbative approach will be presented that is equivalent

to a summation to all orders of the density-functional expansion. This method develops further the ideas of Curtin and Ashcroft [48] and of Denton and Ashcroft[49, 50]. This theory is applied to the phase transitions considered in Section 2, and in the case of the isotropic to nematic transition, results are obtained incorporating liquid structure information due to the numerical solution of nonlinear integral closures of the Ornstein-Zernicke equation[52].

Finally, in Section 5, application of the density-functional methods presented in Sections 2 and 4 to the hard-sphere liquid will be presented. Recent improvements[51] in our knowledge of the liquid structure of the hard-sphere liquid allow a very accurate model of the hard-sphere solid phases to be constructed, and in addition to the usual thermodynamic and structural properties, solid phase elastic constants can be obtained. An Einstein-like model of lattice vibrations can thus be formulated, and used to indicate what type of corrections one can expect to the free energy due to elastic fluctuations.

The results for these studies all indicate that the combination of the inclusion of higher-order terms in the density-functional expansion and the use of accurate liquid structure allow the *ab initio* construction of accurate theories for phase transitions in fluids. Section 6 summarizes the results of this Chapter, and discusses future perspectives for the density-functional approach.

3.2 First-Order Phase Transitions in the Hard-Ellipsoid Fluid

3.2.1 Model and General Theory

The hard ellipsoid model is a simple model for liquid crystal systems and has been the subject of some study. The Hamiltonian is that of point masses which in addition to a translational degree of freedom $\mathbf{r}$ possess orientational degrees of freedom $\hat{\mathbf{e}}$ which are vectors of unit length. Throughout this work, the combination of vectors $(\mathbf{r}, \hat{\mathbf{e}})$ will be referred to with the notation X. Axially symmetric molecules can be described by these degrees of freedom, and for two axially symmetric hard cores, there is a function $D(X, X')$ that describes the distance of closest approach for two hard cores at coordinates X and X'. For hard cores, the intermolecular potential is thus

$$\begin{aligned} U(X,X') = \quad & 0, \quad |\mathbf{r}-\mathbf{r}'| > D(X,X') \\ & \infty, \quad |\mathbf{r}-\mathbf{r}'| < D(X,X'). \end{aligned} \tag{3.1}$$

For almost any shape other than spheres (where the function D is just a constant, the sphere diameter), closed-form expressions for the distance of closest approach are unavailable. In this work, an approximate explicit form for the function $D(X, X')$ is used (due to Berne and Pechukas[53]) that accurately describes the distance of closest approach of ellipsoids of revolution with axial symmetry diameter $2A$ and minor diameters $2B$:

$$D(X,X') = 2B\left(1 - \chi\frac{(\hat{\mathbf{r}}\cdot\hat{\mathbf{e}})^2(\hat{\mathbf{r}}\cdot\hat{\mathbf{e}}')^2 - 2\chi(\hat{\mathbf{r}}\cdot\hat{\mathbf{e}})(\hat{\mathbf{r}}\cdot\hat{\mathbf{e}}')(\hat{\mathbf{e}}\cdot\hat{\mathbf{e}}')}{1-\chi^2(\hat{\mathbf{e}}\cdot\hat{\mathbf{e}}')^2}\right)^{-1/2}. \tag{3.2}$$

The unit vectors $\hat{\mathbf{e}}$ and $\hat{\mathbf{e}}'$ point along the the axis of rotational symmetry, the unit vector $\hat{\mathbf{r}}$ is in the direction of $|\mathbf{r}-\mathbf{r}'|$, and $\chi = (A^2 - B^2)/(A^2 - B^2)$. This expression is obtained by considering the integral of the product of two ellipsoidal, Gaussian

distribution functions, and is a good approximation to the actual closest approach distance.

The grand canonical partition function, including a one-body potential $v(X)$ that will be used only to generate correlation functions, is

$$e^{-W} = \sum_{N=0}^{\infty} \frac{1}{N!} \prod_{i=1}^{N} [\int \frac{d\mathbf{p}_i dX_i}{h^3} \exp(-\beta[\frac{\mathbf{p}_i^2}{2m} + v(X_i) - \mu + \sum_{i<j\leq N} U(X_i, X_j)])] \quad (3.3)$$

where $\beta = (kT)^{-1}$, μ is the chemical potential, $\mathbf{p}_i$ are the momenta conjugate to $\mathbf{r}_i$, m is the molecular mass, $dX_i = d\mathbf{r}_i d\hat{\mathbf{e}}_i/(4\pi)$, and $-W = \beta pV$, p being the pressure. The momentum integration is unrestricted, while the spatial integration over $\mathbf{r}_i$ is over the system volume V and the orientation integration is over the surface of the unit sphere. Due to the fact that the potential is either zero or infinity, a change in the particle mass or temperature is equivalent to a change in chemical potential (and hence in pressure or average density). In this work, all results will be in terms of the particle density ρ in units of $(8AB^2)^{-1}$, which along with the anisotropy A/B, completely describe the system.

This system (using a slightly different $D(X, X')$) has been studied by Frenkel, Mulder and McTague using constant-pressure Monte Carlo simulation[54], yielding the phase diagram of Figure 3.1. This phase diagram is in terms of the variables A/B and ρ, and has a variety of phases. For $A/B = 1$, the case of hard spheres, a transition is seen from an isotropic liquid to a close-packed solid near the fluid density $\rho = 0.95$. For small prolate or oblate anisotropy, this phase is seen to be the orientationally disordered (plastic) crystalline phase. At high enough pressure a transition is expected to an oriented solid phase, which eventually will close-pack to achieve the maximum possible density ($\rho = \sqrt{2}$, for all A/B).

At medium anisotropy ($A/B \approx 1.5$), the isotropic phase directly crystallizes to the oriented solid without an intermediate orientationally disordered crystalline phase. At large anisotropy, an oriented (nematic) liquid phase appears at densities below where

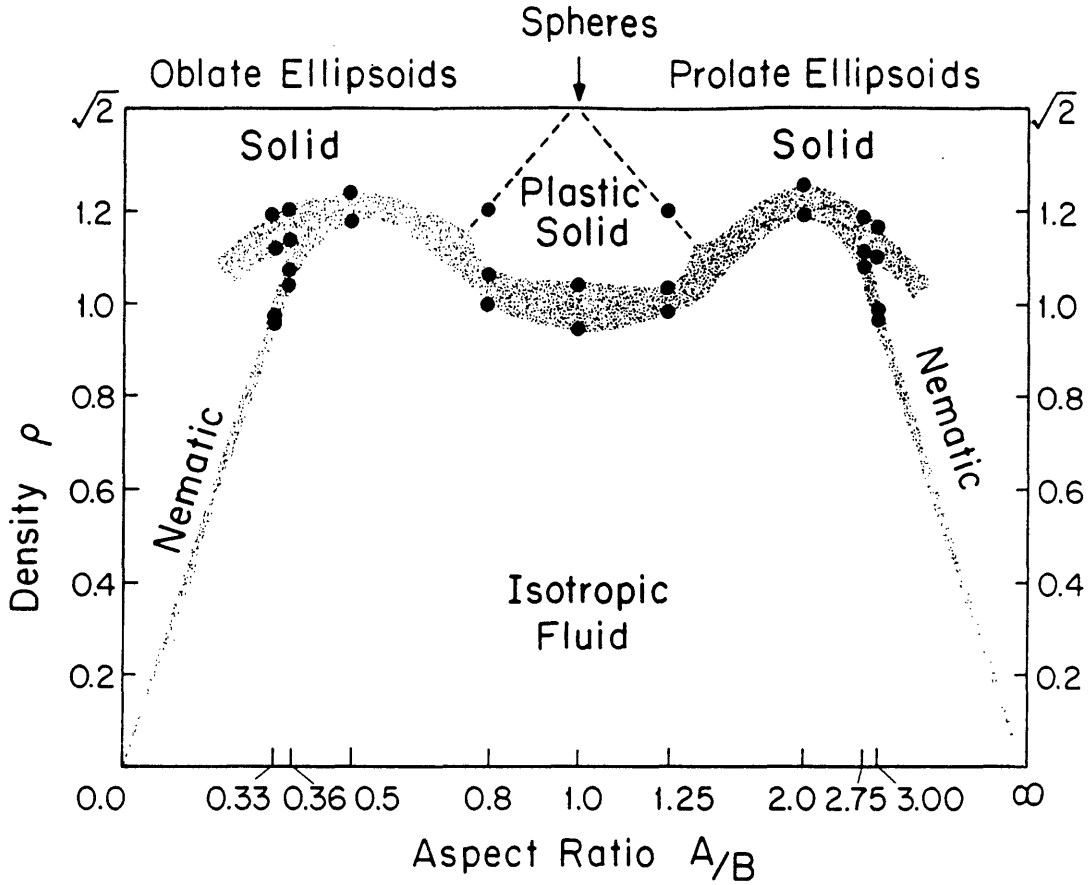

Figure 3.1: Phase diagram of hard ellipsoids of aspect ratio A/B and density ρ, taken from Reference [54]. Shaded regions indicate coexistence regions, and points are from Monte Carlo calculations.

the oriented solid is stable, and as one goes toward either hard needles ($A/B \gg 1$) or hard platelets ($A/B \ll 1$), the isotropic to nematic transition density goes to zero. As can be seen from Figure 3.1, the phase diagram is essentially symmetric under $A/B \rightarrow B/A$, or equivalently under $\chi \rightarrow -\chi$. All the transitions reported in Monte Carlo simulation are first-order except that from the plastic to the oriented solid, which is reported to be second order or possibly weakly first order, with the orientational order parameter tending toward zero as the plastic phase is approached from within the solid phase.

An alternate, analytical approach to understanding the hard ellipsoid system is through a functional expansion of the thermodynamical potential about the isotropic liquid state, in powers of the deviation of the one-body density from its isotropic state. This yields a mean-field description of ordering in the system that uses the one-body density as a functional variational parameter. Below, the basic theory, originally due to Ramakrishnan and Yussouff[38], and later developed by others [42, 43, 44, 45] is

briefly summarized.

If the momentum integration is carried out in equation (3.3), a simpler form is obtained:

$$e^{-W} = \sum_N (N!)^{-1} \prod_i [\int dX_i \exp[-u(X_i) - \beta \sum_{i<j\leq N} U(X_i, X_j)]], \tag{3.4}$$

where the effective one-body potential is $u(X) = \beta(v(X) - \mu) + 3\log\Lambda$ for a thermal wavelength $\Lambda = [h^2/(2\pi mkT)]^{1/2}$. The field $u(X)$ is easily seen to generate the distribution functions of the system: if the one-body density operator is $\rho(X) = \sum_{i=1}^{N} \delta(X - X_i)$, then

$$\begin{aligned} &\rho(X) = <\rho(X)> = \frac{\delta W}{\delta u(X)}, \\ &<\rho(X)><\rho(X')>[g(X,X') - 1] = \\ &\quad <\rho(X)\rho(X')> - <\rho(X)><\rho(X')> = -\frac{\delta^2 W}{\delta u(X)\delta u(X')}, \end{aligned} \tag{3.5}$$

etc.

The potential associated with W that is an intrinsic functional of the one-body density $\rho(X)$ is obtained by Legendre transformation,

$$\beta F = \max_{u(X)} [W - \int u(X)\rho(X)], \tag{3.6}$$

and in the case $v(X) = 0$ (no external spatially dependent chemical potential), F is the plain old extensive Helmholtz free energy of the system. The functional derivatives of this object with respect to the density are[40]

$$\frac{\delta^s}{\delta\rho(X_1)\cdots\delta\rho(X_s)}(\int \rho(X)[\log\rho(X) - 1]dX - \beta F) = C^{(s)}(X_1 \cdots X_s), \tag{3.7}$$

where $C^{(s)}$ denote the direct correlation functions. For the isotropic liquid with $v = 0$, $C^{(1)} = \log(\rho) + u$, and $C^{(2)}$ is the familiar Ornstein-Zernicke[55] direct pair correlation

function.

Noting the inverse of the transformation (3.6)

$$W = \min_{\rho(X)}[\beta F + \int u(X)\rho(X)], \tag{3.8}$$

and assuming that the direct correlation functions are known in the isotropic state where $\rho(X) = \rho_0$, the potential W can be functionally expanded around the isotropic state. In this expansion, both $\rho(X)$ and u are treated as independent functional parameters: they are later linked through the functional minimization in (3.8). For the purposes of this work, there will be no external potential and equal chemical potentials for all configurations of the one-body distribution. This leads to the expansion for the dimensionless grand potential

$$\begin{aligned}\Delta w = \frac{W - W_0}{\rho_0 V} = 1 + \frac{1}{\rho_0 V}\int dX \rho(X)[\log\frac{\rho(X)}{\rho_0} - 1] \\ -\frac{1}{2\rho_0 V}\int dX dX' C^{(2)}(X, X'; \rho_0)[\rho(X) - \rho_0][\rho(X') - \rho_0],\end{aligned} \tag{3.9}$$

which has been truncated at second order in the deviations from the isotropic state where the potential takes on the value W_0. The $\rho(X)$ that minimizes this expression is the stable equilibrium configuration of the system, and when two local minima switch global stability, there is a phase transition. Fluctuations about these solutions are ignored in this theory, but should not be of great importance in the completely entropy-driven first-order transitions that will be later studied. It should be noted that this theory is strictly valid only when the isotropic liquid is the stable thermodynamical state, since the existence of isotropic liquid direct correlations is assumed.

The physical interpretation of the terms in this expansion is straightforward. The term which consists of a single integral (sometimes called the 'local' term) is essentially the difference in Helmholtz potential between the inhomogeneous and homogeneous states for an ideal gas ($U = 0$). Thus this term is often referred to as the 'ideal gas' term. The remaining, nonlocal terms thus take into account the interactions U

between the particles, and the sum of these terms is often referred to as the 'excess' Helmholtz potential difference between the homogeneous and inhomogeneous states.

The usual approach to such a theory is to first obtain some approximation to the function $C^{(2)}$ for the liquid state, and then to choose a parametrization of the one-body density that is appropriate for the type of phase transitions that are expected. With these two objects specified, the functional (3.9) is completely defined and calculation proceeds by numerical minimization of Δw with respect to the parameters in $\rho(X)$. When a configuration other than the isotropic liquid satisfies $\Delta w = 0$, this ordered and the isotropic phases are in coexistence. All the properties of ordered phases at the transition can thus be identified.

This type of theory has been successfully applied to the study of crystallization of particles interacting via spherical pair potentials including the case of hard spheres[38, 42, 43, 44], using the large amount of knowledge that has been collected about the liquid state of this system. Singh and Singh[45] have pioneered the study of transitions to the plastic and nematic states in the hard-ellipsoid system using this theory. There are uncertainties in their work, the most important of which is the lack of information about the function $C^{(2)}$, which even in the case of the isotropic state, is a function of four independent variables, forcing the use of what is essentially a guess for $C^{(2)}$. Other problems with the initial study are that the oriented crystal phase was not considered, and that the parametrization of the plastic phase was done so that the rather narrow real-space lattice peaks associated with hard-core crystallization could not be generated. In the remainder of this work, efforts to remedy these problems are described.

3.2.2 A Numerical Optimization Study of Two-Body Direct Correlations of Hard Ellipsoids

As can be seen from its functional definition (3.7), the pair direct correlation function (DCF,$C^{(2)}(X, X')$, denoted $C(X, X')$ for the remainder of this paper) of a homoge-

neous isotropic fluid of density ρ_0 satisfies the Ornstein-Zernicke relation[55]

$$g(X,X') - 1 = C(X,X') + \rho_0 \int dX"(g(X,X'') - 1)C(X'',X'), \tag{3.10}$$

where $g(X,X')$ is the dimensionless pair distribution of (3.5). This equation indicates that C is a short-ranged object that through the nonlinear integral equation above, generates the possibly long-ranged correlations in g. In fact, C has a range comparable to that of the interparticle potential. For the hard-sphere fluid, C has been shown numerically[56] to rapidly drop to zero outside the region $|\mathbf{r} - \mathbf{r}'| < D$. The main property of $g(X,X')$ is that for any hard core system it vanishes inside the hard core region $|\mathbf{r} - \mathbf{r}'| < D(X,X')$.

This suggests an approximation for C for a hard-core system. If it is assumed that $C = 0$ outside the hard core region, then equation (3.10) becomes closed once the boundary $D(X,X')$ is specified, since C and g will be nonzero on disjoint domains. If the integral equation is written in terms of a single function $\tau = g - C$, then it is clear that $g = -C$ at the boundary, since τ must be a continuous function. This approximation, due to Percus and Yevick (PY)[57] can be derived as a low-order truncation of a systematic functional expansion[40].

The PY equation has been an important tool in the study of hard-core fluids due to the fact that it is exactly soluble for the case of hard spheres[58]. The PY DCF is extremely simple in structure:

$$\begin{aligned} C(X,X') = C_0(x) = \quad & a + bx + \eta a x^3/2, \quad x \leq 1 \\ & 0, \qquad\qquad x > 1 \\ & x = |\mathbf{r} - \mathbf{r}'|/D \quad , \end{aligned} \tag{3.11}$$

with $a = -(1+2\eta)(1-\eta)^{-4}$, $b = 6\eta(1+\eta/2)(1-\eta)^{-4}$, and $\eta = \pi\rho_0 D^3/6$, for spheres of diameter D. This DCF gives good account of the behavior of the isotropic phase of the hard-sphere system and has been the basis of the successful efforts to

study the crystallization of hard spheres via the density-functional expansion (3.9). Unfortunately, no solutions for anisotropic hard cores exist, so one is forced to guess a suitable DCF for such systems.

For the case of hard ellipsoids, the DCF has been assumed to resemble the hard sphere DCF with the sphere diameter replaced with the orientation-dependent distance of closest approach of the molecules, and with the packing fraction η replaced with the corresponding ellipsoid fluid packing fraction $4\pi AB^2\rho_0/3$. This approximation, due to Pynn and Wulf[59, 60], is known to be asymptotically correct for either low anisotropy or low density, but little is known about its validity at densities near freezing and for strong molecular anisotropy where strong orientational correlations are expected. The possibility that the overall strength of the direct correlations as a function of relative orientation is incorrectly accounted for by this approximation seems likely considering the much lower transition densities obtained for the isotropic to nematic fluid transition in the ellipsoid fluid by density functional calculations using this DCF[45] than by Monte Carlo computations[54].

Here the approach is taken of choosing trial correlation functions and then using the Percus-Yevick equation to identify an optimal solution. Here, the one-parameter trial solutions are

$$\begin{aligned} C(X,X') &= C_0(|\mathbf{r}-\mathbf{r}'|/D(X,X'))[1+\alpha P_2(\hat{\mathbf{e}}\cdot\hat{\mathbf{e}}')] \\ g(X,X') &= g_0(|\mathbf{r}-\mathbf{r}')/D(X,X'))[1+\alpha P_2(\hat{\mathbf{e}}\cdot\hat{\mathbf{e}}')], \end{aligned} \tag{3.12}$$

where $P_2(\mu) = (3\mu^2-1)/2$, and g_0 is the PY correlation function[61]. These trial correlations allow the relative strength and anisotropy of direct correlations for parallel and perpendicular molecular configurations to be adjusted, and also satisfy the requirement that $g = -C$ on the surface of the hard core region $|\mathbf{r}-\mathbf{r}'| = D(X,X')$. Integration of the PY equation squared over the hard core region yields a functional that quantifies the accuracy of the trial solution, and thus should be minimized with

respect to α to obtain the best solution. Integration over only the core region emphasizes the DCF rather than the pair distribution, and limits the integration to a finite region, which is important numerically. The error functional is thus explicitly

$$I(\alpha) = \int dX[1 + C(X,0) + \rho \int dX' C(X',0)(g(X,X') - 1)]^2. \qquad (3.13)$$

$I(\alpha)$ has been computed numerically for prolate ellipsoids with anisotropies $A/B =$ 1.00, 1.22, 1.53, 2.00, and 3.00 (corresponding to χ =0.0, 0.2, 0.4, 0.6, and 0.8) and for packing fractions $\eta = 0.1, 0.2, 0.3, \cdots, 0.7$ ($\eta = 0.7405$ is the close packing density) over appropriate ranges of α. The inner integral in in (3.13) was computed using adaptive integration with 80000 points in the five-dimensional region $|\mathbf{r}'| < D(X',0)$, while the outer integration was done by Monte Carlo sampling of the region $|\mathbf{r}| < D(X,0)$. Computation of each value $I(\alpha)$ required 800 seconds on a Cyber 205 computer. For $A/B = 1.0$ (spheres) the minimum of $I(\alpha)$ is at $\alpha^* = 0.0$ for all η , while for $A/B = 1.22$, the minima are shifted to slightly positive α^* for large η . This shift becomes much larger for larger A/B, confirming that the Pynn-Wulf approximation is inaccurate for large anisotropy and density. The trial function is found to greatly improve the error in the solution for large η and A/B: for $\eta = 0.4$ and A/B=2, $I(\alpha^*)$ is approximately one-third of the value taken at $\alpha = 0$.

This correction makes the DCF more negative, corresponding to a larger free energy cost, for parallel ellipsoid configurations. For perpendicular configurations, the correction makes the DCF less negative, corresponding to a smaller free energy cost for these configurations. This is consistent with the fact that the Pynn-Wulf DCF overestimates the stability of the large-anisotropy nematic fluid. For all the anisotropies studied, α^* is zero within the resolution of the calculation for densities $\eta \leq 0.1$. The numerical results are displayed in Figure 3.2: linear fits through $\eta = 0$, $\alpha^* = 0$ were done for each A/B, and are summarized in Table 3.1. The errors shown in Figure 3.2 are due to uncertainties in estimating the location of the minima, which are due to the approximately 10 % errors in the values of the error integral. There is

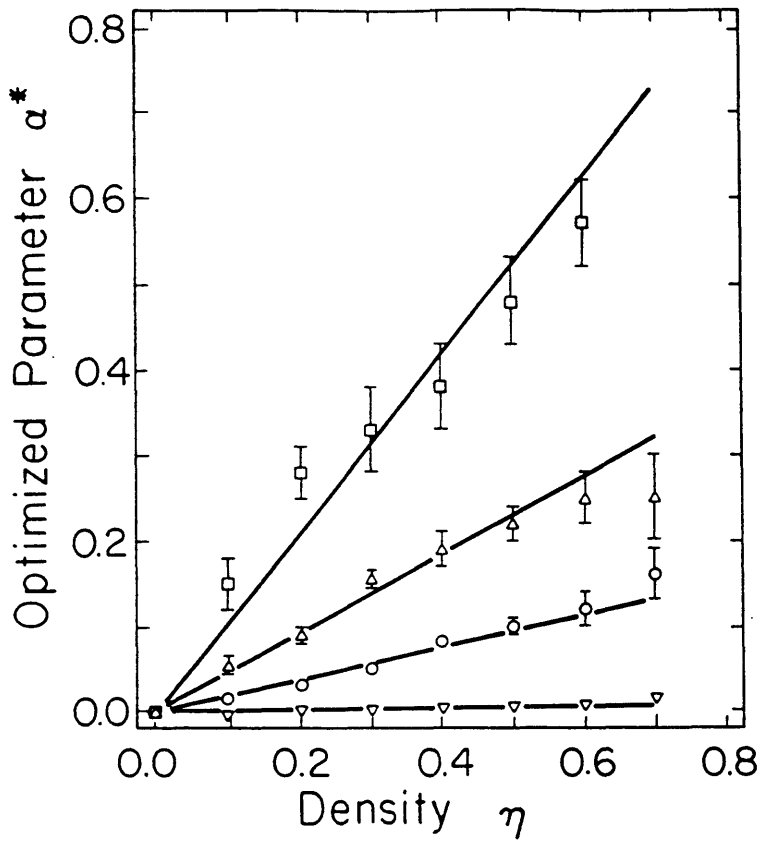

Figure 3.2: Numerical results and linear fits for α^* vs η. $\bigtriangledown, \bigcirc, \bigtriangleup, \square$ represent the positions of minima for α for A/B = 1.22, 1.53, 2.00, and 3.00, respectively.

A/B	fit m	N	χ^2 of fit	$Q(\chi^2, N-1)$
1.22	0.007±0.003	8	6.9	0.44
1.53	0.19 ±0.01	8	6.6	0.48
2.00	0.46 ±0.02	8	6.9	0.44
3.00	1.04 ±0.05	7	11.6	0.07

Table 3.1: Summary of fits of $\alpha^* = m\eta$. The errors in m reflect $\Delta\chi^2 = 1$, corresponding to the boundaries of the 68% confidence region. Q is the probability of χ^2 exceeding the quoted value. N is the number of data points per fit.

no reason to expect $\alpha^* = m\eta$, but this form fits the data well using one parameter, and satisfies $\alpha^* = 0$ when $\eta = 0$ and $d\alpha^*/d\eta > 0$, which are the main features of the existing results. Until higher-precision calculations are done, it is difficult to say whether a more complicated function (e.g. $\alpha^* = m\eta^p$) is more appropriate to describe the data.

3.2.3 Transitions to Crystalline Phases

A. Calculation of Grand Potential

The calculation that has been done is a direct calculation of the excess grand potential for the crystalline phases, followed by numerical minimization of the resulting nonlinear functional. The first step is to specify the one-body distribution in terms of as few parameters as possible that still allow a reasonable description of the ordered phase. Past studies of freezing of hard cores have indicated that the positional distribution consists of rather narrow peaks centered at the real-space lattice sites of a close-packed lattice. This suggests a positional distribution of Gaussian functions centered on FCC lattice sites, requiring three parameters, the average solid density, the real-space lattice constant, and the real-space Gaussian width.

So far, this is suitable to describe the plastic phase, but not the oriented solid. The only practical way to model this additional phase is to assume azimuthal orientational symmetry (invariance of the orientational distribution under rotations about the 3-axis), and to then multiply the positional distribution described above by a orientational distribution that depends only on the polar orientational degree of freedom. This procedure adds at least one more parameter to the distribution describing the degree of orientational symmetry-breaking. In addition, from the Monte Carlo results it is expected that the solid phase real-space lattice will be tetragonally distorted, requiring another parameter. In this work, the tetragonal distortion is introduced by rescaling the 3-component of the positional degree of freedom, turning the spherically symmetric lattice site distributions on a cubic lattice into ellipsoidal distributions

centered on a tetragonally distorted lattice.

Thus, the one-body distribution is written as $\rho(X) = \rho(\mathbf{r})\rho(\hat{\mathbf{e}})$, with the normalization conditions $V^{-1}\int_V dr\rho(\mathbf{r}) = \rho_1$ and $\int d\hat{\mathbf{e}}\rho(\hat{\mathbf{e}}) = 1$. Explicitly, these distributions are

$$\begin{aligned}\rho(\mathbf{r}) &= \rho_1\Delta\pi^{-3/2}\sigma^{-3}x_T^{-1}\sum_{\mathbf{s}\in\mathbf{T}}\exp(-\sigma^{-2}[(r_1-s_1)^2+(r_2-s_2)^2+x_T^{-2}(r_3-s_3)^2]) \\ &= \rho_1\sum_{\mathbf{k}\in\mathbf{U}}e^{-(\sigma\mathbf{k}/2)^2}e^{i\mathbf{k}\cdot\mathbf{r}} = \rho_1\sum_{\mathbf{k}\in\mathbf{U}}a_{\mathbf{k}}e^{i\mathbf{k}\cdot\mathbf{r}}, \qquad (3.14)\end{aligned}$$

where the direct FCC and inverse BCC lattices are

$$\begin{aligned}\mathbf{T} &= \{(c/2)[n_1(0,1,1)+n_2(1,0,1)+x_Tn_3(1,1.0)]\}, \\ &\quad n_i = 0,\pm1,\pm2,\cdots, \\ \mathbf{U} &= \{(2\pi/c)[m_1(-1,1,1)+m_2(1,-1,1)+x_T^{-1}m_3(1,1,-1)]\}, \\ &\quad m_i = 0,\pm1,\pm2,\cdots,\end{aligned}$$

and the orientational distribution is

$$\rho(\hat{\mathbf{e}}) = 1 + b_2P_2(\mu). \qquad (3.15)$$

μ is the cosine of the polar orientational angle, measured from the 3-axis, and $P_2(\mu) = (3\mu^2-1)/2$. Δ is the volume per lattice site, and is $\Delta = c^3x_T/4$ for the FCC lattice.

This choice of distribution has five parameters: the ordered phase density ρ_1, the real-space lattice peak width σ and lattice constant c, the tetragonal distortion x_T, and the amount of orientational ordering b_2. These are sufficient parameters to characterize the structural properties of the two expected crystalline phases. These parameters will be determined for different values of the liquid density ρ_0 by minimization of the grand potential functional.

The first, local term in the functional (3.9) is easily computed because it additively

separates into contributions due to the orientational and positional distributions, and also because the parameter x_T can be scaled out of the calculation. The ideal gas term thus becomes

$$(\rho_0 V)^{-1} \int dX \rho(X)[\log \frac{\rho(X)}{\rho_0} - 1] = \tag{3.16}$$
$$= r_1[\int_V \frac{d\mathbf{r}\rho(\mathbf{r})}{V\rho_1} \log \frac{\rho(\mathbf{r})}{\rho_1} + \int_{-1}^{1} \frac{d\mu}{2}\rho(\mu)\log\rho(\mu) + \log r_1 - 1],$$

where $r_1 = \rho_1/\rho_0$ is the solid density relative to the liquid density. The orientational integral can be done exactly in terms of b_2:

$$\int_{-1}^{1} \frac{d\mu}{2}\rho(\mu)\log\rho(\mu) \tag{3.17}$$
$$= \log(1+b_2) + (\frac{4-2b_2}{3})[(\frac{2-b_2}{3b_2})^{1/2}\tan^{-1}(\frac{3b_2}{2-b_2})^{1/2} - 1] - \frac{b_2}{3}$$

for $-1 < b_2 < 2$. The positional integral can be accurately obtained numerically using the separation

$$\int_V \frac{d\mathbf{r}\rho(\mathbf{r})}{V\rho_1} \log \frac{\rho(\mathbf{r})}{\rho_1} = \frac{I_2}{I_1} - \log I_1 \tag{3.18}$$

where

$$\begin{aligned}
I_1 &= \int' \sum_{\mathbf{s}} e^{-\sigma^{-2}(\mathbf{r}-\mathbf{s})^2}, \\
I_2 &= \int' \sum_{\mathbf{s}} e^{-\sigma^{-2}(\mathbf{r}-\mathbf{s})^2} \log(\sum_{\mathbf{s}} e^{-\sigma^{-2}(\mathbf{r}-\mathbf{s})^2}) \\
&= -\int' (\mathbf{r}/\sigma)^2 e^{-(\mathbf{r}/\sigma)^2} + \int' e^{-(\mathbf{r}/\sigma)^2} \log(1 + \sum_{\mathbf{s}\neq 0} e^{-(\sigma^{-2}[(\mathbf{r}-\mathbf{s})^2 - \mathbf{r}^2])}) \\
&+ \int' \sum_{\mathbf{s}\neq 0} e^{-([\mathbf{r}-\mathbf{s}]/\sigma)^2}[-(\mathbf{r}/\sigma)^2 + \log(1 + \sum_{\mathbf{s}\neq 0} e^{-(\sigma^{-2}[(\mathbf{r}-\mathbf{s})^2 - \mathbf{r}^2])})],
\end{aligned}$$

where

$$\int' = 32c^{-3} \int_0^{c/4} dr_1 \int_0^{c/4} dr_2 \int_0^{c/2} dr_3 \tag{3.19}$$

In these integrals, the parameter x_T has been rescaled to 1: the fact that the integrals are volume-normalized allows this to be done. The $s = 0$ term in I_1 is a product of three error functions, while the remaining terms decrease rapidly as $e^{-(|\mathbf{s}|/\sigma)^2}$ and can be easily approximated with Gaussian numerical integration. The first term of I_2 is reducible to incomplete gamma functions, and again, the other terms are easily approximated by Gaussian integration. For the σ that will be obtained, the summations over $\mathbf{s}$ can be truncated at first nearest neighbors.

The second, nonlocal term in (3.9) is somewhat harder to calculate. It is first reduced to the form

$$\begin{aligned}
&(2\rho_0 V)^{-1} \int dX dX' C(X, X'; \rho_0)[\rho(X) - \rho_0][\rho(X') - \rho_0] \\
&= -\eta(4a + 3b + a\eta)(1 - \chi^2)^{-1/2} F_1(\chi)(1 - 2r_1) \qquad (3.20) \\
&- \frac{12\eta r_1^2}{A/B} \sum_{n=0}^{\infty} \frac{(-1)^n |2B\mathbf{k}|^{2n}}{2n!} \left(\frac{a}{2n+3} + \frac{b}{2n+4} + \frac{a\eta/2}{2n+6} \right) \\
&\int \frac{d\hat{\mathbf{r}} d\hat{\mathbf{e}} d\hat{\mathbf{e}}'}{(4\pi)^3} (\hat{\mathbf{k}} \cdot \hat{\mathbf{r}})^{2n} \left(\frac{D(X, X')}{2B} \right)^{2n+3} [1 + \alpha P_2(\hat{\mathbf{e}} \cdot \hat{\mathbf{e}}')][1 + 2b_2 P_2(\mu) + b_2^2 P_2(\mu) P_2(\mu')],
\end{aligned}$$

where

$$F_1(\chi) = (1 - \chi^2)^{1/2} \int \frac{d\hat{\mathbf{r}} d\hat{\mathbf{e}} d\hat{\mathbf{e}}'}{(4\pi)^3} \left(\frac{D(X, X')}{2B} \right)^3 = \frac{1}{2} \left((1 - \chi^2)^{1/2} + \frac{\sin^{-1}(\chi)}{\chi} \right) \qquad (3.21)$$

Due to all the integrals in (3.20), this is a difficult expression to evaluate. However, it can be computed if the approximation

$$(\hat{\mathbf{k}} \cdot \hat{\mathbf{r}})^{2n} = \frac{1}{2n+1} + \frac{5n}{2(2n+1)(2n+3)} (3\mu_k^2 - 1)(3\mu_r^2 - 1) \qquad (3.22)$$

is made, which is the truncation of an expansion in spherical harmonics (ignoring the terms with azimuthal dependence that vanish when the integrals in (3.20) are done). This controls the proliferation of powers of the 3-components of the various unit vectors (all terms have at most squares of them) which is important in reducing

the calculation to a reasonable level. It should be noted that this approximation is unneccesary when the order parameter $b_2 = 0$, when only the $1/(2n+1)$ part of the expansion can contribute, and thus will only affect the computations of the oriented solid phase.

The next step is to expand the powers of $D(X, X')$ in terms of the dot products $(\hat{\mathbf{r}} \cdot \hat{\mathbf{e}}), (\hat{\mathbf{r}} \cdot \hat{\mathbf{e}}'), (\hat{\mathbf{e}} \cdot \hat{\mathbf{e}}')$:

$$\left(\frac{D(X,X')}{2B}\right)^{2n+3} = \tag{3.23}$$
$$1 + \sum_{j=1}^{n}\sum_{k=1}^{j} \chi^{2j-k} \frac{(2n+3)(2n+5)(\cdots)[2n+3+2(k-1)](k)(k+1)(\cdots)(j-1)}{k!(j-k)!}$$
$$\sum_{p=0}^{k}(-1)^{k-p}2^{-p}\begin{pmatrix} k \\ p \end{pmatrix}\sum_{q=0}^{p}\begin{pmatrix} p \\ q \end{pmatrix}(\hat{\mathbf{e}}\cdot\hat{\mathbf{e}}')^{2j-k-p}(\hat{\mathbf{e}}\cdot\hat{\mathbf{r}})^{2q+k-p}(\hat{\mathbf{e}}'\cdot\hat{\mathbf{r}})^{p-k-2q},$$

and to do the integrals over the solid angles. These integrals are all of the form

$$I(\{n\};\{m\}) = \tag{3.24}$$
$$\int \frac{d\hat{\mathbf{e}}_1 d\hat{\mathbf{e}}_2 d\hat{\mathbf{e}}_3}{(4\pi)^3}\mu_1^{m_1}\mu_2^{m_2}\mu_3^{m_3}(\hat{\mathbf{e}}_1\cdot\hat{\mathbf{e}}_2)^{n_1}(\hat{\mathbf{e}}_2\cdot\hat{\mathbf{e}}_3)^{n_2}(\hat{\mathbf{e}}_3\cdot\hat{\mathbf{e}}_1)^{n_3},$$
$$n_i \in \{0,1,2,\cdots\}, m_i \in \{0,2\},$$

and vanish unless the n_i are either all even or all odd. These can be expressed in terms of the constants $d_l^n = d^n j_l(x)/dx|_{x=0}$ where the j_l are spherical Bessel functions. In the following, the notation $\sum'$ is a summation over either all even or all odd positive integers l up to the number $\min\{n_i\}$:

$$\begin{aligned} I(\{n\};0,0,0) &= \sum{}'(2l+1)(-1)^{(3l-n_1-n_2-n_3)/2} d_l^{n_1} d_l^{n_2} d_l^{n_3} \\ I(\{n\};2,0,0) &= I(\{n\};0,0,0)/3 \\ I(\{n\};2,2,0) &= \sum{}'(-1)^{(3l-n_1-n_2-n_3)/2} \end{aligned} \tag{3.25}$$

$$
\begin{aligned}
& \Big(\frac{(2l+1)(8l^2+8l-5)}{15(2l-1)(2l+3)} d_l^{n_1} d_l^{n_2} d_l^{n_3} \\
& -\frac{2l(l-1)}{15(2l-1)} d_l^{n_1} d_{l-2}^{n_2} d_{l-2}^{n_3} \\
& -\frac{2(l+1)(l+2)}{15(2l+3)} d_l^{n_1} d_{l+2}^{n_2} d_{l+2}^{n_3}\Big) \\
I(\{n\};2,2,2) \;=\; & {\sum_{l}}' (-1)^{(3l-n_1-n_2-n_3)/2} \\
& \Big(\frac{(2l+1)(35-108l-12l^2+192l^3+96l^4)}{105(2l-1)^2(2l+3)^2} d_l^{n_1} d_l^{n_2} d_l^{n_3} \\
& -\frac{2(l+1)(l+2)(6l+7)}{105(2l+3)^2} (d_l^{n_1} d_l^{n_2} d_{l+2}^{n_3} + d_l^{n_1} d_{l+2}^{n_2} d_l^{n_3} + d_{l+2}^{n_1} d_l^{n_2} d_l^{n_3}) \\
& -\frac{2l(l-1)(6l-1)}{105(2l-1)^2} (d_l^{n_1} d_l^{n_2} d_{l-2}^{n_3} + d_l^{n_1} d_{l-2}^{n_2} d_l^{n_3} + d_{l-2}^{n_1} d_l^{n_2} d_l^{n_3})\Big)
\end{aligned}
$$

Once the expansions of (3.23) are done, the summations over the index n in expression (3.20) can be exactly done by noting that they can all be rewritten as finite combinations of sines, cosines, and integer powers of the variable $z = |2B\mathrm{k}|$. The first few relevant functions are:

$$
\begin{aligned}
\sum_{n=0}^{\infty} \frac{(-1)^n z^{2n}}{(2n+1)!(2n+3)!} &= -\frac{\cos z}{z^2} + \frac{\sin z}{z^3}, \\
\sum_{n=0}^{\infty} \frac{(-1)^n z^{2n}}{(2n+1)!(2n+4)!} &= -\frac{\cos z}{z^2} + 2\frac{\sin z}{z^3} + 2\frac{\cos z}{z^4} - 2\frac{\sin z}{z^4}, \qquad (3.26) \\
\sum_{n=0}^{\infty} \frac{(-1)^n z^{2n}}{(2n+1)!(2n+6)!} &= -\frac{\cos z}{z^2} + 4\frac{\sin z}{z^3} + 12\frac{\cos z}{z^4} - 24\frac{\sin z}{z^4}, \\
& \quad -24\frac{\cos z}{z^4} + 24\frac{\sin z}{z^4}, \qquad (3.27)
\end{aligned}
$$

etc.

Doing these summations is crucial to being able to obtain high enough momentum components of $D(X, X')$ to calculate the grand potential for the crystallization transitions. The rather slowly decaying and oscillating functions that are obtained by combining these summations cannot be treated properly by series expansion in z be-

cause of the fact that for large values of z, the terms in the series become much larger than the sum, but they very nearly cancel out, making the numerical summation impossible. The resummations above require only the solution of linear equations, and the resulting terms appear to always have integer coefficients.

These expressions have been combined into a computer subroutine that computes the excess free energy of a state described by the parameters $(\rho_1, \sigma, c, x_T, b_2)$ for given values of $(\rho_0, A/B)$. This is done by truncating the various infinite sums in the above expression appropriately to achieve a particular numerical accuracy. In the results for crystallization, the k-vector sums were done over the first 1000 symmetry-unrelated inverse lattice vectors (for the tetragonally distorted FCC lattice), and the sum in (3.23) was done up to $j = 20$. This includes all terms in the expansion of the nonlocal term in powers of χ up to χ^{20}, and is suitable for this range of k-vectors for anisotropies up to about $\chi = 0.15$, with total accuracy in the excess dimensionless potential of about 10^{-4} (the excess potential is typically of order unity away from the transitions). Larger anisotropies can be reached by increasing the limit on the j-sum, or by reducing the cutoff on the k-sum.

This scheme to compute the nonlocal term has one difficulty. The truncation of the expansion of the $(\hat{\mathbf{k}} \cdot \hat{\mathbf{r}})^{2n}$ is hard to extend due to the complexity of the remaining integrals (the functions analogous to (3.25) become excessively complicated for larger powers of the z-axis projections of the solid angles), but in principle this could be done. On the other hand, the current form is (within the numerical accuracy due to the truncations of the j and k sums) correct for the plastic phase, and probably close to correct for the solid, since it is seen numerically that the important terms are the terms that are due to the constant term in the expansion of $(\hat{\mathbf{k}} \cdot \hat{\mathbf{r}})^{2n}$.

B. Results

The calculations of crystallization were carried out first with $x_T = 1, b_2 = 0$ to find a stable plastic phase, and then with all five parameters in an attempt to find a stable

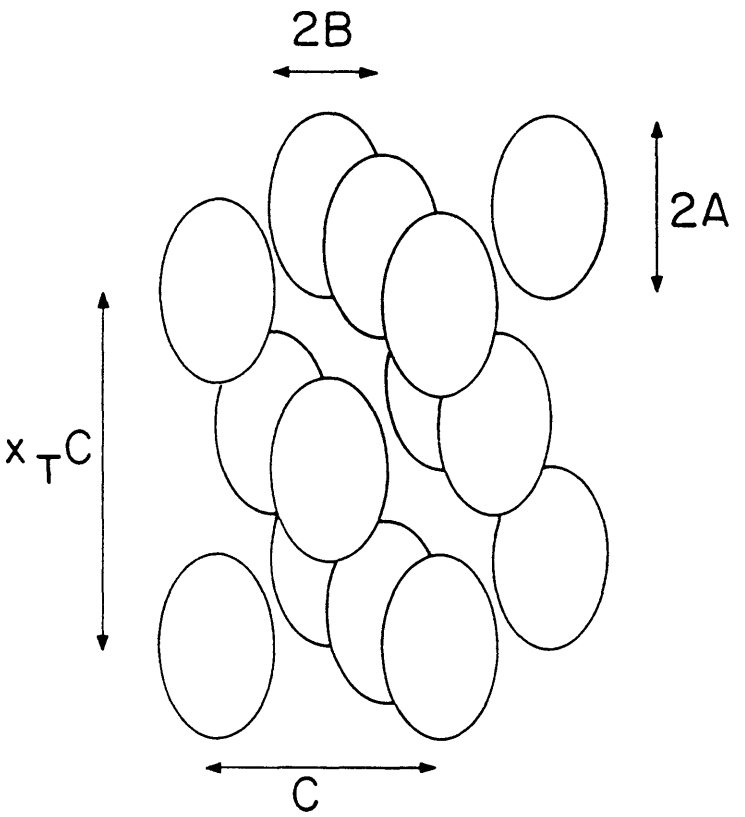

Figure 3.3: FCC oriented solid crystal structure for hard ellipsoids showing structural parameters used in text. In this diagram there is perfect orientational order, which only occurs at close packing. The plastic FCC structure has no tetragonal distortion, and random orientation of molecules.

solid phase. At all times, the parameter b_2 was constrained to be between -1 and 2, which is the region where the corresponding orientational distribution is greater than zero for all values of the polar angle. The minimization was done with a quasi-Newton method that evaluates both first and second derivatives of the potential function with respect to the variational parameters numerically. Values of χ from 0.0 to 0.1 were used. Computation of the expansions of the previous section (to order χ^{20}) takes about 300 seconds on a Cyber 205 computer, but once that is done, calculation of a single value of the grand potential (as a function of the variational parameters and the liquid density) takes about 0.2 seconds on the Cyber, or about 10 seconds on a MicroVAX.

Figure 3.3 shows a section of the solid crystal to illustrate the structural parame-

A/B	ρ_0^*	$(\rho_1^*-\rho_0^*)/\rho_0^*$	$c/(2\sqrt{2}B)$	$\sigma/(2B)$	ρ_D
1.000	0.9461	0.1124	1.065	0.0415	-0.118
1.010	0.9466	0.1119	1.068	0.0417	-0.120
1.020	0.9483	0.1104	1.072	0.0422	-0.118
1.025	0.9497	0.1087	1.075	0.0429	-0.114
1.036	0.9531	0.1060	1.079	0.0434	-0.110
1.041	0.9554	0.1049	1.081	0.0436	-0.108
1.046	0.9580	0.1026	1.083	0.0439	-0.103
1.057	0.9646	0.0965	1.088	0.0450	-0.103
1.067	0.9731	0.0921	1.092	0.0459	-0.096
1.078	0.9843	0.0859	1.095	0.0464	-0.092
1.100	1.0276	0.0677	1.099	0.0451	-0.075

Table 3.2: Properties of plastic phase at the isotropic-to-plastic transition. Listed are aspect ratio, transition density, density difference between coexisting plastic and isotropic phases, lattice constant, lattice site peak width, and the density of defects

ters that are used. The lattice constant c is reported in units of $2\sqrt{2}B$, which is the lattice constant of the close-packed oriented crystalline structure. The peak width σ is given in units of $2B$, which is the distance between the centers of nearest neighbor close-packed ellipsoids in the plane perpendicular to the tetragonal distortion as well as being their minor diameter. The parameters x_T and b_2 are dimensionless.

The results for isotropic to plastic transitions are shown in Table 3.2. These solutions correspond to global minima of the grand potential functional, and an extensive search has been performed over the three-dimensional variational parameter space: for the FCC case, these appear to be the only minima. In fact, to find these solutions was quite difficult because the dependence of the grand potential on the parameter σ is quite strong, and the second derivative matrix ceases to be positive definite outside of the immediate neighborhood of the solutions.

The results shown are for the case $\alpha = 0$. Calculations with α^* as determined in Section III have been done for a few cases over the range $0.0 \leq \chi \leq 0.15$, but α^* is so small in this range that the results are not affected quantitatively in comparison to the $\approx 0.01\%$ error introduced by truncating the various sums in the potential functional. If extension of these calculations is done to larger χ, then the results will begin to be affected: it will later be seen that the isotropic to nematic transitions will be strongly altered by the rather large corrections necessary for $A/B > 2$.

For $A/B = 1$, the calculation reduces to that of Jones and Mohanty[43]. and their results are reproduced for FCC freezing of hard spheres. These transition properties are in good agreement with molecular dynamics simulations[62] with the exception of the value of σ, which is a factor of about three too small in these calculations. As the anisotropy is increased from zero, the transition density is seen to increase. This is also in agreement with the Monte Carlo data[54] and with recent density-functional results of Smithline, Rick and Haymet[46], but in disagreement with the density functional results of Singh and Singh[45]. As the transition density increases, the density discontinuity appears to decrease, until, near $A/B = 1.1$, the transition density begins to rapidly increase toward the close-packing value.

As this is done, the lattice constant is seen to rise as one would expect for the plastic phase. In Figure 3.4, the dependence of this parameter at the transition on anisotropy is shown: it appears to be almost linear in the variable A/B, although it appears to begin to saturate where the transition density starts to increase rapidly. This makes sense, since the plastic phase must on average place the ellipsoid centers farther apart (in units $2B$) as they are made more anisotropic, and for large anisotropies, it is believable that it should become difficult to stabilize the plastic phase due to this effect which tends to expand the crystal. Along with the lattice constant, the peak width σ also increases with anisotropy, although at $A/B = 1.1$, it slightly decreases.

In this work, since all the parameters of the plastic are derived from the functional

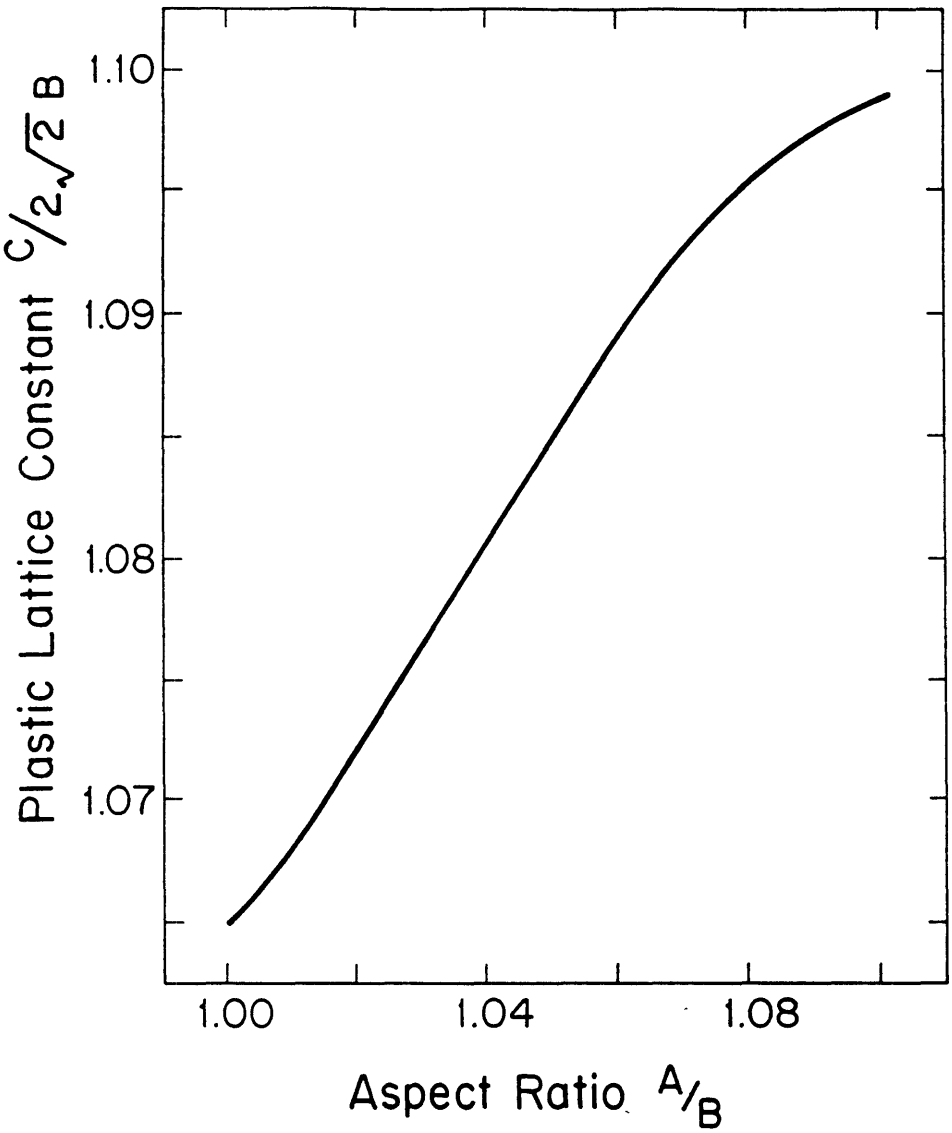

Figure 3.4: Lattice constant of plastic crystal phase at transition from isotropic liquid vs ellipsoid aspect ratio.

A/B	ρ_0^*	$(\rho_1^*-\rho_0^*)/\rho_0^*$	$c/(2\sqrt{2}B)$	$\sigma/(2B)$	x_T	ρ_D
1.041	0.9604	0.1477	1.034	0.0213	1.0590	-0.155
1.046	0.9556	0.1530	1.032	0.0223	1.0645	-0.163
1.051	0.9492	0.1593	1.030	0.0189	1.0701	-0.171
1.057	0.9449	0.1620	1.029	0.0178	1.0766	-0.176
1.062	0.9419	0.1641	1.030	0.0184	1.0818	-0.174
1.067	0.9394	0.1643	1.036	0.0227	1.0876	-0.154
1.078	0.9341	0.1664	1.037	0.0238	1.1022	-0.151
1.100	0.9244	0.1644	1.043	0.0279	1.1223	-0.145

Table 3.3: Properties of oriented solid phase at the isotropic-to-solid transition. Listed are aspect ratio, transition density, density difference between coexisting solid and isotropic phases, lattice constant, lattice site peak width, tetragonal distortion, and the density of defects. The parameter $b_2 = 2$ at all of the transitions listed.

minimization, the solid that is derived may not have one particle in each real-space FCC unit cell, and hence may have on average a net defect density. This density, first computed for density-functional results by Jones and Mohanty[43], is defined as the difference between the solid density and the inverse volume of a unit cell (both measured in terms of the inverse volume $(8AB^2)^{-1}$)

$$\rho_D = \rho_1 - \frac{\sqrt{2}A/B}{x_T}\left(\frac{2\sqrt{2}B}{c}\right)^3 \tag{3.28}$$

and is positive for the case of interstituals, and negative for the case of vacancies. For the plastic phase, a negative defect density is seen, but it decreases with anisotropy as the defects are forced out of the lattice by the hard-core interactions.

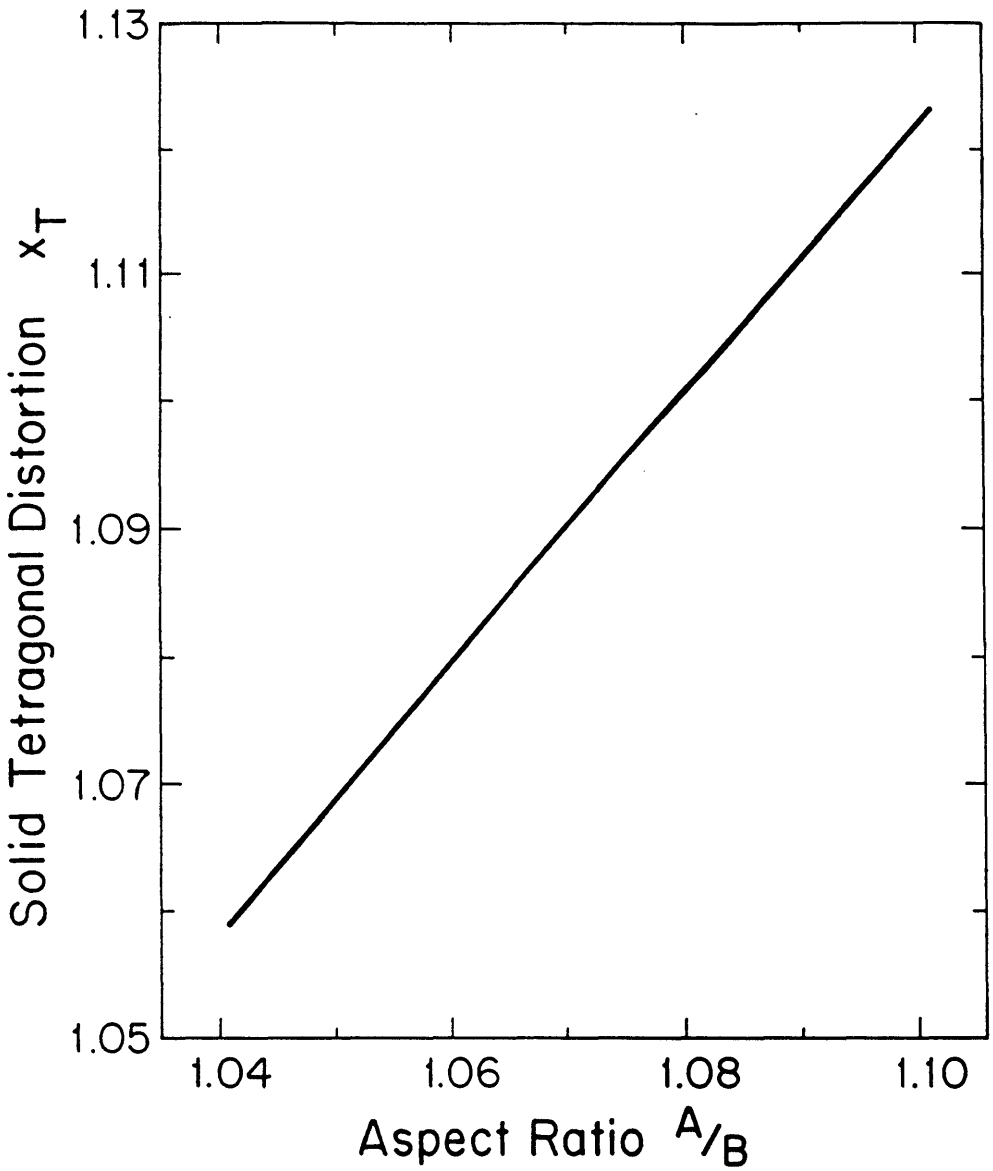

Figure 3.5: Tetragonal distortion of oriented crystal phase at transition from isotropic liquid as a function of ellipsoid aspect ratio.

Table 3.3 shows the results for minimization over all the order parameters for the cases when stable solid phase minima were found in the same range of anisotropies. No stable minima were found for anisotropies below $A/B = 1.041$, while the minima found above that were all for values of the parameter $b_2 = 2$, at the end of its physically allowed range. The remaining parameters are quite stable over the range of anisotropies studied, with the transition density slowly decreasing with increasing anisotropy. The density discontinuity appears to go through a maximum near $A/B = 1.06$, but also changes slowly. The reduced lattice constant and peak width also vary slowly, while the tetragonal distortion (shown in Figure 3.5) increases linearly with A/B, indicating that there is not a large change in the properties of the solid phase apart from a change in the aspect ratio of the crystal unit cell as the anisotropy increases.

As in the Monte Carlo data, the plastic and solid are seen to switch stability as the phases that the isotropic phase first makes a transition to as the anisotropy is increased, although in the theory, this switch is seen at smaller values of A/B than in the Monte Carlo (theory predicts it at 1.045, while the MC results predict it near to 1.2). This theory also can predict the location of the transition from the plastic to the solid by comparing the grand potentials of the two phases, but as remarked previously, this is not strictly valid because of the assumption that direct correlations have liquid symmetry when we in fact are a region of the phase diagram where the plastic phase is supposedly the stable phase. Figure 3.6 shows the excess grand potentials for the plastic and solid phases for the cases $A/B = 1.041$ and $A/B = 1.051$, between which the plastic and solid switch stability. The solid phase potential decreases much faster with increasing density than does the plastic potential.

The combined phase diagram for crystallization transitions from the isotropic liquid is shown in Figure 3.7. The qualitative features of this phase diagram are in agreement with the Monte Carlo phase diagram of Figure 3.1. At the point where the solid and plastic are equally favorable phases, at $A/B \approx 1.040$ and $\rho_1 \approx 0.955$, the

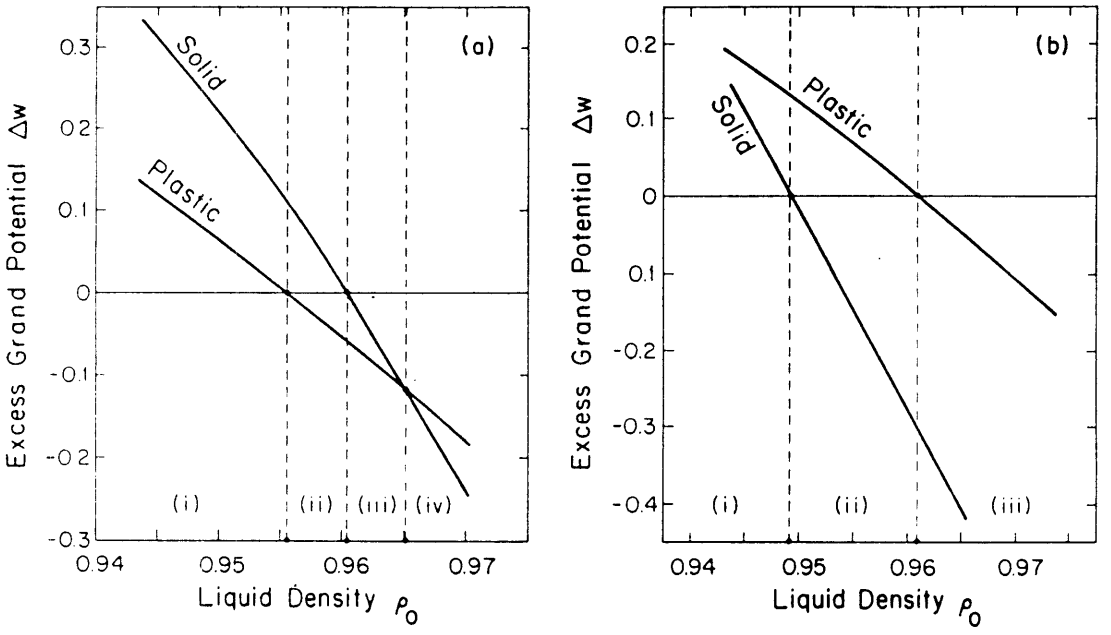

Figure 3.6: Excess grand potential as a function of isotropic fluid density for plastic and solid phases. (a) $A/B = 1.041$. The isotropic phase is stable in (i), the plastic phase is stable in (ii) and (iii), and the solid phase is stable in (iv). In (iii), the solid has become more stable than the isotropic. (b) $A/B = 1.051$. The isotropic phase is stable in (i), while the solid is stable in (ii) and (iii). The plastic is stable with respect to the isotropic phase only in (iii).

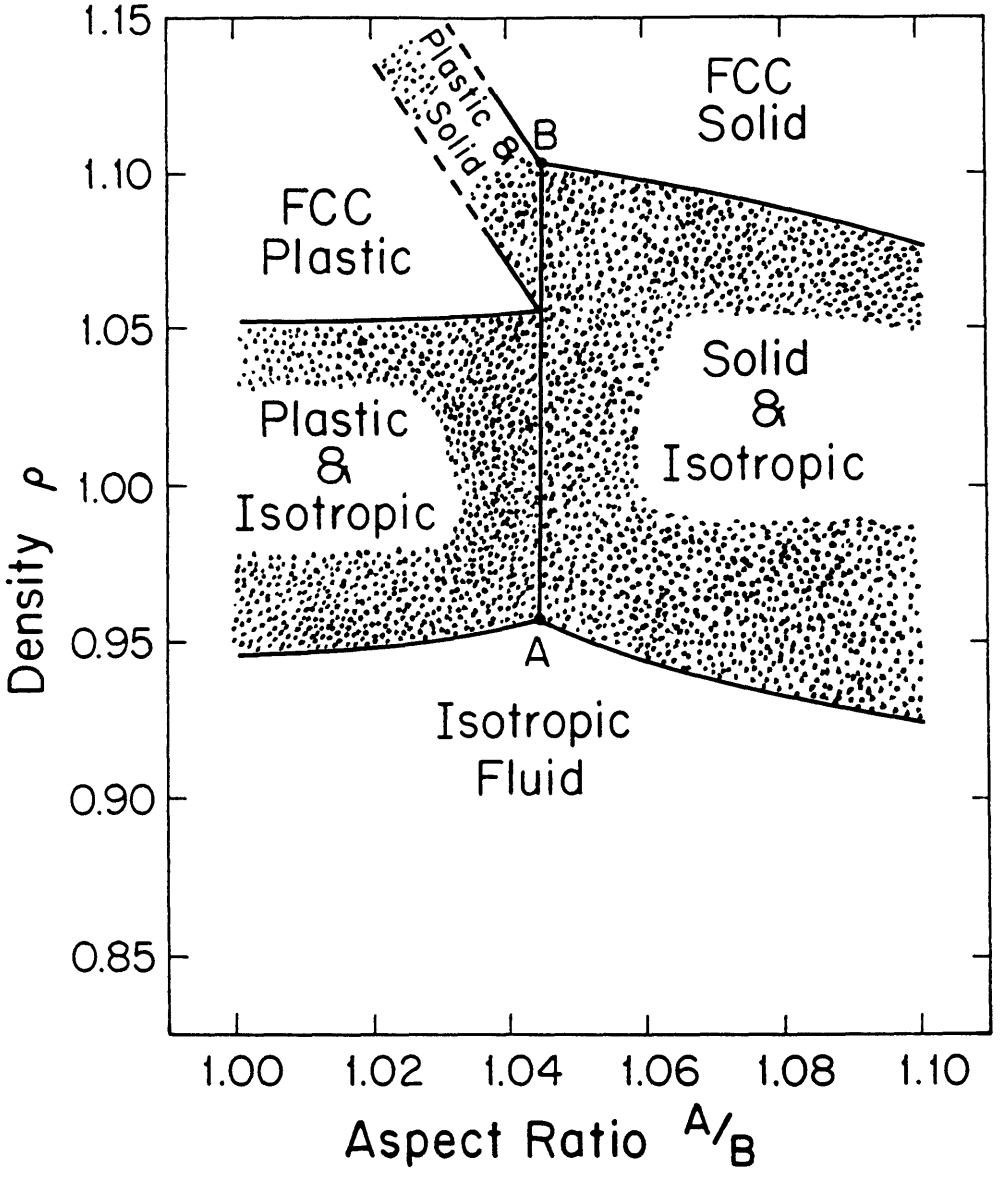

Figure 3.7: Phase diagram combining isotropic-to-plastic and -solid transitions. Transitions from isotropic to plastic and solid phases are as described in Tables 3.2 and 3.3, while the plastic-to-solid transitions shown represent the densities where the plastic and solid exchange stability. Coexistence regions are shaded, and the line AB is a line of three-phase coexistence between the isotropic, plastic and solid phases.

density discontinuities are different (about 0.10 for the plastic and 0.15 for the solid), thus the theory predicts a first-order transition between these phases with a small (≈ 0.05) density discontinuity. However, the simulation result that the orientational order parameter vanishes as one goes toward the solid-plastic phase boundary is not seen here. This is possibly due to the systematic error introduced in the grand potential calculation by the truncation of the sum in the expansion of the term $(\hat{\mathbf{k}}\cdot\hat{\mathbf{r}})^{2n}$. A more complete treatment might produce a better description of this aspect of the solid phase.

3.2.4 Transitions to the Nematic Phase

A. Calculation of Grand Potential

As in the calculation of transitions to the crystal phases, the first step in the nematic calculations is to specify a parametrized density functional. For the uniaxial nematic that is expected, it is sufficient to use a functional of the form

$$\rho(X) = a_0\rho_0 \exp(a_1\mu^2 + a_2\mu^4), \tag{3.29}$$

which has the virtues of being positive for all values of the parameters a_1 and a_2, and being convenient to do calculations with. Thus, the excess grand potential will be a function of three parameters, (a_0, a_1, a_2), as well as the variables $(\rho_0, A/B)$. If we define the one-dimensional integrals

$$q_m = \int_0^1 d\mu \mu^{2m} \exp(a_1\mu^2 + a_2\mu^4),$$

which are calculable using a combination of series expansion and straightforward Gaussian numerical integration, we can express the local term in (3.9) as

$$\int \frac{dX\rho(X)}{V\rho_0}[\log\frac{\rho(X)}{\rho_0} - 1] = a_0[(\log a_0 - 1)q_0 + a_1q_1 + a_2q_2].$$

The average density of the ordered phase is thus $\rho_1 = \rho_0 a_0 q_0$. The nonlocal term is written:

$$\begin{aligned}
&\frac{-1}{2\rho_0}\int \frac{dXdX'}{V} C(X,X';\rho_0)[\rho(X)-\rho_0][\rho(X')-\rho_0] \\
&= -\eta(4a+3b+\eta a)(1-\chi^2)^{-1/2}[(1-\alpha/2)[(1-2a_0q_0)F_1(\chi)+(a_0q_0)^2 \\
&- \sum_{n=1}^{\infty}\frac{(2n-3)!!}{(2n)!!}\chi^{2n}\sum_{j=0}^{n}\binom{2n}{2j}\frac{(2j-1)!!}{(2j)!!}H_{nj}] \\
&+ (\frac{3\alpha}{2})(1-2a_0q_0)(\frac{1}{3}-\sum_{n=0}^{\infty}\frac{(2n-3)!!\chi^{2n}}{(2n)!!(2n+3)}+\sum_{j=0}^{1}\binom{2}{2j}\frac{(2j-1)!!}{(2j)!!}H_{1j} \\
&- \sum_{n=2}^{\infty}\frac{(2n-5)!!}{(2n-2)!!}\chi^{2n-2}\sum_{j=0}^{n}\binom{2n}{2j}\frac{(2j-1)!!}{(2j)!!}H_{nj})], \qquad (3.30)
\end{aligned}$$

where

$$H_{nj} = \left[a_0\sum_{k=0}^{j}(-1)^k\binom{j}{k}q_{k+n-j}\right]^2$$

To obtain this form, the integral

$$\int\frac{d\hat{\mathbf{r}}}{4\pi}\left(\frac{D(X,X')}{2B}\right)^3 = \left(\frac{1-\chi(\hat{\mathbf{e}}\cdot\hat{\mathbf{e}}')^2}{1-\chi^2}\right)^{1/2}$$

has been expanded in powers of $\chi(\hat{\mathbf{e}}\cdot\hat{\mathbf{e}}')^2$.

This calculation is easily implemented as a computer program by truncation of the infinite sums at $n = 20$. In contrast to the crystallization case, the expansions involve much less calculation: all that is being computed is the zero-momentum part of the Fourier transforms of the previous section. There is no problem with convergence in this computation for χ up to 0.9.

B. Results

The same techniques used for crystallization were used to find minima of the grand potential with respect to the nematic functional parameters (a_0, a_1, a_2) for

A/B	α^*/η	ρ_0^*	$(\rho_l^*-\rho_0^*)/\rho_0^*$	a_1	a_2
2.000	0.000	0.7983	0.0220	3.774	0.1632
2.500	0.000	0.6704	0.0355	3.696	0.2745
3.000	0.000	0.5863	0.0518	3.802	0.4209
2.000	0.460	1.2134	0.0005	-6.406	7.193
2.250	0.663	1.1155	0.0009	-6.624	7.436
2.500	0.820	1.0437	0.0015	-7.193	8.066
2.750	0.943	0.9877	0.0021	-7.601	8.512
3.000	1.040	0.9417	0.0028	-8.210	9.198

Table 3.4: Properties of nematic phase at the isotropic-nematic fluid transition. Listed are aspect ratio, value of correction parameter used, transition density, density difference between the coexisting nematic and isotropic phases, and the two orientational distribution parameters. The transitions with $\alpha = 0$ agree with those reported by Singh and Singh[45].

different ellipsoid anisotropies and isotropic fluid densities. Since the optimization of the direct correlation function in Section III was carried out only for ellipsoid aspect ratios up to $A/B = 3$, and since extrapolation of the α^* beyond that point is not reasonable, the calculations here are restricted to aspect ratios less than 3. The values of the correction α^* between the calculated points have been obtained by linear interpolation.

The parameters for the isotropic to nematic transitions are shown in Table 3.4. The first three rows are results for the case α^*, in which case the results are, to four significant digits, identical to those reported by Singh and Singh[45] for this transition. Thus the parametrization chosen here can describe the angular distributions of Singh

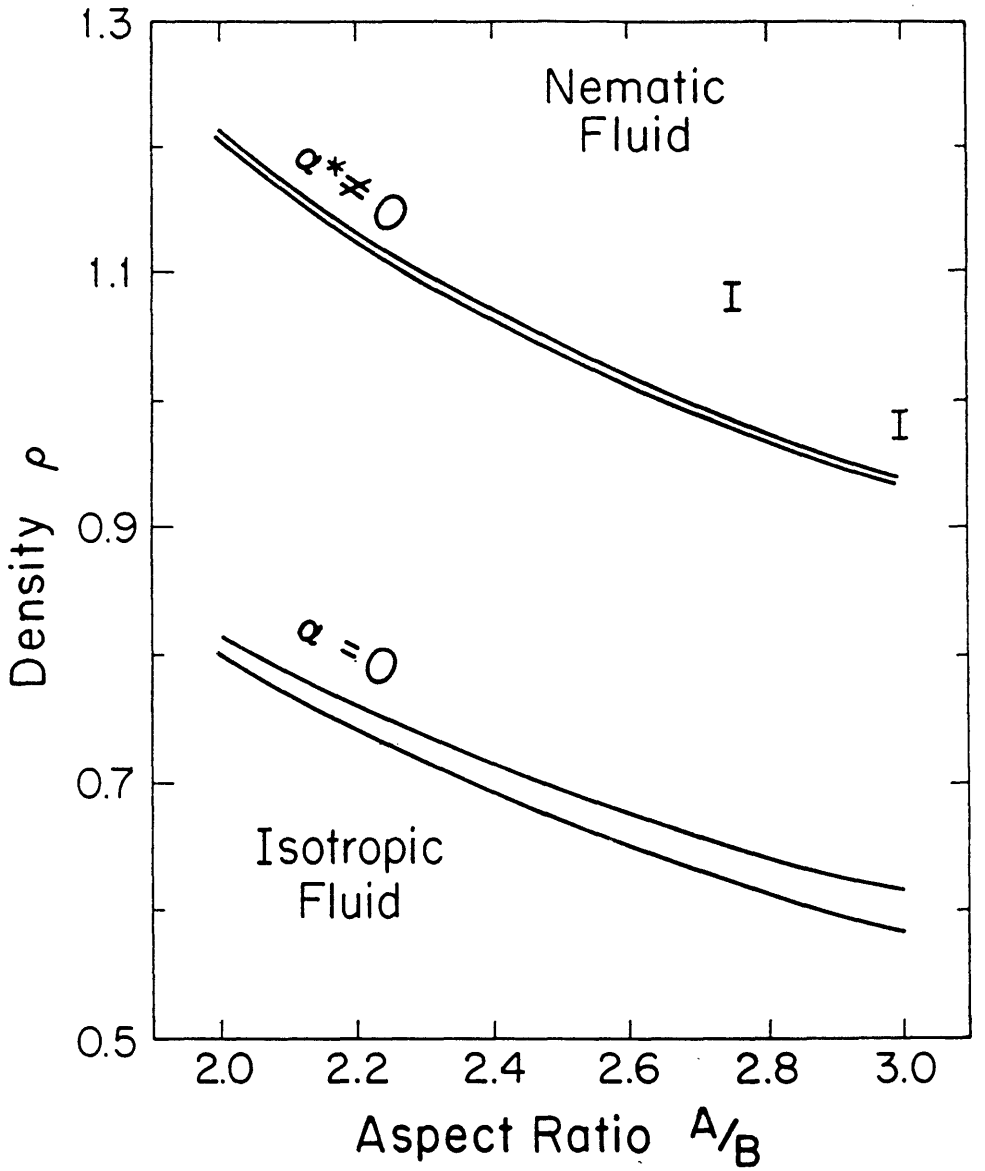

Figure 3.8: Phase diagram for isotropic and nematic transitions. The lower transitions are for $\alpha = 0$, while the upper set are for α^* as determined above. The bars denote the coexistence densities of the isotropic and nematic phases in the MC work of Frenkel *et al*[63].

and Singh (who used a sum of Legendre polynomials as an orientational density functional). However, there is a problem with the result: the transition densities are much too low in comparison to both Monte Carlo results[54] and other theoretical studies[63, 64] of this transition. When the calculations are redone with the correction α^* (bottom of Table 3.4), the transition densities are increased to near those given by the Monte Carlo calculations (which report transitions for $A/B = 2.75$ and 3.00 at densities of 1.12 and 1.10, respectively), due to the large decrease in the direct correlations for parallel molecular configurations. The density difference between the isotropic and nematic phases at the transition becomes much smaller than for the case with no correction (typically going from larger than 3% to smaller than 0.3%), which is smaller than that seen in the simulations (which report 1% to 2% discontinuities[63]). However, for densities slightly higher than those at the transition, the density discontinuity rapidly increases to near the level seen in the simulations: for example, at $A/B = 3$, the fractional change in density for an isotropic density of 0.9417 is 0.3%, while at an isotropic density of 0.9500, the density change is up to 1%. The phase diagram obtained for the uncorrected and corrected transitions, along with Monte Carlo data[63] is displayed in Figure 3.8.

3.2.5 Summary

Understanding the behavior of anisotropic fluid systems is a continuing theoretical challenge. However, using the density functional theoretical framework with the information that is available about the direct correlations in fluids, it has been shown here that models can be at least qualitatively studied. In addition, the method of optimizing the DCF has been seen to be a practical method in studying the hard ellipsoid fluid. Future increases in computational speed will make more sophisticated variational studies possible. Here, the DCF has been optimized using the Percus-Yevick integral equation, and has allowed a better characterization of the structure of the ellipsoid fluid than that possible with guessed DCFs. At large anisotropies, the

DCFs used in the past appear to be deficient and require substantial modification, but for the case of nearly spherical molecules, only small corrections to the Pynn-Wulf DCF are required.

Crystallization near $A/B = 1$ has been studied in detail for the first time allowing orientational as well as positional ordering. The correct topology is seen in the resulting phase diagram, although some quantitative details of the computer simulations are not reproduced. Over the range of anisotropies studied here, the effects of the DCF corrections are small. However, more work is required to extend the isotropic-solid phase boundary to the region $A/B > 1.5$ where the DCF correction will begin to affect the transition properties: the phase boundary should be driven to higher fluid densities similar to those seen in the MC phase diagram by the supression of parallel orientational direct correlations. The transitions to the nematic phase for $A/B > 2$ that have been studied here are strongly affected in this way by the rather large variational corrections to the DCF that are required for these anisotropies.

Immediate improvements and extensions of the work presented here are possible. The fact that the parameter $b_2 = 2$ for all oriented solid solutions indicates that a density functional capable of having sharper angular peaks than possible with the function P_2 and that takes into account higher order terms in the expansion of $(\hat{\mathbf{k}}\cdot\hat{\mathbf{r}})^{2n}$ is probably necessary. The orientational contribution to the local term (3.16) (which is positive) is not enough to offset the negative contribution of the nonlocal term (3.20) with the parametrization chosen here. A good start would be to use something like the distribution used to describe the nematic phase. There are technical complications associated with evaluating the nonlocal term in the density functional with this type of orientational distribution, but if one assumed both the orientational and positional distributions to be sharply peaked, it would be possible to approximate the integrals.

The problem of the rapidly increasing freezing density for the isotropic to plastic transition may also be due to the orientational distribution chosen: in the plastic phase, the orientational distribution should generally have the cubic symmetry of

the crystal rather than being uniform. Including these features in the orientational distribution, plus extending the truncation of equation (3.22) should give a better description of the solidification transitions, possibly including the feature of the computer experiments that the uniaxial orientational order is reduced as one approaches the plastic phase from the solid. These improvements, combined with the extension of the crystallization calculations to $A/B > 2$ would allow a complete density-functional phase diagram to be computed for the ellipsoid system.

The author wishes to thank A. N. Berker for encouragement and support, and also to thank the MIT Gravitational Cosmology Group for the use of one of their computers for part of this work. This research was supported by the National Science Foundation under Grant No. DMR-87-19217, by the Joint Services Electronics Program under Contract No. DAAL 03-86-K0002, and also by a Natural Sciences and Engineering Research Council (Canada) Postgraduate Scholarship. Computer facilities at the John von Neumann Supercomputer Center were also used, under Grant No. NAC-1290.

This Section has been published[12] as an article in Physical Review A.

3.3 The Liquid Structure of Highly Anisotropic Molecules

Attention has focused in recent years on the direct correlation functions (DCFs) of isotropic fluids, which, being the second functional derivatives of the excess Helmholtz free energy with respect to density, play the central role in density-functional theories of phase transitions. These types of theories have been much more successful when applied to systems with spherically symmetric interactions than when applied to fluids composed of anisotropic molecules. The most successful, unified density-functional approach to freezing of anisotropic particles to date was presented in the previous section. In that work, it was seen that the Pynn-Wulf[59, 60] approximation to the DCF failed to be appropriate even at moderate densities for elongated molecules (aspect ratio $A/B > 2$ or so), and strong corrections to it were required. Since it is known that the Pynn-Wulf DCF gives good account of the thermodynamics (i.e. the isotherm) of the isotropic liquid phase, there must be some strong orientational dependence of the DCF that does not contribute to the compressibility (which is the zero total angular and linear momentum part of the DCF).

It is natural to ask whether there is a simple, physically motivated way to understand this discrepancy. Here, an exact solution for the DCF of a one-dimensional system will be used to argue that a basic physical property has been overlooked in the construction of theories for phase transitions in systems composed of anisotropic particles in three dimensions.

3.3.1 A Solvable One-Dimensional Anisotropic Fluid Model

The N-particle Hamiltonian of the one-dimensional model is that of hard cores that can translate along a line, but which have additional orientational degrees of freedom

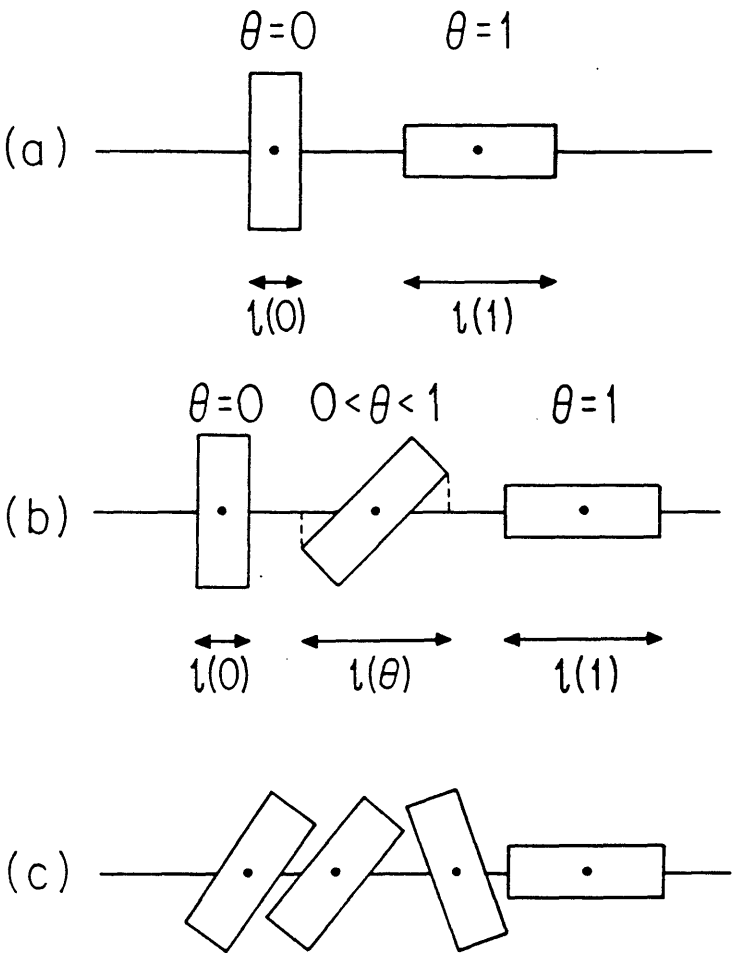

Figure 3.9: Types of orientational degrees of freedom and hard cores. (a) Two-level system: cores are allowed to have either $\theta = 0$ or $\theta = 1$, and do not overlap. (b) Continuous system I: cores have a continuous range of orientations, and their projections onto the line of translational motion are not allowed to overlap. Here, $D(\theta, \theta') = [l(\theta) + l(\theta')]/2$. (c) Continuous system II: cores have a continuous range of orientations, and their projections onto the line may overlap as long as the cores themselves do not. In this case, $D(\theta, \theta')$ cannot be written in the form $[l(\theta) + l(\theta')]/2$.

on which the hard-core radii depend[65]:

$$H_N(\{x_i, p_i, \theta_i, \pi_i\}_{i=1}^N) = \sum_{i=1}^{N} t(p_i, \pi_i) + \sum_{1 \le i < j \le N} v(\frac{|x_i - x_j|}{D(\theta_i, \theta_j)}), \tag{3.31}$$

where x_i are the translational degrees of freedom, p_i are the momenta conjugate to x_i, θ_i are the orientational degrees of freedom, and π_i are their conjugate momenta. $v(s) = 0$ for $s \geq 1$, while $v(s) = \infty$ for $s < 1$. The function $D(\theta_i, \theta_j)$ thus represents the distance of closest approach for molecules of orientation θ_i and θ_j: all closer distances are disallowed by the exclusion potential v. Note that D =constant is the case of a fluid of hard cores of length D, first treated exactly by Tonks[66]. Here the cases

$$D(\theta_i, \theta_j) = [l(\theta_i) + l(\theta_j)]/2 \tag{3.32}$$

are considered. This includes hard cores that interact as shown in Figure 3.9. Figure 3.9(a) shows the geometry for a system with two allowed orientations, while Figure 3.9(b) shows a system with continuous orientational degrees of freedom: note that in order to satisfy the condition (3.32), the hard cores interact so that their vertical projections onto the translational axis do not overlap. The case where the projections may overlap but the hard-core regions themselves do not (Fig 3.9(c)) has more complicated structure than (3.32), and will not be considered here.

Systems of particles with orientational degrees of freedom can be considered as mixtures of many 'pure' species each constrained to have a particular value of orientation all at equal chemical potential[67]. The approach to doing the statistical mechanics of (3.31) taken here will to first study a generalized system with different chemical potentials $\mu(\theta)$ for each orientation and to then impose that they are all equal.

The pair correlation function for the fluid is defined as

$$g(x, x', \theta, \theta') = < \sum_{i \neq j} \delta(x - x_i)\delta(x' - x_j)\delta(\theta - \theta_i)\delta(\theta - \theta_j) > / \rho(\theta)\rho(\theta') \tag{3.33}$$

where the average <> is taken in the grand canonical ensemble and where $\rho(\theta)$ is the number density of particles with orientations between θ and $\theta + d\theta$. This object is related to $c(x, x', \theta, \theta')$, the generalization of the single-component pair direct correlation function of Ornstein and Zernicke[55] by the integral equation[68]

$$g(x, x', \theta, \theta') - 1 = c(x, x', \theta, \theta') + \int dx'' d\theta'' [g(x, x'', \theta, \theta'') - 1]\rho(\theta'')c(x'', x', \theta'', \theta'). \tag{3.34}$$

Stell[69] has shown that for hard-core interactions with ranges of the form considered here, the direct correlation function $c(x, x', \theta, \theta')$ vanishes for $|x - x'|/D(\theta, \theta') > 1$. Lebowitz[68] and Wertheim[70] have solved this equation for arbitrary density distributions, obtaining

$$-c(x, x', \theta, \theta') = \begin{cases} b(\theta, \theta') - d\lambda(\theta, \theta') & 0 \leq |x - x'| \leq \lambda(\theta, \theta'), \\ b(\theta, \theta') - d\lambda(\theta, \theta') & \lambda(\theta, \theta') \leq |x - x'| \leq D(\theta, \theta'), \\ 0 & |x - x'| \geq D(\theta, \theta'), \end{cases} \tag{3.35}$$

where $\lambda(\theta, \theta') = |l(\theta) - l(\theta')|/2$, $b(\theta, \theta') = [1 - R + \rho D(\theta, \theta')](1 - R)^{-2}$, $d = \rho(1 - R)^{-2}$, $\rho = \int d\theta \rho(\theta)$, and $R = \int d\theta \rho(\theta) l(\theta)$. ρ is the total number density and R is the packing fraction, or length fraction of the system occupied by hard cores.

The density derivatives of the chemical potentials can be obtained from the direct correlations[68], and the case of interest $\mu(\theta) = \mu$ can then be expressed as

$$\int d\theta [R - \rho l(\theta)] \exp[-\rho l(\theta)(1 - R)^{-1}], \tag{3.36}$$

which establishes the relationship between ρ and R. For a system with two orientations $\theta = 0$ and $\theta = 1$, with $l(0) = l_0 < l(1) = l_1$, the integrals over θ are replaced with summations, and equation (3.36) becomes

$$\frac{R - \rho l_0}{\rho l_1 - R} = \exp[-\rho(l_1 - l_0)(1 - R)^{-1}], \tag{3.37}$$

which always has exactly one solution in the physical range $0 < R < 1$. In the limit of low density $\rho l_0 \approx 0$, the solution is $R \approx \rho(l_1 + l_0)/2$, while at high density $\rho l_1 \approx 1$ and $R \approx \rho l_0$. The equation of state can be easily computed using the Gibbs-Duhem relation between the pressure and chemical potentials, and as close-packing is approached, the singularity of the pressure is $p \approx (1 - \rho l_0)^{-1}$, as for the one-component hard-rod fluid[66]. This singular behavior is the only nonanalyticity encountered in the thermodynamics of this sytem, as one would expect from a system in one dimension with short-ranged interactions. It can be easily shown that the structure factor $S(k)$ develops Bragg peaks of height and inverse width proportional to $(1 - \rho l_0)^{-1}$ as $\rho l_0 \to 1$. The same analysis has been applied to a continuous distribution of orientations, and leads to similar results.

The most interesting property of this model, in the context of three-dimensional systems, is the singular behavior of the direct correlations (3.35) at finite densities. For orientational configurations such as those shown in Figure 3.10, as the particle separation is reduced beyond the point of contact (Figure 3.10(a)), the direct correlations begin to increase in strength (Figure 3.10(b)). However, when the position shown in Figure 3.10(c) is reached, the direct correlations stop increasing with decreasing particle separation at some orientation-dependent value. All smaller interparticle spacings for these orientations (as in Figure 3.10(d)) have the same direct correlation.

3.3.2 Structure of Three-Dimensional Fluids

The same behavior as described above is seen in the Percus-Yevick approximation for the direct correlation function matrix for mixtures of hard spheres of different radii: all configurations of two spheres where one is entirely inside the other have the same direct correlation[68]. Unfortunately, analytic solutions to the $d = 3$ Percus-Yevick equation are not available for systems of anisotropic molecules, but examination of the DCF density expansion[71] is useful. The first few terms of this series are shown

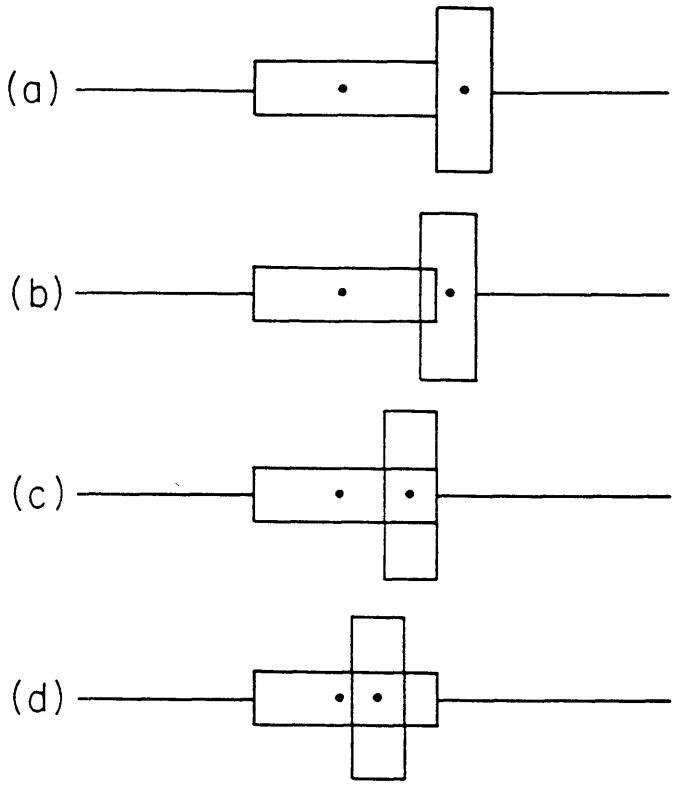

Figure 3.10: Regimes of different direct-correlation function behavior for fixed orientation. (a) Point of contact. Direct correlations jump from zero to a finite (negative) value. (b) Particles are partially overlapped. Absolute value of direct correlation is decreasing linearly with increasing particle separation. (c) Maximum overlap configuration. All particle separations smaller than this [e.g. (d)] have the same direct correlation.

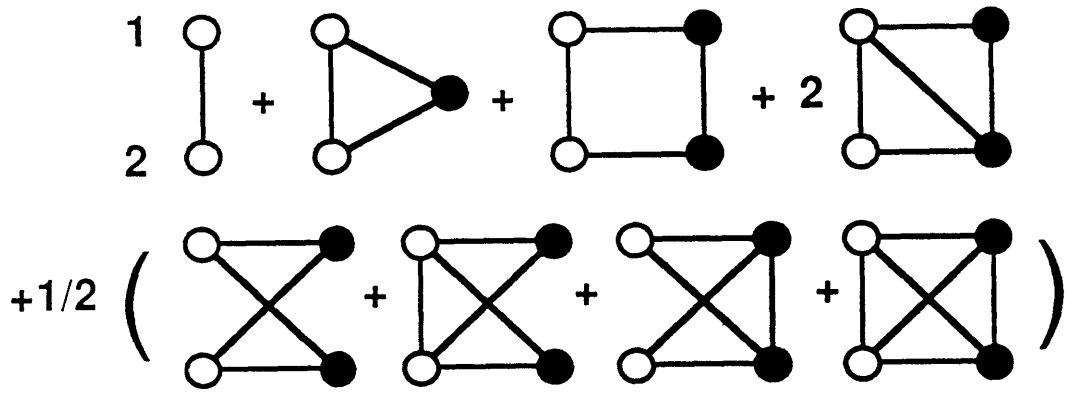

Figure 3.11: Density expansion for the direct correlation function, $c(1,2)$. A bond between vertices i and j represents a term $\exp(-v(i,j)/kT) - 1$, where v is the pair interaction potential. Filled vertices are integrated over all configurations, and each graph also is multiplied by a factor ρ for each filled vertex.

in Figure 3.11. The lowest-order term in this series for $c(1,2)$ is -1 if the hard cores at coordinates 1 and 2 overlap and 0 otherwise, and thus generates the lowest-order contribution to the 'jump' in the DCF at hard-core contact. The first-order term is an integral over one field point where the integrand takes on the value $-\rho$ for configurations where the particles with coordinates 1 and 2 overlap with each other as well as with the field particle. The integrand is zero for other configurations. For elongated particles, most of these configurations will be ones where the integrated particle axis is out of the plane containing the particle axes of the two external points, and only field particle positions that are near to the overlap of the external particles will contribute. Therefore the absolute value of this term will be roughly the product of the density and the volume of overlap of the external particles. Similar arguments can be applied to the higher-order terms in the series, which lead one to the conclusion that the direct correlations should grow in strength roughly according to the hard-core overlap[72]. Even more compelling evidence of this behavior has recently been provided by Lago and Sevilla in a numerical solution of the Percus-Yevick closure for spherocylinders in three dimensions[73], where it is explicitly seen that there is a 'plateau' in the direct correlation function as a function of particle separation for the 'T'-orientations analogous to those of Figure 3.10.

Thus, direct correlations of elongated molecules should not continue to increase quickly past points where molecules interpenetrate or 'punch through' one another, as in Figure 3.10(c) and (d). However, in almost all of the existing density-functional work on the isotropic-nematic transition that has been done to date, the direct correlations have been assumed to depend on the center-of-mass separation[45, 74] rather than the overlap volume, and the strength of direct correlations for orientationally disordered configurations has therefore been overestimated. It is no surprise that these theories all underestimate the isotropic-to-nematic transition density. The previous section described the one approach to this problem where an attempt was made to calculate the DCF[11]. That work indicated that the center-of-mass dependent DCF

approximations overestimate the strength of direct correlations for nonparallel molecular configurations. Taking this into account led to a large improvement in prediction of the transition density.

The additional insight provided by this model suggests a better approximation to the direct correlation function for anisotropic particles. The commonly used approximation of Pynn and Wulf[59, 60] which obtains direct correlations for anisotropic hard cores from the Percus-Yevick hard-sphere direct correlation function C_{hs} evaluated at the equivalent packing fraction η (density in units of inverse hard-core volume) and with the particle separation (in sphere diameters) replaced by the particle separation scaled by the orientation-dependent distance of closest approach $D(X, X')$ (X represents the position and orientation degrees of freedom for a molecule) can be easily modified to include a dependence on molecular overlap:

$$\begin{aligned} C(X, X'; \eta) &= C_{hs}(|\mathbf{r} - \mathbf{r}'|/D(X, X'; \eta), |\mathbf{r} - \mathbf{r}'| \geq d(X, X'), \\ &\quad C_{hs}(d(X, X')/D(X, X'; \eta), |\mathbf{r} - \mathbf{r}'| < d(X, X'), \end{aligned} \tag{3.38}$$

where $d(X, X')$ is the distance at which molecular interpenetration begins. This modification is based on the idea that beyond the punch-through point, the volume of overlap of elongated molecules is roughly constant. This result still reduces to the known Percus-Yevick results for the hard sphere fluid and for the fully aligned hard-ellipsoid fluid, since for these systems, the punch-through point always occurs at zero particle separation.

For hard prolate ellipsoids of revolution of major semiaxis A and minor semiaxis B in three dimensions, an approximate d is:

$$d(X, X') = D(X, X') \left(\frac{A - B}{A + B}\right) [(\widehat{\mathbf{e_1}} \cdot \hat{\mathbf{r}})^2 + (\widehat{\mathbf{e_2}} \cdot \hat{\mathbf{r}})^2][1 - (\widehat{\mathbf{e_1}} \cdot \widehat{\mathbf{e_2}})^2] \tag{3.39}$$

where $\hat{\mathbf{e}}_1$, $\hat{\mathbf{e}}_2$, and $\hat{\mathbf{r}}$ are unit vectors in the directions of the orientation of the major axes of molecules 1 and 2, and of the interparticle separation. The modified direct

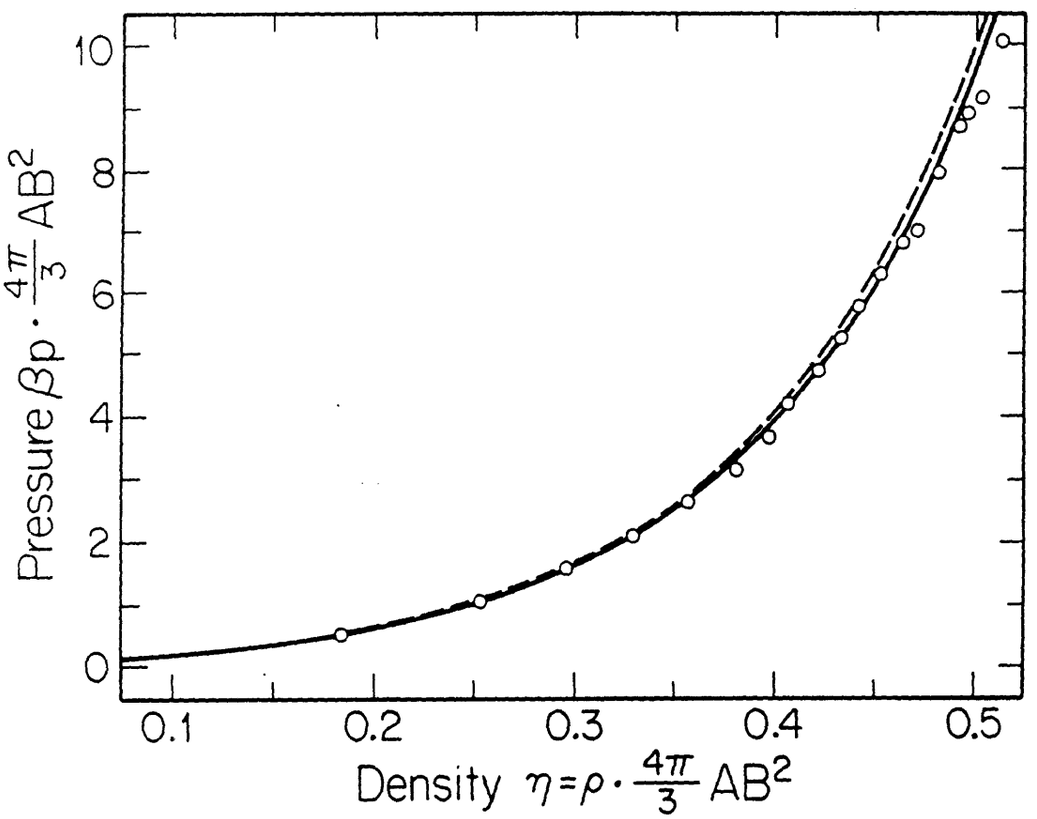

Figure 3.12: Pressure vs density for hard ellipsoids with $A/B = 3$ in three dimensions. Pressure is in units of temperature divided by ellipsoid volume, while density (packing fraction) is in units of inverse ellipsoid volume. Circles indicate Monte Carlo results of Mulder *et al*[63], the dashed curve is the Pynn-Wulf result, and the solid curve is the result of this paper with direct correlations constant beyond the point of interpenetration of the ellipsoids.

correlations reduce the isotropic phase pressure below the value obtained via the Pynn-Wulf direct correlation function, closer to Monte Carlo simulation results[63], as shown for $A/B = 3$ in Figure 3.12. In addition to leading to an improved description of thermodynamic properties, the orientational dependence that this effect generates will strongly affect density-functional theories of liquid ordering that require direct correlations of fluids composed of highly anisotropic molecules, and a study of this is in progress for the isotropic to nematic transition for hard elongated particles.

The author wishes to thank A. N. Berker for support and encouragement. This research was supported by the National Science Foundation under Grant No. DMR-87-19217, by the Joint Services Electronics Program under Contract No. DAAL 03-86-K0002, and also by a NSERC (Canada) Postgraduate Scholarship.

This Section has been published[13] as an article in Physical Review Letters.

3.4 A Nonperturbative Density-Functional Theory of Freezing of Anisotropic Particles

by J. F. Marko and W. A. Curtin

The previous sections have dealt with the treatment of freezing in molecular systems via functional expansion of the grand potential about the homogenous state, an approach due to Ramakrishnan and Yussouff[38]. This approach, although successful, is not really a systematic approach to the freezing problem because of the fact that the expansion parameter $\rho(X) - \rho_0$ is not small for all X. Because we possess limited information about $C^{(3)}$ and higher direct correlation functions, it is thus difficult to estimate the contributions of higher-order terms in the density-functional expansion. In this section, a nonperturbative density-functional theory of freezing, based on recent work by Curtin and Ashcroft[48], and Denton and Ashcroft[49, 50] is presented.

3.4.1 General Approach

A nonperturbative alternative to the RY approach has been developed by Curtin and Ashcroft[48] which sheds some light onto the behavior of the complete density-functional expansion. This approach begins with the partition of the density functional for the Helmholtz free energy into ideal gas and excess portions

$$F[\rho] = F_{id}[\rho] + F_{ex}[\rho]. \tag{3.40}$$

$F_{id}[\rho]$ is precisely the Helmholtz potential of the inhomogeneous fluid, ignoring the effect of intermolecular interactions:

$$F_{id}[\rho] = \int dX \rho(X)[\log \Lambda^3 \rho(X) - 1]. \tag{3.41}$$

The thermal wavelength is defined through

$$\Lambda^3 = \int \frac{d^d p d^{d'} \pi}{h^{d+d'}} e^{-\beta t(\mathbf{p},\boldsymbol{\pi})}. \tag{3.42}$$

$(\mathbf{p}, \boldsymbol{\pi})$ are the momenta and other degrees of freedom (e.g. angular momentum) that can be integrated out trivially. This leaves the excess Helmholtz free energy, which can be quite generally be written in the form of a local excess free energy density

$$F_{ex}[\rho] = \int dX \rho(X) f(X; [\rho]), \tag{3.43}$$

where the integrations represent integration of the translational coordinate $\mathbf{r}$ over system volume V, and integration of remaining orientational or internal degrees of freedom, normalized so that $\int dX = V$.

In analogy to the local-density approximation used in the theory of electronic structure, the local-density approximation (LDA) for f is

$$f(X; [\rho]) = f_0(X; \rho(X)) \tag{3.44}$$

where f_0 is the (assumed known) excess Helmholtz free energy per particle of the fluid state. While this approximation may be suitable to study inhomogeneities induced in a fluid by a weak external potential, the LDA obviously cannot lead to a theory for ordering in a fluid due to intermolecular interactions.

If we introduce a new 'effective density' $\bar{\rho}(X)$, we can rewrite (3.43) as

$$F_{ex}^{WDA}[\rho] = \int dX \rho(X) f_0(\bar{\rho}(X)). \tag{3.45}$$

In principle, the right choice of $\bar{\rho}$ will recover the exact excess potential (3.43). In practice, Curtin and Ashcroft[48] studied the case where the effective density is writ-

ten as a weighted average:

$$\bar{\rho}(X) = \int dX' \rho(X') w(X, X'; \bar{\rho}(X)). \tag{3.46}$$

This theory is generally referred to as the 'weighted-density approximation' or WDA.

The form of w is set by requiring that in the homogeneous limit $\rho(X) \to \rho$, the known properties of the uniform liquid of density ρ are recovered. This limit applied to (3.46) reveals that

$$\int dX' w(X, X'; \bar{\rho}(X)) = 1. \tag{3.47}$$

Imposing that the second functional derivative of the excess potential with respect to the density $\rho(X)$ in the homogeneous limit gives the second direct correlation function of the liquid, i.e.

$$C^{(2)}(X, X'; \rho) = -\beta \lim_{\rho(X) \to \rho} \frac{\delta^2 F_{ex}([\rho])}{\delta\rho(X)\delta\rho(X')}, \tag{3.48}$$

leads to a set of integro-differential equations that determine w uniquely.

This approach has been extremely successful in the study of a variety of phase transitions[48, 75, 76, 77] in fluid systems where the particles interact via spherically symmetric interactions. The WDA outperforms the RY theory significantly in predicting the localization of particles near lattice sites at the freezing transition (the RY theory typically predicts Lindemann ratios that are a factor of four too small for hard spheres) and gives a better account of the entropy difference between the coexisting liquid and solid phases at the freezing point. The WDA also has the virtue of being a suitable technique to study the ordered phase past the freezing transition[77]. In addition, the practical implementation is aided by the fact that the effective density (3.46) is everywhere significantly lower (typically > 30%) than that of the average ordered phase density, which are densities where liquid structure is well understood. The RY theory requires knowledge of liquid structure at the density of the liquid that has the same chemical potential as the solid, which is typically a density only 10% or so below that of the solid.

The secret to the success of the WDA in a variety of arenas is due to the fact that actually it is an approximate summation to all orders of the density-functional expansion. This comes about due to the 'feedback' of $\bar{\rho}$ in the definition of the weighted density (3.46). In the homogeneous limit, $\rho(X) \to \rho$, which leads to $\bar{\rho}(X) \to \rho$, the WDA satisfies the following infinite set of sum rules:

$$-\beta \int dX_3 \cdots dX_s \lim_{\rho(X)\to\rho} \frac{\delta^s F_{ex}^{WDA}([\rho])}{\delta\rho(X_1)\cdots\delta\rho(X_s)}$$
$$= \frac{\partial^{s-2}}{\partial\rho^{s-2}} C^{(2)}(X_1, X_2; \rho) = \int dX_3 \cdots dX_s C^{(s)}(X_1, \cdots X_s; \rho) \qquad (3.49)$$

for $s = 0, 1, 2, \cdots$. In addition, Curtin[76] has shown that the WDA gives good account of the three-body DCF $C^{(3)}$ at high densities for cases that do not follow directly from this sum rule. This probably is due to the fact that the sum rules so constrain the behavior of the WDA $C^{(3)}$ that it is forced to be near the correct result for many values of the three coordinates.

One way to interpret this situation is that for small inhomogeneities, the WDA has as its limiting form the RY theory to second order in $\rho(X) - \rho$, plus higher-order terms which use liquid structure information which satisfy all of the sum rules (3.49). This situation contrasts markedly with the situation for the RY theory truncated at second order, where after two functional differentiations, the remaining excess free energy clearly is independent of the ordered phase density, and vanishes under further functional differentiation.

Unfortunately, the generalization of the WDA to nonspherical particles involves a large computational effort, due to the necessity of solving five-dimensional nonlinear integro-differential equations. However, Denton and Ashcroft[49, 50] have recently proposed a theory which retains many of the desirable features of the WDA which does not lead to a large numerical calculation. This 'modified WDA' (MWDA) considers the excess Helmholtz free energy to be derived from that of the liquid at a single

effective density:

$$F_{ex}^{MWDA}[\rho] = \int dX \rho(X) f_0(\bar{\rho}) = N f_0(\bar{\rho}). \tag{3.50}$$

This effective density is written as a complete contraction of the physical density over a weighting operator w:

$$\bar{\rho} = N^{-1} \int dX \rho(X) \int dX' \rho(X') w(X, X'; \bar{\rho}), \tag{3.51}$$

where N is the number of particles in the system.

The imposition of the same conditions as used in the WDA in the homogeneous limit of the MWDA leads to the same normalization condition (3.47), but now the weight function w is determined by equation (3.48) without any trouble as

$$w(X, X'; \rho) = -\frac{\rho f''(\rho)}{2V f'(\rho)} - \frac{C^{(2)}(X, X'; \rho)}{2\beta f'(\rho)}, \tag{3.52}$$

where the primes represent differentiation with respect to the density argument, and $\beta = (kT)^{-1}$. The effective density is thus

$$\bar{\rho} = \frac{\rho \bar{\rho} f''(\bar{\rho})}{f'(\bar{\rho})} - \frac{1}{2\beta \rho f'(\bar{\rho})} \int dX dX' \rho(X) \rho(X') C^{(2)}(X, X'; \bar{\rho}). \tag{3.53}$$

Clearly, the form of the MWDA is much simpler than that of the WDA, but again, due to the feedback of $\bar{\rho}$ in the definition of the effective density, all the sum rules (3.49) are exactly satisfied. For the freezing of hard spheres, the MWDA gives results that are essentially identical to those obtained by the WDA with a large reduction in the complexity of the numerical calculations[49, 50]. This agreement is due to the fact that in addition to having the same second-order density-functional expansion and satisfying the same infinite set of sum rules, the MWDA and WDA are identical in two limits - the homogeneous limit and the limit of infinitely localized particles (delta-function distributions). Since the solid phase distributions at freezing are quite localized, this is not too far from the delta-function limit, and thus it is not

unreasonable to expect that the WDA and MWDA will give nearly the same results.

The theory of Denton and Ashcroft[50] generalized to the case of anisotropic molecules as presented above can be readily applied to problems such as those considered in Section 3.2. We now move on to some illustrative applications of the MWDA to freezing in molecular systems.

3.4.2 Isotropic-Plastic Transition of Hard Ellipsoids

The calculation of transitions to the plastic crystal phase described in Section 3.2 for slightly prolate ellipsoids using the MWDA is straightforward. The two-body DCF used in these calculations is the Pynn-Wulf form (i.e. the DCF of Section 3.2 with $\alpha = 0$). which was found to be a good approximation in the case of small anisotropy. It should be remembered that the Pynn-Wulf DCF becomes exact in the limit of low density, and that the MWDA requires liquid state information at relatively low densities, which make this approximation suitable.

The integral in (3.51) is almost identical to the second-order contribution to the excess energy of Section 3.2, and the only additional piece of information required is the excess potential per particle of the ellipsoid liquid. Recalling that the two-body DCF is exactly the second functional derivative of the excess free energy, the volume integral of the DCF can be integrated with respect to density twice to yield the excess potential:

$$\beta f = \frac{1}{2}\left(1 + \frac{\sin^{-1}(\chi)}{\chi(1-\chi^2)^{1/2}}\right)\left(\frac{3}{2}(1-\eta)^{-2} - \frac{3}{2} - \log(1-\eta)\right), \qquad (3.54)$$

where $\chi = (A^2 - B^2)/(A^2 + B^2)$ and $\eta = \pi AB^2\rho/6$ for prolate ellipsoids of long axis A and short axes B.

The final note about the calculations is that following the work of Curtin and Ashcroft[48], the calculations have been done in the so-called perfect crystal approximation, where the structure of the ordered phase is restricted to have a density of one

particle per lattice site. There has been much debate over the interpretation of the defect densities obtained from calculations such as those in Section 3.2, but this point is moot in the case of the WDA and MWDA, which appear to predict very low defect densities compared to the rather high vacancy concentrations predicted by the RY theory[77]. The perfect crystal approach thus is suitable for the MWDA calculations, as well as expedient, as it reduces the number of free parameters in the Gaussian crystal parametrization. For an FCC crystal with lattice constant c as described in Section 3.2, this condition is simply

$$c = \left(\frac{4}{\rho}\right)^{1/3}, \tag{3.55}$$

where ρ is the overall solid phase density. This follows from the fact that the FCC crystal contains four particles per cube of edge c.

Given the solid density, there is only one parameter to minimize over in the structure as parametrized in Section 3.2, namely the localization parameter D/σ. Minima in the Helmholtz potential are sought for given solid phase density, which determine the structural properties and Helmholtz potential of the plastic phase. The melting point and coexisting liquid properties can be determined by finding the point at which the liquid and solid of the same chemical potential have the same thermodynamical pressure (i.e. grand canonical potential). Thus, the same calculations as in the RY case are done in the end to locate the freezing line, but the density-functional minimization is done in the canonical ensemble.

Table 3.5 lists the coexistence properties of the isotropic liquid and the plastic solid as a function of anisotropy. As can be seen from comparison with Table 3.2, the transition properties are similar to those obtained with the RY theory except that the transition is seen at a slightly lower liquid density, and also that the localization at the transition is a much more reasonable value (simulations of the hard sphere solid near melting typically yield values of D/σ of 8 or so[48]). The chemical potential has been computed using units where the cube of the thermal wavelength is equal to

A/B	ρ_l	ρ_s	βp	$\beta\mu$	$\sigma/2B$	$c/2B$
1.000	0.8770	1.0189	9.2626	13.027	0.0951	1.577
1.025	0.8970	1.0209	10.168	14.048	0.0917	1.577
1.050	0.9242	1.0269	11.564	15.584	0.0867	1.573
1.075	0.9642	1.0412	14.003	18.170	0.0789	1.566
1.100	1.0408	1.0761	20.401	24.546	0.0642	1.549
1.105	1.0785	1.0962	24.712	28.613	0.0569	1.540

Table 3.5: Stucture and thermodynamics of isotropic to plastic transtions for slightly anisotropic ellipsoids in MWDA theory. A/B is the aspect ratio of the ellipsoids, ρ_l and ρ_s are the densities of the coexisiting liquid and solid phases, p is the pressure, μ is the chemical potential, $\sigma/2B$ is the localization parameter and $c/2B$ is the FCC lattice constant. The unit of volume is taken to be $8AB^2$.

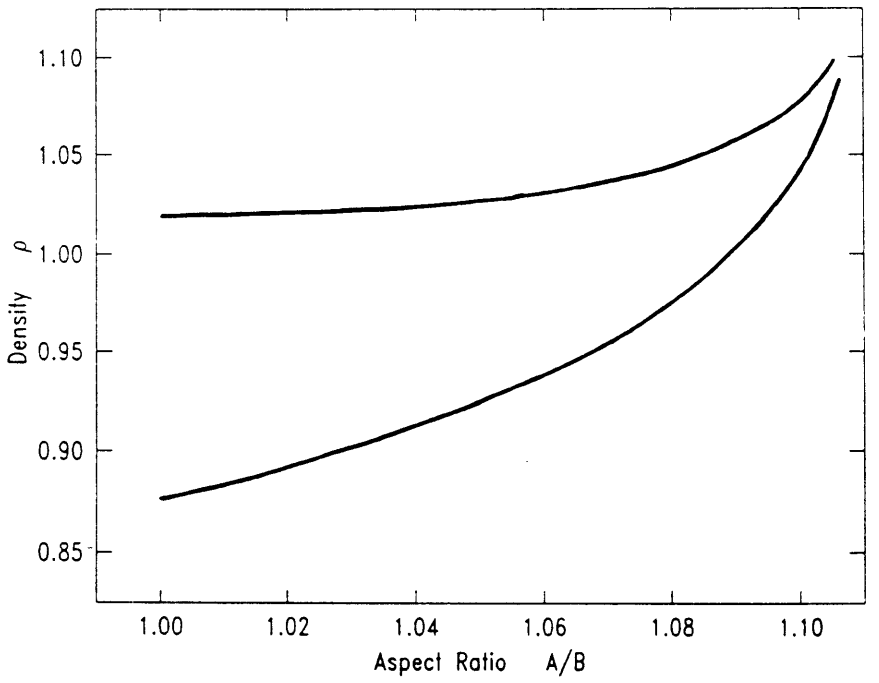

Figure 3.13: Phase diagram for isotropic to plastic transitions for ellipsoids in MWDA theory. Upper and lower loci denote the coexisting solid and liquid densities at freezing, as a function of anisotropy A/B.

the molecular volume. As in the RY case, it is found that as anisotropy is increased, the transition density (in units of molecular volume) increases. The resulting phase diagram for isotropic-plastic transitions is shown in Figure 3.13. Also as seen in the RY theory, there is a rapid increase in transition density beyond $A/B = 1.05$. This suggests that this feature is an artifact not of the structure of the theories, but rather is probably due to the parametrization of the plastic solid phase, which has no dependence on the orientational degree of freedom.

3.4.3 Isotropic-Nematic Transition of Hard Ellipsoids

As seen in Section 3.2, at high anisotropy, the first transition seen as density is increased is a first-order transition to the oriented nematic liquid phase. Here, we describe the application of the MWDA to this problem, which includes a reformulation of the RY theory that yields more insight into its structure. This reformulation was done to use the recently obtained liquid structure information of Perera *et al*[52] for hard ellipsoids.

As in the previous subsection, the Pynn-Wulf result for the excess potential (3.54) will be used, as it is well known that this expression gives an accurate account of the thermodynamics of the isotropic phase over a wide range of densities and anisotropies[45]. However, as was found in Section 3.2, and explained in Section 3.3, the Pynn-Wulf approach fails rather badly in predicting the orientational dependence of the DCF. Here, an expansion in rotational invariants allows liquid structure data to be directly used to correct the Pynn-Wulf results.

As in Section 3.2, the one-body density is taken to depend on only the angle between the orientational degree of freedom and the z-axis:

$$\rho(X) = \rho(\hat{\mathbf{e}}) = \rho \exp(a_1(\hat{\mathbf{e}} \cdot \hat{\mathbf{z}})^2 + a_2(\hat{\mathbf{e}} \cdot \hat{\mathbf{z}})^4) \left[\int_0^1 dx \exp(a_1 x^2 + a_2 x^4)\right]^{-1} \qquad (3.56)$$

where ρ is the average ordered phase density. Expansion of the density in spherical

harmonics allows the equation for the effective density (3.51) to be written as

$$\bar{\rho} = -\frac{\rho\bar{\rho}f''(\bar{\rho})}{2f'(\bar{\rho})} - \frac{1}{2\rho f'(\bar{\rho})}\sum_{l=0}^{\infty}(2l+1)c_l b_l^2 \tag{3.57}$$

where the angular momentum components of ρ and $C^{(2)}$ are:

$$\begin{aligned} b_l &= \int \frac{d\hat{\mathbf{e}}}{4\pi} P_l(\hat{\mathbf{e}}\cdot\hat{\mathbf{z}})\rho(\hat{\mathbf{e}}) \\ c_l &= \int \frac{d\hat{\mathbf{e}}d\hat{\mathbf{e}}'}{(4\pi)^2} P_l(\hat{\mathbf{e}}\cdot\hat{\mathbf{e}}')\int \frac{d\hat{\mathbf{r}}d\hat{\mathbf{r}}'}{V} C^{(2)}(X,X';\bar{\rho}). \end{aligned} \tag{3.58}$$

$P_l(x)$ are the usual Legendre polynomials, and the angular integrations are over the surface of the unit sphere.

The physical interpretation of the c_l is clear. c_0 is simply the compressibility of the isotropic phase:

$$\beta(\frac{\partial p}{\partial \rho}) = 1 - \rho c_0(\rho) \tag{3.59}$$

while higher l components represent the second-order response of the excess Helmholtz potential to a density perturbation of the form of a lth order Legendre polynomial of angle. $k = (1-\rho c_2)^{-1}$ is, the Kerr constant[78], which describes the second order free energy response to a field that couples weakly to the orientational degree of freedom.

The RY theory can be compactly written in terms of these integrals: the excess Helmholtz potential difference to second order from equation (3.30) can be rewritten as

$$\Delta w_2 = -\frac{1}{2}\sum_l (2l+1)\rho_0 c_l(\rho_0)(\frac{b_l}{\rho_0} - \delta_{l,0})^2, \tag{3.60}$$

where we recall that ρ_0 is the density of the liquid phase that the functional expansion is being carried out around. When added to the ideal gas part of the grand potential, the grand potential difference between the nematic and isotropic phases can be written as

$$\Delta w = \frac{1}{2} = \sum_l (2l+1)(k_l(\rho_0))^{-1}(\frac{b_l}{\rho_0} - \delta_{l,0})^2 + \mathcal{O}(a_l^3). \tag{3.61}$$

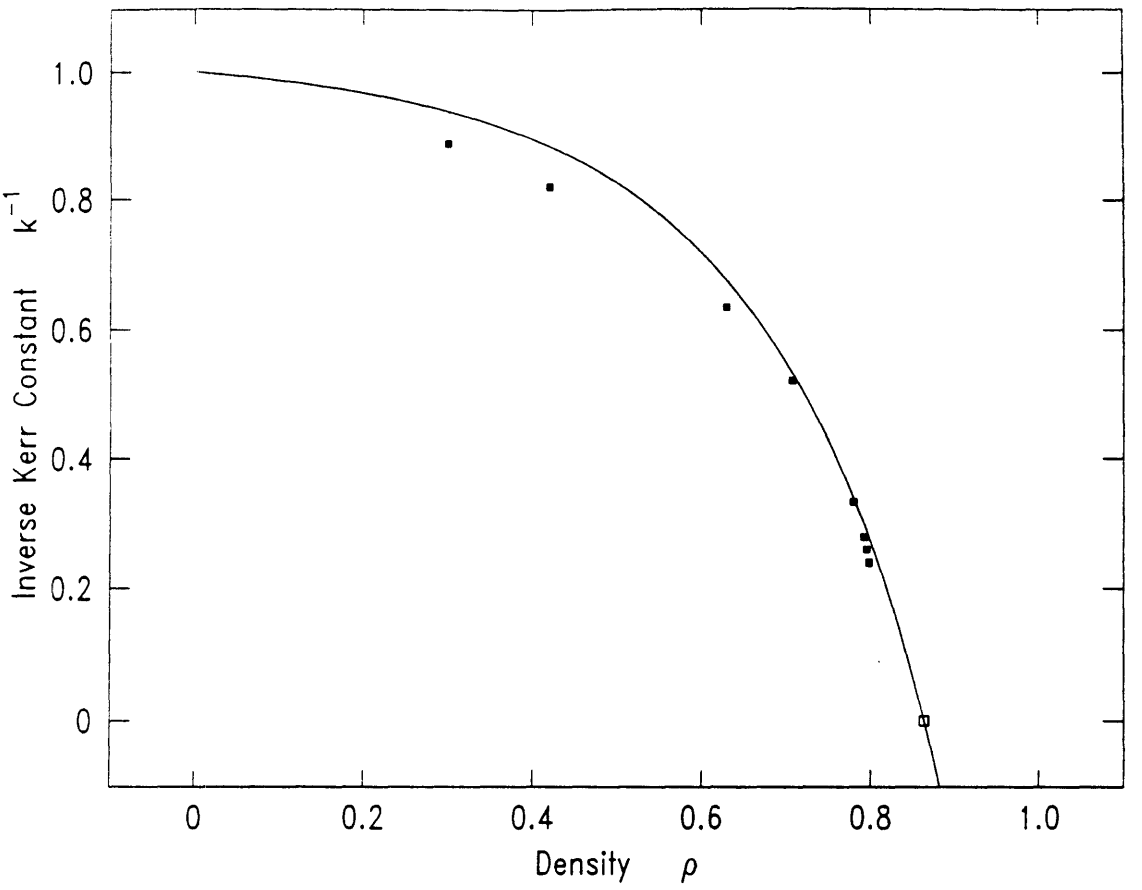

Figure 3.14: Inverse Kerr constant as a function of isotropic phase density for prolate hard ellipsoids of aspect ratio $A/B = 3$ obtained from numerical solution of the hypernetted-chain closure of the Ornstein-Zernicke equation by Perera *et al*[52]. The filled squares indicate the integral equation data[80], while the curve indicates the Pynn-Wulf expression scaled to the zero-crossing points of k^{-1}, as described in the text. The zero-crossing density extracted from Patey's data is indicated by an open square.

This formulation indicates the role of the $k_l^{-1} = 1 - \rho c_l$ as the Landau coefficients corresponding to the order parameters b_l. The existence of cubic terms in this expansion (there are cubic terms in both the ideal gas Helmholtz potential, and of course in the third-order DCF term) indicate that generally the phase transitions will be first order in the mean field theory. When any of the k_l^{-1} approach zero, the isotropic phase becomes unstable, and we can expect a phase transition to a state with nonzero b_l. This formulation of the density-wave instability theory was worked out using Mayer graphs in a remarkable paper several years ago[79].

The expression of the theory in terms of these objects allows the use of liquid

structure information recently calculated by Perera *et al*[52], who report the Kerr constants as a function of density as shown in Figure 3.14. What has been done with these data points is that the Pynn-Wulf c_2 integral has been multiplied by a constant so that the $k^{-1} = 1 - u\rho c_2$ thus obtained vanishes at the point where the integral equation results predict. This constant is $u = 0.0927$, 0.3002, and 0.4173 for $A/B = 2, 3$, and 5, respectively. The resulting inverse Kerr constant for $A/B = 3$ is also shown in Figure 3.14. Clearly these expressions do not asymptotically agree at low densities, but this is not really important, as it is necessary for them to agree well only at densities slightly below the transition to the nematic phase. For the purposes of this work, it is important that we have a smooth function representing k for densities near freezing, and this approach is convenient and effective.

With this, the theory is complete, and transitions to the nematic phase can be computed: both RY results and MWDA results using the liquid structure information described above are shown in Table 3.6. The MWDA and RY result in very similar results, which are in good agreement with the simulation results of Frenkel *et al*[63], including the values for the density discontinuity at the transition, which was predicted in Section 3.2 to be much smaller than that observed in simulations. The similarity in the RY and MWDA results indicates that for the isotropic to nematic transition, the differences in density (as a function of angular variable) are globally small enough that the RY theory gives a good account of the grand potential difference, even without the inclusion of higher-order DCF contributions. It should be noted that due to the lack of the sharp structure in $\rho(X)$ seen in the crystallization problem, the MWDA effective density $\bar{\rho}$ is quite close to the coexisting isotropic liquid density at the transition.

3.4.4 Summary

The work presented here indicates that the MWDA is a powerful tool for the study the statistical mechanics of inhomogeneous phases of fluids using the density-functional

A/B	ρ_l	ρ_n	βp	$\beta\mu$	a_1	a_2
2	1.2172	1.2302	60.821	61.295	2.945	0.099
	1.2171	1.2186	60.803	61.279	2.912	0.097
3	0.8430	0.8752	11.209	17.181	2.848	0.230
	0.8418	0.8503	11.139	17.098	3.038	0.264
	0.968	0.987	18.70	25.7		
5	0.6018	0.6392	5.0163	10.657	2.797	0.453
	0.5988	0.6154	4.9424	10.532	3.146	0.314

Table 3.6: MWDA isotropic-nematic transition parameters for aspect ratio $A/B = 2, 3, 5$. Reported are the densities of the coexisting isotropic and nematic phases (ρ_l and ρ_n), the pressure p and chemical potential μ, and the order parameters a_1 and a_2 at the transition. For each anisotropy, the first line indicates the MWDA result, the second the RY result, and in the case $A/B = 3$, the third line indicates values from constant-pressure MC simulations[63].

approach. For crystallization, the MWDA gives good account of all aspects of the structure and thermodynamics near first-order transitions, and has the virtues that it can be used to study the ordered phase (due to its nonperturbative nature), and that it requires liquid structure information at rather low densities. The MWDA appears to repair the defect of the RY expansion that 'too localized' structures are predicted at freezing.

In the case of orientational ordering, the differences between the RY and MWDA theories are less, due to the less dramatic variation in $\rho(X) - \rho$. A more important ingredient to the theory of isotropic-nematic transitions in the hard core system studied here is the liquid structure information, and it is found that the recent results of Perera *et al*[52] greatly improve the predictions of both density-functional theories.

3.5 Thermodynamics of Hard-Sphere Solids

3.5.1 Introduction

The hard-sphere system is of fundamental importance in the study of first-order crystallization transitions. Since the 1940's it has been known that there is a liquid to close-packed solid transition in a fluid of hard spheres[81, 82], but which close-packed structure is stable at the freezing point is still unknown. Since its introduction to the study of freezing[38], the density-functional approach has offered an accurate structural and thermodynamical description of the crystallization of simple liquids[83].

Molecular dynamics (MD) studies indicate that the face-centered-cubic (FCC) crystal is slightly more stable than the hexagonal-close-packed (HCP) structure near close-packing[84, 85], but the only simulation study of this question near the melting point, a Monte Carlo (MC) study, is inconclusive[86]. Simulation studies are difficult near the melting point, because the free energy differences between different close-packed states are small, and appear to be strongly affected by finite-size effects. Existing density-functional work on this problem[89, 91] has been done using liquid structure information which, as explained below, is unsuitable for the study of the FCC/HCP question.

In this Section, the FCC, HCP, and BCC hard-sphere crystal states are studied using a density-functional approach which combines two recent theoretical developments. The first is recent work by Groot *et al*[51], who have provided a parametrization of the two-body direct correlation function (DCF) based on accurate MC simulations of the hard-sphere liquid. The use of this data in a new weighted-density-functional theory which satisfies all sum rules for the two-body direct correlation function[48, 49, 50] exactly (assuming that the exact two-body DCF is known) results in a highly predictive theory for hard-sphere solids.

Using this theory, the Helmholtz free energy of the FCC crystal is calculated to be slightly below that of the HCP crystal at densities near the melting point, due

to the different third- and further-neighbor coordination shells of the two lattices. The behavior of the hard-sphere liquid direct correlation function is such that this small structural difference causes the FCC state to have a lower excess Helmholtz potential. However, although this free energy difference is in agreement with the limits set by simulations, it is so small that further improvements in the theory may change it significantly. The BCC state is found to always be higher in Helmholtz free energy than the two close-packed states studied, and the free energy difference is in good agreement with recent Monte Carlo and density-functional studies[77]. Using this density-functional approach, the elastic constants of the solid considered can be computed, and they are in good agreement with all Monte Carlo information.

3.5.2 Theory and Calculation

The density-functional theory used in this study was recently developed by Denton and Ashcroft[49, 50] and is closely related in structure to the weighted-density approximation developed by Curtin and Ashcroft[48]. The numerical results obtained by the two theories are numerically nearly identical[50], and agree well with simulation results for freezing of hard spheres. The approach begins with the usual partition of the Helmholtz potential of an inhomogeneous liquid with spatially varying density $\rho(\mathbf{r})$ into 'ideal gas' and 'excess' parts:

$$F = F_{id} + F_{ex} \tag{3.62}$$

where the ideal gas portion is

$$F_{id} = \int d\mathbf{r}\rho(\mathbf{r})[\log \Lambda^3 \rho(\mathbf{r}) - 1] \tag{3.63}$$

and where the excess potential is expressed in terms of the liquid excess Helmholtz

potential per particle f_0 evaluated at an effective density $\bar{\rho}$:

$$F_{ex} = N f_0(\bar{\rho}) \tag{3.64}$$

This effective density is defined in terms of an weight function w:

$$\bar{\rho} = N^{-1} \int_V d\mathbf{r} d\mathbf{r}' \rho(\mathbf{r}) \rho(\mathbf{r}') w(\mathbf{r}, \mathbf{r}'; \bar{\rho}) \tag{3.65}$$

This weight function is chosen so that the second functional derivative of the excess free energy $F_{ex} = N f_0(\bar{\rho})$ with respect to $\rho(\mathbf{r})$ yields the two-body direct correlation function $C^{(2)}$ of the uniform liquid in the homogeneous limit $\rho(\mathbf{r}) \to \rho$. This leads to the simple equation for the effective density:

$$\begin{aligned} \bar{\rho} &= -\frac{\rho\bar{\rho}f''(\bar{\rho})}{2f'(\bar{\rho})} - \frac{1}{2\rho\beta f'(\bar{\rho})} \int_V \frac{d\mathbf{r}d\mathbf{r}'}{V} \rho(\mathbf{r})\rho(\mathbf{r}')C^{(2)}(|\mathbf{r}-\mathbf{r}'|;\bar{\rho}), \\ &= -\frac{\rho\bar{\rho}f''(\bar{\rho})}{2f'(\bar{\rho})} - \frac{1}{2\rho\beta f'(\bar{\rho})} \sum_{\mathbf{k}} |a_{\mathbf{k}}|^2 C^{(2)}(|\mathbf{k}|;\bar{\rho}), \end{aligned} \tag{3.66}$$

where the crystal symmetry of the ordered phase, and the isotropic symmetry of the liquid phase have been anticipated in the use of the Fourier transforms

$$\begin{aligned} a_{\mathbf{k}} &= \int_V \frac{d\mathbf{r}}{V} e^{i\mathbf{k}\cdot\mathbf{r}} \rho(\mathbf{r}) \\ C^{(2)}(k;\rho) &= 4\pi \int_v dr r^2 \frac{\sin kr}{kr} C^{(2)}(r;\rho). \end{aligned} \tag{3.67}$$

The feedback of $\bar{\rho}$ in (3.65) leads to the exact satisfaction of all two-point sum rules that relate higher order direct correlation functions to $C^{(2)}$[50].

This density-functional theory requires the two-body direct correlation function and the excess Helmholtz potential of the isotropic liquid, for values of $\bar{\rho}$ about 30% below the freezing density. In this region of densities, both of these quantities are

extremely well known. The excess Helmholtz potential per particle used here,

$$\beta f_0 = (1-\eta)^{-2} + 2(1-\eta)^{-1} - 3, \tag{3.68}$$

is that obtained from the Carnahan-Starling[87] equation of state, which is known to be accurate to within 0.3% at densities of interest here. The variable η is the fluid density in units of the sphere volume $\pi D^3/6$, where D is the sphere diameter. As mentioned above, the DCF used is a parametrization of MC results due to Groot *et al*[51].

The final ingredient of the theory is a choice of parametrization of the solid density $\rho(\mathbf{r})$, which will be minimized over (for given average solid density ρ_s) to obtain the stable structure. Simulations[82] and experiments[88] indicate roughly Gaussian distributions of particles about lattice sites near the crystallization transition. Thus, we choose a lattice of gaussian distributions which can be written as

$$\begin{aligned}
\rho(\mathbf{r}) &= \rho_s \Delta (\pi\sigma^2)^{-3/2} \sum_{\mathbf{s}\in\mathbf{T}} e^{-([\mathbf{r}-\mathbf{s}]/\sigma)^2} \\
&= \rho_s \sum_{\mathbf{k}\in\mathbf{U}} e^{-(\sigma|\mathbf{k}|/2)^2} n_b^{-1} \sum_{j=1}^{n_b} e^{i\mathbf{k}\cdot(\mathbf{r}-\mathbf{b}_j)} \\
&= \rho_s \sum_{\mathbf{k}\in\mathbf{U}} a_{\mathbf{k}} e^{i\mathbf{k}\cdot\mathbf{r}},
\end{aligned} \tag{3.69}$$

for a set of real-space lattice sites $\mathbf{T}$ with a possible basis $\{\mathbf{b}_j\}_{j=1}^{n_b}$ and an associated Bravais inverse lattice U. The real-space, inverse-space, and basis vectors for the FCC, BCC and HCP lattices are summarized in the Appendix. Thus, the structural parameters describing these lattices are the average solid density ρ_s, the peak width of the Gaussian site distributions σ, and the lattice constant c, which appears as a prefactor of the real-space lattice vectors.

The calculations presented in this section have been done with the intention of comparing them to hard-sphere solid simulation results. These simulations are done in the canonical ensemble, i.e. with the number of particles fixed. In addition, the

singular hard sphere potential, the boundary conditions, as well as the lack of particle number fluctuations preclude the possibility of the observation of any appreciable density of either vacancies or interstituals. To properly take this into account, these density-functional calculations have been done with the 'perfect crystal' assumption, namely that $\rho(\mathbf{r})$ be constrained to have precisely one particle per lattice site. This constraint is most easily incorporated as a relationship between the lattice constant c, and the solid density ρ_s: $\rho_s c^3 = 4$, 2 , or $\sqrt{2}$ for the FCC, BCC, and HCP lattices, respectively, as defined in the Appendix. This leaves only the localization σ as a free variational parameter.

The previous studies of the relative stability of close-packed hard-sphere crystals[89, 90, 91] have all used the exact solution[58] of the Percus-Yevick (PY) equation for the correlation functions of hard spheres[57]. Although convenient, the PY DCF is exactly zero at distances beyond the sphere diameter D, as opposed to simulation results that indicate an initially positive, then rapidly decaying, oscillating tail outside the hard core region[51, 92]. This is an important factor for the study of the relative stability of FCC and HCP crystals since the excess free energy involves the convolution of the density with the DCF, as in (3.66), which is a general feature of density-functional theories.

As remarked by Colot and Baus[89], this expression cannot distinguish between FCC, HCP, or even randomly stacked close-packed planes if C cuts off at the sphere diameter, since the distance to, and number of first- and second-neighbor sites of these structures are the same, and the Gaussian lattice site distribution widths seen in simulations are typically 0.12 to 0.15 in units of nearest-neighbor distances, at densities near melting. For this type of DCF, only the ideal gas part of the Helmholtz potential will break the degeneracy of the different close-packed structures, and probably only very weakly, again due to the expected narrowness of the site distributions.

This degeneracy of FCC and HCP structures resulting from the use of the PY DCF has been reported by a variety of workers[89, 90, 91], indicating that indeed,

the ideal gas contribution does not break the degeneracy of the grand potential per particle of FCC and HCP crystals by more than 10^{-5} near the melting point, using the Gaussian lattice parametrization. Thus, any significant difference in FCC and HCP free energies will be due to the contribution to the excess free energy from the tail region of the DCF.

3.5.3 Thermodynamics and Structure of Hard-Sphere Solids

Minima for the free energy functional exist over a range of densities from approximately $\rho D^3 = 0.92$ to 1.33 for the FCC, HCP and BCC solids studied here. From the Helmholtz potential, the pressure and chemical potential can be extracted, and using the Carnahan-Starling free energy (3.68) and the coexistence condition that the pressures of the solid and liquid phases be equal point (for a liquid and solid with the same chemical potential), the freezing point can be located.

The results for the Helmholtz free energies of FCC, HCP, and BCC crystals are summarized for two densities in Table 3.7, and displayed for a range of densities, along with the liquid free energy in Figure 3.15. The free energies quoted are the absolute Helmholtz free energy per particle minus the kinetic contribution $\log \Lambda^3 \rho_s - 1$, as is conventionally reported. The difference in the FCC and HCP free energies is extremely small ($\Delta f < 0.0020$ for densities near melting), but the FCC state systematically has a lower free energy. By comparison, the FCC-BCC free energy difference is much larger.

Comparison with the MC results[77, 86] indicates that this theory systematically underestimates the Helmholtz free energy. This has been reported by Curtin and Ashcroft[48] and by Denton and Ashcroft[50] for the WDA and MWDA theories using the Percus-Yevick $C^{(2)}$. However, the free energy differences between the FCC and BCC states are in better agreement with the corresponding Monte Carlo results, as reported by Curtin and Runge[77] for WDA calculations. The FCC state Helmholtz

Crystal Type	Density $\rho_s D^3$	$\beta f + 1 - \log \Lambda^3 \rho_s$ DFT	MC
fcc	1.0409	5.5730	5.9222(10)
	1.1000	6.0582	6.5397(09)
hcp	1.0409	5.5751	5.9234(10)
	1.1000	6.0610	6.5404(11)
bcc	1.0409	5.8697	6.094
	1.1000	6.5825	6.878

Table 3.7: Helmholtz potential for FCC, HCP and BCC solids. Results of the calculations of the text, and of Monte Carlo simulations [77, 86] are shown. The values shown are for the potential $\beta F/N - \log \Lambda^3 \rho_s + 1$.

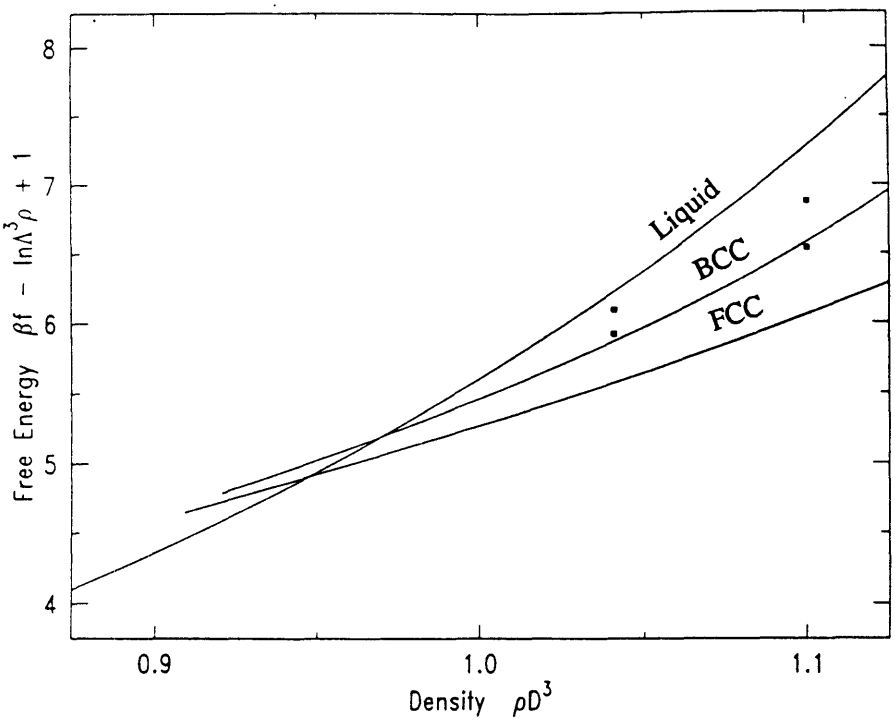

Figure 3.15: Helmholtz free energy per particle for hard-sphere liquid, and the FCC and BCC solids. The liquid free energy shown is due to equation (3.68). The FCC and BCC curves indicate the results of the calculations described in the text, while the points represent the FCC and BCC MC results described in Table 3.7.

free energy crosses that of the liquid before either the HCP or BCC states, indicating that in the canonical ensemble it is the stable ordered phase at freezing. At higher densities, the FCC phase continues to have the lowest Helmholtz potential.

The pressure of the FCC solid is in fairly good agreement with simulation results, as shown in Table 3.8, although again it is somewhat underestimated by the density-functional calculations. The mean-square deviation of particles from their lattice positions for the FCC solid, which in terms of the localization is $< r^2 >= 3\sigma^2/2$, as a function of density is shown in Table 3.9, along with MD[93] results. Finally, the freezing parameters, which for the FCC solid indicate the true freezing point, while for the HCP and BCC solids indicate where they are in coexistence with the metastable liquid state, are shown in Table 3.10. As in the case of the Helmholtz potential, the grand potential of the solids appear to be underestimated, resulting in a prediction of freezing at lower densities than that observed in the simulations.

The question of the relative stability of the FCC and HCP phases is addressed

Density $\rho_s D^3$	Pressure $\beta p D^3$ DFT	MC
0.9899	7.880	9.904(7)
1.0409	9.331	11.672(6)
1.1314	13.504	16.64 (2)
1.1785	17.076	20.79 (3)
1.2728	31.949	37.69 (8)

Table 3.8: Pressure of the FCC solid. Density-functional and Monte Carlo[86] results are given.

Density $\rho_s D^3$	MS Deviation $\langle r^2 \rangle / D^2$ DFT	MD
0.9959	0.01882	0.03120(60)
1.0516	0.01338	0.01860(30)
1.1314	0.008093	0.00920(13)
1.1785	0.005842	0.00573(14)
1.2298	0.003857	0.00312(03)

Table 3.9: Mean distance squared of particles from lattice sites. Density functional results, and MD results of Young and Adler[93] are given.

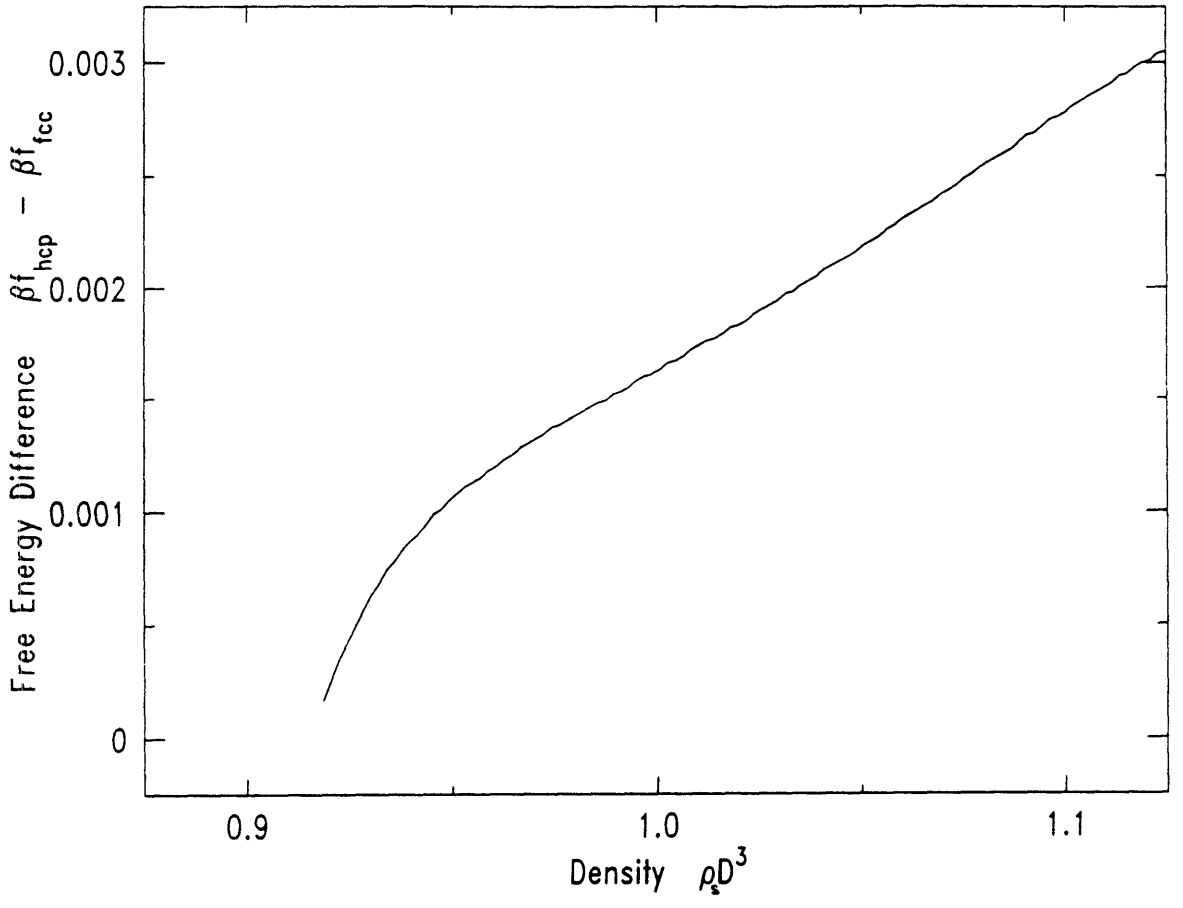

Figure 3.16: Helmholtz potential difference between FCC and HCP solids from DF calculations.

Calc'n	$\rho_l D^3$	$\rho_s D^3$	$\rho_s D^3 - \rho_l D^3$	$\Delta S / Nk$	$L = \langle r^2 \rangle^{1/2} / a_{nn}$
MC fcc	0.94	1.04	0.10	1.16	0.126
DF fcc	0.8854	1.0318	0.1464	1.3013	0.1105
DF hcp	0.8857	1.0318	0.1461	1.3004	0.1103
DF bcc	0.9292	1.0141	0.0849	0.9111	0.1712

Table 3.10: Freezing parameters for hard spheres. Density-functional (DF) calculation results and MC results[50] are given. Densities of coexisting liquid and solid, as well as the entropy per particle difference between the coexisting phases and the Lindemann ratio L are given. $L = (3/2)^{1/2}\sigma/a_{nn}$, where a_{nn} is the nearest-neighbor lattice distance.

in Figure 3.16, which shows the free energy difference as a function of density. The free energy difference (which is also the entropy difference, since the internal energy is always zero for the hard-sphere fluid) is consistent with the results of Frenkel and Ladd[86], who have estimated the entropy difference per particle of these phases near melting to be between $-0.001k$ and $0.002k$. Thus, the small free energy difference in these calculations is consistent with the MC results, and suggests that the FCC phase is slightly more stable than the HCP phase.

3.5.4 Elastic Constants for the FCC Hard-Sphere Solid

Another set of quantities that can be computed using the type of theory presented here are the static elastic constants, which describe the second-order response of the solid to an externally imposed strain. Here the calculation of elastic constants follows as described by Runge and Chester[94].

For an elastic deformation $\mathbf{r} \rightarrow \mathbf{r} + \mathbf{u}$, Lagrangian strain parameters are defined

as

$$\eta_{ij} = \frac{1}{2}\left[\frac{\partial u_i}{\partial r_j} + \frac{\partial u_j}{\partial r_i} + \frac{\partial u_k}{\partial r_i}\frac{\partial u_k}{\partial r_j}\right], \tag{3.70}$$

and the Helmholtz potential is expanded as

$$\frac{F[\eta]}{V} = \frac{F[\eta = 0]}{V} + T_{ij}\eta_{ij} + \frac{1}{2}C_{ijkl}\eta_{ij}\eta_{kl} + \mathcal{O}(\eta^3). \tag{3.71}$$

The stress tensor of the unstrained solid is simply

$$T_{ij} = -p\delta ij \tag{3.72}$$

where p is the thermodynamical pressure.

The C_{ijkl} are the isothermal elastic constants. and for a system with cubic symmetry, many of them are zero. Of the 21 nonzero ones, only three are independent, $C_{1111} = C_{11}$, $C_{1122} = C_{12}$, and $C_{1212} = C_{44}$. The remaining 18 can be recovered by observing that C_{ijkl} is invariant under all one-to-one mappings of the coordinate axis labels onto themselves (i.e. invariance under the cubic group), as well as more generally under any composition of the operations $ijkl \rightarrow jikl$, $ijkl \rightarrow ijlk$, and $ijkl \rightarrow klij$. This allows the free energy response in terms of actual elastic transformations to be directly calculated.

One transformation used was

$$\begin{aligned} x &\rightarrow x \\ y &\rightarrow y \\ z &\rightarrow z + \epsilon z \end{aligned} \tag{3.73}$$

to which there is a response

$$\frac{\Delta F}{V} = -p\epsilon + \frac{1}{2}(C_{11} - p)\epsilon^2. \tag{3.74}$$

Another transformation is

$$\begin{aligned} x &\rightarrow x + \epsilon x \\ y &\rightarrow y + \epsilon y \\ z &\rightarrow z \end{aligned} \tag{3.75}$$

to which there is a response

$$\frac{\Delta F}{V} = -2p\epsilon + \frac{1}{2}(2C_{11} + 2C_{12} - 2p)\epsilon^2. \tag{3.76}$$

Finally,

$$\begin{aligned} x &\rightarrow x + \epsilon y \\ y &\rightarrow y + \epsilon x \\ z &\rightarrow z \end{aligned} \tag{3.77}$$

was used, to which there is a response

$$\frac{\Delta F}{V} = +\frac{1}{2}(4C_{44} - 2p)\epsilon^2. \tag{3.78}$$

Accompanying these transformations are dual transformations of the inverse lattice, which allow the free energy response to be easily calculated. Computations for $\epsilon = 0$, 0.0001, and 0.0002 were done, with minimization of the free energy with respect to the structural parameter σ in the strained configurations, which of course affects the second order response. As a check of the computations, it was verified that the linear response was the appropriate multiple of the pressure of the solid, which was also obtained from the density derivative of the Helmholtz potential of the unstrained system.

The results of elastic constant calculations using this method are shown in Table

Calculation Type	Density $\rho_s D^3$	Elastic Constants (βD^3=1) C_{11}	C_{12}	C_{44}
DF	0.9899	26.635	2.460	29.288
MC		46(2)	11.8(3.0)	33.5(1.0)
DF	1.0409	38.694	8.044	37.171
MC		68(3)	18.2(2.0)	46(1)
DF	1.1314	80.942	27.555	61.402
MC		133(3)	34.6(2.0)	94(2)
DF	1.1786	109.17	41.756	80.631
MC		207(8)	56.8(6.0)	150(2)
DF	1.2727	364.97	217.68	164.74
MC		627(12)	149(11)	478(10)

Table 3.11: FCC hard-sphere solid elastic constants. Along with the calculations described in the text are shown MC results[95].

3.11, along with MC results, also for hard-sphere FCC solids. The agreement near the melting point is reasonably good, compared to WDA treatments using the Percus-Yevick DCF[96].

3.5.5 Elastic Fluctuations

One interesting aspect of density-functional theories such as the one presented here is that they are bridges from the description of a fluid in terms the microscopic degrees of freedom of the constituent particles to a description in terms of the one-body field $\rho(\mathbf{r})$. The fluctuations in individual particle positions are completely taken into account (assuming perfect inclusion of all liquid structure information) subject to the constraint on the one-body density. The fact that the saddle-point approximation is used makes it clear that the minimization calculations such as those presented above are the 'mean-field' descriptions of the ordered phase.

This suggests that one should consider fluctuations of the one-body density about its mean-field value, and the first family of fluctuations to consider in the case of three dimensional crystalline solids are elastic fluctuations. The elastic constants computed above are the 'masses' of elastic waves in a general Landau expansion of $-\beta F$ about the mean-field free energy:

$$\begin{aligned}\beta(F-F_0) &= -\beta p\int d^d r\eta_{ii}(\mathbf{r}) + \frac{1}{2}\beta C_{ijkl}\int d^d r\eta_{ij}(\mathbf{r})\eta_{kl}(\mathbf{r}) \\ &\quad +\beta D_{ijklmn}\int d^d r\partial_m\eta_{ij}(\mathbf{r})\partial_n\eta_{kl}(\mathbf{r}) + \cdots . \end{aligned} \tag{3.79}$$

Computation of the elastic wave dispersion tensor D requires a supercell approximation and is a calculation easily within the range of current supercomputers. However, even with just the mass terms C we can say something about the size of corrections to the free energy that arise from elastic fluctuations. For $D = 0$, the Hamiltonian (3.79) is completely decoupled, and represents independent elastic oscillators. Clearly, these oscillators cannot be smaller than the volume per lattice site since fluctuations

at smaller than that scale cannot be elastic, and are presumably taken into account by the liquid structure used in the construction of the density functional. Physically, we expect that to regard different regions of the lattice to be independently strained, they must be somewhat larger, say n sites in size (which can be made precise by computing the tensor D and higher-order versions of it, which will cut off the fluctuations below some characteristic length $(D/C)^{1/2} \approx n^{1/3}$).

Thus we consider the statistical mechanics of the N-particle solid, focusing on the elastic fluctuations of N/n regions of volume n/ρ. The free energy of these fluctuations takes the harmonic oscillator form

$$\begin{aligned} \Delta F &= -\frac{N}{n\beta} \log \left[\int \{d\eta_{ij}\} \exp(-\frac{\beta n}{2\rho} C_{ijkl}\eta_{ij}\eta_{kl}) \right] \\ &= \frac{N}{2n\beta} \log \det \left(\frac{\beta n C_{(ij)(kl)}}{2\pi\rho} \right). \end{aligned} \tag{3.80}$$

For a crystal with full cubic symmetry, this can be reduced to

$$\Delta \left(\frac{\beta F}{N} \right) = \frac{1}{2n} \log[(\frac{\beta n}{\pi\rho})^6 C_{44}^3 C_{11}(C_{11}^2 - C_{12}^2)] \tag{3.81}$$

which for elastic constants as determined above (either the MC or DF results at $\rho_s = 1.0409$) produces the difference $\Delta\beta F/N \approx 0.5$ seen between MC and density-functional results for $n \approx 30$. This corresponds to the free energy contribution of regions of a few lattice sites across undergoing independent elastic fluctuations, which is physically very reasonable. Whether or not the free energy difference is dominated by this contribution, or whether non-elastic fluctuations are important, is an open question.

3.5.6 Summary

In this section, the problem that has been used as a benchmark for density-functional theories of freezing, that of the crystallization of hard spheres, has been reconsid-

ered using a weighted-density approximation recently introduced by Denton and Ashcroft[50]. The use of this theory, in combination with a recently published[51] parametrization of MC results for $C^{(2)}$ results in a highly predictive theory of freezing. The general characteristics of WDA theories, namely, structural properties of the ordered phase in good agreement with simulation results, a BCC phase with slightly higher free energy than the close-packed phases, and a slight underestimate of the absolute free energy of the ordered phases are seen in this approach. This underestimate of the free energy leads to a slight underestimate of the isotherm of the solid and the liquid-solid coexistence properties, as has been reported by Curtin and Runge[77].

Here, the additional step of the calculation of the elastic constants of the FCC solid has been taken, and their size and dependence on density are in rough agreement with simulation results. The indicated approach is to use the WDA theory to try to obtain results in better agreement with the simulation results for the elastic constants. If they can be computed reliably, computations of the dispersion tensor D would be more believable.

A scheme to correct the mean-field density-functional free energies presented here for the contributions of elastic deformations of the lattice has been suggested. It has been shown that given the elastic properties and some physical assumptions about the nature of elastic fluctuations near the first-order phase transition, the discrepancy between the results of the WDA theories and the simulations can be attributed to this contribution. However, this question will not be completely settled by the computation of this correction, as the thermodynamics of other fluctuations (i.e. defects in the crystal structure) must also eventually be studied.

The question of whether the FCC or HCP structures are stable at freezing has also been examined, and the current theory shows a free energy difference between these states that is within the limits set by Monte Carlo simulations. It would be interesting to find out how much the results here are affected by the general parametrization (the so-called Fourier parametrization[91]) and in particular to find out whether the free

Parameter	FCC lattice	BCC lattice	HCP lattice
$\{\vec{c}_i\}$	(0,1/2,1/2)	(-1/2,1/2,1/2)	(1,0,0)
	(1/2,0,1/2)	(1/2,-1/2,1/2)	(1/2,$\sqrt{3}$/2,0)
	(1/2,1/2,0)	(1/2,1/2,-1/2)	(0,0,$\sqrt{8/3}$)
n_b	1	1	2
$\{\vec{b}_i\}$	(0,0,0)	(0,0,0)	(0,0,0)
			(0,$-1/\sqrt{3}$,$\sqrt{2/3}$)
$\{\vec{d}_i\}$	(-1,1,1)	(0,1,1)	(1,$-1/\sqrt{3}$,0)
	(1,-1,1)	(1,0,1)	(0,$2/\sqrt{3}$,0)
	(1,1,-1)	(1,1,0)	(0,0,$\sqrt{3/8}$)
a/c	$1/\sqrt{2}$	$1/\sqrt{3}$	1
a^3/Δ	$\sqrt{2}$	$3\sqrt{3}/4$	$\sqrt{2}$

Table 3.12: Vectors and constants defining lattices used in calculations. Lattice data for the FCC and BCC Bravais lattices and the HCP lattice, which consists of a hexagonal Bravais lattice with a two-point basis, are given.

energy difference between FCC and HCP is strongly affected.

3.5.7 Appendix: Lattice Vectors and Constants

In this appendix, the various constants and vectors that describe the lattices used in this work are summarized. The real-space lattice sets are all of the form

$$\mathbf{T} = \{c(n_1\mathbf{c}_1 + n_2\mathbf{c}_2 + n_3\mathbf{c}_3 + \mathbf{b}_j), n_i = 0, \pm 1, \pm 2, \cdots, j = 1, \cdots n_b\} \tag{3.82}$$

where the set $\{\mathbf{b}_j\}$ is a n_j-vector basis. The inverse lattices are of the form

$$\mathbf{U} = \{(2\pi/c)(m_1\mathbf{d}_1 + m_2\mathbf{d}_2 + m_3\mathbf{d}_3), m_i = 0, \pm 1, \pm 2, \cdots\} \tag{3.83}$$

The lattice constant c has the dimension of length. Table 3.12 lists the vectors and constants $\mathbf{b}_i, n_b, \mathbf{c}_i, \mathbf{d}_i$, the nearest-neighbor distance a, and Δ, the volume per lattice site, for each lattice considered.

3.6 Perspectives on Freezing in Complex Fluid Systems

In this Chapter a variety of methods and applications of density-functional theory to the description of phase transitions in three-dimensional fluid systems have been presented. By extending the ideas of Ramakrishnan and Yussouff[38] to include orientational as well as translational ordering, it has been shown that one can construct mean field theories for phase transitions in systems composed of nonspherical particles. We have also seen that the extension of the RY theory to include contributions of higher-order direct correlations is a step which leads to a large improvement in the predictive power of the theory.

Molecular anisotropy destabilizes the plastic crystal phase

In the case of crystallization, the effect of aniostropy of constituent particles has been studied. In agreement with simulations, it has been found that the plastic phase is destabilized by increasing anisotropy to the point that the orientationally ordered crystalline solid becomes always lower in free energy. This effect is overly dramatized in the present theory due to the fact that the possibility of the breaking of full rotational symmetry down to cubic symmetry before finally realizing the uniaxial symmetry of the oriented solid is not considered. I suspect that a more general treatment using a full expansion of the orientational distribution in spherical harmonics will result in a phase diagram in close agreement with the simulation results. In the case of the study of the oriented solid, this will increase the technical difficulty of the calculations, but if an expansion in orthogonal functions used, such a calculation should be possible. The difficult problem with calculations involving many order parameters is of course the numerical minimization of the resulting free energy functional: this will require the use of a supercomputer.

Accurate liquid structure leads to accurate description of phase transitions at high anisotropy

The formation of a orientationally ordered phase has also been studied with the same sort of theory, and it has been seen that the important ingredient is reliable liquid structure information. The misleading results of early efforts[45] have been demonstrated to be due to the use of bad assumptions about liquid structure, and through the study of one-dimensional fluid models and comparison with recent studies of integral equation closures of the Ornstein-Zernicke equation[52, 73], it has been shown that for prolate, anisotropic hard cores, the relevant quantity that the direct correlations depend on is not the separation of the hard cores, but rather it is the overlap volume.

This (in retrospect, obvious) result has serious consequences for the strength of the component of the direct correlations that couple to the uniaxial order parameter, shifting the phase transition to up to 50% higher densities. This realization will be an important factor in the construction of density-functional theories to address the interesting problem of the effect of molecular symmetry (i.e. hard core shape) on the symmetry of the observed phases. The type of study presented here probably will be useful in developing some intuition for the behavior of the DCF for other extended hard-core objects such as platelets, rods, polymers, models of proteins and enzymes, and the like.

I would like to stress that such studies should not be attempted without accurate liquid structure information: in the last two years it has been demonstrated that this information can be obtained for anisotropic hard cores by numerical solution of the conventional integral equations. The oft-quoted excuse that the failure of the theory must be due to the structure of the RY functional appears to be unfounded: liquid structure is the key ingredient.

Higher-order DCF contributions improve the theory

The development of weighted-density approximations has added an important tool to the density-functional arsenal. Historically, problems with the RY theory have been blamed on the 'lack of higher-order terms in the functional expansion'. The WDA is a method of constructing a density functional which augments the RY theory with an approximate summation to all orders. Many of the most important terms are taken into account exactly due to the preservation of sum rules related to the pair DCF (which is presumed known). The problem with the original theory of Ashcroft and Curtin[48] is its numerical complexity.

The extension of recent work of Ashcroft and Denton[50] has resulted in the MWDA, which is a workable version of the WDA applicable to phase transitions involving both orientational and translational degrees of freedom. The resulting theory is no harder to study than the RY theory, and repairs many of the pathologies of that approach. These problems centered on the excessively narrow real-space one-body distributions seen in the application of the theory to crystallization, as well as associated problems such as the behavior of the pressure and entropy at freezing transitions. It is my feeling that the current MWDA and WDA theories yield good descriptions of freezing. If accurate liquid structure information is used in them, any remaining discrepancies between their predictions and simulation and experimental results are due purely to the parametrization of the one-body distribution function, and to the mean-field approximation implicit in the variational formulation of the theory. An interesting note is that in the case of orientational freezing, the RY and MWDA approaches agree very well, and that the liquid structure information is by far the dominant factor in the success of calculations.

Fluctuation spectra are calculable

A good question, considering the above comments, is whether it is possible to compute the free energy of fluctuations around the mean-field solutions studied in this work.

As a first step, I have considered the computation of elastic constants of the FCC hard-sphere solid. This has worked out reasonably well, the results near melting being in reasonable agreement with simulations and recent full WDA work[96]. This is to be contrasted with the strikingly bad results[97] that follow from the RY theory. These problems, such as the prediction of elastic instabilities of supposedly ordered phases, are a consequence of the lack of excess free energy contributions at higher than second order in the one-body density (elastic properties are due to second derivatives of the free energy with respect to parameters in the one-body density, and in the RY theory, the resulting constants really have more to do with the liquid than with the solid phase). The next step in the consideration of elastic fluctuations is to redo the present calculations using the full WDA approach.

Building Landau theories from scratch

If the computation of zero-momentum fluctuations are possible, than it seems reasonable that the full long-wavelength 'phonon' spectrum for the hard-sphere solid should be calculable, allowing the determination of the stiffness tensor described in Section 3.5. This would allow the correction of the free energy (and hence all of the thermodynamical potentials) through the integration of the resulting Gaussian phonon free energy density. The crude arguments of the final subsection of Section 3.5 suggest that this correction may complete the model of the hard-sphere solid, and lead to an accurate description of its thermodynamics.

This program is indicative of a method to treat phase transitions in fluids using an *ab initio* approach similar to that starting to be applied to solid state systems[98]. The problem with studying fluid systems from the point of view of Landau theory is of course the many Landau parameters that proliferate, and the large number of phase diagrams that are compatible with the free energy functional. The density-functional approach to inhomogenous classical fluids, like its namesake applied to the inhomogeneous electron gas in solid state physics, is a tool which can be applied to

the computation of Landau parameters. This casts the density-functional approach as a recipe for coarse-graining the mechanical, many-body Hamiltonian of a liquid, and for thus arriving at a free energy density compatible with our machinery for studying the effect of fluctuations of the collective modes consistent with the symmetry of the phase under our consideration.

Chapter 4

Monte-Carlo Renormalization Group Approach to Critical Phenomena

4.1 Introduction

Since Ma[99] demonstrated the possibility of uniting the Monte Carlo (MC) and renormalization-group (RG) techniques, much work has been done on RG analysis of simulations of lattice systems[100, 101, 102, 103, 104, 105]. Ma's original study used a simulation of a several-interaction Hamiltonian, but the later studies have focused on the simulation only of the original, extremely short-range Hamiltonian, and have proceeded via the anlysis of the statistics of the successive Kadanoff blockings of the lattice. Because of this, these studies (typically of systems of 64×64 spins) have been able to study only the first few (< 5, for a rescaling factor $b = 2$) iterations of the rescaling transformation. For systems with relatively simple fixed-point structure, this technique nonetheless has proven to be a powerful quantitative tool.

However, the full power of the RG technique is realized by the possibility of performing many iterations of a scaling transformation and to thereby explore RG flows among a variety of competing attracting and repelling fixed points, or to compute expectation values of operators away from the fixed points. This capability is desirable for the theoretical study of relatively complicated systems with competing interactions that arise in experimental situations. Often the only suitable tool in these cases is the truncated position-space RG technique[106], but because of the difficulty of redoing these types of calculations with larger and larger clusters (due to the exponential increase in the number of states that must be summed over) the accuracy and convergence properties of these approximations are usually unknown.

In this chapter, we present an approach to position-space renormalization that allows the computation of RG flows and corresponding recursion matrices (the derivatives of the recursion relations that relate the interactions before to those after the RG transformation). The idea centers on the use of the Metropolis MC algorithm[107] to simulate a relatively small ($< 16 \times 16$ spin) section of the system of interest. Using a majority-rule blocking transformation to define renormalized spins, expectation values of operators that appear in the Hamiltonian of the renormalized system are thus

calculated. Following this, the couplings that correspond to these expectation values are extracted, which yields the renormalized Hamiltonian. This new Hamiltonian is simulated, and the process is repeated.

The fact that the full renormalized Hamiltonian is used allows the RG flows to be followed indefinitely. The recursion matrix is known at every step, and as a result, can be used to compute the expectation value of any operator that appears in the Hamiltonian, or, if the system renormalizes to a fixed point, its eigenvalues are directly related to the exponents that describe the singular behavior of the free energy of the system at the critical point.

Section 4.2 briefly reviews the renormalization group, and its formal application to the statistical mechanics of lattice systems. In Section 4.3, this approach is applied to the two-dimensional square lattice Ising model, the critical properties of which are known in detail. The renormalized interactions are obtained by exploiting the fact that the number of states of the 16-spin renormalized system is relatively small, which allows the direct calculation of expectation values of renormalized operators for particular values of renormalized couplings. Matching this result to the operator expectations obtained from the MC calculation results in a set of RG equations which can be solved for the renormalized couplings. Our results are competitive with traditional MCRG results that use 10 to 100 times as much computer time.

This initial study does not really point out the advantages of our approach due to the fact that the $d = 2$ Ising model has a rather large critical scaling region with a fixed-point Hamiltonian that is not radically different from the nearest-neighbor 'bare' Hamiltonian. A model which has somewhat different properties results from generalizing the Ising model to the Q-state Potts model. In two dimensions, this model has a tricritical point as a function of Q, at $Q = 4$. This dramatic change is accompanied by the emergence of an additional relevant thermal eigenvalue corresponding to an operator that measures the 'vacancy' density[108]. These vacancies are regions where one of the Q order parameters does not dominate over the others.

These regions become increasingly important as Q increases.

The question of how these vacancies emerge from the nearest-neighbor Potts Hamiltonian has not been addressed by MCRG methods before, for the reason that the 'bare' model is quite far away from the fixed-point Hamiltonian, and as a result is inaccessible by analysis of the first 2 or 3 blockings of the bare system. Our approach, described in Section 4.4, avoids this problem, and we observe signs of the appearance of an additional relevant eigenvalue as Q is increased. We present quite detailed structural information concerning the Potts fixed point, and find leading critical exponents in good agreement with the exact results.

4.2 General Theory

Although the ideas of the renormalization group are applicable to the calculation of any aspects of statistical-mechanical or quantum-mechanical many-body systems, it is important to remember that RG techniques were developed to study the problem of critical phenomena in equilibrium statistical mechanics. A critical point terminates a line of first-order phase transitions, and thus, as one leaves a liquid-gas (or ferromagnetic) critical point along the first-order line, the difference in density (magnetization) of the coexisting ordered phases increases from zero. This indicates that as one approaches the critical point, the correlation length diverges to infinity. The consequent failure of conventional perturbative many-body theory to describe critical phenomena eventually forced Kadanoff, Wilson, and Fisher[5, 6, 109] to think about the notion that rescaling the spatial coordinates using a homogeneous transformation $\mathbf{x}' = b^{-1}\mathbf{x}$ rescales the correlation length: $\xi' = b^{-1}\xi$.

This purely geometrical process obviously reduces the correlation length at the expense of increasing the density of the microscopic degrees of freedom (molecules, or perhaps local moments in a ferromagnet) by a factor b^d, where d is the spatial dimensionality. Kadanoff recognized that if it were possible to 'thin out' the degrees of freedom by this volume-rescaling factor while preserving the value of the total free energy and the symmetry properties of the Hamiltonian, then a mapping in the space of all Hamiltonians with the symmetry and dimensionality of the original would result. Because the new Hamiltonian has a correlation length shorter than the old one, it would correspond in some sense to a system similar in structure to the original, but at a higher temperature, or further away from the critical point.

To formalize this procedure, we present here a version of the RG program developed by Wilson[6], and apply it to lattice systems following the ideas of Swendsen[105]. In order to study Hamiltonian flows, we first express the general Hamiltonian repre-

senting the interactions between discrete degrees of freedom on a regular lattice:

$$-\beta H = \sum_{\mathbf{r}} \sum_{\alpha} J_\alpha S_{\alpha,\mathbf{r}} \tag{4.1}$$

where the sum over $\mathbf{r}$ is over lattice sites, and $\beta = 1/kT$. The operators (which are all 'classical', being c-number functions of the spins) $S_{\alpha,\mathbf{r}}(\{s\})$ represent different symmetry-unrelated functions of the underlying set of spins $\{s\}$. The parameters J_α are dimensionless constants describing the importance of the operators, and we anticipate that these will be 'finite-ranged', or rapidly decreasing with the range of the operators. Position-space RG calculations rely on the property that they converge rather rapidly with the inclusion of an increasing number of increasing-range interactions. To some extent this has been empirically demonstrated to be true[6, 105].

In the position-space formulation, the coarse-graining, or reduction in density of the degrees of freedom, is carried out via the mapping of spins $\{s\}$ onto 'blocked' or coarse-grained spins $\{s'\}$ using some operator $P(\{s'\};\{s\})$, via the renormalization group transformation

$$e^{-\beta H'[\{s'\}]} = \sum_{\{s\}} e^{-\beta H[\{s\}]} P(\{s'\};\{s\}). \tag{4.2}$$

Since the value of the free energy is to be preserved by this RG transformation, we require the projection operator to satisfy the normalization condition

$$\sum_{\{s'\}} P(\{s'\};\{s\}) = 1. \tag{4.3}$$

This is achieved if the projection operator is composed of a product of independent blocking operators that each map b^d old spins to one spin s', each satisfying the condition (4.3). In this chapter, all of the problems will use $b = 2$ on two-dimensional, square lattices, and will use projection operators that map $b^d = 4$ neighboring spins

to one new spin, thus preserving the square lattice.

The transformation equation (4.2) implicitly defines recursion relations relating the old interactions J_α to a new set J'_β:

$$J'_\alpha = R^{(b)}_\alpha(\{\mathbf{J}\}), \tag{4.4}$$

for a length-rescaling factor b. The utility of this approach comes from the realization that fixed points $\mathbf{J}^* = \mathbf{R}^{(b)}(\mathbf{J}^*)$ of this transformation must correspond to points where the correlation length is either zero or infinite. The correlation length is zero only at infinite temperature, when the degrees of freedom are uncoupled, or at zero temperature, when there are no fluctuations about an ordered configuration. The nontrivial case of infinite correlation length corresponds to a critical point. This point must be unstable to some perturbations in the couplings, since any nearby point has a finite correlation length, and will rescale to a point in the Hamiltonian space with a shorter correlation length.

Expanding around the fixed point (assuming the analyticity of the recursion relations) we obtain

$$J'_\alpha - J^*_\alpha = \frac{\partial J'_\alpha}{\partial J_\beta}(J_\beta - J^*_\beta) + \text{nonlinear terms.} \tag{4.5}$$

The recursion matrix $\partial\mathbf{J}'/\partial\mathbf{J}$ can be diagonalized, and excursions from the fixed point can be written in terms of linear scaling fields g_i, the normalized eigenvectors $\mathbf{O}_i$, and eigenvalues $\lambda_i^{(b)}$ to reexpress (4.5) in diagonal form:

$$\mathbf{J}' - \mathbf{J}^* = g'_i\mathbf{O}_i = \lambda_i^{(b)} g_i \mathbf{O}_i, \tag{4.6}$$

where $\mathbf{J} - \mathbf{J}^* = g_i\mathbf{O}_i$.

Composition of these rescaling transformations along with the fact that rescaling

by a factor $b = 1$ is the identity operation indicates that

$$\lambda_i^{(b)} = b^{y_i}. \tag{4.7}$$

These eigenvalues must satisfy $y_i < d$ since no expectation value can increase with rescaling faster than the volume of the system. The sign of these eigenvalues indicates the stability of the corresponding direction $\mathbf{O}_i$. If y_i is less than zero, the direction is relevant, and under rescaling, perturbations in that direction are amplified. If the eigenvalue is less than zero, the direction is irrelevant, and perturbations in its direction are deamplified under RG transformation. If a fixed point has a very limited number of relevant directions, a mechanism for the experimentally observed universality of the rescaling behavior[110] exists: many paths through the parameter space will result in critical renormalization-group trajectories that asymptotically renormalize to the fixed point and then leave along the (one) relevant direction. The case of marginal relevance of the leading eigenvalue ($y = 0$) requires consideration of nonlinear terms in the fixed-point expansion, and although it is interesting, it will not be discussed here.

Experimentally, it is possible to selectively impose perturbations that break the symmetry of the Hamiltonian (i.e. magnetic field), and since the symmetry of the Hamiltonian is preserved under renormalization it is thus physically relevant to partition the eigenvalues into those that correspond to symmetry-breaking (magnetic, or odd) scaling fields h_i, $y_{h_1} > y_{h_2} > y_{h_3} > \cdots$ and those corresponding to symmetry non-breaking (often called thermal, or even) scaling fields t_i, $y_{h_1} > y_{h_2} > y_{h_3} > \cdots$. Universality observed experimentally suggests that there will usually be one relevant magnetic, and one relevant thermal direction.

An important symmetry property of the recursion matrix is that in the absence of symmetry-breaking fields, it can always be made block diagonal. One block contains the set of interactions coupling to operators with expectation values invariant under the symmetry operations of the Hamiltonian that relate the ordered phases, with con-

sequently nonzero expectation values above and at the critical point. The eigenvalues of this block are the thermal ('even') eigenvalues. The other block corresponds to those interactions that couple to operators whose expectation value is zero above and at the critical point, but nonzero in the ordered phases, and eigenvalues of this block are the magnetic ('odd') eigenvalues.

Again using the fact that the free energy has been preserved by renormalization, we can write the effect of rescaling on the free energy as

$$f(\{t\};\{h\}) = b^{-d} f(\{b^{y_t} t\};\{b^{y_h} h\}), \tag{4.8}$$

and thus rescaling using $b = t^{-1/y_{t_1}}$ indicates the form of the free energy to be the homogeneous form

$$f(\{t\};\{h\}) = t^{d/y_{t_1}} f(1, t_2 t_1^{-y_{t_2}/y_{t_1}}, \cdots; h_1 t_1^{-y_{h_1}/y_{t_1}}, h_2 t_1^{-y_{h_2}/y_{t_1}}, \cdots), \tag{4.9}$$

which indicates the critical exponents $2 - \alpha = d/y_{t_1}$ and $\Delta = y_{h_1}/y_{t_1}$. The remaining critical exponents can be derived from these via straightforward application of their definitions[110]. This makes clear the connection between the response to the rescaling transformations and the thermodynamics in the critical region, and explains the experimentally observed universality of the critical exponents in terms of the universality of the RG flows on the critical manifold. This analysis also applies to the case where there is more than one relevant thermal direction. Crossover phenomena resulting from the fact that the asymptotic behavior is controlled by additional fixed points are described by the ratio of the relevant eigenvalues[109].

Away from the fixed points, the recursion matrix continues to play an important role. If one wishes to compute the expectation value of some operator S_α, it is computed by differentiation of the partition function with respect to the coupling J_α from the Hamiltonian (4.1) that is conjugate to it. Using the fact that the partition function is conserved, we can use the chain rule of differentiation to compute the

expectation value in terms of renormalized couplings $J_\alpha^{(i)}$:

$$\begin{aligned} < S_\alpha > &= \frac{1}{NZ}\frac{\partial Z}{\partial J_\alpha} = \frac{\partial J_{\alpha_1}^{(1)}}{\partial J_\alpha}\frac{b^{-d}}{N^{(1)}Z}\frac{\partial Z}{\partial J_{\alpha_1}^{(1)}} = \cdots \\ &= \frac{\partial J_{\alpha_1}^{(1)}}{\partial J_\alpha} b^{-d}\frac{\partial J_{\alpha_2}^{(2)}}{\partial J_{\alpha_1}^{(1)}} \cdots b^{-d}\frac{\partial J_{\alpha_n}^{(n)}}{\partial J_{\alpha_{n-1}}^{(n-1)}} b^{-d}\frac{1}{N^{(n)}Z}\frac{\partial Z}{\partial J_{\alpha_n}^{(n)}}, \end{aligned} \tag{4.10}$$

where the factors b^{-d} arise from the rescaling, which reduces the number of times that S_α appears in the Hamiltonian. After some number (typically $n \approx 20$ for $b = d = 2$) of renormalizations, the renormalized couplings will be close enough to a trivial (attractive high- or low-temperature) fixed point that the final term in the product can be simply approximated. Thus any expectation value can be computed to any desired accuracy, assuming that the global renormalization-group flows are known.

The recursion relations $\mathbf{J}'(\mathbf{J})$ must be obtained from the RG transformation (4.2) by performing a summation over the 'old' spins $\{s\}$. Two problems arise: in a thermodynamically large system, an infinite number of interactions are required to close the transformation, and to sum out any finite fraction of the spins (which must be done for any $b > 1$), an infinite many-body problem must be solved.

The first problem is dealt with easily: it is expected that along RG flows starting from short-ranged Hamiltonians, interactions will remain relatively short-ranged (even at the fixed point), making a truncation procedure appropriate. The second problem is more serious: for Ising systems, the number of spins that one can sum over using a computer is limited to less than 30 or so. For more complicated degrees of freedom, this limitation becomes even more severe.

An alternative to the exact calculation of expectations in the canonical ensemble is the Monte Carlo (MC) method first introduced by Metropolis[107]. This method is based on the replacement of the summation over all configurations of a system using the canonical probablility distribution such as that appearing in (4.2) with a biased random walk through the phase space of the system. This walk is described by a set of transition probabilities T_{ij} between states i and j with energies E_i and E_j.

Consider the case $E_j > E_i$, and let $T_{ij} = W_{ij}t_{ij}$ and $T_{ji} = W_{ij}$. If we consider many independent processes (i.e. many isolated steps far apart in the MC run) then we can write the number of initial states of type i as N_i, and thus the number of transitions that occur are between states i and j are

$$\begin{aligned} N_{i\to j} &= N_i W_{ij} t_{ij} \\ N_{j\to i} &= N_j W_{ij}. \end{aligned} \tag{4.11}$$

The change in the difference between the number of processes that are in the two states is therefore

$$\Delta(N_i - N_j) = N_i W_{ij}(t_{ij} - Nj/Ni). \tag{4.12}$$

In the limit of a long MC walk, and consequently many processes, we expect this difference to go to zero, and the ratio of the probability that the system is in state j to to that for state i will consequently tend to

$$\frac{p_j}{p_i} = t_{ij}. \tag{4.13}$$

If we assign $W_{ij} = 1$ and $t_{ij} = e^{-(E_j - E_i)}$, then the different configurations of the system are visited with a probability that is exactly proportional to their Boltzmann weight, and averages of operators over the MC run will be identical to the corresponding averages obtained from the canonical ensemble. Using this sort of calculation the summation of (4.2) can be approximately done for although not infinite, much larger systems, to an accuracy that can be increased by increasing the length of the MC run.

The calculation of renormalized couplings centers about the computation of expectation values of operators A_i that depend on the 'new', blocked spins $\{s'\}$, which can be computed in three ways. The first is simply the sum over the original spin configurations, using the initial Hamiltonian to compute Boltzmann weights, the second

is the sum over block spin configurations using the Boltzmann weights corresponding to the renormalized Hamiltonian, and the third is a sum over the MC configurations from a simulation of the initial Hamiltonian:

$$\begin{aligned} < A_i(\{s'\}) > &= Z^{-1} \sum_{\{s\}} e^{-\beta H[\{s\}]} P(\{s\};\{s'\}) A_i(\{s'\}) \\ &= Z^{-1} \sum_{\{s'\}} e^{-\beta H'[\{s'\}]} A_i(\{s'\}) \\ &= N_{\rm MC}^{-1} \sum_{\rm MCS} P(\{s\};\{s'\}) A_i(\{s'\}) \end{aligned} \tag{4.14}$$

where the normalization factors are $Z = \sum_{\{s\}} e^{-\beta H} = \sum_{\{s'\}} e^{-\beta H'}$ and $N_{\rm MC} = \sum_{\rm MCS} 1$, and MCS refers to the set of MC configurations. For any set of operators $\{A_i\}$, the first equation of (4.14) defines equations relating their MC expectation values to the inital interactions, and through the second equation in (4.14), to the renormalized interactions.

For a sufficiently small system, the expectation values can be computed first directly from the MC simulation, and then again (for a sufficiently small renormalized system) exactly in terms of the renormalized couplings. Requiring the consistency of the two sets of expectation values thus determines the renormalized interactions. This approach is used in Section 4.3 to treat the $d = 2$ Ising model, where a 8×8 system is renormalized to a 4×4 system, whose $2^{16} = 65536$ states may be readily enumerated. The recursion matrix can be calculated by solving the matrix equation

$$\frac{\partial < A_i >}{\partial J'_\alpha} \frac{\partial J'_\alpha}{\partial J_\beta} = \frac{\partial < A_i >}{\partial J_\beta}, \tag{4.15}$$

which again results from the use of the chain rule. The required derivatives with respect to renormalized and initial couplings are obtained as

$$\frac{\partial < A_i >}{\partial J'_\alpha} = Z^{-1} \sum_{\{s'\}} e^{-\beta H'[\{s'\}]} A_i(\{s'\}) \sum_{\mathbf{r}'} S'_{\alpha,\mathbf{r}'}$$

$$= N_{\rm MC}^{-1} \sum_{\rm MCS} A_i(\{s'\}) \sum_{\mathbf{r}} S_{\alpha,\mathbf{r}}, \tag{4.16}$$

directly from the renormalized couplings, and from the MC simulation, respectively.

For models more complicated than the $d = 2$ Ising model, the enumeration of the blocked spin states necessary in the calculation outlined above becomes impossible. For example, for the three-state Potts model, the exact calculation of expectation values in a 4×4 system would require a summation over $3^{16} = 43,046,721$ states, which is a large computation. One would like to be able to simulate larger systems, and to treat the resulting larger blocked systems, which is clearly impractical using the exact enumeration approach. One alternative is to compute the expectation values required using simulations of the renormalized system directly, but for more than one interaction, this is problematic due to the fluctuations inherent to MC results, which make the comparison of differences between expectation values from independent MC simulations difficult.

Fortunately, an ingenious method has been developed by Swendsen[102] to compute the coupling constants that correspond to a given sequence of MC configurations. Applying this technique to the sequence of renormalized spins from the MC simulation thus will yield the renormalized couplings. Consider the expectation value of a local operator A that depends on a set of spins $\{\sigma\}$. The set of spins $\{s\}$ are all of the spins that are A does not depend on, and thus the union of the two sets is the complete set of spins. In terms of the Hamiltonian, the expectation value of this operator is

$$< A >= Z^{-1} \sum_{\{s,\sigma\}} e^{-\beta H[\{s,\sigma\}]} A(\{\sigma\}), \tag{4.17}$$

where $Z = \sum_{\{s,\sigma\}} e^{-\beta H[\{s,\sigma\}]}$.

Defining the portion of the Hamiltonian that is all terms that contain $\sigma - s$ and

$\sigma - \sigma$ terms as $-\beta\tilde{H}$, the difference $-\beta H + \beta\tilde{H}$ is independent of σ, and we can write

$$< A >= Z^{-1} \sum_{\{s\}} e^{-\beta H + \beta\tilde{H}} \sum_{\{\sigma\}} e^{-\beta\tilde{H}[\{s,\sigma\}]} A(\{\sigma\}), \tag{4.18}$$

and thus, renaming the spins σ as τ, and inserting an additional summation over a new set of spins σ, we obtain

$$< A >= Z^{-1} \sum_{\{s,\sigma\}} e^{-\beta H[\{s,\sigma\}]} e^{\beta\tilde{H}[\{s,\sigma\}]} n^{-1} \sum_{\{\tau\}} e^{-\beta\tilde{H}[\{s,\tau\}]} A(\{\tau\}), \tag{4.19}$$

where $n = \sum_{\{\sigma\}} 1$. This is the average of a local operator over the canonical distribution of the full Hamiltonian, that depends explicitly on the coupling constants in $\tilde{H}$, and thus given the MC expectation values A_i for operators on the renormalized spins, the interactions that give rise to them can be recovered. Obviously, enough independent operators must be considered to allow the interactions of interest to be uniquely determined by the resulting RG equations.

The approach to truncating the number of interactions will be to study the general Hamiltonian on a small cluster of adjacent sites. The set of operators $\{A_i\}$ will be all of the operators that thus appear in the Hamiltonian. The RG flows will be considered only in the subspace of interactions that correspond to operators that are invariant under the global symmetries of the Hamiltonian at the critical point of interest. The recursion matrix can be computed for the other, symmetry-breaking interactions without computing flows for those interactions, as described above. Applications of these ideas to some models that display critical and tricritical phenomena in two dimensions will occupy the remainder of this chapter.

4.3 Application of the MCRG to Critical Phenomena of the Two-Dimensional Ising Model

Our first application of the MCRG technique outlined in the previous Section is to the critical phenomena of the two-dimensional square-lattice Ising model. The Hamiltonian for the $N \times N$ site model is

$$-\beta H = \sum_{i,j=1}^{N} J s_{i,j}(s_{i+1,j} + s_{i,j+1}), \tag{4.20}$$

where the spins $s_{i,j}$ take on the values ± 1. Periodic boundary conditions are assumed. This well-understood system is a good testing ground for MCRG techniques since the free energy is known exactly in zero field[110, 111], which gives us exact knowledge of the critical coupling, critical energy, critical exponents, and many other quantities.

The MC calculation was of the conventional single spin-flip type which accepts spin flips if the energy of the system is decreased, and accepts them with a probability $e^{-\beta \Delta H}$ if the energy difference ΔH caused by the flip is positive.

The choice of projection operator used to coarse-grain the spins is a product of four-spin plaquette block projection operators, which means that the length rescaling factor is $b = 2$. The four spins of an elementary plaquette are projected to a single new spin using

$$P(\{s'\};\{s\}) = \prod_{\text{plaquettes } p} [1 + s'_p \text{sign}(2s_{p,1} + s_{p,2} + s_{p,3} + s_{p,4})]/2 \tag{4.21}$$

as shown in Figure 4.1. The action of this projection operator is to make the renormalized spin s'_p essentially equal to the sign of the sum of spins on the plaquette. One spin in each plaquette is given a 'double vote' to ensure a majority for each configuration without disturbing the up-down symmetry. This projection operator

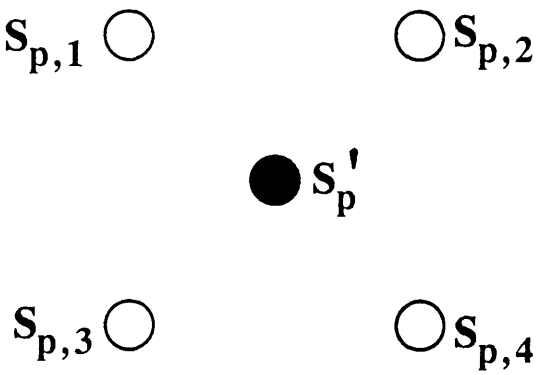

Figure 4.1: Set of four spins on an elementary plaquette of the square lattice that are renormalized to a single spin s'_p.

trivially satisfies the normalization (4.3) required to preserve the free energy.

The operators that were focused on in this study were the short-ranged cluster expectations

$$R(\sigma_1,\cdots,\sigma_n) =< \delta_{s'_1,\sigma_1},\cdots,\delta_{s'_n,\sigma_n} >= N_{\rm MC}^{-1}\sum_{\rm MCS} P(\{s'\};\{s\})\delta_{s'_1,\sigma_1},\cdots,\delta_{s'_n,\sigma_n} \quad (4.22)$$

which for a cluster of n spins, leads to 2^n expectation values. Taking the symmetries of the spins (for zero field) into account reduces the number of independent expectation values to a number equal to the number of operators that can be constructed on the cluster that observe the same symmetries.

The size of the system that we have focused on is 8×8 spins, which renormalizes to 4×4 spins, allowing the sum of (4.14) relating the renormalized interactions to the expectation values R to be evaluated exactly. Periodic boundary conditions are used in both the original and renormalized systems. Local cluster sizes of $n = 2,3,$ and 4 spins have been used in RG transformations with 1, 2 and 3 even, and 1, 2 and 2 odd interactions, respectively. The RG flows are calculated in the subspace where all the odd interactions are zero, but in order to extract the magnetic eigenvalues, derivatives with respect to the odd interactions are calculated.

Figure 4.2 shows the shapes of the clusters used in the calculation of (4.22) for various numbers of spins considered. For $n = 2$, the nearest-neighbor cluster averages are computed, and with no odd interactions and the fact that the overall partition sum normalization is lost, there is only one normalization-independent combination of the four averages (in the limit of a long MC run), which is conveniently expressed as $R(++)R(--)/[R(+-)]^2$. This quantity obtained from the MC run on the blocked 8×8 system is matched to that obtained from exact enumeration of the 4×4 renormalized system by adjustment of the nearest-neighbor coupling constant (with all other couplings zero). The renormalized coupling thus obtained allows determination of the fixed point of the resultant RG transformation, and the recursion matrix leads to the critical exponents. Our results are shown in Table 4.1 along with other MCRG

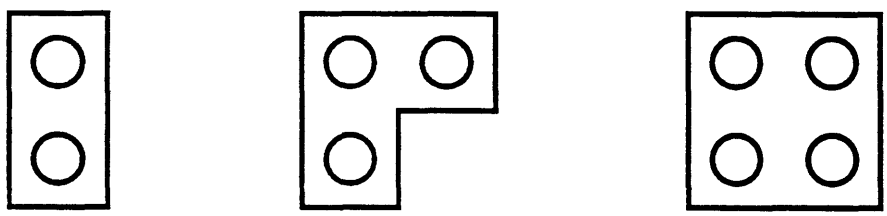

Figure 4.2: Shapes of clusters of $n = 2$, 3 and 4 spins within the renormalized system that have been used in our initial study. These have been used in RG transformations involving 1, 2, and 3 even interactions, respectively.

calculation	n	n_e	n_o	MCS/S	J_c	$\{J^*\}$	y_t	y_h
exact		1	1		0.4406...		1	1.875
this paper	2	1	1	1×10^5	0.446(2)	0.446(2)	0.92(2)	1.898(2)
	3	2	2	2×10^4	0.434(2)	0.342(4) 0.069(7)	0.97(2)	1.856(4)
	4	3	2	2×10^4	0.4409(1)	0.353(8) 0.071(14) 0.009(5)	1.01(2)	1.871(7)
PSRG		3			0.420	0.307 0.084 -0.004	0.937	
previous MCRG		7	4	2×10^6	0.4406...	0.3527(7) 0.0944(10) -0.0075(10) -0.0094(6) -0.0046(4) -0.0019(9) -0.0043(2)	0.997(3)	1.8758(2)

Table 4.1: MCRG applied to $d = 2$ Ising model. Exact results are as tabulated by Stanley[110]. Our MCRG results are as described in the text: n is the number of spins in the local clusters, and n_e and n_o are the number of even and odd interactions considered. MCS/S is the number or MC steps per site per RG transformation, J_c is the critical nearest-neighbor coupling, and the J^* are the interactions of the fixed-point Hamiltonian. The fixed-point interactions are listed in the order of nearest-neighbor pair, next-neighbor, and four-spin (plaquette). y_t and y_h are the scaling dimensions obtained from the largest eigenvalues of the even and odd recursion matrices, respectively. The results of Nauenberg and Nienhuis[112] are truncated position-space RG results, while those of Swendsen[102, 105] are MCRG. Additional interactions used by Swendsen are third neighbor pair, fourth neighbor pair, fifth neighbor pair, and a four-spin interaction on the elementary plaquette of one of the sublattices.

calculations and exact information.

For $n = 3$, there are two unique combinations of the R's for the case of no odd interactions: this leads to the extraction of a nearest-neighbor and next-neighbor interaction from the RG transformation. For the case of derivatives with respect to odd interactions, we have used a one-spin and a three-spin interaction. In the same way as above, we have located the fixed point by sweeping the nearest-neighbor interaction of the initial system and watching the RG flows: the critical value of the nearest-neighbor interaction initiates a flow that ends at the fixed point (in practice, it ends up near the fixed point and after many iteractions of the RG begins to flow away to the weak- or strong-coupling fixed points). The derivative matrix can then be diagonalized to yield the scaling exponents listed in Table 4.1.

Similarly, for $n = 4$, there are three even interactions corresponding to the three unique R's in zero odd fields. Two odd interactions are distinguished on this cluster, and we have computed fixed point and critical properties as shown in Table 4.1.

The values for the critical nearest-neighbor interaction of the unrenormalized model have been obtained by computing the mean and statistical errors of initial conditions that lie in the region where it is not certain that the flows lead to the strong- or weak-coupling fixed points. The width of this region shrinks as the MC runs are lengthened. The values for the fixed point interactions and eigenvalues reflect the mean and statistical errors of the RG iterations that start over this range that lie closest to the fixed-point values.

As can be seen from Table 4.1, the errors of the critical values are small for relatively short MC runs (20000 MCS/S), and quickly converge to the exact $d = 2$ square lattice Ising value. At the same time, the structure of the fixed-point Hamiltonian and its eigenvalues converge to a form similar to that obtained from position-space truncation approximation and Swendsen's MCRG calculations. The critical exponents also rather quickly converge to values consistent with the exact results. This is very encouraging, as our calculations are done with much shorter computation times and

allow the RG flows to be followed for many iterations with no change in the finite-size effects that are introduced at each step. By comparison, the work of Swendsen[102] typically is done using a single MC run of $> 10^6$ MCS/S on a 32×32 lattice which allows at most four successive $b = 2$ blockings to be examined.

4.4 Application of the MCRG to Critical and Tricritical Phenomena of the Q-state Potts Model

In this section, we describe the application of the MCRG to the two-dimensional, ferromagnetic Q-state Potts model, which is a generalization of the Ising model. The Hamiltonian for this model on a $N \times N$ square lattice is

$$-\beta H = \sum_{i,j=1}^{N} J(\delta_{s_{i,j},s_{i+1,j}} + \delta_{s_{i,j},s_{i+1,j}}), \tag{4.23}$$

where periodic boundary conditions are assumed, $J > 0$, and the spins s take on Q states, i.e. $s \in \{1, 2, 3, \cdots, Q\}$. For $Q = 2$, this model becomes the Ising model of (4.20) with a coupling $J_{\text{Ising}} = J_{Q=2}/2$. This model was first studied by Potts[113], and since that time, much exact information concerning it[114] has been obtained. This includes information concerning the extension of the model to noninteger values of Q, but in this Section, only integers $Q \geq 2$ will be considered. The model with $J < 0$ is also not considered here.

It is known that the model (4.23) has a phase transition at a critical coupling of $J_c = \log(1 + \sqrt{Q})$, a result that follows from self-duality[114]. Below the transition, there are Q coexisting phases corresponding to the Q degenerate zero-temperature configurations, each of which can be selected by suitably defined symmetry-breaking fields. In the absence of symmetry-breaking fields, the Potts model has a global Q-fold permutation symmetry corresponding to invariance under relabelings of the Q states.

For $Q \leq 4$ the transition is known to be second-order, but is first-order (with a nonzero latent heat) for $Q > 4$[115]. This is somewhat surprising since for $Q \geq 3$ there are cubic terms in the Landau free energy which lead to a mean-field theory with a first-order transition. Conversely, early RG theories for the Potts model pre-

dicted continuous transitions for all Q. Finally, the work of Berker *et al*[108] showed how the change in order of the transition could be understood in terms of the RG flows of a generalized Potts 'lattice-gas'[108]. The main idea introduced is that an additional thermal direction becomes relevant for $Q > 4$, causing flows starting from the Hamiltonian (4.23) near criticality to lead to a new fixed point which has an eigenvalue of b^d, which corresponds to a first-order transition.

The study outlined above included vacancy states explicitly, but in principle, it should be possible to implictly treat the vacancies by including interactions that couple to configurations of spins that correspond to local vacancies. For MCRG, this is desirable since it reduces the number of degrees of freedom per site and which in turn dramatically reduces the number of distinct interactions in the Hamiltonian for a given cluster size. Previous MCRG work has been along these lines[101, 116] and has indicated that such a study should be feasible, although the fact that only small numbers of RG transformations can be done using the Swendsen technique confuses the identification of the fixed point and its associated eigenvalues. Here, we apply methods similar to those used in the previous Section to the Potts model.

The first ingredient of the MCRG is the projection operator. The fact that the pure Potts states are the only degrees of freedom per site suggests a simple majority rule projection, and as in the previous Section, we form a product of plaquette projection operators:

$$P(\{s'\};\{s\}) = \prod_{\text{plaquettes } p} \delta_{s'_p, M(s_{p,1}, s_{p,2}, s_{p,3}, s_{p,4})}, \tag{4.24}$$

where the function M takes on the Potts state that the majority of the four plaquette spins are in, or if there is a tie, it takes on the value $s_{p,1}$. The δ is the Kronecker delta, thus (4.24) satisfies the normalization requirement (4.3), and exactly reduces to the Ising projection operator employed in the previous Section.

The operator averages that were focused on in this study are simply the expectation values of the operators that appear in the Hamiltonian, ensuring a 1-1

correspondence between expectation values and the interactions. In the language of Section 4.1, this means we are taking $\{A_i\} \equiv \{S'_\alpha\}$. This step trivializes the selection of expectation values for use in constructing the RG equations, which is important since the number of operators that are needed to form the general Hamiltonian on a cluster of n Potts spins depends on the number of states per site Q.

As remarked in Section 4.1, the number of states for even a 4×4 spin Q-state Potts system precludes the use of the exact enumeration technique, and as a result, we use the method of Swendsen outlined in Section 4.2 to compute renormalized coupling constants. This no longer requires us to consider a 8×8 initial system, so all of the calculations in this Section have been done using simulations of 16×16 spin Potts systems. A single spin-flip MC technique has been used, as described in Section 4.1.

The calculations have been done for interactions that form the general Potts Hamiltonian on clusters of $n = 2$, 3, and 4 sites on an elementary plaquette, as shown in Figure 4.2. The operators that are required in for each case can be derived from the general Q-state plaquette Hamiltonian of Dasgupta[117]:

$$\begin{aligned} -\beta H(s_1, s_2, s_3, s_4) &= G + J_1(\delta_{12} + \delta_{24} + \delta_{13} + \delta_{34})/4 + J_2(\delta_{14} + \delta_{23}) \\ &+ J_3(Q^3\delta_{1234} - Q^2[\delta_{124} + \delta_{243} + \delta_{431} + \delta_{312}] \\ &\quad + Q[\delta_{12} + \delta_{24} + \delta_{43} + \delta_{31} + \delta_{14} + \delta_{23}] - 3) \\ &+ J_4(Q^2[\delta_{124} + \delta_{243} + \delta_{431} + \delta_{312}] \\ &\quad - 2Q[\delta_{12} + \delta_{24} + \delta_{43} + \delta_{31} + \delta_{14} + \delta_{23}] + 8) \\ &+ J_5(Q^2\delta_{14}\delta_{23} - Q[\delta_{14} + \delta_{23}] + 1) \\ &+ J_6(Q^2[\delta_{12}\delta_{34} + \delta_{13}\delta_{24}] - Q[\delta_{12} + \delta_{24} + \delta_{43} + \delta_{31}] + 2) \end{aligned} \tag{4.25}$$

where the notation $\delta_{ijk\cdots lm} = \delta_{s_i s_j}\delta_{s_j s_k}\cdots\delta_{s_l s_m}$. The constant G is an overall additive contribution to the free energy which is not computed along the RG flow since the absolute normalization of the partition function is lost due to the use of the MC method.

The J_α are the 'even' interactions invariant under the Q-fold permutation symmetry, and are the interactions that form the description of the RG flows. The plaquette Hamiltonian is of course invariant under the rotational and reflection symmetry operations that leave the lattice unchanged, and is also invariant under Q-fold permutations of the states. The structure of the operators O_i that couple to J_i, $i = 3, 4, 5, 6$ has been chosen so that each one has an expectation value of zero at infinite temperature, and for $Q \geq 4$ the equation $a_3 O_3 + a_4 O_4 + a_5 O_5 + a_6 O_6 = 0$ is only satisfied for $a_3 = a_4 = a_5 = a_6 = 0$. This has been found to greatly improve the ability of nonlinear equation-solving subroutines to solve the resulting RG equations.

To compute the odd block of the recursion matrix, it is necessary to calculate the expectation values of operators that would break the permutation symmetry of the Hamiltonian (4.25). For the four-site plaquette, the general set of operators that select state 1 is:

$$
\begin{aligned}
O_7 &= Q(\bar{\delta}_1 + \bar{\delta}_2 + \bar{\delta}_3 + \bar{\delta}_4) - 4 \\
O_8 &= Q(Q\bar{\delta}_1 - 1)(\delta_{12} + \delta_{13}) + Q(Q\bar{\delta}_4 - 1)(\delta_{34} + \delta_{24}) \\
O_9 &= Q(Q\bar{\delta}_1 - 1)\delta_{14} + Q(Q\bar{\delta}_2 - 1)\delta_{23} \\
O_{10} &= Q^2(Q\bar{\delta}_1 - 1)(\delta_{123} + \delta_{124}) + Q^2(Q\bar{\delta}_4 - 1)(\delta_{134} + \delta_{234}) \\
O_{11} &= Q(Q\bar{\delta}_1 - 1)(\delta_{24} + \delta_{34}) + Q(Q\bar{\delta}_2 - 1)(\delta_{13} + \delta_{34}) \\
&\quad + Q(Q\bar{\delta}_3 - 1)(\delta_{12} + \delta_{24}) + Q(Q\bar{\delta}_4 - 1)(\delta_{12} + \delta_{13}) \\
O_{12} &= Q(Q\bar{\delta}_1 + Q\bar{\delta}_4 - 2)\delta_{23} + Q(Q\bar{\delta}_2 + Q\bar{\delta}_3 - 2)\delta_{14} \\
O_{13} &= Q^3(Q\bar{\delta}_1 - 1)\delta_{1234} \\
O_{14} &= Q^2(Q\bar{\delta}_1 - 1)\delta_{234} + Q^2(Q\bar{\delta}_2 - 1)\delta_{341} \\
&\quad + Q^2(Q\bar{\delta}_3 - 1)\delta_{412} + Q^2(Q\bar{\delta}_4 - 1)\delta_{123} \\
O_{15} &= Q^2(Q\bar{\delta}_1 + Q\bar{\delta}_4 - 2)(\delta_{12}\delta_{34} + \delta_{13}\delta_{24}) \\
O_{16} &= Q^2(Q\bar{\delta}_1 + Q\bar{\delta}_2 - 2)\delta_{14}\delta_{23},
\end{aligned}
\tag{4.26}
$$

where the notation $\delta_{ij\ldots kl}$ is as used in (4.25), and where $\bar{\delta}_i = \delta_{s_i,1}$ are again Kronecker delta functions.

This long list of interactions corresponds to the different ways that assigning states to the four spins on a plaquette break the symmetry of the plaquette. For $Q < 4$, or for clusters that are only part of a plaquette, the number of interactions that are required is reduced. Table 4.2 lists the required interactions for each Q and cluster size n. It should be noted that in the Ising case $Q = 2$, the interactions $J_1/2$, $J_2/2$, and J_3 are precisely the first- and second-neighbor and the four-spin interactions considered in the previous section. It is important to not use too many even interactions, as this will cause the RG equations to be overdetermined. If too many odd expectation values are retained, the consequence is that some number of the eigenvalues of the odd block of the recursion matrix will be zero.

Table 4.3 lists the exact information known concerning the Potts model. Listed are the square lattice critical nearest-neighbor couplings, and the leading, and next-to-leading thermal and magnetic scaling exponents. Tables 4.4, 4.5, and 4.6 show our MCRG results for the $n = 2$, 3, and 4 calculations, respectively. For $n = 2$, we have carried out rather extensive calculations for $Q = 1$, 2, 3, 4, 5, and 10, and for $Q > 4$, the transition continues to be second order since the recursion relation $J_1'(J_1)$ is continuous, and thus must have a fixed point. However, many of the trends of the exact information are correctly reproduced: the critical coupling and thermal exponents increase with Q (although more slowly than do the exact values), and the $Q = 3$ magnetic exponent is indeed below that of the $Q = 2$ magnetic exponent. In addition, the next-to-leading magnetic eigenvalue is probed for $Q > 2$, and is relevant, increasing with Q, as does the exact result. Each RG transformation was obtained from a lengthy MC run consisting of 5000 MCS/S equilibration followed by 100000 MCS/S of data-taking.

For the three-site clusters ($n = 3$), much more information is obtained. In addition to improved estimates for the critical nearest-neighbor couplings, a fixed point Hamil-

n	Q	n_e , n_o	{α}
2	2	1	1
		1	7
	3 +	1	1
		2	7,8
3	2	2	1,2
		2	7,10
	3 +	3	1,2,4
		6	7,8,9,10,11,12
4	2	3	1,2,3
		2	7,10
	3	5	1,2,3,4,5
		9	7,8,9,10,11,12,13,14,15
	4 +	6	1,2,3,4,5,6
		10	7,8,9,10,11,12,13,14,15,16

Table 4.2: Interactions that must be kept for different Q for different cluster size n. n_e and n_o reflect the total number of even and odd operators required in each case. The numbers $\{\alpha\}$ indicate which of the even and odd operators described in (4.25) and (4.26) must be included in the calculation. The first and second lines in each case describe the even and odd interactions, respectively.

Q	J_c	y_t	y_{t2}	y_h	y_{h2}
2	0.881374	1	-1	1.875	-0.125
3	1.005053	1.2	-0.8	$1.86\underline{6}$	$0.66\underline{6}$
4	1.098612	1.5	0	1.875	0.875

Table 4.3: Exact information known for $d = 2$ square-lattice Q-state Potts models for $Q = 2, 3, 4$. $J_c = \log(1 + \sqrt{Q})$ is the critical nearest-neighbor coupling, and y_t,y_{t_2}, y_h, and y_{h_2} are the leading thermal, next-to-leading thermal, leading magnetic, and next-to-leading magnetic scaling exponents, respectively. The next-to-leading thermal and magnetic exponents are as computed by Nienhuis[118] and den Nijs[119].

Q	$J_c = J^*$	y_t	$\{y_{h\,i}\}$
2	0.892(1)	0.93(1)	1.886(2)
3	1.017(2)	1.08(1)	1.875(2) 0.61(2)
4	1.102(3)	1.16(1)	1.863(3) 0.62(2)
5	1.172(3)	1.24(1)	1.860(3) 0.68(3)
10	1.418(3)	1.45(1)	1.855(5) 0.69(3)

Table 4.4: MCRG results for Q-state Potts model calculations using two-site Hamiltonian. Listed for each Q are the critical (and thus fixed-point) nearest-neighbor coupling, as well as the corresponding thermal exponent y_t. The magnetic exponent(s) are also listed.

Q	J_c	$\{ J^*_\alpha \}$	$\{ y_{t\,i} \}$	$\{ y_{h\,i} \}$
2	0.8678(5)	0.65(2)	0.94(1)	1.853(9)
		0.15(2)	-1.9(1)	-0.50(5)
3	0.9848(5)	0.66(3)	1.08(2)	1.817(10)
		0.15(5)	-1.20(5)	0.58(3)
		0.03(2)	-2.1(1)	-0.56(5)
4	1.0782(5)	0.73(8)	1.18(4)	1.801(25)
		0.19(4)	-0.83(13)	0.69(6)
		0.03(2)	-2.0(2)	-0.5(1)

Table 4.5: MCRG results for Q-state Potts model calculations using three-site Hamiltonian. Listed for each Q are the critical nearest-neighbor coupling, and the corresponding fixed point couplings. Thermal and magnetic scaling exponents are listed in order of relevance.

Q	J_c	$\{J^*_\alpha\}$	$\{y_{t\,i}\}$	$\{y_{h\,i}\}$
2	0.871(1)	0.65(3) 0.15(2)	0.96(3) -1.8(3)	1.850(9) -0.48(9)
3	0.990(1)	0.72(5) 0.15(1) 0.002(7) 0.008(4) -0.002(8)	1.14(3) -1.14(8)	1.834(5) 0.60(3)

Table 4.6: MCRG results for Q-state Potts model calculations using four-site Hamiltonian. Listed for each Q are the critical nearest-neighbor coupling, and the corresponding fixed point couplings. Thermal and magnetic scaling exponents are listed in order of relevance.

tonian different from the nearest-neighbor Hamiltonian is obtained. The second-neighbor coupling at the fixed point is roughly a quarter of the nearest-neighbor coupling's strength, for Q=2, 3 and 4. For $Q \geq 3$, there is a three-site even interaction at the fixed point, which is much smaller than the other two interactions. The leading thermal exponents are about the same values as those obtained from the $n = 2$ runs, but now we have access to the leading irrelevant exponent, which although not zero at $Q = 4$, increases with increasing Q. The next-to-leading magnetic exponents are about the same as those obtained from the $n = 2$ runs, indicating that the additional three-site odd interactions do not play a big role for $Q = 3$ and 4. However, the very bad estimate for y_{h_2} in the Ising case indicates that larger odd interactions must be considered. The computations for the $n = 3$ case consisted of runs of 20000 MCS/S equilbration and 80000 MCS/S data-taking.

Our largest calculations have been for the case $n = 4$, where there are 3, 5, and 6 even interactions kept in the cases $Q = 2$, 3 and 4, respectively. In the Ising ($Q = 2$) case, further improvement in the estimate of the critical coupling is obtained, and the value of the four-site even interaction at the fixed point is very small. The other interactions are about the same as obtained from the $n = 3$ calculations, indicating the convergence of the thermal part of the calculation. However, the magnetic part of the computation appears to not have converged yet, as the next-to-leading magnetic eigenvalue is still significantly below the exact value of $-1/8$.

For the case $Q = 3$, the four-site calculations lead to values of the critical exponents that change in accordance with the exact results. We find that the leading thermal scaling exponent is 1.14 ± 0.03, which is close to the exact result of 1.2, and the next-to-leading thermal exponent is -1.14 ± 0.08, which is not too far away from the exact value -0.8. In comparison to the Ising case, we find that the magnetic scaling exponents are very similar to those obtained from the three-site calculations, suggesting that they have converged for $Q = 3$.

For the 4-state Potts model, our calculations are still in progress, but it appears

that the critical coupling is near $K_c = 1.09$. The scaling exponents also appear to be quite reasonable: $y_t \approx 1.3$, and $y_h \approx 1.85$. The next-to-leading magnetic eigenvalue is about $y_{h_2} \approx 0.7$, which as in the $Q = 3$ case, is about the same as that obtained from the three-site calculations. The next-to-leading thermal exponent is lower yet than that from the three-site computation, and is near $y_{t_2} \approx -0.4$. These values are preliminary, and depend strongly on the fixed point interactions, which we are continuing to determine.

Chapter 5

Multifractal Trees and Multiscaling Properties of Critical Phenomena

5.1 Introduction

It has been long been recognized that nonlinear physical systems can give rise to complicated patterns, but the classification of the dynamics responsible for their creation, or even the characterization of the pattterns themselves, has been lacking. The recent focus of many researchers on the study of trajectories of low-dimensional dynamical systems at the edge of chaos[120, 121] and of diffusion-limited aggregation processes[122] has led to the realization that the understanding of scaling properties of patterns arising in these situations may be important in understanding the relationship between the underlying dynamics and the emergent patterns.

The study of scaling properties of correlations in field theories defined on a d-dimensional Euclidean space dates at least as far back as to 1914, to the work of Ornstein and Zernicke on critical opalescence[55], but the notion that a geometrical object may itself have nontrivial scaling properties is generally attributed to Mandelbrot[123]. If we consider a regime where the mass of the portion of an object enclosed in a d-dimensional region of characteristic length l scales as

$$M_l \approx l^{D_F}, \tag{5.1}$$

Mandelbrot has taught us that we should not expect *a priori* that D_F is an integer, but to admit that it can be any number between 0 and d. An equivalent statement is that the two-point mass-mass correlation function has the scaling form

$$< \rho(\mathbf{r}')\rho(\mathbf{r}) > \approx |\mathbf{r} - \mathbf{r}'|^{D_F - d}, \tag{5.2}$$

which in light of our experiences with critical phenomena, seems quite possible. The exponent D_F, which we recognize as being analogous to the correlation function exponent $2 - \eta = d - 2x$ of critical phenomena, is usually called the 'mass dimension' or 'fractal dimension' of the object in question.

Many experimental realizations of 'fractals' have been discovered, but the study

of the two examples mentioned above (trajectories at the transition to chaos, growth probabilities on DLA cluster surfaces) led to the remarkable discovery that the mass dimension was not the only geometrical critical exponent, and that the q-point functions have associated with them scaling indices which do not follow the law $x_q = qx$ as is normally the case in critical phenomena[124]. Thanks to the efforts of Mandelbrot[125], Frisch and Parisi[126], Hentschel and Procaccia[127], and Jensen *et al*[128], the generalized dimensions, which in terms of the x_q and support dimension (fractal dimension of the set on which the distribution of interest is nonzero) D_0, have the form $D_q = D_0 - x_q/(q-1)$, have been given a geometrical interpretation. Measures (any function of a metric defined on any set) which possess such a set of scaling exponents are termed multifractals.

The generalized dimensions D_q allow a fuller characterization of scaling properties of a measure than available through the use of the mass dimension alone. In some cases, there is universality of the entire function D_q across a broad range of physical systems. This set of exponents can also be considered to be analogous to the free energy of a statistical mechanical model (which itself is an exponent that describes how the partition function scales with the size of the system). In many cases, this analogy can be made complete, allowing a description of a geometrical object in terms of a effective Hamiltonian[128]. This suggests that different sorts of D_q can be classified in terms of the type of underlying statistical-mechanical description. Feigenbaum, Jensen, and Procaccia have studied the inverse problem of finding the microscopic model that globally describes a particular D_q[129].

In Section 5.2, a more directed approach to studying the properties of the statistical-mechanical descriptions of geometrical objects possessing multifractal measures will be presented. Instead of examining the global 'thermodynamics' of a measure, the 'low-temperature' properties will be singled out for study. For a series of objects whose generalized dimensions are exactly soluble, numerical studies of the measures have been carried out to determine whether the elementary excitations can be char-

acterized. This type of analysis appears to be practical in many cases, and allows additional insight to be gained into the structure of a given strange set.

Section 5.3 reports an interesting discovery concerning our old friend, critical phenomena. Through the analysis of simulation data, it has been found that moments of the magnetization field of the two-dimensional Ising model at its critical point scale with exponents that do not depend linearly on the moment q.

5.2 Asymptotic Behavior of the Generalized Dimensions of Multifractal Trees

by J. F. Marko and G. T. Pickett

5.2.1 Introduction

The nonlinear physics of growth phenomena or chaos in dynamical systems generate complicated patterns possessing measures that are multifractal[121, 122]. The utility of multifractal spectra in describing these objects is that features of these spectra may be universal. Here, some simple models for the growth of multifractal 'trees' are considered, and via the mapping of the cross-section geometry to Boltzmann weights of statistical-mechanical models, the possibility of universal singular behavior of the generalized dimensions is examined. In these models, the important parameters are the symmetries and 'dimensionality' of the branch-splitting process.

The asymptotic behavior of the generalized dimensions will be shown to be dominated by the contributions of elementary excitations above the ground state of the equivalent statistical-mechanical model. It is found that often this spectrum of low-lying states is discrete, leading to an exponential decay of the generalized dimensions. This behavior is not altered by the inclusion of uncorrelated disorder into these trees. We have also carried out direct numerical studies of finite realizations of these trees, and we have found that the behavior found analytically is not difficult to obtain directly from the data for a multifractal set. A simple application of these methods to the study of the critical period-doubling attractor is presented, indicating that the sparsest regions of this set are exactly described by a tree of the form considered here.

We include a description a tree model that corresponds to the $d = 2$ Ising model, and we study the consequent critical behavior seen in the generalized dimensions. Applications and directions for further development of these ideas will also be presented.

5.2.2 General Theory

In this section we present definitions and formalism that will be used in the remainder of this paper, and we also nonrigorously summarize the results of Halsey *et al*[128]. A measure is a distribution defined on some set. The underlying set of points on which the measure is strictly nonzero is called the support of the measure. The support may itself be a singular set: in fact, in this paper we will be considering measures that take on the values 1 or 0 for points on or off the support, respectively. The support is itself 'embedded' in a Euclidean space of dimension d.

If we cover the support with 'boxes', or a collection of closed sets, where these boxes are of a characteristic edge length l, then the minimum number N_l of boxes needed to cover this region diverges as l is reduced to zero, and is assumed to follow the scaling law

$$N_l \approx l^{-D_0}, \tag{5.3}$$

where D_0 is the 'mass', or 'fractal' dimension of the support. This is the upper bound on the fractal dimension of any subset of the support. Note that D_0 may be any number (possibly noninteger) between 0 and the space dimension d.

Suppose that the measure μ is defined in terms of a metric $d^d x$. Given a set of boxes $\{B_i\}$ of edge sizes $\{l_i\}$, then we can form the integrals of the measure in the boxes:

$$p_i = \int_{B_i} d^d x \mu(\mathbf{x}). \tag{5.4}$$

Adding up the qth powers of these integrals, divided by the τth moment of the box edge lengths yields the 'partition function'[128] Γ:

$$\Gamma(q, \tau, \{B_i\}) = \sum_i \frac{p_i^q}{l_i^\tau}. \tag{5.5}$$

We shall now examine the relation between q and τ that results from the equation $\lim_{l_i \to 0} \Gamma(q, \tau) = 1$.

The function $\tau(q)$ is essentially the generalized dimensions D_q of Hentschel and

Procaccia[127]: the two are related by

$$D_q = \frac{\tau(q)}{q-1}. \tag{5.6}$$

In addition to representing the scaling laws associated with the integrated q-point distribution functions, it has been found that there is a relation between $\tau(q)$ and the dimension of subsets of the measure with particular local power-law singularities.

Locally, the integrated submeasures depend on the lengths as $p \approx l^{\alpha}$ where α may vary from point to point on the set in a possibly singular manner. In addition, the number of boxes that have local scaling exponents between α and $\alpha + d\alpha$ will scale as $N(\alpha, \alpha + d\alpha, l) \approx d\alpha l^{-f(\alpha)}$ for a set of boxes of size l. This tells us that the contribution to the partition function from the region of the set with α in this range will be between the limits

$$d\alpha\rho(\alpha)l_0^{-f(\alpha)+\alpha q-\tau} \quad \text{and} \quad d\alpha\rho(\alpha)l_1^{-f(\alpha)+\alpha q-\tau} \tag{5.7}$$

where ρ is a nonsingular function, and l_0 and l_1 are the bounds of the sizes of the boxes.

Thus, requiring $q(\tau)$ to be defined to keep (5.5) of order unity in the limit that the sizes of all the boxes go to zero implies the relation $\tau = \alpha q - f$ if the condition $f''(\alpha) < 0$ holds. The interpretation of f is clear: it is the mass, or fractal dimension of the subset of points of the support with a local scaling index α. The advantage of computing $f(\alpha)$ using this approach is that the set of moments (5.5) are easily computed, given a finite approximation to a measure. From the relation between q and τ, f and α can be computed using the Legendre transformation:

$$\begin{aligned} \alpha &= \frac{d\tau}{dq} \\ f &= \alpha q - \tau. \end{aligned} \tag{5.8}$$

Happily, the result that $f(\alpha)$ is well defined and smooth while $f''(\alpha)$ is negative seems to be generic for a wide variety of singular measures and strange sets, using a variety of covering sets whose sizes go to zero in different ways[128].

5.2.3 Growth of Multifractal Trees

Consider the growth of a tree in two dimensions, where the direction of growth is along the y-axis. The intersection of a line parallel to the x-axis with the tree thus gives a set of points. For any underlying growth dynamics, there is a mapping that relates such a set of points at some time to the sets at earlier times. Here, a simple set of algorithms is considered where growth proceeds through a succession of tip-splittings. The points in the cross-sections are associated with a set of intervals which they are centered in, and the growth is constrained so that each of these intervals contains all of its daughter intervals.

At the ith splitting, each branch splits into Q_i daughters, so that the total number of intervals after n steps is $N_n = Q_n Q_{n-1} Q_{n-2} \cdots Q_1$. The splitting is such that the daughter intervals are contained within the parent, and a nth-level node of a tree with $Q_n = 3$ is shown in Figure 5.1. Any point (and its interval) in the nth cross-section is labeled by a sequence of symbols $(s_n, s_{n-1}, \cdots, s_1)$, with $1 \leq s_i \leq Q_i$. The lengths l of the intervals at step $n+1$ may thus be related to those at step n by a scaling function[128] σ:

$$l(s_{n+1}, s_n, \cdots, s_1) = \sigma(s_{n+1}, s_n, \cdots, s_1) l(s_n, s_{n-1}, \cdots, s_1). \tag{5.9}$$

The scaling function should be less than 1 at each node to ensure that all paths down the tree lead to asymptotically zero-length daughters.

Recalling the partition function (5.5), we note that the set of intervals at level n form a covering set of the fully developed ($n = \infty$) set whose lengths go to zero as n grows in size. The measure of interest in this Section is simply the mass, or the number of nodes, contained in boxes that cover the fully developed set. The fraction of the total number of nodes that is contained in each of the daughter intervals at level n is precisely N_n^{-1}. Normalizing the total mass so that $\int d\mu = 1$, the equation

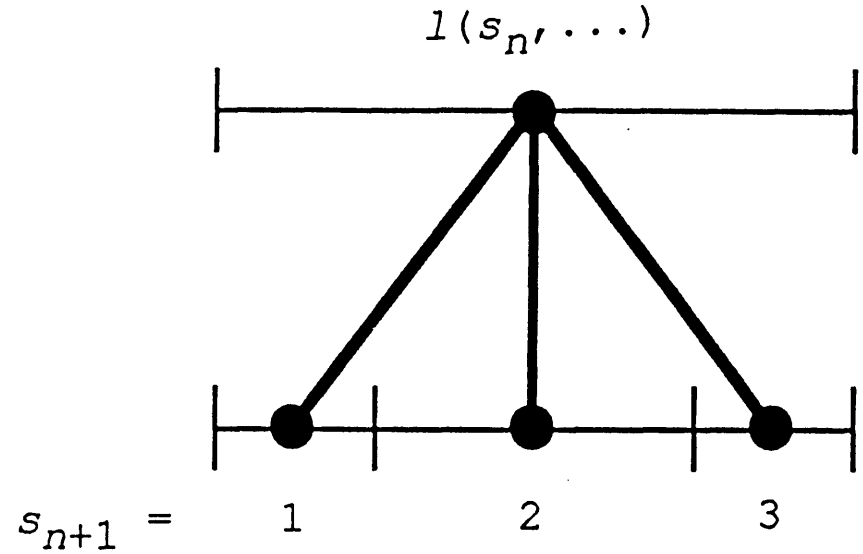

Figure 5.1: Branching with $Q_n = 3$. In this example, the union of the daughter intervals is the entire parent interval, but there could be gaps between the daughter intervals.

$\Gamma(q,\tau) = 1$ becomes simply

$$N_n^q = \sum_{\{s_n,\cdots,s_1\}} \sigma(s_n,\cdots)^{-\tau}\sigma(s_{n-1},\cdots)^{-\tau}\cdots\sigma(s_2,s_1)^{-\tau}l(s_1)^{-\tau}. \qquad (5.10)$$

The equation (5.10) looks like a transfer matrix formulation of the partition function for a classical spin Hamiltonian. q is essentially the free energy, since N_n is just the total number of states, while τ plays the role of the inverse temperature. Consequently, the possibility of phase transitions[130], and in particular, 'universal' singular (critical) behavior of $q(\tau)$ exists. Since one would expect σ to depend more strongly on the recent symbols $(s_{n+1}, s_n, \cdots)$ than on the earlier ones $(\cdots, s_2, s_1)$, one is led to consider the simplest case when the dependence of the scaling function σ is only on the two most recent symbols (s_{n+1}, s_n).

In this Section, we will focus mainly on the study of the behavior of the $q(\tau)$ for different types of these trees, since this is the quantity that is naturally related to the free energy of the related statistical-mechanical models. It should be noted that

this sort of model has been used successfully to globally describe the critical attractor for both the period-doubling and quasiperiodic transitions to chaos in dynamical systems[129]. Recently, a coarse-graining approach to the study of fractal growth that results in trees of exactly this sort has been used to successfully predict the mass dimension of patterns in the general dielectric breakdown model, which includes Eden growth and DLA as special cases[131].

5.2.4 Trees Corresponding to $d = 1$ Statistical Models

A. Tree Structure and Asymptotic $q(\tau)$

In the cases where the splitting order $Q_i = Q$ is the same at each iteration, the $q(\tau)$ are related to the free energies of one-dimensional statistical models. A simple example is $Q = 2$, with a scaling function

$$\sigma(s_{n+1}, s_n) = b + (a - b)\delta_{s_{n+1}s_n}, \tag{5.11}$$

where δ is the Kronecker delta function, and a and b are positive numbers less than 1 satisfying $a + b \leq 1$. This model corresponds through equation (5.10) to the $d = 1$ Ising model, and $q(\tau)$ is exactly calculable using the constant-measure partitions:

$$q = \frac{\log(a^{-\tau} + b^{-\tau})}{\log 2}. \tag{5.12}$$

Figure 5.2 displays the first few splittings leading to the growth of this tree for the case $a = 0.667$, $b = 0.333$, and Figure 5.3 shows the corresponding $f(\alpha)$ derived from the relation (5.12). The geometrical interpretation of $f(\alpha)$ presented in the previous subsection seems reasonable, as $f \leq 1$, and the minimum and maximum α occur on sets of zero dimension, which are of course the singularities associated with the paths down the tree corresponding to the symbol sequences $1, 1, 1, 1, \cdots$ and $1, 2, 1, 2, \cdots$ (and also with the sequences obtained from these by performing the permutation $1 \leftrightarrow 2$).

If the form (5.11) is used for $Q \geq 3$, then the correspondence is to the $d = 1$ Q-state Potts model. An important feature of the fact that the scaling index τ is meaningful for all values from negative to positive infinity is that antiferromagnetic interactions occur in the effective statistical models, and for the Potts case, the finite entropy per site of the ground state translates into a nonzero fractal dimension at one end (or both ends) of the $f(\alpha)$ spectrum. Figure 5.4 shows $f(\alpha)$ obtained for $Q = 4$

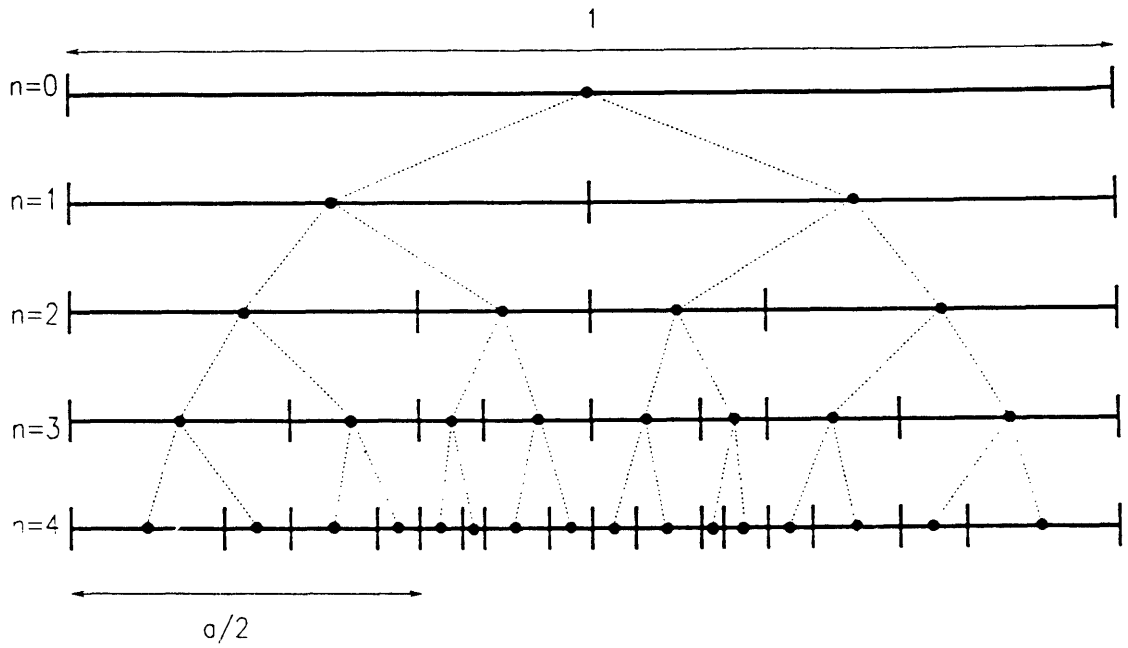

Figure 5.2: $Q = 2$ tree with $a = 0.667$, $b = 0.333$. The $q(\tau)$ for the fully developed cross-section corresponds to the free energy of the $d = 1$ Ising model.

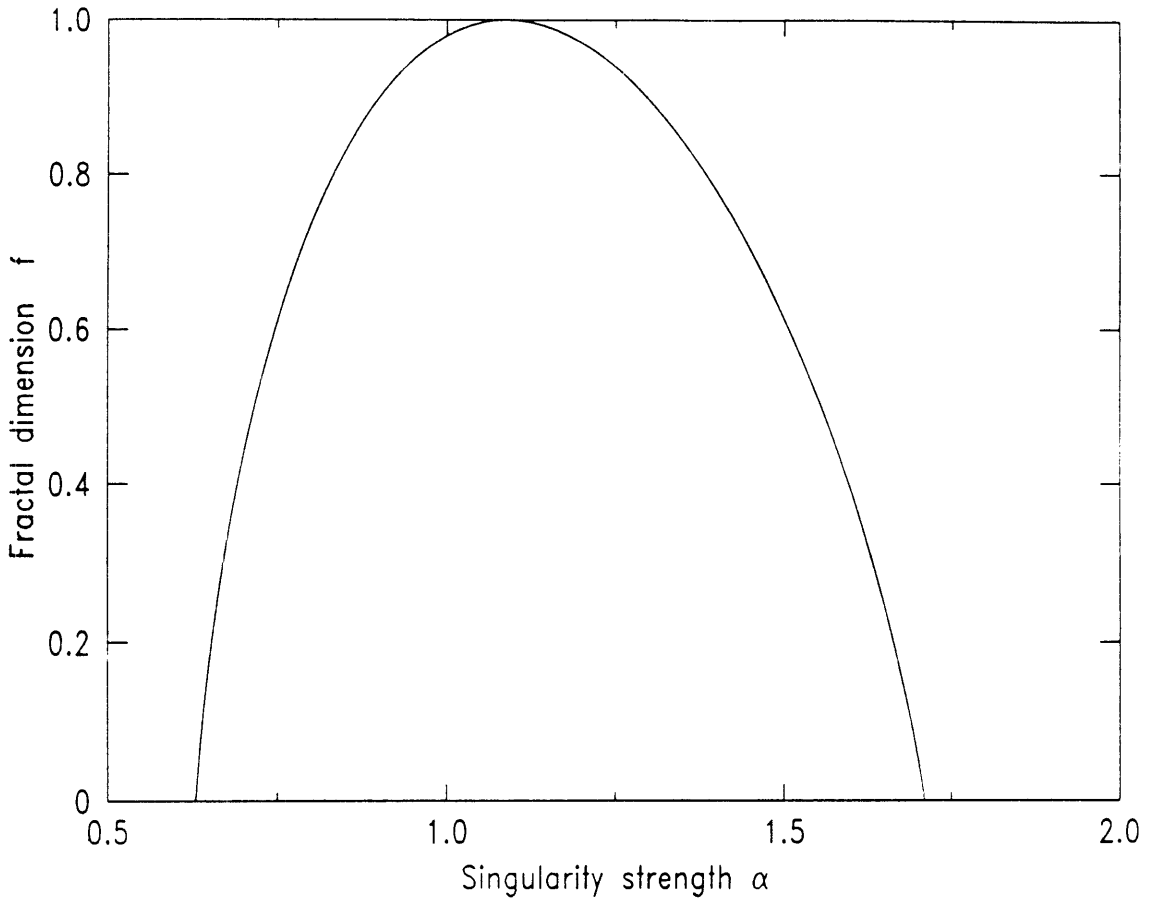

Figure 5.3: $f(\alpha)$ for the $Q = 2$ tree of Figure 5.2. Note that the different singularities are on sets bounded below by the dimension of the support, $d = 1$. Also, note that because $a + b = 1$ in this case, the fractal dimension of the set, or the maximum f, is also 1.

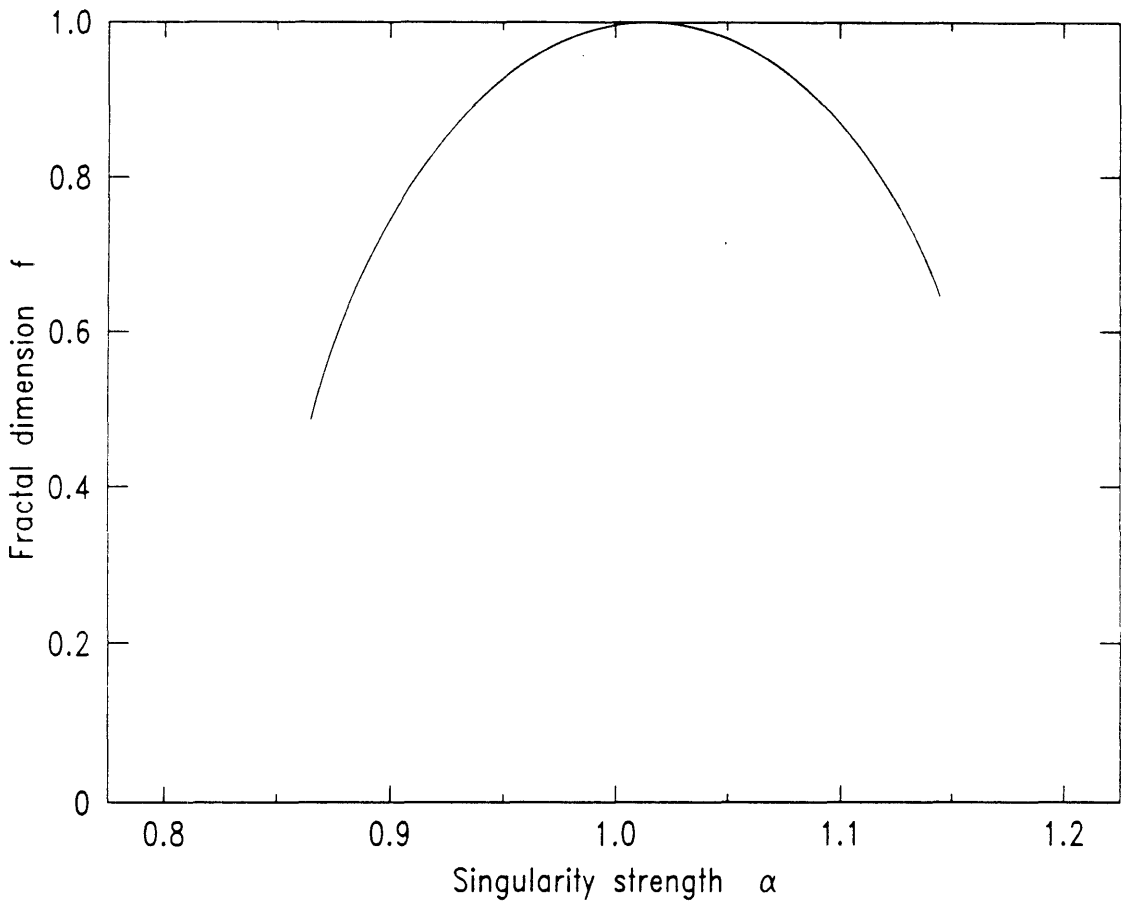

Figure 5.4: $f(\alpha)$ for the $Q = 4$ tree corresponding to the scaling function (5.13). Again the maximum f is 1, but the minimum f is nonzero due to the finite fractal dimension of the sets with maximum and minimum local scaling indices α.

using the scaling function

$$\sigma(s_{n+1}, s_n) = b + (a - b)\delta_{\bar{s}_{n+1},\bar{s}_n}, \tag{5.13}$$

where $\bar{s} = s \bmod 2$, for the case $a = 0.3$, $b = 0.2$. The $q(\tau)$ for trees with constant Q and with a scaling function $\sigma(s_{n+1}, s_n)$ which is invariant under Q-fold global permutations of the spins can be factored into a product of 'generators'[128], and is

$$q = (\log Q)^{-1} \log \sum_{s=1}^{Q} \sigma(s, s')^{-\tau} \tag{5.14}$$

Statistical models of this sort with a global permutation symmetry can have critical phase transitions. In the case of $d = 1$ models, this transition is observed at zero temperature, which corresponds to $\tau = \pm\infty$. Renormalization-group analysis of discrete-state models in $d = 1$ display zero-temperature unstable fixed points leading to a universal singular free energy of the form $e^{-\beta\Delta}$, where Δ is the energy gap between the ground and first excited state. This asymptotic behavior is also clear from (5.14).

This leads in the models described above to a $q(\tau)$ of the form

$$q(\tau) \approx C_{\pm}\tau + Ae^{-\Delta_{\pm}|\tau|}, \tag{5.15}$$

where c and Δ are constants that depend on the details of the scaling function. For the $Q = 2$ measure described above with the scaling function of (5.11), the asymptotic behavior of $q(\tau)$ is

$$q \approx C_{\pm}\tau + (\log 2)^{-1}e^{-\Delta|\tau|}, \tag{5.16}$$

where $C_+ = -\log(\min\{a, b\})/\log 2$, $C_- = -\log(\max\{a, b\})/\log 2$, and $\Delta = |\log(a/b)|$.

B. Analysis of the Two-Scale Tree

To determine whether this behavior described above can be identified through direct

Set size	1/l	C_+	Δ_+	C_-	Δ_-
4096	16	1.252	0.2016	0.7602	0.3340
	32	1.246	0.3201	0.7647	0.4166
	64	1.282	0.4822	0.7633	0.3145
	128	1.289	0.5498	0.7636	0.3110
	256	1.289	0.3193	0.7687	0.2956
	512	1.285	0.4355	0.7573	0.4368
65536	32	1.246	0.4135	0.7650	0.4151
	64	1.282	0.4817	0.7633	0.3145
	128	1.288	0.5439	0.7616	0.3160
	256	1.286	0.3138	0.7543	0.4777
	512	1.280	0.4211	0.7573	0.4368
	1024	1.299	0.5401	0.7596	0.3460
	2048	1.301	0.6022	0.7697	0.4244
exact		1.322	0.4055	0.7370	0.4055

Table 5.1: Constant-length partition analysis of $q(\tau)$ for the measure of (5.11) for the case $a = 0.6$, $b = 0.4$.

analysis of finite approximations of such a measure, we have generated refinements of the $Q = 2$ measure described by the scaling function (5.11) containing 2^{12} and 2^{16} points for the case $a = 0.6$, $b = 0.4$. We have solved $\Gamma(q, \tau) = 1$ numerically for partitions made up of boxes of constant length and constant measure (number of points). Least-squares fitting of the different $q(\tau)$ thus obtained to the form

$$q = C_\pm \tau + A_\pm e^{-\Delta_\pm |\tau|} \tag{5.17}$$

was done, resulting in the extracted C and Δ shown in Tables 5.1 and 5.2.

Set size	1/ p	C_+	Δ_+	C_-	Δ_-
4096	8	1.219	0.3975	0.8231	0.3848
	16	1.247	0.4018	0.8008	0.3861
	32	1.265	0.4175	0.7871	0.3873
	64	1.278	0.4492	0.7775	0.3877
	128	1.290	0.5039	0.7700	0.3854
	256	1.302	0.5562	0.7637	0.3778
65536	32	1.259	0.3907	0.7891	0.3848
	64	1.270	0.3953	0.7802	0.3856
	128	1.278	0.4055	0.7738	0.3866
	256	1.284	0.4266	0.7688	0.3884
	512	1.290	0.4657	0.7648	0.3908
	1024	1.295	0.5238	0.7613	0.3938
	2048	1.301	0.5925	0.7580	0.3965
exact		1.322	0.4055	0.7370	0.4055

Table 5.2: Constant-measure partition analysis of $q(\tau)$ for the measure of (5.11) for the case $a = 0.6$, $b = 0.4$.

The results that most clearly indicate the scaling behavior come from the constant-measure calculations. We find, based on these calculations, that in the constant-length case, $C_+ = 1.27 \pm 0.02$, $\Delta_+ = 0.40 \pm 0.08$, $C_- = 0.760 \pm 0.005$, and $\Delta_- = 0.37 \pm 0.06$. From the constant-measure calculations, we conclude that $C_+ = 1.27 \pm 0.01$, $\Delta_+ = 0.40 \pm 0.01$, $C_- = 0.77 \pm 0.01$, and $\Delta_\pm = 0.390 \pm 0.005$. These results indicate that from simple analysis of rough approximations to multifractal measures, the asymptotic behavior of $q(\tau)$ can be readily identified. It is important to keep in mind that the asymptotic behavior should not be studied in the regime where the calculation of $\Gamma(q,\tau)$ is dominated by boxes of a single length or a single measure. In this limit, the correction due to the next-to-leading box length or measure will always appear to be of the form (5.17).

C. Asymptotic Structure of the Critical Period-Doubling Attractor

We have applied this type of analysis to a study of the structure of the critical period-doubling attractor[120], which is a set with structure similar to the fully-developed tree cross-section studied above[132]. A finite realization of the set was obtained by generating iterates of $x = 0$ using the logistic map $f(x) = \lambda(1 - 2x^2)$ at the critical point $\lambda = 0.837005134\cdots$. The fractal dimension of the attractor[132] is $D_0 = 0.5380451435\cdots$, thus the constant-length boxing described above is not practical for computing $q(\tau)$ since most of the boxes will be empty. Much more suitable are the constant-measure partitions used by Halsey *et al*[128]. This natural measure is displayed in Table 5.5. The iterates of $x = 0$ under the critical map are at the endpoints of the intervals, and the ordering property that higher iterates are contained within the partition formed by the first 2^n iterates of $x = 0$ is apparent.

Constant-measure computations of $q(\tau)$ using this partition have been carried out, and fits to the form (5.17) result in the parameters displayed in Table 5.3. The values of $C_+ = \log(\alpha_{PD}^2)/\log 2$ and $C_- = \log(\alpha_{PD})/\log 2$ where $\alpha_{PD} = 2.502907875\cdots$, are known exactly[120]. and our estimates from the fit result of $C_+ = 2.60 \pm 0.02$ and

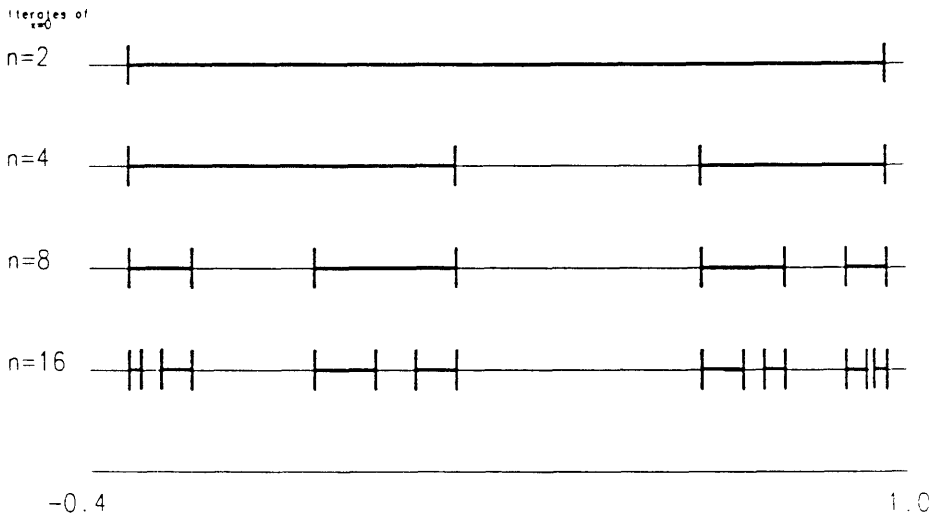

Figure 5.5: Constant-measure partition of the critical period-doubling attractor. The partitions constructed using the first $n = 2, 4, 8$, and 16 iterates of $x = 0$ are indicated. Note the property that the partitions form nested closed sets, and that each box thus contains a fraction $(n/2)^{-1}$ of the set.

1/p	C_+	C_-	Δ_-
1024	2.759	1.410	0.8056
2048	2.588	1.403	0.8052
4096	2.600	1.402	0.8047
8192	2.633	1.426	0.8037
exact	2.647	1.324	0.8087

Table 5.3: Asymptotic behavior of the period-doubling attractor. The exact values shown indicate the results discussed in the text.

$C_- = 1.41 \pm 0.01$ are reasonably consistent with these values. The value that we extract for the decay constant as $\tau \to -\infty$ is $\Delta_- = 0.805 \pm 0.001$. Recalling that $\Delta_- = |\log(a/b)|$ allows the interpretation of this constant as the ratios of the length rescaling factors dominant in the vicinity of the 'strongest' (largest α) singularity on the measure.

The renormalization-group approach allows an accurate numerical analysis of $q(\tau)$ to be done in the vicinity of $\tau = -\infty$[132]. The asymptotic behavior in this limit can be obtained analytically as

$$q(\tau) \approx (\log 2)^{-1}[\tau \log \alpha_{PD} + |a_1|^{-\tau}], \tag{5.18}$$

where $a_1 = -0.4454512238\cdots$ is the linear coefficient in the Taylor expansion of Feigenbaum's univeral function[120]. From comparison with (5.17), we obtain $\Delta_- =$

$\log(a_1) = 0.808667525\cdots$, which is in good agreement with our result obtained from the direct analysis of the measure. The behavior of $q(\tau)$ in the limit $\tau \to \infty$ is not as clear from either the RG or our numerical analysis, and we are continuing to try to understand it.

D. Effect of Uncorrelated Disorder on the Two-Scale Tree

The two measures analysed above are due to 'deterministic' growth, and satisfy exact local scaling laws. However, we expect randomness to play a role in many experimental realizations of multifractal trees. Here we introduce a disordered version of the two-scale tree studied previously. If there is a small amount of uncorrelated disorder, we find that the asymptotic behavior studied previously will be unchanged.

The disordered measure is similar to the two-level measure constructed above, except that the scaling function depends on the level of refinement n and the interval i introduced at that step. The scaling function is thus

$$\sigma(s_{n+1}, s_n, i) = b_{n,i} + (a_{n,i} - b_{n,i})\delta_{s_{n+1}s_n}, \tag{5.19}$$

where $a_{n,i} + b_{n,i} \leq 1$ and $a_{n,i}$ and $b_{n,i}$ are positive. In the case of uncorrelated disorder treated here, $a_{n,i}$ and $b_{n,i}$ are independent random variables with some distribution $P(a,b)$, where $\int dadbP(a,b) = 1$. The $q(\tau)$ thus defined self-averages, and is explicitly

$$q(\tau) = \int_0^1 da \int_0^1 dbP(a,b) \log(a^{-\tau} + b^{-\tau})/\log 2. \tag{5.20}$$

The self-averaging over the probability distribution and the simple form are properties of the independence of the random variables for different n. The same form follows when the random variables are of the form $a_{n,i} = a_n$, $b_{n,i} = b_n$.

We have considered the particular case where

$$\begin{aligned} P(a,b) &= (a_1 - a_0)\delta(b - 1 + a), a_0 < a < a_1 \\ &= 0, \text{otherwise}, \end{aligned} \tag{5.21}$$

with $0 < a_0 < a_1 < 1/2$, and where δ is the Dirac delta. As $\tau \to \pm\infty$, q behaves as

$$\begin{aligned} q &\approx C_{\pm}\tau, \text{where} \\ C_+ &= \frac{-1}{(a_1 - a_0)\log 2}\int_{a_0}^{a_1} dx \log x \\ C_- &= \frac{-1}{(a_1 - a_0)\log 2}\int_{a_0}^{a_1} dx \log(1 - x). \end{aligned} \tag{5.22}$$

The approach to the limiting slope is more difficult to determine analytically, but since the part of $q(\tau)$ that remains after the linear piece is removed is of the form

$$q - C_{\pm}\tau = \frac{-1}{(a_1 - a_0)\log 2}\int_{a_0}^{a_1} dx \log(1 + [x/(1-x)]^{\pm\tau}), \tau \to \infty \tag{5.23}$$

we can bound the decay to the linear limit between the exponentials $[a_0/(1-a_0)]^{|\tau|}/\log 2 < q - C_{\pm}\tau < [a_1/(1-a_1)]^{|\tau|}/\log 2$, as $|\tau| \to \infty$. This suggests that the observed decay will also be exponential, somewhere between these limits. Numerical integration of the function (5.23) leads to a confirmation of this: for $a_0 = 0.2$ and $a_1 = 0.4$, we observe that $q - C_{\pm} \approx e^{-\Delta|\tau|}$ as $\tau \to \pm\infty$, with $\Delta = 0.44 \pm 0.01$.

We have calculated $q(\tau)$ from 2^{12}- and 2^{16}-point realizations of this measure, and the results for the asymptotic behavior that we have extracted from constant-length and constant-measure partitions are shown in Tables 5.4 and 5.5, respectively. These results indicate that, as in the uniform case, there is a scaling range of length or measure in which consistent results are obtained. This is a direct indication of the self-averaging of the scaling, as these results have been obtained from a single realization of this random measure. From the constant-length analysis, we estimate $C_+ = 1.86 \pm 0.03$, $\Delta_+ = 0.36 \pm 0.14$, $C_- = 0.55 \pm 0.01$, and $\Delta_- = 0.3 \pm 0.1$. From the constant-

Set size	1/l	C_+	Δ_+	C_-	Δ_-
4096	16	2.016	0.6384	0.5773	0.3586
	32	1.834	0.3722	0.5444	0.2178
	64	1.974	0.5201	0.5455	0.7238
	128	1.762	0.1776	0.5834	0.5369
	256	1.851	0.2977	0.6667	0.5344
	512	1.897	0.3889	0.7500	0.5938
65536	32	1.835	0.3725	0.5440	0.1838
	64	1.976	0.5208	0.5485	0.6154
	128	1.762	0.1720	0.5386	0.3603
	256	1.853	0.3059	0.5553	0.2202
	512	1.900	0.3935	0.5625	0.4751
	1024	1.812	0.3165	0.6250	0.5249
	2048	1.882	0.3793	0.6875	0.5564
exact		1.765	0.44(1)	0.5195	0.44(1)

Table 5.4: Results of analysis of constant-length calculations of $q(\tau)$ for the disordered measure. The values marked 'exact' are obtained from the computations outlined in the text.

Set size	1/ p	C_+	Δ_+	C_-	Δ_-
4096	8	1.842	0.6485	0.6363	0.1778
	16	1.787	0.8100	0.6164	0.6187
	32	1.730	0.4645	0.5834	0.2829
	64	1.819	0.3944	0.5900	0.5484
	128	1.795	0.4113	0.5777	0.3448
	256	1.764	0.3584	0.5474	0.3781
65536	32	1.730	0.4392	0.5911	0.2823
	64	1.819	0.3919	0.5875	0.5304
	128	1.795	0.4018	0.5879	0.5039
	256	1.764	0.3663	0.5590	0.4284
	512	1.720	0.2955	0.5379	0.3960
	1024	1.737	0.4134	0.5311	0.3679
	2048	1.762	0.3258	0.5403	0.3614
exact		1.765	0.44(1)	0.5195	0.44(1)

Table 5.5: Results of analysis of constant-measure calculations of $q(\tau)$ for the disordered measure. The values marked 'exact' are obtained from the computations outlined in the text.

measure calculations, we find $C_+ = 1.76 \pm 0.03$, $\Delta_+ = 0.37 \pm 0.05$, $C_- = 0.57 \pm 0.01$, and $\Delta_- = 0.46 \pm 0.05$. The constant-measure results, in addition to having smaller errors on the $\Delta_\pm$, are in better agreement with the results $C_+ = 1.765$, $\Delta_\pm = 0.44$, and $C_- = 0.5195$ obtained numerically from (5.22) and (5.23).

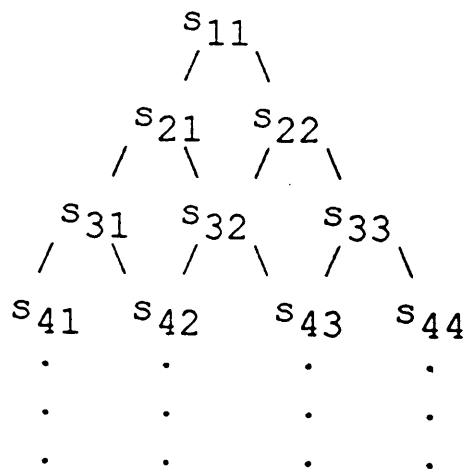

Figure 5.6: Comparison rule for $d = 2$ model. Lines represent δ's.

5.2.5 A Tree Corresponding to a $d = 2$ Statistical Model with Finite-τ Critical Behavior

We conclude this study with a speculative generalization of the trees discussed in the preceeding section. We begin with the observation that trees for which $\log Q_n$ increases as n^{d-1} can be related to statistical models in d dimensions. Consider a case where the branches split into 2^n offspring at the nth step: to label these new branches, n new 2-state symbols must be introduced to code the structure, denoted as a 'row' $\{s_{n,1}, s_{n,2}, \cdots, s_{n,n}\}$. One simple scaling function to relate the nth and $n+1$th interval lengths is

$$\sigma(\{s_{n+1,1}, \cdots s_{n+1,n+1}\}, \{s_{n,1}, \cdots s_{n,n}\} = \exp(-G_n + K \sum_i [\delta_{s_{n,i}s_{n+1,i}} + \delta_{s_{n,i}s_{n+1,i+1}}]), \tag{5.24}$$

where the δ's are Kronecker delta symbols, and G_n grows quickly with n to crush the many new intervals of each iteration into the parent intervals. This scaling function can be interpreted as assigning the lengths according to a comparison of successive rows of symbols, as shown in Figure 5.6.

A suitable G_n is

$$G_n = (n+1)\log 2 + 2n|K|, \tag{5.25}$$

which leads to a $q(\tau)$ for the fully developed set of the form

$$q\log 2 = \tau(2|K| + \log 2) + \psi(-\tau K), \tag{5.26}$$

where $\psi(J)$ is the free energy per site of the $d = 2$ square-lattice Ising model. This can be expressed as the integral[133]:

$$\psi(J) = \log(2\cosh 2J) + \int \frac{d\theta}{2\pi} \log[(1 + \sqrt{1 - x^2 \sin^2\theta})/2], \tag{5.27}$$

where $x = 2\tanh 2J/\cosh 2J$.

Figure 5.7 shows the first few levels of growth of this tree for the case $e^K = 1.092$. As can be seen from this picture, the branching rate grows exponentially with the growth. From the above analytical result, we can compute the $f(\alpha)$ shown in Figure 5.8. It has the usual convex shape, and has a range of singularities residing on sets of dimension between 0 and about 0.8. The shapes of this curve and the corresponding $q(\tau)$ do not indicate the nonanalyticities that occur near $\alpha = 0.93$ and $\alpha = 0.72$ which correspond to the ferromagnetic and antiferromagnetic critical points of the underlying statistical model. The nonanalyticity is best revealed in a plot of α *vs* τ, which corresponds to a plot of the internal energy of the model as a function of inverse temperature. Figure 5.9 reveals the phase transition plainly as a divergence in the slope $\alpha(\tau)$. An easy test for this sort of a phase transition in a multifractal spectrum is thus simply to examine $\alpha(\tau)$.

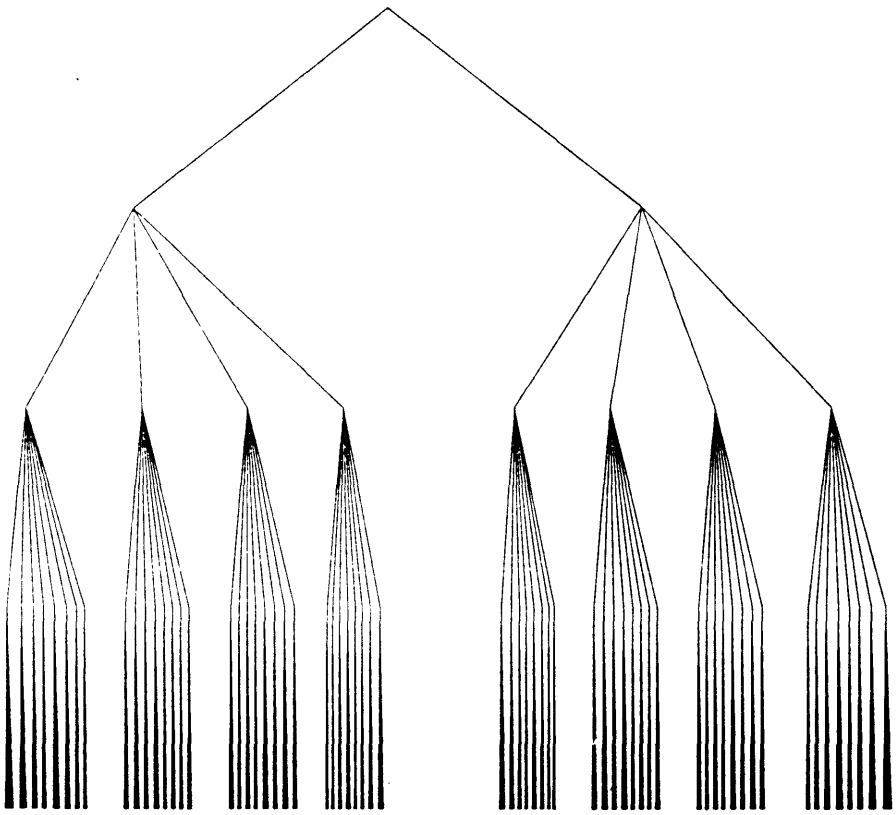

Figure 5.7: Tree corresponding to $d = 2$ Ising model after three tip splittings.

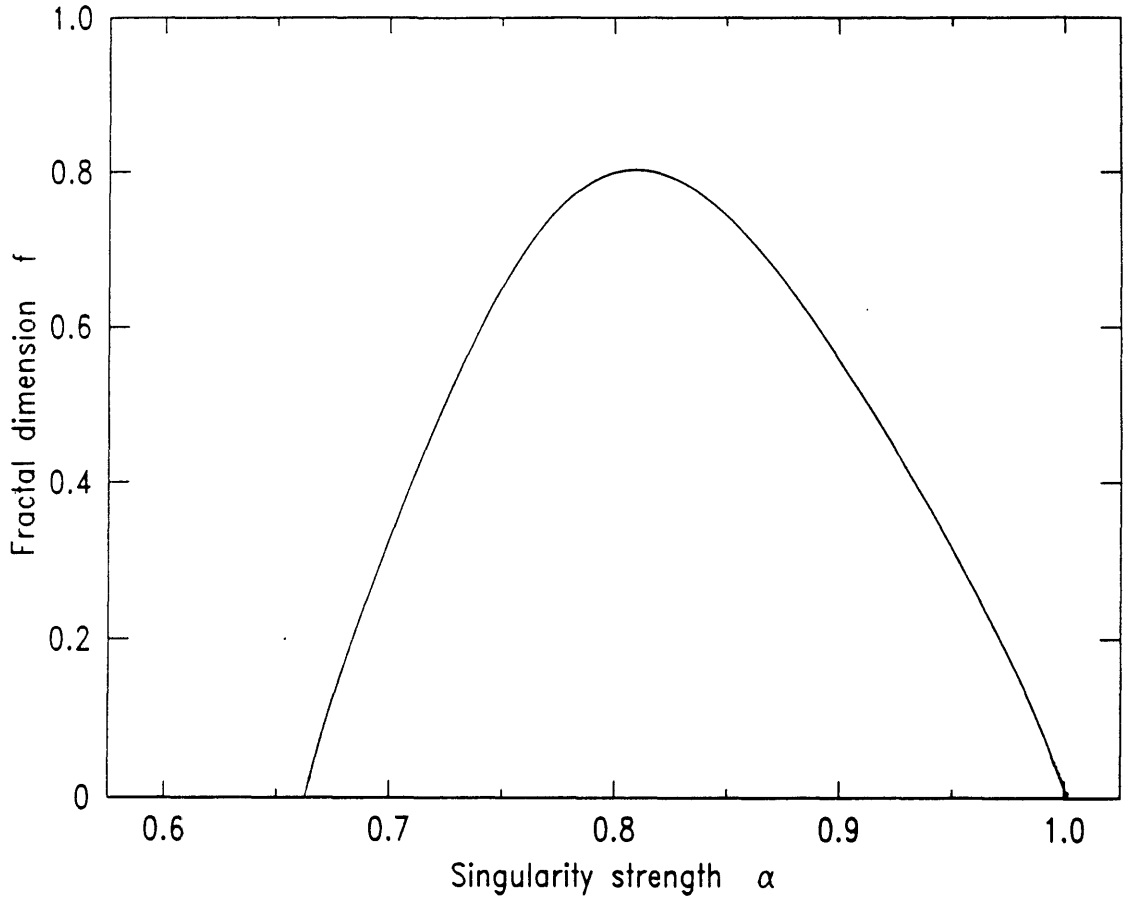

Figure 5.8: $f(\alpha)$ for the tree of Figure 5.7.

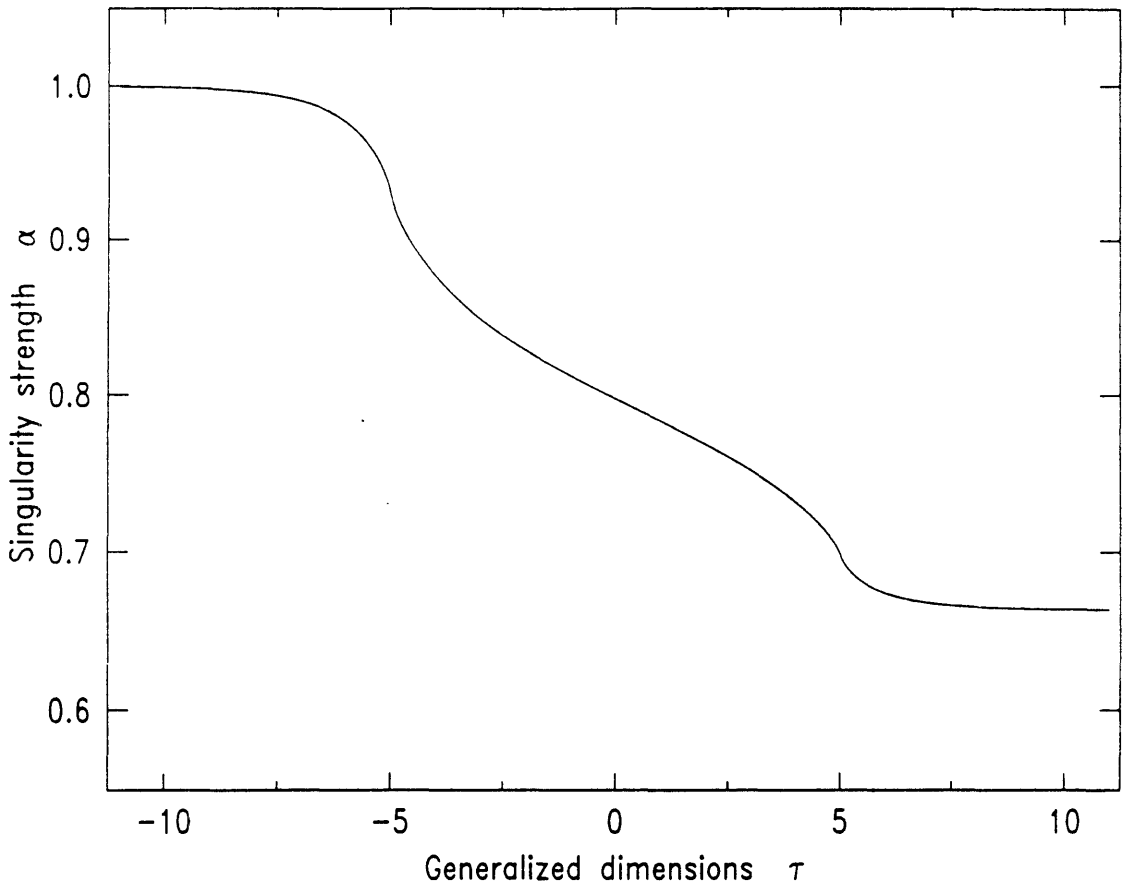

Figure 5.9: $\alpha(\tau)$ for the tree of Figure 5.7. The divergences in the slope of this function correspond to critical phenomena in the underlying $d = 2$ Ising model.

5.2.6 Summary and Perspectives

In this Section, we have presented a general approach to the study of trees which asymptotically develop multifractal cross-sections. The generic behavior of $q(\tau)$ for these models as $\tau \rightarrow \infty$ is an exponential approach to the limiting linear asymptote. This exponential approach can be interpreted as due the contribution of low-lying excitations to the free energy of an equivalent statistical-mechanical model.

We have found that from direct analysis of relatively coarse finite approximations to these measures, one can extract this 'energy gap' which corresponds to the ratio of the leading and next-to-leading rescalings associated with the strongest (or weakest) singularities on the measure. For the period-doubling attractor, this analysis allows results of the RG calculation of Bensimon *et al* to be interpreted in a new, geometrical way, and allows a better understanding of the singularities on the measure that are important in the limit $q \rightarrow -\infty$. It would be worthwhile to study the $q \rightarrow \infty$ limit of the period-doubling attractor in order to compare the structure of the corrections to the singularities dominant in that limit as well.

The effect of uncorrelated disorder has been found to be minimal on the measures considered above. Disorder of this sort completely self-averages, and the asymptotic behavior continues to be of the form of an exponential approach to the linear limit. We are planning to study correlated disorder of the sort recently applied to transport phenomena in random media[134]. It would be interesting to know if the type of disorder in a scale-invariant structure can be identified by examining the asymptotic behavior of $q(\tau)$.

Applications of the analysis techniques and models presented in this Section include the further study of well-known multifractal measures such as those encountered in the study of dynamical systems, but we believe that the utility of this approach lies in the diagnosis of the different scalings that are important for measures that are less well understood. Growth probability measures for diffusion-limited aggregation[122] are not well understood, and the examination of the asymptotic behavior of $q(\tau)$ for

these objects might well give some insight into the structure of these measures, as well as giving guidance to the current effort being aimed at constructing dynamical RG theories of the growth[135]. Of special interest is the peculiar breakdown of the convergence of the $\tau(q)$ for negative q, which is interpreted as a type of phase transition[136].

An interesting application of these ideas is to the description of the scaling properties of disintegration processes. Consider a solvent, in which there is a weak solution of a long polymer, and a cutting enzyme. The polymer, and later its daughter fragments, are cut randomly. As this uncorrelated disintegration process is allowed to proceed, the distribution of the lengths (masses) of the fragments will satisfy exactly calculable and nontrivial scaling laws related to the random measure model introduced here. We are beginning to study the scaling of this dilute-limit dynamics. A light-scattering experiment on such a system should allow direct access to the distribution of fragments, and thus to its multiscaling properties.

Finally, we note that the geometrical object corresponding to the $d = 2$ Ising model is a bizzare geometrical object in search of an experimental realization. Perhaps the most important lesson that it teaches us is to consider $\alpha(\tau)$, as this sort of phase transition is invisible in either $f(\alpha)$ or $\tau(q)$. We note that experimental realizations of this sort of object might not require the splitting Q_i to increase at an exponential rate if the interactions grow in 'range' (of the dependence of σ on preceeding symbols) as the growth proceeds. The saving grace is that the usual mechanisms of universality will come into play and govern any type of nonanalyticity that is observed. Thus, the identification of important symmetries and 'dimensionalities' corresponding to dynamics underlying tree growth is of great importance.

One of us (JFM) would like to thank S. Zaleski for his instruction and guidance during the early stages of this work, and both of us thank A. N. Berker for his steadfast support and encouragement.

This research was supported by the National Science Foundation under Grant

No. DMR-87-19217, and by the Joint Services Electronics Program under Contract No. DAAL 03-89-C0001. Parts of this work have been published in the Materials Research Society Extended Abstracts[14], and by the Massachusetts Institute of Technology[15].

5.3 Multiscaling Analysis of Critical Phenomena

The recent development of ideas concerning the scaling properties of strange sets has included an explosion of work on the study of the scaling of moments of singular measures. If we consider a measure (distribution) $d\mu$, and cover its support with boxes $\{B_l^{(i)}\}$ of some characteristic size l, we can compute the sum of powers of the integrals of the measure in the boxes:

$$S(l,q) = \sum_i M_i^q, \tag{5.28}$$

where $M_i = \int_{B_l^{(i)}} d\mu$. If the measure is scale invariant, we expect that the dependence of $S(l,q)$ is a power law:

$$S(l,q) \approx l^\tau, \tag{5.29}$$

for l much larger than any microscopic cutoff, but much smaller than any macroscopic scale. The exponent τ depends on q, and it has been shown that in many cases, the function $\tau(q)$ can be related to the spectrum of singularities $f(\alpha)$ which describes the fractal dimension f of points at which the measure has a local power law singularity described by the exponent α[128].

This picture has been applied to many different types of scale-invariant strange objects including attractors of dynamical systems at the edge of chaos[120, 121], and the growth probability measure of diffusion-limited aggregation[122]. However, to date no application of these ideas has been made to our oldest example of a complex scale invariant pattern, critical phenomena. Here I report some preliminary results of multiscaling analyses of two-dimensional critical phenomena. Through the analysis of Monte-Carlo simulations of critical spin systems, I have found that the function $\tau(q)$ is not linear. I present a framework for the study of this phenomenon and I present a preliminary interpretation for the results.

Consider an isotropic, homogeneous spin system on a d-dimensional hypercubic lattice at its critical point. The magnetization field $m(\mathbf{x})$ is assumed to have scale-

invariant correlations, and to satisfy $< m(\mathbf{x}) >= 0$ for all points $\mathbf{x}$. We apply the sum (5.28) to the measure $d\mu = dm$. The boxes are taken to be d-dimensional cubes a length l on each edge, and we assume the unit of length to be the lattice constant. We are interested in the limit $0 \ll l \ll L$, where L is the size of the entire system. In this limit, we expect the scaling law (5.29) to hold, since l is the only length scale in the problem. The number of boxes needed to cover the system is $(L/l)^d$, leading to the usual result that $\tau(q = 0) = -D_0$, the dimension of the support (in this case, the space dimension, d). For even moments of the measure, (5.28) is well-defined, but for other q, we must replace M_i with $|M_i|$, since the magnetization fluctuates around zero. This is an important modification of the usual multifractal formalism, as the sum of the $q = 1$ moments is no longer equal to the integral of the measure over the entire set. The lack of this additivity property will change the behavior of the resulting $\tau(q)$ markedly.

In order to compute the $\tau(q)$ thus defined for the simplest model of critical phenomena, the two-dimensional Ising model, I have undertaken Monte Carlo simulation of the square-lattice model at criticality. The usual Metropolis simulation method was used, with an equilbration period of 10000 steps per site, and then the spins were studied every 200 steps per site beyond that point. Fluctuations of the bulk magnetization and the total energy around the exactly known critical values were observed, indicating that equilibrium was reached. Figure 5.10 shows a typical spin distribution for a 256×256 system.

For 100 spin configurations thus studied for the 256×256 system, the values of the sums of the moments $S(l, q)$ were computed as described above for a variety of box edge sizes l, and the logarithms of the resulting sums *vs* $\log_2 l$ are shown for a variety of q in Figure 5.11. Fits of the data to the power-law form (5.29) are shown, and there is good evidence for scaling over a restricted range of l. In order to extend the scaling region, I have studied a 1024×1024 site system, using the same equilibration time (10000 MCS/S) and number of steps (200 MCS/S) between analyses. 40 snapshots of

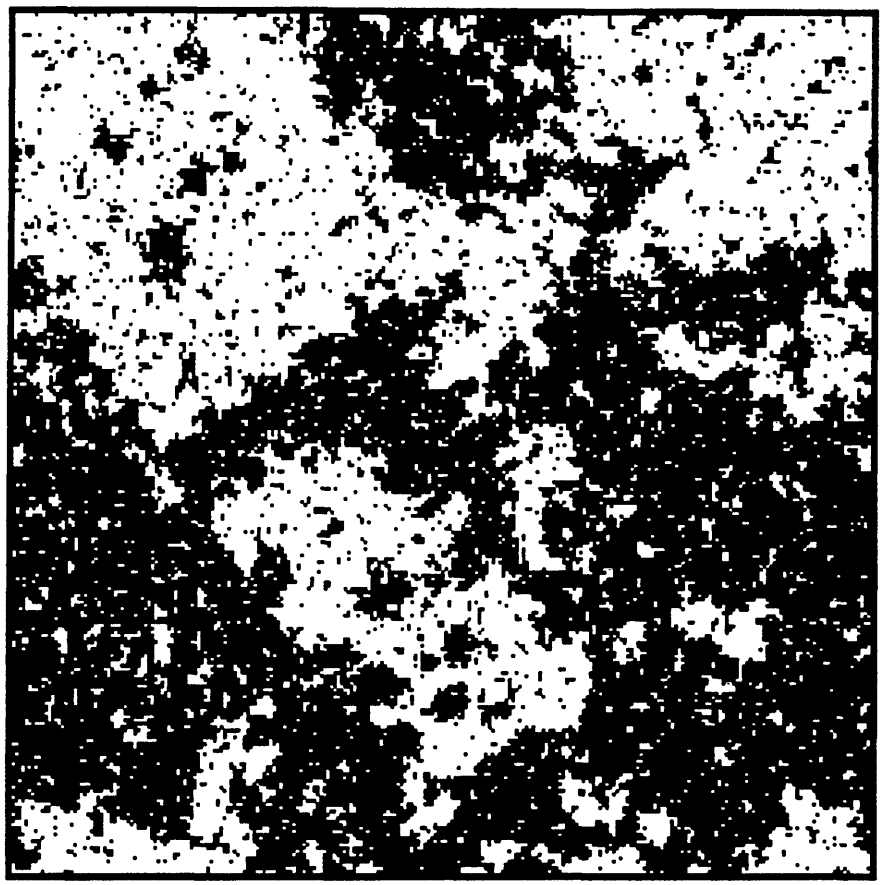

Figure 5.10: 256 × 256 site Ising model at criticality. Up and down spins are represented by black and white regions. The lack of a characteristic size to the fluctuations is evident.

this large system were studied, with results for $S(l,q)$ shown in Figure 5.12. A larger scaling range is seen, extending from $l = 4$ to $l = 64$, which leads me to conclude that indeed, the power-law scaling expected is observed.

From the fits shown in Figures 5.11 and 5.12, the exponents τ for different q have been extracted, as shown in Figure 5.13. Included are results obtained from simulation of the triangular lattice Ising model obtained by placing a second-neighbor bond on each elementary plaquette of the square lattice, and changing the coupling strength to that for the critical triangular model. The equilibration, data taking, and analysis for the triangular model was identical to that for the 256×256 site square-lattice model.

Extremely good agreement for positive q is observed between the results of the two square and the the triangular models considered. Although this $\tau(q)$ is nearly straight, the small error bars of these results allow the derivative $d\tau/dq$ to be computed, and nonlinear behavior is evident, as shown in Figure 5.14. Slight differences are seen between the three sets of results, but the qualitative feature that the slope increases rapidly as q increases from zero, and then saturates to a value near 1.875 beyond $q = 4$ is shared. Table 5.6 lists the $\tau(q)$ for the different models for several values of q. The values and errors are the averages and standard deviations of the set of $\tau(q)$ obtained from analysis of each 'snapshot' of a particular run.

An important difference between the $\tau(q)$ here and that associated with singular measures is that here, $d\tau/dq$ increases with q. This is a consequence of the non-additivity of the integrals of the magnetization: this should be contrasted with the usual application to multifractals where $d^2\tau/dq^2$ is always negative[127]. Correspondingly, the function $f(\alpha)$ related by the Legendre transformation of $\tau(q)$[128] has no geometrical interpretation.

A first approach to considering these moments is to treat the case of even integer

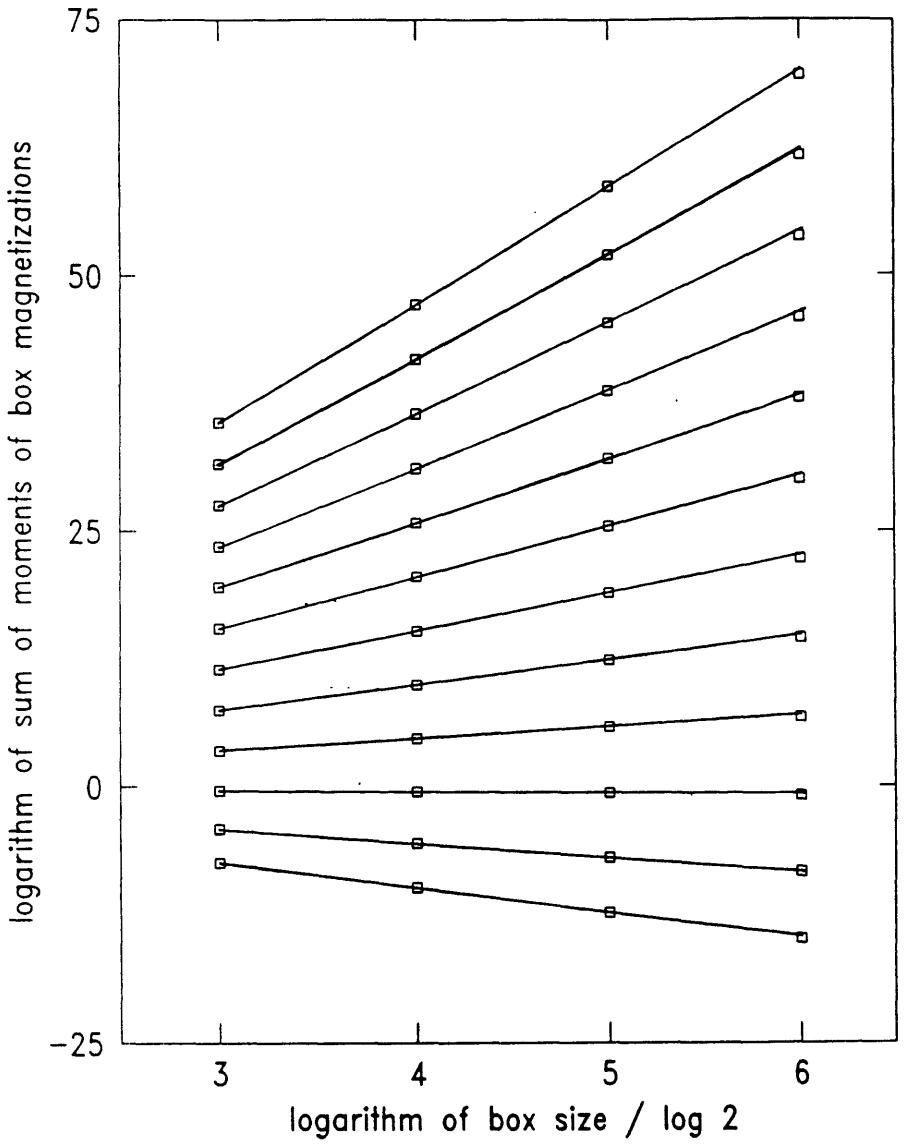

Figure 5.11: Logarithm of $S(l,q)$ *vs* $\log_2 l$ for 256×256 Ising model data. Data for $q = -1, 0, 1, 2, \cdots, 10$ are shown from the bottom to the top of the figure. Open squares indicate the MC results, and lines represent the fits to the form $a + \tau \log l$, which correspond to the power laws $S(l,q) \approx l^{\tau}$. The error bars on the MC results are smaller than the boxes shown, and thus the MC results are in good agreement with the proposed scaling.

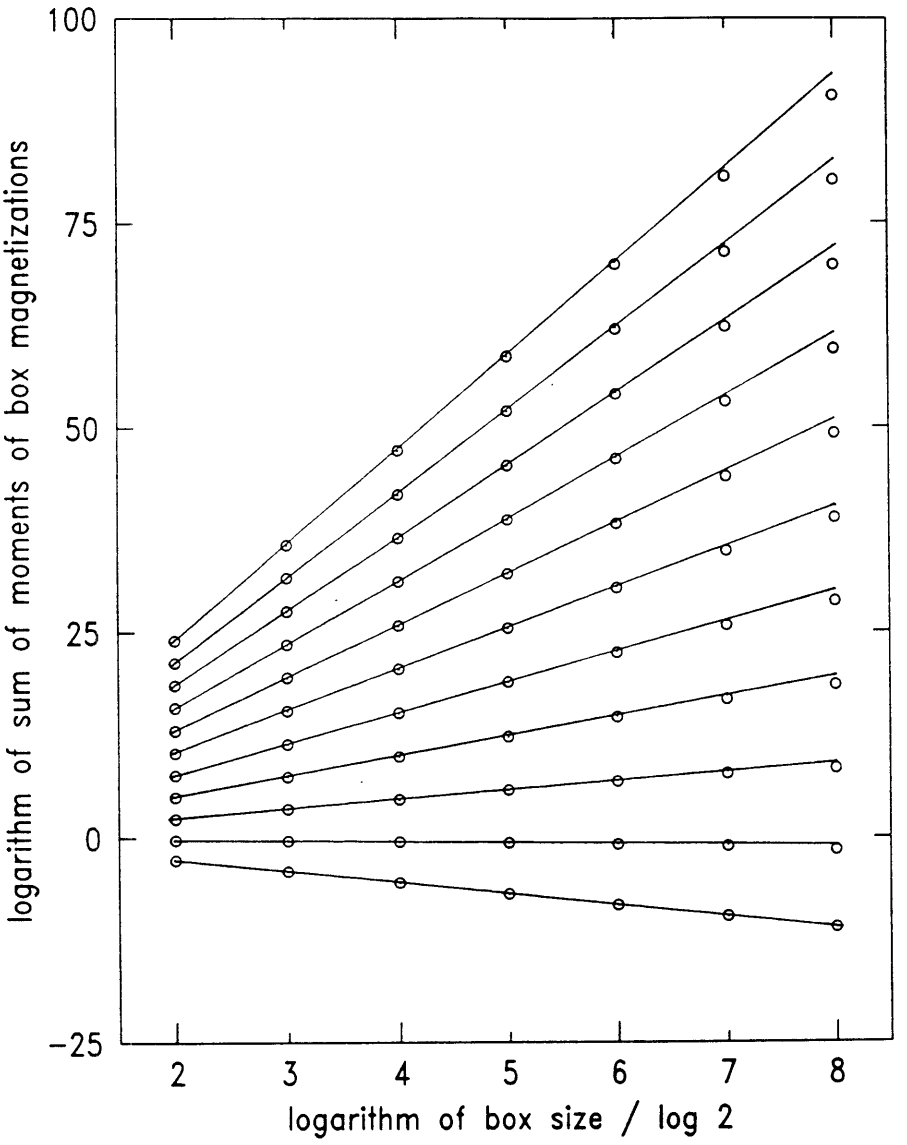

Figure 5.12: Logarithm of $S(l,q)$ *vs* $\log_2 l$ for 1024×1024 Ising model data. Data from $q = 0$ to $q = 10$ in steps of 1 are shown from the bottom to the top of the figure. Circles indicate the MC results, and points represent the fits as in the 256×256 case. Good agreement of the MC data with the proposed scaling is observed.

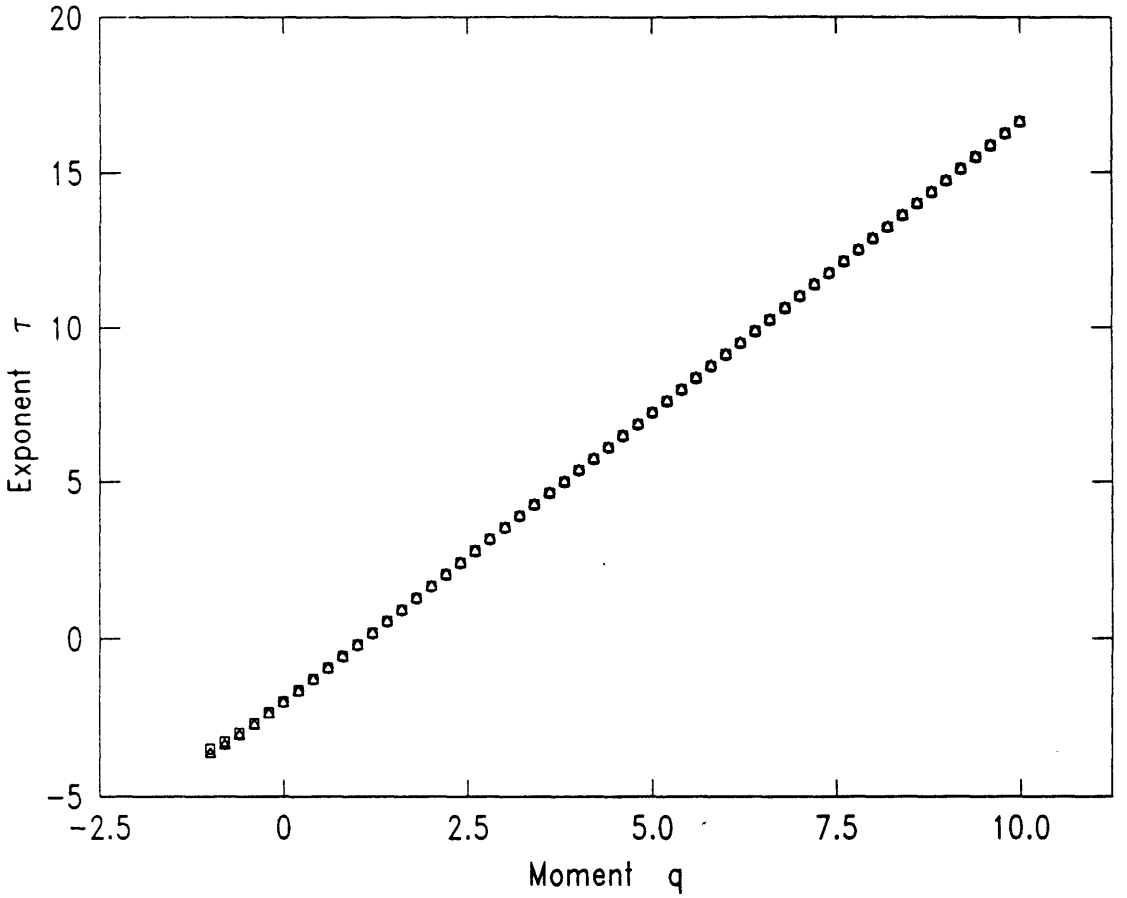

Figure 5.13: Moment scaling exponents τ for q between -1 and 10 for the critical two-dimensional Ising model. Squares indicate the 256 × 256 results, while circles indicate results from the 1024 × 1024 simulations. Triangles indicate results from the 256 × 256 site critical triangular model obtained by placing one second-neighbor bond on each elementary square plaquette. All of these results are in extremely good agreement for $q > 0$. Error bars on these results are smaller than the symbols.

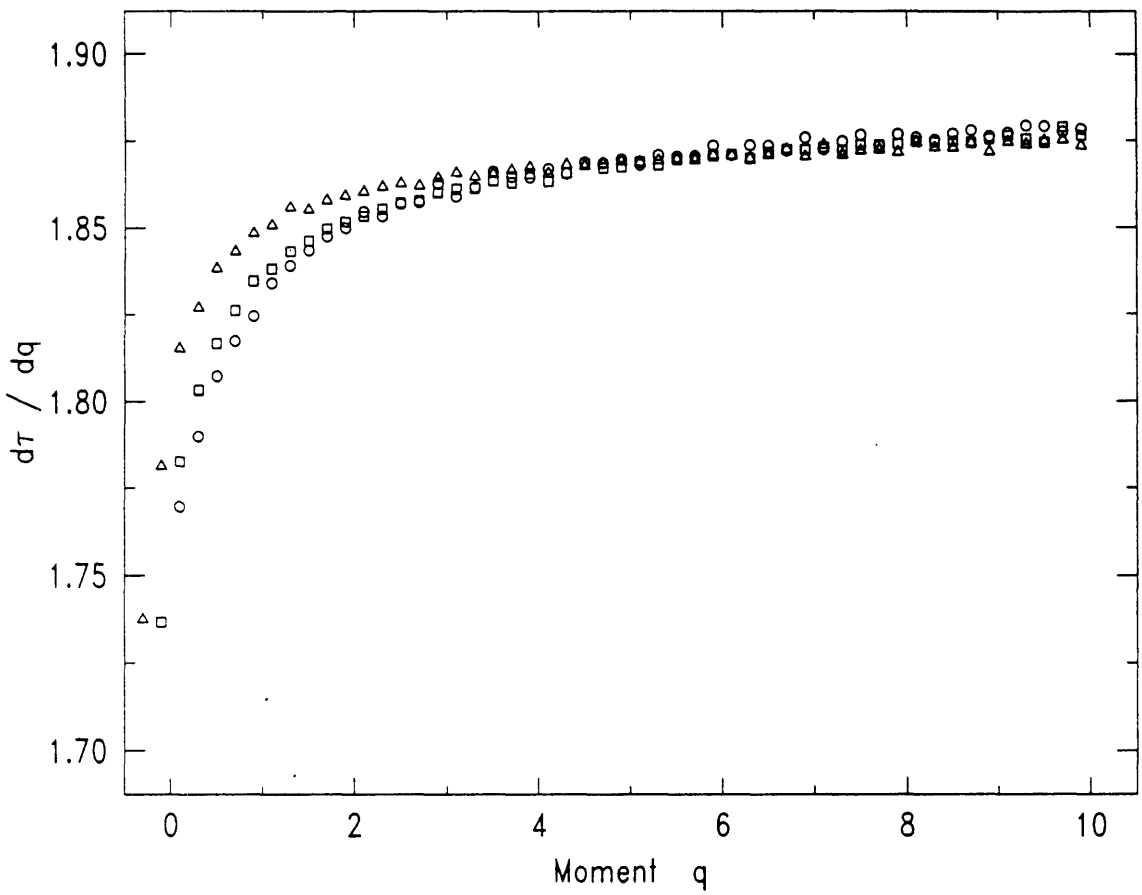

Figure 5.14: Derivative of $\tau(q)$ from Ising model MC results. Squares, circles, and triangles are results from the 256×256 square lattice, the 1024×1024 square lattice, and the 256×256 triangular lattice studies, respectively. The two square lattice simulations lead to nearly identical results, while the triangular lattice results appear to be quantitatively slightly different for small q. The data are all in excellent agreement beyond $q = 4$. The fact that all the curves approach 1.75 as $q \to 0$ is discussed in the text.

q	τ			
	256 x 256 square MC	256 x 256 triangular MC	1024x1024 square MC	1.875 q - 2
0	-2	-2	-2	-2
1	-0.18(4)	-0.16(5)	-0.194(8)	
2	1.66(6)	1.70(8)	1.648(12)	1.75
3	3.52(8)	3.56(10)	3.506(15)	
4	5.38(9)	5.43(11)	5.369(17)	5.5
5	7.24(11)	7.29(13)	7.237(20)	
6	9.12(12)	9.16(14)	9.108(22)	9.25
7	10.99(13)	11.04(15)	10.98(2)	
8	12.86(13)	12.91(16)	12.86(3)	13
9	14.74(14)	14.78(16)	14.73(3)	
10	16.62(15)	16.66(17)	16.61(3)	16.75

Table 5.6: τ *vs* q for the $d = 2$ critical Ising model magnetization. The first three columns represent data from MC simulation of the 256×256 square lattice, the 1024×1024 square lattice, and the 256×256 triangular lattice models, respectively. The errors quoted are the standard deviations of the τ's obtained from fits for each of the 'snapshots' in each MC run. The fourth column is the value taken by the formula $-2 + 1.875q$ discussed in the text.

q greater than 2. In this case, we can rewrite (5.28) as

$$S(l,q) = \sum_i \int_{B_l^i} d\mathbf{x}_1 m(\mathbf{x}_1) \int_{B_l^i} d\mathbf{x}_2 m(\mathbf{x}_2) \cdots \int_{B_l^i} d\mathbf{x}_q m(\mathbf{x}_q) \tag{5.30}$$

If we consider a large system, the sum over boxes corresponds to a sum over all possible magnetizations of a single box weighted by the usual Boltzmann factor, and thus we write (5.30) as

$$S(l,q) = (\frac{L}{l})^d < \int_{B_l} d\mathbf{x}_1 \cdots d\mathbf{x}_q m(\mathbf{x}_1) \cdots m(\mathbf{x}_q) >, \tag{5.31}$$

where the <> represent the thermal average.

The result[7] that

$$< m(\mathbf{x}_1/b) \cdots m(\mathbf{x}_q/b) >= q b^{x_h} < m(\mathbf{x}_1) \cdots m(\mathbf{x}_q) > \tag{5.32}$$

for well separated points $\mathbf{x}_i$ suggests the result

$$S(l,q) = L^d l^{-d+q(d-x_h)}, \tag{5.33}$$

where $x_h = d - y_h$ is the scaling dimension of the magnetization. For the $d = 2$ Ising model, $x_h = 0.125$, which suggests that for even $q > 2$, $\tau = -2 + 1.875q$.

This formula is in fair agreement with the results of Table 5.6 for the largest values of q studied, but for smaller q, the MC results are significantly below this result. The slope $d\tau/dq$ of Figure 5.14 is seen to be approximately $y_h = 1.875$ for $q \approx 10$, but for smaller q, it is significantly smaller. The failure of the law (5.33) is due to one of three causes: first, the step from (5.30) to (5.31) may not be valid for the critical system. The second possible cause is that because the integral over the q-point function (5.32) brings the $\mathbf{x}_i$ near each other, different scaling laws may be seen due to the operator products[7]. Finally, the scaling law (5.33) may be indeed correct, and the MC results may be slowly convergent with increasing system size.

Below $q = 2$, $d\tau/dq$ is definitely less than $d - x_h = 1.875$. If the function $\tau(q)$ is analytic in a region $q \geq 0$, we can formulate a cumulant expansion in terms of the quantities $L_l^{(i)} = \log|M_l^{(i)}|$:

$$\begin{aligned} \tau \log l &\approx \log S(l,q) = \log[\sum_i e^{qL_l^{(i)}}] \\ &= d(\log L - \log l) + \log[1 + (l/L)^d \sum_i (e^{qL_l^{(i)}} - 1)] \\ &= d(\log L - \log l) + q < L_l > + \frac{1}{2} q^2 < (L_l - < L_l >)^2 > + \mathcal{O}(q^3), \end{aligned} \tag{5.34}$$

where the averages are defined as $< X >= (l/L)^d \sum_i X^{(i)}$. Unlike the case of the application of this formalism to singular measures, the logarithms $L_l^{(i)}$ are all bounded (for positive q, boxes with zero measure do not play a role), and thus these moments are well defined. In particular, the fact that the second moment is positive indicates that $d^2\tau/dq^2$ will always be positive or zero for this type of scaling analysis.

Thus, the slope of $\tau(q)$ as $q \to 0$ is the average of the logarithm of the magnetization of the boxes of edge l, a result familiar as the replica method used in the study of quenched disorder[137]. Since the magnetization of a 'droplet' of size l is known to scale[5] as $M_l \approx l^{2-\eta}$, it seems reasonable that

$$< L_l >= (2 - \eta) \log l, \tag{5.35}$$

although to arrive at this result, an assumption concerning the average of the logarithms of the magnetizations analogous to the step leading to (5.31) is implicit. Interestingly enough, $d\tau/dq$ for $q = 0$ is in good agreement with this result for the $d = 2$ Ising case, where $2 - \eta = 1.75$, as can be seen from Figure 5.14.

Recent results suggest that the critical $d = 2$ Ising model is a tricritical point in the larger space of the dilute $Q = 1$ Potts model[138]. The additional relevant magnetic direction, which has an associated scaling dimension $x_H = 5/96 = 0.05208\cdots$, was originally suspected to be playing a role in the multiscaling seen here. The fractal

dimension of the largest cluster of the critical Ising model is[138, 139] $D_c = d - x_H = 1.947\cdots$, and thus it was suspected that for large q, the 'full' boxes covering this cluster would dominate $S(l,q)$. However, this would lead to $d\tau/dq \approx 1.947\cdots$ for $q \to \infty$, which does not seem to be the case. The Ising 'droplets' appear to dominate the scaling behavior of even quite large moments of the spin distribution.

In order to clarify these ideas, I have also applied this multiscaling analysis to the magnetization of the $d = 2$, $Q = 3$ Potts model[114], which has somewhat different critical behavior than the $d = 2$ Ising model. This critical point is known exactly for the square lattice model, the magnetic exponent is $x_h = 2/15 = 0.1333\cdots$, and the fractal dimension[139] of the largest cluster of like spins is $D_c = 28/15 = 1.866\cdots$. The results of the analysis of the traceless magnetizations $m(x) = 3\delta(s(x),t) - 1$, where $s(x)$ is the Potts spin, t is the label for the order parameter ($t = 1,2,3$), and δ is a Kronecker delta function, for a 256×256 square-lattice model using the same MC simulation parameters used for the sqaure-lattice Ising model above, are shown in Figures 5.15 and 5.16. The former shows the scaling of the sums of the moments: good scaling is obtained over approximately the same range of box sizes. The latter Figure indicates $d\tau/dq$, and it is consistent with a rise from the vicinity of $2 - \eta = 26/15 = 1.7333\cdots$ for $q \approx 0$ to near $2 - x_h = 28/15 = 1.8666\cdots$ for larger q.

There are many questions that have been raised by this work. The first is just the convergence of the analysis of the simulation results. There have been innumerable MC studies of quite large critical spin systems of this sort, and the reanalysis of existing data using this approach will probably prove quite interesting. On the analytical side, the formal justification of the step from (5.30) to (5.31) would allow the failure of this approach to be blamed on the use of the wrong scaling form for the q-point functions. Exact computation of $S(l,q)$ may be possible for some models: this would be extremely interesting.

In lieu of the complete $S(l,q)$, some exact information concerning the small-q expansion (5.34) would be welcome: both the justification of the assumption of an-

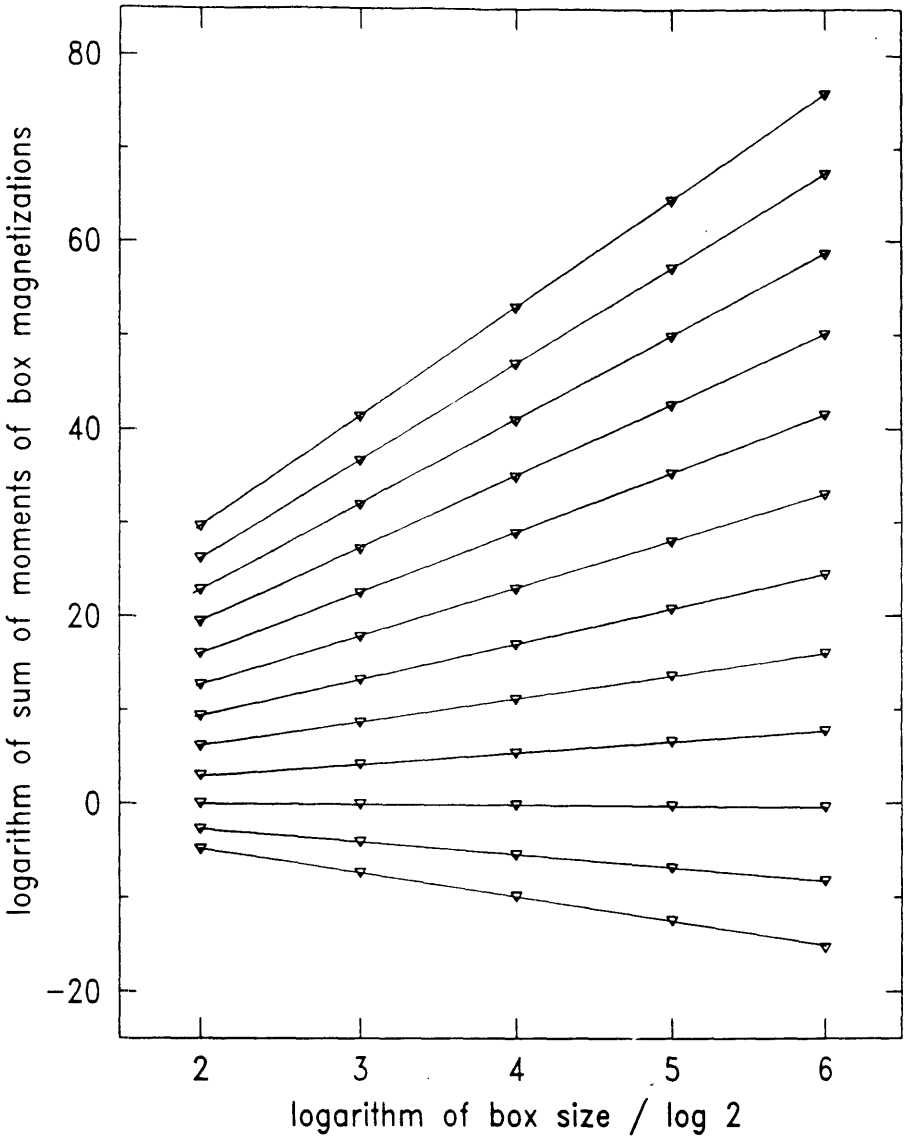

Figure 5.15: Scaling behavior of $S(l,q)$ for the $d = 2$, $Q = 3$ Potts model. Down triangles indicate the results of analysis of MC data, while the lines are the linear fits. The sets of data run from $q = -1$ to $q = 10$ from the bottom to the top of the Figure. Scaling is observed over a range comparable to that seen for the $d = 2$ Ising model.

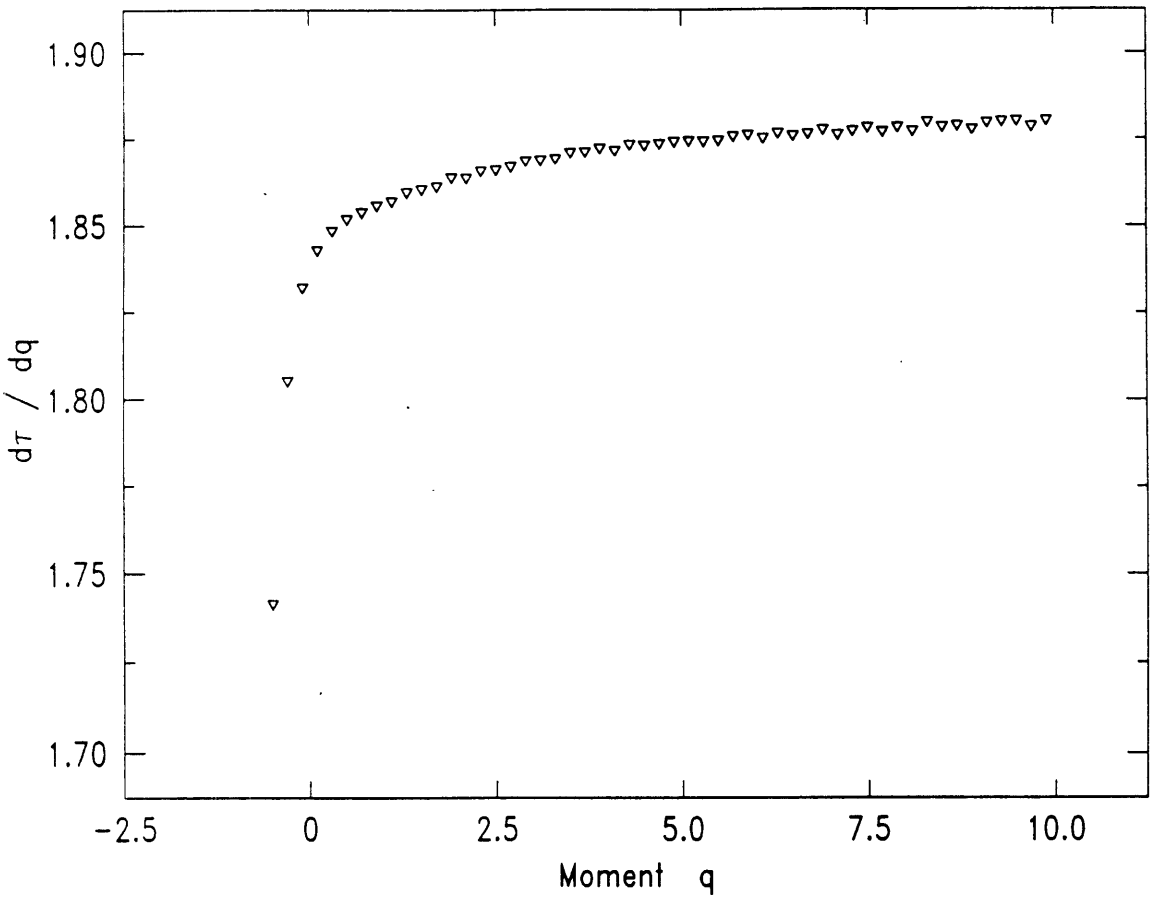

Figure 5.16: $d\tau/dq$ for the $Q = 3$ Potts model. As a function of moment q, the slope of τ rises from below 1.80 near $q = 0$ to slightly above 1.88 for $q \approx 10$.

alyticity at $q = 0$ and computation of either of the coefficients of the q or q^2 terms would be interesting. Any of these results might indicate how (if at all) the cluster dimensions affect these results. Finally, the study of this analysis applied to different critical models, including the $O(n)$ models[8] would be interesting.

It is a pleasure to acknowledge useful conversations with M. Kardar and B. Duplantier. I thank Professor R. Weiss and Dr. A. Jeffries of the MIT Gravitation and Cosmology Group for generously allowing the use of their computational facilities. This research was supported by the National Science Foundation under Contract No. DMR-87-19217.

Chapter 6

Conclusions and Directions for Future Research

The rather divergent topics bound together in this document indicate the result of several years of exploration of different areas of contemporary condensed matter physics. In this last section, I will indicate the conclusions that I have drawn, and more importantly, my view of what topics should be focused on in the near future.

The contributions to the study of the spin-gas model for reentrance in polar liquid crystals described here add to the body of work supporting this picture of the physics behind the remarkable experimental results that have been obtained in the last few years. The spin-gas theory continues to be a useful tool in understanding the behavior of frustrated polar liquid crystal systems. Microscopic theories based on molecular descriptions of complex liquids have, in my opinion, an important role in helping develop intuition and providing insight into mechanisms behind the novel physics seen in these systems. However, it is important to simultaneously make strong connections between these models and the underlying molecular Hamiltonian and also with their appropriate long-wavelength descriptions.

Advances that we must make in the case of the spin-gas model are to connect the layer model to a three-dimensional model, and also to understand the transformation from fluid degrees of freedom to the 'notch' and lattice approximations that we make. The justification of the triplet approximation, and of the type of prefacing transformation used is also an area requiring work, and perhaps might be addressed via Monte Carlo simulation, or by the use of Monte Carlo renormalization group methods.

A long-wavelength picture of this model is also lacking. There exist Landau theories for frustrated smectics[140], but unfortunately, the old problem of understanding the origin of the parameters in the theory renders this approach merely descriptive. The challenge before us to unify these different points of view is an example indicating why the study of liquid crystal systems has captivated physicists for generations.

The work that has been presented on the density-functional approach to statistical mechanics represents a step toward the first-principles description of phase transitions in fluid systems. The density-functional approach organizes our attack on a classical

statistical mechanical system, and leads us directly to *the* Landau theory for any structured phase. It is then up to the physicist to figure out what one-body density to use, and what to do with the resulting free energies computed from the grand potential functional.

The program for the application of this approach to a model of a fluid system hinges on the availability of liquid structure information. Past workers, including this author, have taken the easy way out by computing liquid structure using a lot of guesswork. The results of this thesis, and also of other workers, indicate that for molecular systems, the predictive power of the density-functional approach is a strong function of the quality of liquid state input. The problem of computation of reliable liquid state information concerning anisotropic molecules will thus be of great interest in the next few years. Recent advances in the numerical solution of the Percus-Yevick and hypernetted-chain closures of the Ornstein-Zernicke integral equation for anisotropic hard cores[52] are very encouraging, but there is also utility to the study of the density expansion for the direct correlation function. The utility of exactly solved limits of simple fluids should not be ruled out, as even one-dimensional models have been shown to be instructive in understanding liquid structure[13].

As the application of the density-functional approach is made to more complex molecular systems, it will become mandatory to use more systematic expansion techniques for the one-body density and for the liquid structure information. The parametrization of the density profile in terms of a few parameters will always be necessary, but the expression of the density using the 'order parameters' corresponding to all the spherical harmonics and plane waves will greatly reduce the work involved with the computation of the free energy functional, and will allow more attention to be paid to the essential physics.

This type of systematization of the density-functional procedure will new types of questions to be addressed. Fluctuations continue to be absent from the density-functional world, and they of course play an important role in the physics of fluids.

The understanding of liquid crystal systems via this approach hinges on our ability to compute elastic constants, and to thereby understand which long-wavelength fluctuations are important. Recently the computation of elastic properties for hard-core fluids via Monte Carlo simulation has become practical[63, 94], a development which should lead to many results that will guide the density-functional studies. The constructive approach to the Landau-Wilson theory of fluids that the density-functional method provides introduces interesting research problems involving the link between molecular structure and emergent structure and thermodynamics in complex fluid systems.

The dynamics of nonlinear systems often gives rise to patterns which are scale invariant. This introduces the study of scaling exponents as a means of characterizing such emergent patterns. Because a pattern produced by some process is a record of the physical process, we hope that classifying the pattern gives insight into the underlying dynamics.

I have discussed some simple models for the growth of multifractal trees, where the dynamics is completely coded into the resulting structure. Through mappings of the generalized dimensions to the free energy of equivalent statistical mechanical models, we have gained insight into methods that can be applied to study experimentally obtained multifractals. I have suggested that some of these models, particularly those incorporating disorder, may be relevant to the static and dynamic scaling of disintegration processes, and I plan to pursue both the theoretical and experimental study of this phenomenon.

Application of the same ideas to the analysis of magnetization distributions of critical spin models indicates that there is more to the geometry of critical phenomena than is generally appreciated. I have found an infinite set of geometrical scaling exponents related to the scaling of moments of the local magnetization. This is interesting because it suggests that families of geometrical scaling exponents, in some cases, may be unique to a universality class described by a smaller set of scaling

exponents. Much work needs to be done to clarify these results before we can claim to understand the geometry of critical phenomena.

In describing these projects, two areas of research that I plan to study further have been addressed. The first is the study of the statistical mechanics of fluids using a molecular Hamiltonian-based approach. The study of the statistical thermodynamics of fluids is an old area of condensed matter theory, but one which continues to be interesting because of the diversity and novelty of experimental results that continue to be obtained.

The second area of interest that I have identified is the understanding of the complex patterns that arise in nonlinear dynamical systems[142]. While low-dimension dynamical systems are to some extent understood[143], an unsettled frontier awaits those who venture into the realm of the dynamics of many degrees of freedom. This area promises to be one of the most exciting areas of condensed matter theory and experiment, and will lead to the study of phenomena outside of the traditional bounds of physics.

Bibliography

[1] H. E. Stanley, *Introduction to Phase Transitions and Critical Phenomena* , Oxford University Press, Oxford (1971), Ch. 10.

[2] J. D. van der Waals, Ph. D. Thesis, University of Leiden (1873).

[3] P. Curie, Ann. Chem. Phys. **5**, 289 (1895); P. Weiss, J. Phys. Radium, Paris **6**, 667.

[4] V. L. Ginzburg, Sov. Phys. Solid State **2**, 1824 (1960).

[5] L. P. Kadanoff, Physics **2**, 263 (1966).

[6] K. G. Wilson, Rev. Mod. Phys. **47**, 773 (1975).

[7] J. Cardy, in *Phase Transitions and Critical Phenomena*, ed. C. Domb and J. Lebowitz, Academic Press, New York (1987), Vol. 11, p. 55.

[8] B. Nienhuis, in *Phase Transitions and Critical Phenomena*, ed. C. Domb and J. Lebowitz, Academic Press, New York (1987), Vol. 11, p. 1.

[9] J. F. Marko, J. O. Indekeu and A. N. Berker, Phys. Rev. A **39**, 4201 (1989).

[10] F. Hardouin, Physica (Utrecht) **140A**, 359 (1986).

[11] J. F. Marko, Phys. Rev. Lett. **60**, 325 (1988).

[12] J. F. Marko, Phys. Rev. A, **39**, 2050 (1989).

[13] J. F. Marko, Phys. Rev. Lett. **62**, 543 (1989).

[14] J. F. Marko, Materials Research Society Extended Abstracts EA-17, *Fractal Aspects of Materials: Disordered Systems* , ed. D. A. Weitz, L. M. Sander and B. B. Mandelbrot, Materials Research Society, Pittsburgh (1988), p. 127.

[15] G. T. Pickett, B.Sc. Thesis, MIT (1989).

[16] J. Valasek, Phys. Rev. **17**, 475 (1921).

[17] P. E. Cladis, Phys. Rev. Lett. **35**, 48 (1975).

[18] W. A. Fertig, D. C. Johnston, L. E. DeLong, R. W. McCallum, M. B. Maple, and B. T. Mattias, Phys. Rev. Lett. **38**, 987 (1977).

[19] G. Toulouse, Comm. on Phys. **2**, 115 (1977).

[20] V. G. Vaks, A. I. Larkin, and Y. N. Ovchinnikov, JETP **22**, 820 (1966).

[21] F. Hardouin, A. M. Levelut, M. F. Achard, and G. Sigaud, J. Chim. Phys. **80**, 53 (1983).

[22] R. Shashidhar, B. R. Ratna, V. Surendranath, V. N. Raja, S. Krishna Prasad and C. Nagabhushan, J. Phys. (Paris) **46**, L445 (1985).

[23] A. N. Berker and J. S. Walker, Phys. Rev. Lett. **47**, 1469 (1981).

[24] J. O. Indekeu and A. N. Berker, Phys. Rev. A **33**, 1158 (1986).

[25] J. O. Indekeu and A. N. Berker, Physica (Utrecht) **140A**, 368 (1986).

[26] J. O. Indekeu, A. N. Berker, C. Chiang, and C. W. Garland, Phys. Rev. A **35**, 1371 (1987).

[27] A. N. Berker and J. O. Indekeu, in *Incommensurate Crystals, Liquid Crystals, and Quasi-Crystals*, J.F. Scott and N.A. Clark, eds. (Plenum, New York, 1987), p. 205.

[28] J. O. Indekeu, Phys. Rev. A **37**, 288 (1988).

[29] J. O. Indekeu and A.N. Berker, J. Phys. (Paris) **49**, 353 (1988).

[30] F. Hardouin, M. F. Achard, N. H. Tinh, and G. Sigaud, Mol. Cryst. Liq. Cryst. Lett. **3**, 7 (1986).

[31] R. F. M. Houtappel, Physica (Utrecht) **16**, 425 (1950).

[32] R. Dabrowski, K. Pyc, J. Prezedmojski, and B. Pura, Mol. Cryst. Liq. Cryst. **129**, 169 (1985).

[33] R. Shashidhar, B. R. Ratna, and S. Krishna Prasad, Mol. Cryst. Liq. Cryst. **130**, 179 (1985).

[34] J. Oitmaa, J. Phys. A **14**, 1159 (1981).

[35] V. N. Raja, B. R. Ratna, R. Shashidhar, G. Heppke, C. Bahr, J. F. Marko, J. O. Indekeu and A. N. Berker, Phys. Rev. A **39**, 4341 (1989).

[36] V. N. Raja, R. Shashidhar, B. R. Ratna, G. Heppke and C. Bahr, Phys. Rev. A **37**, 303 (1988).

[37] R. Shashidhar, Private communication (1989).

[38] T. V. Ramakrishnan and M. Yussouff, Phys Rev. B **19**, 2775 (1979).

[39] D. Mermin, Phys. Rev. **137**, A1441 (1965).

[40] J. L. Lebowitz and J. K. Percus, J. Math. Phys. **4**, 116 (1963).

[41] S. A. Rice and P. Gray, *The Statistical Mechanics of Simple Liquids*, John Wiley and Sons, Inc., New York (1965), Chapter 2.

[42] A. D. J. Haymet, J. Chem. Phys. **78**, 4641 (1983).

[43] G. L. Jones and U. Mohanty, Mol. Phys. **54**, 1241 (1985).

[44] M. Baus and J. L. Colot, Mol. Phys. **55**, 653 (1985).

[45] U. P. Singh and Y. Singh, Phys. Rev. A **33**, 2725 (1986).

[46] S. W. Rick S. J. Smithline and A. D. J. Haymet, J. Chem. Phys. **88**, 2004 (1988).

[47] S. Lago and P. Sevilla, J. Chem. Phys. **89**, 4349 (1988).

[48] W. A. Curtin and N. W. Ashcroft, Phys. Rev. A **32**, 2909 (1985).

[49] W. A. Curtin, Private communication (1987).

[50] A. R. Denton and N. W. Ashcroft, Phys. Rev. A **39**, 4701 (1989).

[51] J. P. van der Eerden, R. D. Groot and N. M. Faber, J. Chem. Phys. **87**, 2263 (1987).

[52] A. Perera, P. G. Kusalik, and G. N. Patey, J. Chem. Phys. **87**, 1295 (1987).

[53] B. J. Berne and P. Pechukas, J. Chem. Phys. **56**, 4213 (1972).

[54] B. M. Mulder D. Frenkel and J. P. McTague, Phys. Rev. Lett. **52**, 287 (1984).

[55] L. S. Ornstein and F. Zernicke, Koninkl. Ned. Akad. Wetenschap., Proc. Ser. B **17** , 793 (1914).

[56] E. W. Grundke and D. Henderson, Mol. Phys. **24**, 269 (1972).

[57] J K. Percus and G. J. Yevick, Phys. Rev. Lett. **110**, 1 (1957).

[58] M. S. Wertheim, Phys. Rev. Lett. **10**, 321 (1963).

[59] R. Pynn, Solid State Commun. **14**, 29 (1974).

[60] A. Wulf, J. Chem. Phys. **67**, 2254 (1977).

[61] W. R. Smith and D. Henderson, Mol. Phys. **3**, 411 (1970).

[62] D. Frenkel and J. P. McTague, Ann. Rev. Phys. Chem. **31**, 491 (1980).

[63] B. M. Mulder and D. Frenkel, Mol. Phys. **55**, 1193 (1985).

[64] J. L. Colot, X.-G. Wu., H. Xu, and M. Baus, Phys. Rev. A **38**, 2022 (1988).

[65] For discussions of thermodynamics of similar systems obtained by transfer-matrix techniques, see L. M. Casey and L. K. Runnels, J. Chem. Phys. **51**, 5070 (1969); J. L. Lebowitz, J. K. Percus, and J. Talbot, J. Stat. Phys. **49**, 1221 (1987).

[66] L. Tonks, Phys. Rev. **50**, 955 (1936).

[67] L. Onsager, Ann. N.Y. Acad. Sci. **51**, 627 (1949).

[68] J. L. Lebowitz, Phys. Rev. **133**, A895 (1964).

[69] G. Stell, Physica (Utrecht) **29**, 517 (1963).

[70] M. S. Wertheim, in *The Equilibrium Theory of Classical Fluids*, edited by H. L. Frisch and J. L. Lebowitz, Benjamin Press, New York, (1964), p. II-281.

[71] T. Morita and K. Hiroike, Prog. Theor. Phys. *23*, 1003 (1960).

[72] For a study of the high-density limit, see Y. Rosenfeld, Phys. Rev. A **32**, 1834 (1985).

[73] S. Lago and P. Sevilla, J. Chem. Phys. **89**, 4349 (1988).

[74] M. Baus, J. L. Colot, X. G. Wu, and H. Xu, Phys. Rev. Lett. **59**, 2184 (1987).

[75] W. A. Curtin and N. W. Ashcroft, Phys. Rev. Lett. **56**, 2775 (1986).

[76] W. A. Curtin, Phys. Rev. Lett. **59**, 1228 (1987).

[77] W. A. Curtin and K. Runge, Phys. Rev. A **35**, 4755 (1987).

[78] S. Kielich, *Dielectric and Related Molecular Processes*, Chemical Society of London, London (1972), Vol. 1, Chapter 7.

[79] J. Stecki and A. Kloczkowski, J. Phys. (Paris) **40**, C3-360 (1979); Mol. Phys. **42**, 51 (1981).

[80] G. Patey, Private communication (1988).

[81] O. K. Rice, J. Chem. Phys. **12**, 1 (1944).

[82] D. Frenkel and J. P. McTague, Ann. Rev. Phys. Chem. **31**, 491 (1980).

[83] A. D. J. Haymet, Ann. Rev. Phys. Chem. **38**, 89 (1987).

[84] D. A. Young and B. J. Adler, J. Chem. Phys. **60**, 1254 (1974).

[85] K. W. Kratky, Chem. Phys. **57**, 167 (1981).

[86] D. Frenkel and A. J. C. Ladd, J. Chem. Phys. **81**, 3188 (1984).

[87] N. F. Carnahan and K. E. Starling, J. Chem. Phys. **51**, 635 (1969).

[88] R. M. Cotterill, E. J. Jensen, W. D. Kristensen, in *Anharmonic Lattices, Structural Transitions, and Melting*, ed. T. Riste, Noordhoft (1974).

[89] J. L. Colot and M. Baus, Mol. Phys. **56**, 807 (1985).

[90] J. D. McCoy, S. Singer and D. Chandler, J. Chem. Phys. **87**, 4853 (1987).

[91] B. B. Laird, J. D. McCoy and A. D. J. Haymet, J. Chem. Phys. **88**, 3900 (1988).

[92] E. W. Grundke and D. Henderson, Mol. Phys. **24**, 269 (1972).

[93] D. A. Young and B. J. Alder, J. Chem. Phys. **60**, 1254 (1974).

[94] K. J. Runge and G. V. Chester, Phys. Rev. A **36**, 4852 (1987).

[95] D. Frenkel and A. J. C. Ladd, Phys. Rev. Lett. **59**, 1169 (1987).

[96] E. Velasco and P. Tarazona, Phys. Rev. A **36**, 979 (1987).

[97] M. V. Jaric and U. Mohanty, Phys. Rev. Lett. **58**, 230 (1987), Phys. Rev. B **37**, 4441 (1988).

[98] K. M. Rabe, Ph.D. Thesis, MIT (1987).

[99] S. K. Ma, Phys. Rev. Lett. **37**, 461 (1976).

[100] R. H. Swendsen, Phys. Rev. Lett. **42**, 859 (1979).

[101] R. H. Swendsen and A. N. Berker, Phys. Rev. B **28**, 3897 (1983).

[102] R. H. Swendsen, Phys. Rev. Lett. **52**, 1165 (1984).

[103] R. H. Swendsen, Phys. Rev. Lett. **52**, 2321 (1984).

[104] R. H. Swendsen and S. Krinsky, Phys. Rev. Lett. **43**, 177 (1979).

[105] R. H. Swendsen, Topics in Current Physics **30** : *Real-Space Renormalization*, ed. T. W. Burkhardt and J. M. J. van Leeuwen, Springer-Verlag, Berlin (1982), Chapter 3.

[106] T. W. Burkhardt and J. M. J. van Leeuwen, Topics in Current Physics **30** : *Real-Space Renormalization*, ed. T. W. Burkhardt and J. M. J. van Leeuwen, Springer-Verlag, Berlin (1982), Chapter 1.

[107] K. Binder, Topics in Current Physics **7** : *Monte Carlo Methods in Statistical Physics*, ed. K. Binder, Springer-Verlag, Berlin (1986), Chapter 1.

[108] A. N. Berker, S. Ostlund, and F. A. Putnam, Phys. Rev. B **17**, 3650 (1978).

[109] M. E. Fisher, Rev. Mod. Phys. **46**, 597 (1974).

[110] H. E. Stanley, *Introduction to Phase Transitions and Critical Phenomena* , Oxford University Press, Oxford (1971), Ch. 3.

[111] L. Onsager, Phys. Rev. **65**, 117 (1944).

[112] M. Nauenberg and B. Nienhuis, Phys. Rev. Lett. **33**, 1598 (1974).

[113] R. B. Potts, Proc. Camb. Phil. Soc. **48**, 106 (1952).

[114] F. Y. Wu, Rev. Mod. Phys. **54**, 235 (1982).

[115] R. J. Baxter, J. Phys. C **6**, L445 (1973), and R. J. Baxter, H. N. V. Temperley and S. E. Ashley, Proc. Roy. Soc. London, Ser. A **358**, 535 (1978).

[116] R. H. Swendsen, D. Andelman, and A. N. Berker, Phys. Rev. B **24**, 6732 (1981).

[117] C. Dasgupta, Phys. Rev. B **15**, 3460 (1977).

[118] B. Nienhuis, J. Phys. A **15**, 199 (1982).

[119] M. P. M. den Nijs, Phys. Rev. B **27**, 1674 (1983).

[120] M. J. Feigenbaum, J. Stat. Phys. **19**, 25 (1978); **21**, 669 (1979), Los Alamos Science **1**, 4 (1980).

[121] M. H. Jensen, L. P. Kadanoff, A. Libchaber, I. Procaccia and J. Stavans, Phys. Rev. Lett. **55**, 2798 (1985).

[122] C. Amitrano, A. Coniglio and F. di Liberto, Phys. Rev. Lett. **57**, 1016 (1986).

[123] B. B. Mandelbrot, *Fractal-Form, Chance and Dimension*, Freeman Press, San Francisco (1977).

[124] K. G. Wilson and J. Kogut, Physics Reports **12**, 75 (1974).

[125] B. B. Mandelbrot, J. Fluid Mech. **62**, 331 (1974).

[126] U. Frisch and G. Parisi, in *Turbulence and Predictability in Geophysical Fluid Dynamics and Climate Dynamics*, ed. M. Ghil, R. Benzi, and G. Parisi, North-Holland, New York (1985).

[127] H. G. E. Hentschel and I. Procaccia, Physica D **8**, 435 (1983).

[128] T. C. Halsey, M. H. Jensen, L. P. Kadanoff, I. Procaccia and B. I. Shraiman, Phys. Rev. A **33**, 1141 (1986); M. H. Jensen, L. P. Kadanoff and I. Procaccia, Phys. Rev. A **36**, 1409 (1987).

[129] M. J. Feigenbaum, M. H. Jensen and I. Procaccia, Phys. Rev. Lett. **57**, 1503 (1986).

[130] D. Katzen and I. Procaccia, Phys. Rev. Lett. **58**, 1169 (1987).

[131] L. Pietronero, A. Erzan, and C. Evertsz, Phys. Rev. Lett. **61**, 861 (1988).

[132] D. Bensimon, M. H. Jensen and L. P. Kadanoff, Phys. Rev. A **33**, 3622 (1986).

[133] R. K. Pathria, *Statistical Mechanics*, Pergamon Press, Oxford (1972), pp. 424-426.

[134] S. Havlin, R. Blumberg-Selinger, M. Schwartz, H. E. Stanley and A. Bunde, Phys. Rev. Lett. **61**, 1438 (1988).

[135] see for example, X. R. Wang, Y. Shapir and M. Rubinstein, Phys. Rev. A **39**, 5974 (1989), and references contained therein.

[136] J. Lee, P. Alstrom and H. E. Stanley, Phys. Rev. A **39**, 6545 (1989).

[137] M. Mezard, G. Parisi and M. A. Virasoro, *Spin Glass Theory and Beyond*, World Scientific, New Jersey (1987), Chapter 1.

[138] A. L. Stella and C. Vanderzande, Phys. Rev. Lett. **62**, 1067 (1989).

[139] B. Duplantier and H. Saleur, Phys. Rev. Lett. **63** (1989), also B. Duplantier, Private communication.

[140] P. Pershan and J. Prost, J. Phys (Paris) **40**, L27 (1979); J. Prost and P. Barois, J. Chim. Phys. **80**, 65 (1983); J. Prost, Adv. Phys. **33**, 1 (1984); P. Barois, J.

Prost and T. C. Lubensky, J. Phys. (Paris) **46**, 391 (1985); P. Barois, Phys. Rev. A **33**, 3632 (1986).

[141] M. P. Allen and D. Frenkel, Phys. Rev. A **37**, 1813 (1988).

[142] H. E. Stanley, *On Growth and Form: Fractal and Non-Fractal Patterns in Physics*, Dordrecht, Amsterdam (1986).

[143] see A. W. Cumming, Ph.D. Thesis, MIT (1988) and references therein.

About the Author

John Marko was born on October 25, 1962 in Kingston-upon-Thames, England, and attended St. Boniface Elementary School, Cartier-McGee Junior High School, and Louis St. Laurent Senior High School, all in Edmonton, Canada. He entered the University of Alberta in 1980, and received the degree of Bachelor of Science there in 1984. Graduate school at the Massachusetts Institute of Technology followed, focusing on research in theoretical condensed matter physics supervised by Professor A. Nihat Berker.

For the next year or two, the author will be at the James Franck Institute of the University of Chicago, under a Postdoctoral Scholarship from the Natural Sciences and Engineering Research Council of Canada.